ABSTRACT

Title of Dissertation: **ACTIVE SUPPRESSION OF VORTEX-DRIVEN COMBUSTION INSTABILITY USING CONTROLLED LIQUID-FUEL INJECTION**

Bin Pang, Ph.D., 2005

Dissertation Directed By: **Professor Kenneth H. Yu, Department of Aerospace Engineering**

Combustion instabilities remain one of the most challenging problems encountered in developing propulsion and power systems. Large amplitude pressure oscillations, driven by unsteady heat release, can produce numerous detrimental effects.

Most previous active control studies utilized gaseous fuels to suppress combustion instabilities. However, using liquid fuel to suppress combustion instabilities is more realistic for propulsion applications. Active instability suppression in vortex-driven combustors using a direct liquid fuel injection strategy was theoretically established and experimentally demonstrated in this dissertation work.

Droplet size measurements revealed that with pulsed fuel injection management, fuel droplet size could be modulated periodically. Consequently, desired heat release fluctuation could be created. If this oscillatory heat release is coupled with the natural pressure oscillation in an out of phase manner, combustion instabilities can be suppressed.

To identify proper locations of supplying additional liquid fuel for the purpose of achieving control, the natural heat release pattern in a vortex-driven combustor was characterized in this study. It was found that at high Damköhler number oscillatory heat release pattern closely followed the evolving vortex front. However, when Damköhler number became close to unity, heat release fluctuation wave no longer coincided with the coherent structures. A heat release deficit area was found near the dump plane when combustor was operated in lean premixed conditions.

Active combustion instability suppression experiments were performed in a dump combustor using a controlled liquid fuel injection strategy. High-speed Schlieren results illustrated that vortex shedding plays an important role in maintaining self-sustained combustion instabilities. Complete combustion instability control requires total suppression of these large-scale coherent structures. The sound pressure level at the excited dominant frequency was reduced by more than 20 dB with controlled liquid fuel injection method.

Scaling issues were also investigated in this dump combustor to test the effectiveness of using pulsed liquid fuel injection strategies to suppress instabilities at higher power output conditions. With the liquid fuel injection control method, it was possible to suppress strong instabilities with initial amplitude of ± 5 psi down to the background noise level. The stable combustor operating range was also expanded from equivalence ratio of 0.75 to beyond 0.9.

ACTIVE SUPPRESSION OF VORTEX-DRIVEN COMBUSTION INSTABILITY USING CONTROLLED LIQUID-FUEL INJECTION

By

Bin Pang

Dissertation submitted to the Faculty of the Graduate School of the
University of Maryland, College Park, in partial fulfillment
of the requirements for the degree of
Doctor of Philosophy
2005

Advisory Committee:
Associate Professor Kenneth H. Yu, Chair
Professor Ashwani K. Gupta
Associate Professor Jungho Kim
Associate Professor James D. Baeder
Assistant Professor Christopher Cadou

Acknowledgements

I would like to express sincere thanks to my advisor, Dr. Kenneth H. Yu, for his guidance, encouragement and support of my research and my life in the last five years. Without him, this work would not have been possible. I would also like to thank my committee members Dr. Ashwani K. Gupta, Dr. James D. Baeder, Dr. Christopher Cadou and Dr. Jungho Kim for their time and advice.

Thanks also go to the many professors and co-workers in the Aerospace Department for their generous help during these years. Special thanks Dr. Andre W. Marshall for providing the Malvern droplet size analysis instrument.

In addition, I am especially grateful to Donald W. Morrison, who read the manuscript and offered helpful English editing suggestions.

My sincere gratitude also goes to my family for their invaluable encouragement and support throughout my entire life.

This research was sponsored by the Office of Naval Research, led by scientific officer Dr. Gabriel D. Roy. The support is gratefully acknowledged.

Table of Contents

Acknowledgements ii
Table of Contents iii
List of Tables v
List of Figures vi
Nomenclature vii
Chapter 1: Introduction 1
1.1 Statement of Problem 1
1.2 Objectives 2
1.3 Scope of Investigation 3
Chapter 2: Literature Review 5
2.1 Thermo-Acoustic Instabilities 5
2.2 Passive Combustion Instability Control 9
2.3 Active Combustion Instability Control 11
Chapter 3: Experimental Apparatus and Diagnostics 13
3.1 Experimental Facilities 13
3.1.1 Dump Combustor Rig 13
3.1.2 Air Supply System 16
3.1.3 Main Fuel Management System 17
3.1.4 Liquid Fuel Injection System 17
3.1.5 Ignition System 18
3.1.6 Combustor and Exhaust Cooling System 19
3.2 Instrumentations and Flow Visualization 19
3.2.1 High-speed Spark Schlieren Imaging Technique 19
3.2.2 CH* Chemiluminescence Measurement 23
3.2.3 Malvern Instrument 23
3.2.4 Particle Image Velocimetry System 26
3.3 Sensors and Actuators 29
Chapter 4: Dynamics of Two-phase Flow Field 33
4.1 Introduction 33
4.2 Transient Characteristics of Controlling Liquid Fuel 34
4.2.1 Liquid Fuel Droplet Size Distribution as a Function of Injection Phase 34
4.2.2 Corresponding Variation in Liquid Fuel Heat Release Fluctuation 45
4.3 Velocity Profile of Controlled Liquid Fuel Droplets 50
4.4 Summary and Discussion 59
Chapter 5: Heat Release Pattern .vs. Vortex Structures 61
5.1 Introduction 61
5.2 Experimental Setup and Instrumentation 61
5.3 Flame Model 64
5.4 Combustor Model 72
5.5 Summary and Discussion 76
Chapter 6: Self-sustained Vortex-driven Combustion Instability Control 78
6.1 Introduction 78
6.2 Low Mach Number Experimental Results 79

6.2.1 Dump Combustor without Control 79
6.2.1.1 Pressure Spectra……79
6.2.1.2 Schlieren Images……86
6.2.1.3 Flame Images……88
6.2.2 Dump Combustor with Open-loop Control 89
6.2.2.1 Pressure Spectra……89
6.2.2.2 Schlieren Images……93
6.2.2.3 Flame Images……..……..95
6.2.3 Dump Combustor with Close-loop Control..... 97
6.2.3.1 Pressure Spectra……97
6.2.3.2 Schlieren Images……99
6.2.3.3 Flame Images……...101
6.3 High Mach Number Experimental Results..... 101
6.4 Summary and Discussion..... 108
Chapter 7: Conclusions and Future Work..... 109
7.1 Conclusions..... 109
7.2 Future Work..... 110
Appendix A – Averaged Droplets Sauter.Mean Diameter……..112
Appendix B – Time-evolution of Droplets Sauter-Mean-Diameter……....132
Appendix C – Phase-locked Schlieren and CH* Image Sequence for Flame Model…..163
Appendix D – Dynamic Pressure Trace and Spectra……...201
Appendix E – Transient Spark Schlieren Image Sequence……219
References……240

List of Tables

Table 5.1: Experimental conditions for jet flame combustion model……...63

Table 5.2: Experimental conditions for combustor model……....71

Table 6.1 Maximum RMS value of the dynamic pressure at 38 Hz of different experimental conditions……..……...83

List of Figures

Fig. 2.1: Reacting Fluid Flow with Heat added at $x=x_f$……..6

Fig. 3.1: Schematic of test rig ……..…….14

Fig.3.2: Picture of test facility. This shows the dump combustor, liquid fuel system and igniter…….15

Fig. 3.3: Air supply system……....16

Fig. 3.4: Liquid fuel injection system……....18

Fig. 3.5: Ignition system…….…...19

Fig. 3.6: Diagram of a typical Schlieren system……....21

Fig. 3.7: Diagram of Malvern/INSITEC In-Line Ensemble Particle Concentration and Size (EPCS) system…….……..24

Fig. 3.8: Diagram of a 2.Dimensional Particle Image Velocimetry system…….…….27

Fig. 4.1: Controlling liquid fuel flow rate .vs. duty cycle…….….33

Fig. 4.2: Controlling liquid fuel flow rate .vs. forcing frequency……..34

Fig. 4.3: Controlling liquid fuel flow rate .vs. forcing pressure……....34

Fig. 4.4: Contour map of fuel flow rate changes with frequency and pressure…….35

Fig. 4.5: Planar Mie-scattering image of a typical fuel spray with the probe area marked for Malvern droplet sizing measurements…….….36

Fig. 4.6: Ethanol droplet size distribution at pressure 20 psi, forcing frequency 125 Hz and 50% duty cycle……....37

Fig. 4.7: Ethanol droplet size distribution at pressure 20 psi, frequency 38 Hz and duty cycle: (a) 25%, (b) 50%, (c) 75%, (d) 100%….……....38

Fig. 4.8: Ethanol droplet size distribution at pressure 20 psi, 50% duty cycle, and forcing frequency: (a) 38 Hz, (b) 100 Hz, (c) 200 Hz, (d) 300 Hz…..……...39

Fig. 4.9: Ethanol droplet size distribution at forcing frequency 38 Hz, 50% duty cycle, and injection pressure: (a) 20 psi, (b) 30 psi, (c) 40 psi, (d) 50 psi…….……..40

Fig. 4.10: Average Sauter-Mean-Diameter as a function of forcing frequency and injection pressure……...41

Fig. 4.11: Phase-locked ethanol droplets size distribution at pressure 20 psi, forcing frequency 125 Hz, 50% duty cycle, phase anger (a) 0˚, (b) 90˚, (c) 180˚, (d) 270˚...…...42

Fig. 4.12: Phase-lock-averaged Sauter-Mean-Diameter variation at different injection conditions……...43

Fig. 4.13: Phase-locked heat release rate variation at different injection conditions……47

Fig. 4.14: A complete cycle of planar Mie-scattering images at forcing frequency 38 Hz, 20 psi and 50% duty cycle…….....49

Fig. 4.15: Planar Mie-scattering images at different forcing conditions: (a) 20 psi, 38 Hz; (b) 20 psi, 280 Hz; (c) 60 psi, 38 Hz; (d) 60 psi, 280 Hz……...49

Fig. 4.16: A sequence of phase-lock-averaged velocity profile images at forcing frequency 38 Hz and injection pressure 20 psi……..51

Fig. 4.17: Phase-lock-averaged velocity profile at same injection pressure 40 psi, same duty cycle 50%, but with different forcing frequency: (a) 38 Hz, (b) 150 Hz, (c) 280 Hz……...52

Fig. 4.18: Phase-lock-averaged velocity profile at same forcing frequency 280 Hz, same duty cycle 50%, but with different injection pressure: (a) 20 psi, (b) 40 psi, (c) 60 psi……...53

Fig. 4.19: Sequence of phase-lock-averaged planar Mie-scattering spray images at different phase of a cycle (a) without combustion; (b) with combustion, liquid fuel was forced at 38 Hz, 20 psi and 50% duty cycle……..54

Fig. 4.20: Phase-averaged velocity profiles of fuel droplets at different phase of a cycle (a) nonreacting case; (b) reacting case, liquid fuel was forced at 38 Hz, 20 psi and 50% duty cycle……...56

Fig. 4.21: Droplets velocity at x = 41.32 mm from dump plane at different phase angle (a) 0°; (b) 90°; (c) 180°; (d) 270°, liquid fuel was forced at 38 Hz, 20 psi and 50% duty cycle……...57

Fig. 5.1: Vortex-stabilized jet flame model……...61

Fig. 5.2: Combustor model……....62

Fig. 5.3: (a) Flow dynamic time; (b) Chemistry time……....64

Fig. 5.4: (a) Strouhal number; (b) Damköhler number…….…….65

Fig. 5.5: Phase-locked instantaneous Schlieren images of a cycle at forcing amplitude 20V and forcing frequency 240 Hz……....66

Fig. 5.6: Phase-lock-averaged Schlieren images of a cycle at forcing amplitude 20V and forcing frequency 240 Hz……..66

Fig. 5.7: Phase-locked CH* Chemiluminescence oscillation images of a cycle at forcing amplitude 20V and forcing frequency 240 Hz…….…..68

Fig. 5.8: Phase-resolved visualization of instantaneous Schlieren and CH* chemiluminescence images of a cycle at forcing amplitude 20V and forcing frequency 240 Hz…….…...68

Fig. 5.9: Effect of forcing amplitude at 180 Hz (a) 5V, (b) 10V, (c) 15V, (d) 20V from top to bottom: spark Schlieren images, averaged Schlieren images, CH* chemiluminescence oscillations images, superimposed composite images……..69

Fig. 5.10: Effect of forcing frequency at 20V (a) 180 Hz, (b) 240 Hz, (c) 300 Hz, (d) 360 Hz from top to bottom: spark Schlieren images, averaged Schlieren images, CH* chemiluminescence oscillations images, superimposed composite images……..70

Fig. 5.11: (a) Strouhal number; (b) Damköhler number…….…...71

Fig. 5.12: Schlieren images and CH* chemiluminescence oscillations images at equivalence ratio of 0.7 test conditions……..72

Fig. 5.13: Schlieren images and CH* chemiluminescence oscillations images at equivalence ratio of 0.6 test conditions……..73

Fig. 5.14: Luminescence images at equivalence ratio: (a) 0.6, (b) 0.65, (c) 0.7…….…...74

Fig. 6.1: Typical pressure oscillation when combustion instability occurs……...79

Fig. 6.2: Dynamic pressure signal in the chamber during stable combustion……...80

Fig. 6.3: FFT of dynamic pressure signal inside the chamber during stable combustion…..…….……...81

Fig. 6.4: Dynamic pressure signal inside the chamber during unstable combustion…....81

Fig. 6.5: FFT of dynamic pressure signal inside the chamber during unstable combustion…….82

Fig. 6.6: Contour map of the dynamic RMS pressure at 38 Hz of different experimental conditions……..….83

Fig. 6.7: A sequence of averaged Schlieren images taken for the uncontrolled case…....85

Fig. 6.8: Flame structure of no combustion control case……...86

Fig. 6.9: Dynamic pressure signal inside the chamber for open-loop control methods……..88

Fig. 6.10: FFT of dynamic pressure signal inside the chamber for open-loop control methods……..89

Fig. 6.11: Dynamic pressure signal inside the chamber for different conditions……..89

Fig. 6.12: FFT of dynamic pressure signal inside the chamber for different conditions……...90

Fig. 6.13: A sequence averaged Schlieren images taken for the open-loop control case……92

Fig. 6.14: Vortex convection velocity at different test conditions…….....93

Fig. 6.15: Flame structure of open loop control case…….....94

Fig. 6.16: Flame structure of open loop control case…….....94

Fig. 6.17: Dynamic pressure signal inside the chamber for different test conditions…....96

Fig. 6.18: FFT of dynamic pressure signal inside the chamber for different test conditions……...97

Fig. 6.19: A sequence of Schlieren images for the close-loop control case……..98

Fig. 6.20: A sequence of flame images for the close-loop control case……....99

Fig. 6.21: Dynamic pressure signal inside the chamber with no control condition...…..101

Fig. 6.22: FFT of dynamic pressure signal inside the chamber with no control condition……..101

Fig. 6.23: Dynamic pressure signal inside the chamber with open-loop control condition……..102

Fig. 6.24: FFT of dynamic pressure signal inside the chamber with open-loop control condition……..103

Fig. 6.25: Dynamic pressure signal inside the chamber with close-loop control condition……..103

Fig. 6.26: FFT of dynamic pressure signal inside the chamber with close-loop control condition……..104

Fig. 6.27: Onset of the combustion instability with different control strategies…….…105

Nomenclature

D	Droplet diameter
Da	Damköhler number
D_0	Initial droplet diameter
D_{32} (SMD)	Sauter mean diameter
E	Energy
e	Specific internal energy
f	Frequency
h	Heat transfer coefficient
h_{fg}	Heat of formation
h_{RP}	Heat of reaction
k	Thermal conductivity
Nu	Nusselt number
p	Pressure
Pr	Prandtl number
Q	Heat release rate of a burning droplet
Q_{max}	Maximum heat release rate of a burning droplet
q	Heat release per volume (or specific heat release)
R	Specific gas constant
Re	Reynolds number
T	Temperature
T_∞	Free stream temperature

T_f	Droplet temperature
T_{fb}	Fuel boiling point temperature
T_g	Gas temperature
t	Time
u	Velocity
V	Volume
x	Position
γ	Ratio of specific heat
Δ	Change in
ε	Acoustic energy density
ϕ	Equivalence Ratio
ρ	Density
ρ_f	Density of fuel droplet
τ	Characteristic time
τ_{chem}	Chemistry time
τ_{flow}	Flow dynamic time

Subscripts

chem	Chemistry
g	Gas
f	Flame; fuel
fb	Fuel boiling point

0	Initial condition
∞	Free stream

Superscripts

-	Mean component
'	Fluctuating component

Chapter 1: Introduction

1.1 Statement of Problem

Continuous combustion processes prevail in many fields including propulsion, heating and power generation. In some circumstances, the combustion process is smooth enough that the pressure oscillations inside the chamber are small. However, under some conditions, the combustion is so rough that the pressure fluctuations inside the chamber become quite large and unacceptable.

Combustion instability, which refers to sustained undesired large amplitude pressure and velocity oscillations inside the chamber due to the coupling between unsteady heat release and acoustic movements of flow field, can occur at a wide range of frequencies depending on various parameters such as system geometry, flow parameters, the equivalence ratio and the fuel type.

These instabilities are prevalent in combustion systems because even a tiny fraction of the available chemical energy is sufficient to produce unacceptably large unsteady motions if coupled with its resonant characteristics. Moreover, the fact that the combustion chambers are almost closed could make this problem worse since the processes that attenuate unsteady motions are weak.

To reduce NO_X emissions, gas turbines are being designed to operate in a lean, premixed mode of combustion. However, it is well known that these lean premixed operating conditions are especially susceptible to combustion instabilities.

Advanced propulsion applications require smaller, lighter combustors operating under higher pressure and temperature conditions and complying with higher environmental standards. The combustion processes in those confined systems usually

also favor excitation of unsteady motions over a broad range of frequencies due to the high energy densities and low losses in combustion chambers.

Although the energy involved in the combustion instability is only a small portion of the available chemical energy, these large amplitude pressure oscillations can cause substantial detrimental effects such as severe mechanical vibrations, cyclic fatigue, high levels of acoustic noise, increased heat transfer, excessive erosion of chamber walls, and reduced performance. In ramjets, large pressure fluctuations inside the combustion chamber can push the shock out of the inlet duct and reduce the mass flow coming into the ramjet and cause inlet unstart.

Much research work has been done on this problem since the 1980s [1-6], when the suppression of combustion instabilities was demonstrated in laboratories in reduced scale rigs. However, the actual physical mechanisms associated with combustion of realistic fuels are not been clearly understood. These large amplitude oscillations remain the most challenging problems in the effort to develop, produce, and upgrade combustion processes in realistic propulsion systems. To maximize benefits from the laboratory studies and extend their application to realistic propulsion systems [7-12], a lot of work still needs to be done to obtain efficient and stable combustion.

1.2 Objectives

Combustion instability is a very complex problem and involves nonlinear interactions among acoustic waves, vortex movement and unsteady heat release. Although combustion instability and active combustion control have been studied for many years, some of the problems are still not very well understood. These include

mechanisms of combustion instability, optimum control strategy and role of liquid fuel in the instability and possible control processes.

For this dissertation work, the investigation focused on active suppression of vortex-driven combustion instability using controlled liquid-fuel injection. The primary goal of this study was to understand the physical mechanisms responsible for onset of instabilities in model ramjet dump combustors and explore active ways to control the large amplitude pressure oscillations inside the chamber. This research had the following three technical objectives:

- Better understand physical mechanisms responsible for active control of combustion instabilities in liquid-fueled combustors,
- Demonstrate active combustion control using pulsed liquid fuel injection in a laboratory scale dump combustor simulating a ramjet burner, and
- Study limitations associated with scaling the results by conducting experiments at realistic velocity conditions.

1.3 Scope of Investigation

To achieve the above objectives, a series of experimental studies were conducted. The studies can be classified into four phases that include: simple component level experiments; construction of a test rig and qualification experiments; a detailed case study and a scale-up study. Since gaseous fueled active control had been examined by many others [8-12], only liquid-fueled active control was considered in this dissertation work. Moreover it is more practical to utilize liquid fuel instead of gaseous fuel in real situations [13]. Only suppression of vortex-driven combustion instabilities was investigated because it appeared to be the most common type of instabilities that cause

problems in air-breathing propulsion systems. Lastly, since the main focus of this thesis was to understand the physical mechanisms behind combustion instability control, a simple phase-delay type controller was considered in much of this study. A more sophisticated control system involving a LQG adaptive controller was employed only during the last phase when scale-up testing was conducted.

The following key tasks were carried out to complete the investigation:

1. Detailed pulsed fuel spray characterizations including droplet size distribution and velocity profiles were obtained, and heat release patterns resulting from the controlled liquid fuel droplets were analyzed.

2. Natural heat release patterns in the vortex-driven combustion process were investigated as a function of time and with respect to the axial location of convecting vortices.

3. A dump combustor test facility was built and systematically studied to acquire the complete map of pressure oscillations inside the chamber at different operating conditions.

4. Extensive liquid-fueled active combustion control experiments were conducted to reveal the basic physical mechanisms associated with the combustion instability and its control for a selected case that was easily repeatable.

5. The ability to suppress large amplitude pressure oscillation at combustor inlet Mach number of 0.3 was examined to check the effectiveness of liquid fuel injection control strategies at realistic flow velocities.

Chapter 2: Literature Review

2.1 Thermo-Acoustic Instabilities

The first observation of combustion oscillation was the "singing flame" which was discovered by Higgins [14] in 1777. Later Le Conte [15] discovered the "dancing flame" where a flame pulses in sync with the audible beats of music. Around 1850, Rijke [16] discovered that sound can be generated by placing a heat source in the lower half of a vertical tube that is open at both ends. These are classic examples of Thermo-Acoustic phenomena that reveal how energy transforms from thermal sources to acoustic forms.

As a result of his studies of acoustic waves generated and sustained by heat addition, Lord Rayleigh first stated his famous criterion in 1878 [17]:

"If heat be periodically communicated to, and abstracted from, a mass of air vibrating (for example) in a cylinder bounded by a piston, the effect produced will depend upon the phase of the vibration at which the transfer of heat takes place. If heat be given to the air at the moment of greatest condensation, or be taken from it at the moment of greatest rarefaction, the vibration is encouraged. On the other hand, if heat be given at the moment of greatest rarefaction, or abstracted at the moment of greatest condensation, the vibration is discouraged."

The importance of the phase relationship between the pressure oscillations and the unsteady heat fluctuations in encouraging the instability was clearly demonstrated in the following years.

In a mathematical framework by Chu and Kovasznay [18], a tube hosting a localized heat release zone as shown in Fig. 2.1 was used to represent the dynamic behavior of a combustion chamber. The origin of the thermo-acoustic combustion

instability was analytically described and combustion instability control strategies were developed based on the analysis provided below.

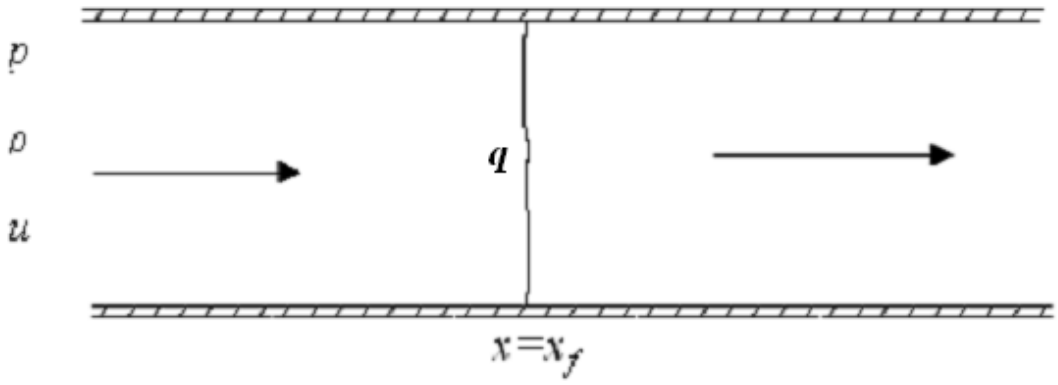

Fig. 2.1: Reacting Fluid Flow with Heat added at $x=x_f$.

Assuming the flow is inviscid, stationary, and perfect and with negligible thermal conductivity to the surroundings, the reactive gas dynamics conservation equations for this one-dimensional flow in the longitudinal direction of the combustor are:

Continuity: $$\frac{\partial \rho}{\partial t} + \frac{\partial (\rho u)}{\partial x} = 0 \qquad (2.1)$$

Momentum: $$\rho \frac{\partial u}{\partial t} + \rho u \frac{\partial u}{\partial x} + \frac{\partial p}{\partial x} = 0 \qquad (2.2)$$

Energy: $$\rho \frac{\partial e}{\partial t} + \rho u \frac{\partial e}{\partial x} = -p \frac{\partial u}{\partial x} + q \qquad (2.3)$$

Equation of State: $$p = \rho RT \qquad (2.4)$$

Where t and x are time and space, respectively, ρ, u, p, and e are the density, velocity, pressure, and specific internal energy respectively, q is the heat release rate per unit volume, and R is the gas constant.

Since only the small perturbation behavior at the onset of the instability is under consideration here, the system can be linearized by separating the variables into their respective mean and small perturbation components.

$$p(x,t) = \overline{p}(x) + p'(x,t) \tag{2.5}$$

$$u(x,t) = \overline{u}(x) + u'(x,t) \tag{2.6}$$

$$\rho(x,t) = \overline{\rho}(x) + \rho'(x,t) \tag{2.7}$$

$$q(x,t) = \overline{q}(x) + q'(x,t) \tag{2.8}$$

where the over bar denotes a mean part of a variable and the prime denotes a perturbation part of a variable.

By substituting the separated variables into the conservation equations and noticing that the mean flow should also satisfy the above three conservation equations, the governing equations for the perturbations can be simplified as the following two equations:

$$\overline{\rho}\frac{\partial u'}{\partial t} + \overline{\rho}u\frac{\partial u'}{\partial x} + \rho' u\frac{\partial \overline{u}}{\partial x} + \frac{\partial p'}{\partial x} = 0 \tag{2.9}$$

$$\frac{\partial p'}{\partial t} + u\frac{\partial p'}{\partial x} + \gamma\overline{p}\frac{\partial u'}{\partial x} + \gamma p'\frac{\partial \overline{u}}{\partial x} = (\gamma - 1)q' \tag{2.10}$$

Multiplying Eqn. (2.9) by u' and Eqn. (2.10) by $p'/(\gamma\rho')$, and combining these two equations, the change of acoustic energy inside the combustion chamber can be summarized here:

$$\frac{\partial}{\partial t}[\varepsilon] + \overline{u}\frac{\partial}{\partial x}[\varepsilon] = \frac{\gamma - 1}{\gamma}\frac{p'q'}{\overline{p}} - \frac{\partial \overline{u}}{\partial x}[\rho' u'\overline{u} + \frac{p'^2}{\overline{p}}] - \frac{\partial}{\partial x'}(u'p') - \frac{u'p'}{\gamma\overline{p}}\frac{\partial p'}{\partial x} \tag{2.11}$$

where $\varepsilon = \frac{1}{2}\overline{\rho}u'^2 + \frac{1}{2}\frac{p'^2}{\gamma\overline{p}}$ represents the acoustic energy density. The first term is the kinetic acoustic energy and the second one is the potential acoustic energy. Just like any oscillating systems, the periodic conversion from one form of energy to the other sustains the oscillatory behavior.

The right hand side of Eqn. (2.11) represents the acoustic sources. If considering only those cases in which the heat release becomes the dominating source of acoustic energy generation, the above equation can be reduced to:

$$\frac{D\varepsilon}{Dt} \approx \frac{\gamma - 1}{\gamma} \frac{p'q'}{\overline{p}} + higher\ order\ terms \tag{2.12}$$

Integrating Eqn. (2.12), the change in acoustic energy of a combustor due to the coupling between heat release fluctuation q' and pressure fluctuation p' during one period T can be introduced as:

$$\Delta E \approx \frac{\gamma - 1}{\gamma} \int_V \int_t^{t+T} \frac{p'q'}{\overline{p}} d\tau dV \tag{2.13}$$

So, if the natural fluctuations in the combustion and flow dynamic processes are such that both p' and q' move in the same direction so that $\Delta E > 0$, the pressure oscillation will grow and resonant instability will occur. On the other hand, p' is out of phase with q', the oscillation will be dampened. The importance of their phase relationship was also demonstrated in previous experiments [19-20].

Based on the mathematical expression of Rayleigh's criterion, it is clearly shown that thermoacousic instabilities can be best controlled when oscillatory energy is added to the system at the frequency of the instability and 180 degrees out of phase with respect to the unstable pressure oscillations. Thus, an effective active control system should be able to generate an oscillatory energy addition process that will satisfy $\Delta E < 0$.

2.2 Passive Combustion Instability Control

Passive combustion control strategy is the earliest and so far the only practical method to suppress combustion instabilities in propulsion systems.

Two passive methods exist to treat combustion instabilities: one involves changing the design of the system to shift the unwanted frequencies [21]; another attempts to directly dampen the feedback by changing the boundary conditions.

A natural way of eliminating combustion instabilities is to avoid the undesirable pressure oscillation frequencies by changing the geometry of the propulsion system or adjusting the distributions of fuel injectors. This requires expensive full-scale experiments and can be impractical during the later stages of propulsion systems development.

Conventional passive devices such as baffles, acoustic liners and resonant cavities have become commonplace and have been employed in combustion chambers, thrust augmentors and liquid rockets for many years to control combustion instabilities. To some extent, these passive means have been employed very successfully to suppress certain types of acoustic instabilities such as transverse mode or radial mode instabilities.

Baffles are essentially rigid walls extending along the axis of the chambers. They can discourage the presence of some resonance by changing the local geometry and also dissipating energy due to viscous forces. But because of structural integrity issues and performance losses, the baffles can extend only part of the way along the axis of the chambers. This constraint strongly reduces the effectiveness of baffles.

It is now standard procedure to integrate liners in the development of thrust augmentors. These perforate liners can effectively attenuate the high frequency pressure oscillations in radial and tangential modes. However, they are ineffective at reducing low frequency pressure oscillations that occur due to geometric limitations, because the

required geometry dimensions of acoustic liners increase as the desired frequency decreases.

Resonant cavities are just like Helmholtz resonators. These cavities reduce pressure oscillations in such a way that instead of affecting the combustion instability process directly, they just provide a way to lose energy in the unwanted frequency range. That is to say, resonant cavities dampen the pressure fluctuations resulting from the action of viscous forces. Since the required dimensions of resonant cavities also increases as the frequency decreases, these cavities can only be employed to treat high frequency pressure oscillations in actual propulsion systems. Another limitation of resonant cavities is that for a given geometrical configuration, they only work on a relatively narrow band of frequencies.

A common shortcoming of utilizing passive control means to suppress the combustion instabilities is that they are developed largely by trial-and-error and are usually time-consuming and costly because the shapes and frequencies of the troublesome pressure oscillations are unknown in advance. Another disadvantage is that extra space is needed to fit these passive devices into the combustion chamber and unwanted additional loads are added. The worst drawback of passive control is that the frequency ranges of these devices are severely limited. Once the operating condition of combustion chamber changes, these apparatus are useless dead weight.

2.3 Active Combustion Instability Control

Instead of modifying combustor geometries to suppress large-amplitude pressure oscillations, active control methods suppress combustion instability by controlling the relationship between heat release fluctuations and pressure oscillations. With the

development of modern microprocessors and electronic hardware, active combustion control has gained more and more interest in instability suppression research because of its wide applicability.

The strategies and control systems that were utilized in previous active combustion controls varied greatly in nature [5], [22-23]. Since this work exclusively focused on experimental studies, only literature related to experimental investigations is presented here.

Tsien, H.S. [24] theoretically explored stabilizing combustion in a rocket motor by controlling the supply of liquid propellant in 1953. Marble and Cox [25] further extended this idea in more complicated low frequency stability problems. But no experimental results were reported due to inadequate sensors and instruments at that time.

Active combustion instability control has gained renewed interest since the 1980s. Sreenivasan, Raghu and Chu [26] demonstrated suppression oscillations in a Rijke tube by introducing a secondary heater in 1985. Dines [27] and Heckl [28] utilized loudspeakers to inject acoustic waves to control combustion instabilities in their experiments. Bloxsidge controlled instabilities by modulating the primary fuel-air mix flow with a mechanical shaker [2], [29]. Lang and Poinsot [8], [9], [30] reported combustion instabilities control with loudspeakers as actuators in their studies. Langhorne, Dowling, and Hooper [4] introduced a controlled secondary supply of fuel upstream of the flameholder to suppress large amplitude pressure oscillations. This method is an attractive approach for controlling combustion instabilities in full-scale systems. A similar technique was employed by Gutmark et al [31-39]. Recent studies

include the use of an electrical discharge method by Afanasiev et al. [40] and a pilot burner by Hermannn et al [41].

Chapter 3: Experimental Apparatus and Diagnostics

3.1 Experimental Facilities

A schematic of the experimental setup that was used for this study is shown in Fig. 3.1 along with a picture in Fig. 3.2. It consisted of six main components: (1) an axisymmetric dump combustor to carry out the experiment, (2) an air supply system to provide air into the combustor rig, (3) a fuel supply system to introduce the main fuel ethylene, C_2H_4, (4) a controller fuel system that directly inject liquid fuel ethanol, C_2H_6O, into the dump combustor in order to suppress combustion instabilities, (5) an ignition system to initiate the combustion of the premixed air-ethylene mixture, and (6) a cooling system to lower the exhaust gas temperature.

3.1.1 Dump Combustor Rig

The combustor was made from a 102 mm inner diameter, 13 mm thickness stainless steel cylinder. The total combustion chamber length was 610 mm. For flow visualization and optical measurement purposes, the upstream half of the round combustor could be replaced with a square cross-section chamber. Due to the nature of longitudinal combustion instability observed in this study, the instability dynamics was unaffected by this replacement. This was verified before conducting the combustion instability control experiments. A Kistler 211B5 Piezotron miniature dynamic pressure transducer was flush mounted on the bottom plate of the dump combustor 50 mm, downstream from the dump plane, to monitor the pressure oscillation inside the combustion chamber. Two 101.6 mm wide, 304.8 mm long, 12.7 mm thick quartz windows were mounted on both sides of the dump combustor to provide optical access to the flow field. UT3300-2 Ceramic paper was adhered to the glass-metal interfaces to

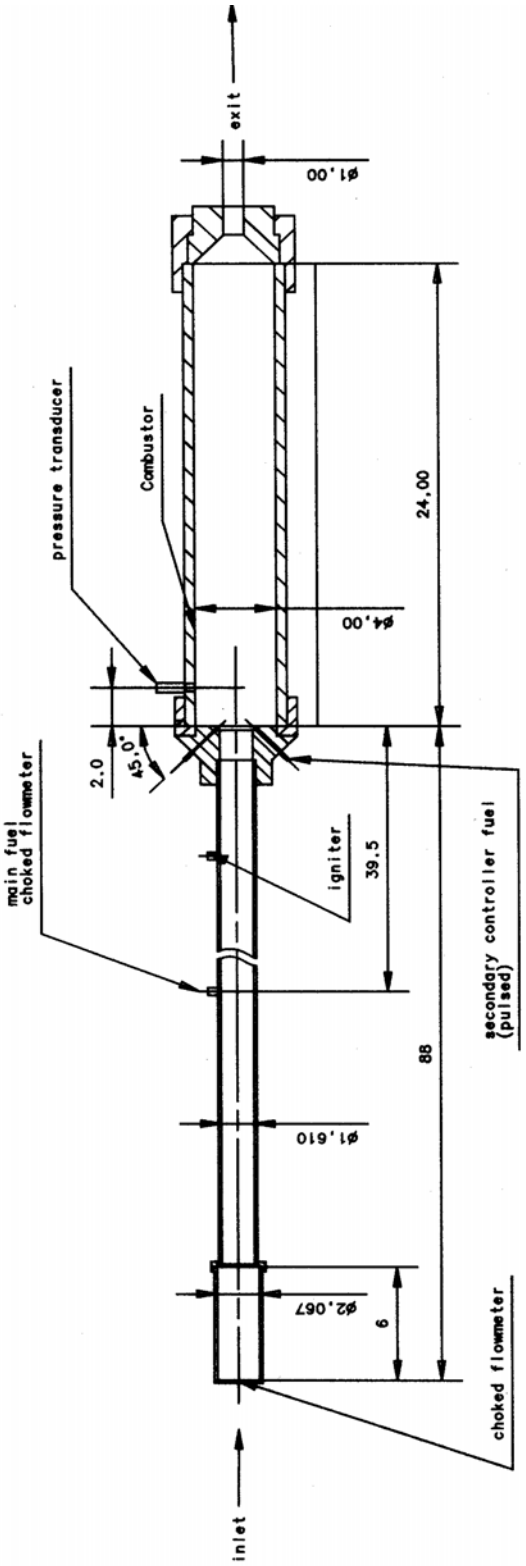

Fig.3.1: Schematic of test rig.

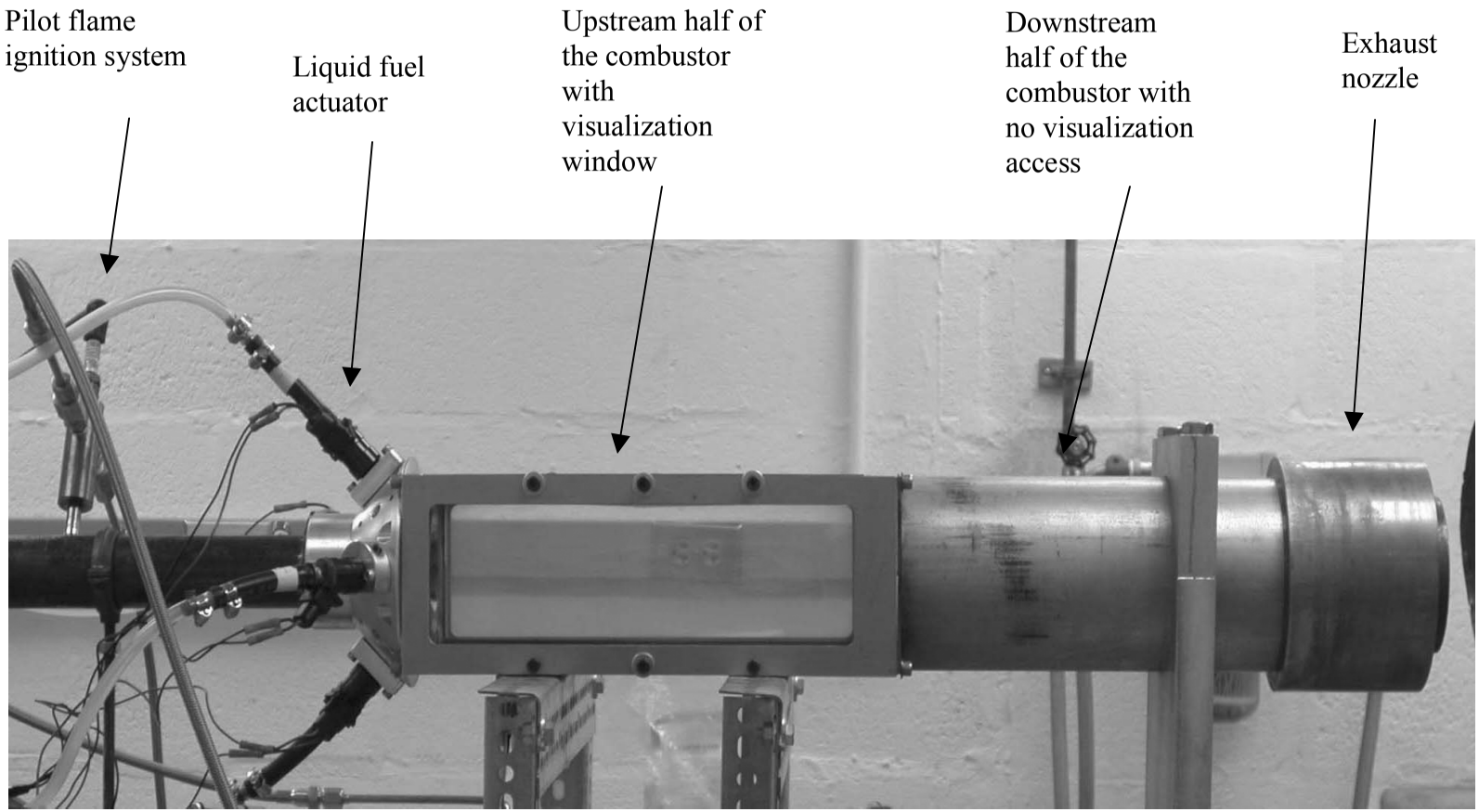

Fig. 3.2: Picture of test facility. This shows the dump combustor, liquid fuel system and igniter.

provide cushion and prevent leakage. A central 38 mm diameter converging nozzle that was placed at the end of the chamber was used as an exhaust nozzle in the low speed test conditions. In high-speed experimental cases, the dump combustor was operated without further restriction of the exhaust nozzle.

3.1.2 Air Supply System

The schematic of the air supply system is shown in Fig. 3.3. High pressure air up to 185 psi was provided by a stationary, single-stage, oil-injected screw type compressor GA75. Before the air was introduced into the test rig, the pressurized air from the compressor was fed into a non-cycling refrigerated dryer AD-400 to remove moisture. A gas/air filter P8C-187-25 was also installed to separate the oil from the compressed air before it entered the laboratory. The maximum flow rate of the compressor was 0.208 kg/s. Air was brought into the dump combustor rig through 41 mm inner diameter circular steel pipes. A Wilkerson R40-0C regulator and a choked circular orifice were used to meter the flowrate. The orifice flow meter was installed 2.24 m upstream of the dump plane inside the steel pipe. The orifice diameter was 6.35 mm in low Mach number experiments and 10.16 mm in high Mach number experiments. The stagnation air pressure was measured by a Setra 206 static pressure transducer that was flush mounted on to the circular pipe section, and was placed 2 m upstream of the dump plane.

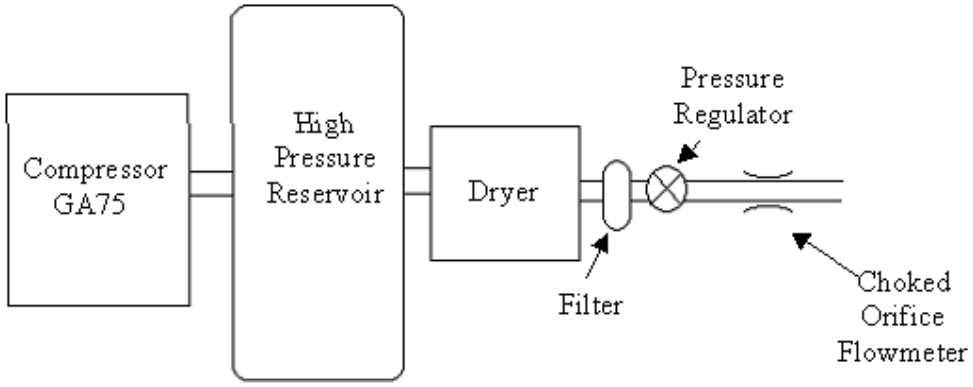

Fig. 3.3: Air supply system.

3.1.3 Main Fuel Management System

Part the fuel in the propulsion systems is injected upstream and enters the combustor in a prevaporized and premixed state. To simulate this portion of the fuel management system, all the main fuel used in this study was injected at 1.0 m upstream of the dump plane. The main fuel (ethylene, C_2H_4), was supplied from a high pressure bottle and was injected transversely through a choked orifice into the air flow in low Mach number test conditions. At high Mach number conditions, the location of the main fuel injection was moved further upstream to 1.8 m from the dump plane for better mixing. The flow rates of ethylene were maintains within ± 1% of the desired value using the choked orifices and Wilkerson regulators. Solenoid valves controlled operation of all fuel lines. The stagnation pressures were monitored using Setra 206 pressure transducers.

The air and ethylene mixture was premixed before coming into the combustion chamber. Flame stabilization was achieved through continuous ignition by the hot combustion products in the recirculation zone just after the dump plane. This was used to imitate real ramjet combustor operating conditions.

3.1.4 Liquid Fuel Injection System

The liquid fuel injection system is illustrated as in Fig. 3.4. Ethanol was pressurized by compressed air and then introduced into the automotive fuel injectors Borsh 2-18519 employed in this work. A standard car battery was used to power these automotive injectors. To switch the injector on and off, a pulse signal created by a Wavetek 195 universal waveform generator was sent to a solid state relay that controlled the fuel injectors.

Eight ports for installing the fuel injectors were made along the circumference of the dump plane. A maximum of eight actuators could be installed in this rig to suppress the large amplitude pressure oscillations occurring inside the chamber. For low Mach number operating conditions, only two pulsed automotive fuel injectors were used to modulate secondary liquid fuel to control the pressure fluctuations. These two injectors were opposite to one another and pointed at an angle of 45 degrees with respect to the premixed air-fuel flow. For high Mach number experimental conditions, four actuators were employed to supply liquid fuel ethanol C_2H_6O for controlling purposes. These four fuel injectors were also directed to the premixed flow at 45 degrees but located 90 degrees apart around the periphery of the dump plane as illustrated in Figure 3.2.

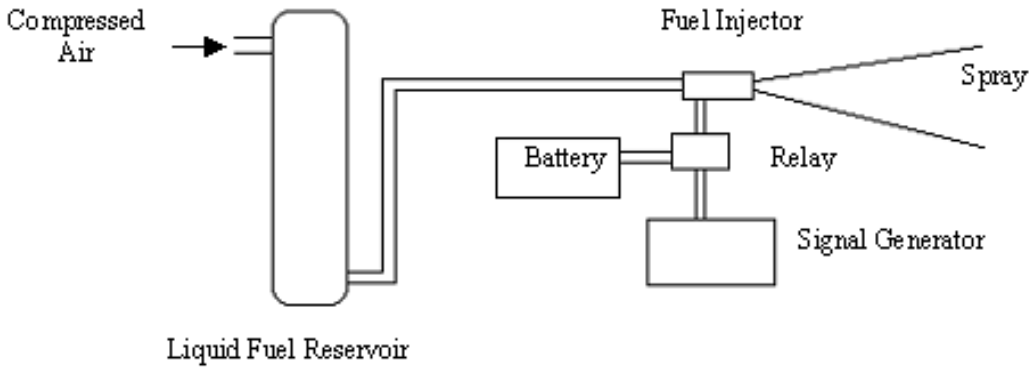

Fig. 3.4: Liquid fuel injection system.

3.1.5 Ignition System

A small cylindrical burner as sketched in Fig. 3.5 was placed 267 mm upstream of the dump plane and was used to ignite the air-ethylene mixture. Air and hydrogen were used as oxidizer and fuel respectively in this pilot burner system that was ignited by a spark plug. The burner injected hot combustion products that were used to start the combustion process of the premixed air and ethylene.

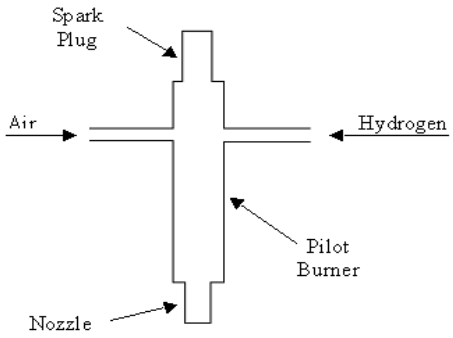

Fig. 3.5: Ignition system.

3.1.6 Combustor and Exhaust Cooling System

The exterior of the combustor was cooled by spraying tap water onto the metal surface. Six spray nozzles were connected to a pressurized water line to cool the combustor surface. Also, tap water was sprayed into the outflow combustion products through swirl atomizers to cool the gas mixture before it was released into the exhaust duct.

3.2 Instrumentations and Flow Visualization

3.2.1 High-speed Spark Schlieren Imaging Technique

Schlieren photography is one of the simplest and most widely used methods in flow visualization research. In this study, large coherent structures periodically shed

during the instability were imaged at 30º phase intervals to understand their roles in combustion instabilities.

The basic principle of the Schlieren technique is that when light passes through an inhomogeneous medium, it will be deflected due to local variations in the optical path and redistributed in the image plane. The refraction of the light depends on the thermodynamic state of the medium, mostly the density. Thus, depending on the density gradient, a pressure wave within a transparent medium can be visible in Schlieren images. A typical Schlieren setup consists of a light source, several lenses, and an image recording system as shown in Fig. 3.6. In this study, A HHT31 Digital Stroboscope from Omega Technologies Company with a frequency range from 0.5 to 233.33 flashes per second was used as the light source. One of the two light bulbs inside the stroboscope had to be blocked to obtain a clean point light source. By setting this light source at the focus point of the converging lens, the observed flow field was illuminated by the evenly distributed passing light. The second converging lens was placed on the other side of the flow field to collect the light passing the test section. A knife-edge was laid on the focus point of the second lens to block all the undeflected light to form a clear Schlieren image. Neutral density filters were used to adjust the intensity of the collected light before entering the camera.

Two methods can be employed to obtain and record the Schlieren image formed in the image plane. In this study, a traditional charge-couple device (CCD) camera Pulnix TM-7CN with an adjustable shutter speed from 1/60 to 1/10,000 seconds was incorporated to capture the Schlieren images. Images were then displayed on a Sony high-resolution Trinitron Monitor and simultaneously recorded to super-VHS tape. Later,

the recorded images were digitized using the Global lab software from Data Translation Company. High-speed Schlieren images in this study were acquired through a high-resolution, High-speed Photron Ultima 1024 camera from Photron^{TM} USA Inc. With up to 16000 frames per second and synchronization capability with external events, this high-speed camera system can easily capture highly unsteady flows.

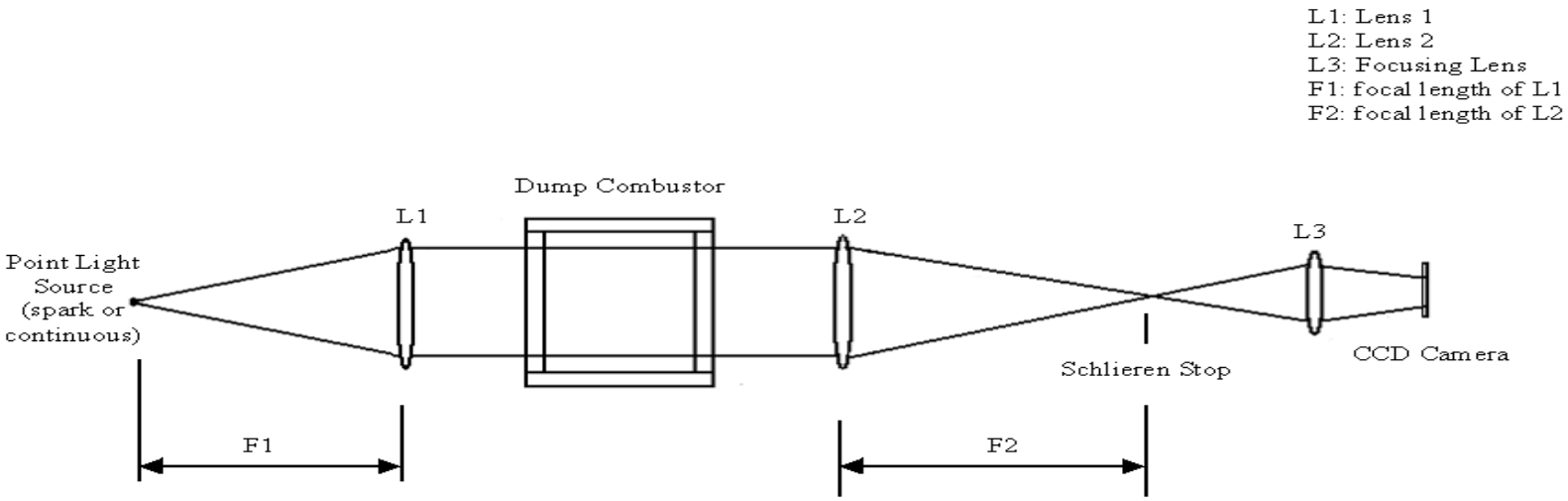

Fig. 3.6: Diagram of a typical Schlieren system.

3.2.2 CH* Chemiluminescence Measurement

Chemiluminescence refers to exoergic chemical reactions that create molecules in electronically excited states and then relax via fluorescence or phosphorescence. The light emitted from these chemical reactions has differing degrees of intensity, lifetime and wavelength. The most common emitted lights are in the visible region.

A linear relationship exists between heat release and the intensity of chemiluminescence from species such as CH*, and OH*, such that the chemiluminescence intensity from CH*, and OH* will be a good indicator of local heat release [42-43].

By using a filter of 3 nm bandpass centered on 410 nm, the chemiluminescence of excited radicals CH* was measured with a CCD camera, and a spatially resolved heat release pattern was deduced.

3.2.3 Malvern Instrument

The Malvern/INSITEC In-Line Ensemble Particle Concentration and Size (EPCS) system from Malvern Instruments Limited Company was utilized to characterize the instantaneous liquid fuel droplet size distribution to better understand their roles in the suppression of combustion instabilities.

Based on the laser diffraction technique, the EPCS system is designed to continuously measure and feed back particle size distribution information from a pneumatically conveyed stream of powder or aerosol. In this study, liquid ethanol droplets from the fuel injectors were analyzed.

The EPCS system contains five primary components: the optical head, an electronic interface, the computer, computer interface cards, and the software. A general system layout is shown in Fig. 3.7.

A Class II Diode Laser with a 1 mW Maximum CW is the light source for the EPCS system. When droplets are sprayed into the path of the laser beam, some of the light is absorbed while others are scattered. The receiving lens collects the incident beam and scattered light within the open aperture of the optics. The optical properties, refractive index and particle size, and surrounding medium around the particle determine how the light is scattered and absorbed. The diffraction component of the bulk of the scattered signal can be calculated based on Fraunhoffer diffraction theory. Although the detailed physics are beyond the scope of this study, more information can be found in Ref [44]. The bulk diffraction signal information, then, is transmitted to the computer, which calculates, records and saves the particle size distribution and pertinent attributes of the distribution and simultaneously displays the information in a time history window.

Compared to a counting instrument that only measures one particle at a time, the Malvern/INSITEC Ensemble Particle Concentration and Size instrument can simultaneously measure the size distribution of a large group of particles. Another advantage of the Malvern instrument is that it can measure the particle size distribution of both a static field and a dynamic field. The specific Malvern instrument used in this study can acquire a snapshot of the particle size distribution in 500 microseconds. In this way, high-speed time resolved measurements become feasible in rapidly changing flow fields such as pulsed fuel sprays.

Malvern/INSITEC has a FLASH mode for fast data acquisition that can acquire bursts of light scattering measurements at up to 2500 Hz and synchronize with external events. The data can quickly be analyzed and presented as a time history to show the time-resolved particle size distribution variations. Unfortunately, the FLASH mode was not installed for the measurements reported here, so a continuous mode was used to take all the measurements. Since the pulsed fuel injector operated in a periodic fashion and the instrument's acquisition time was fast, instantaneous fuel droplet size distributions at different phases of a cycle could be detected.

Real Time Particle Sizer (RTSizer) for Windows^{TM} from Malvern was used to process the data and continuously collect particle size information, analyze on-line, and report both the particle size distribution and pertinent attributes of the distribution such as Sauter-Mean-Diameter D_{32} and Span at 1-2 second update intervals.

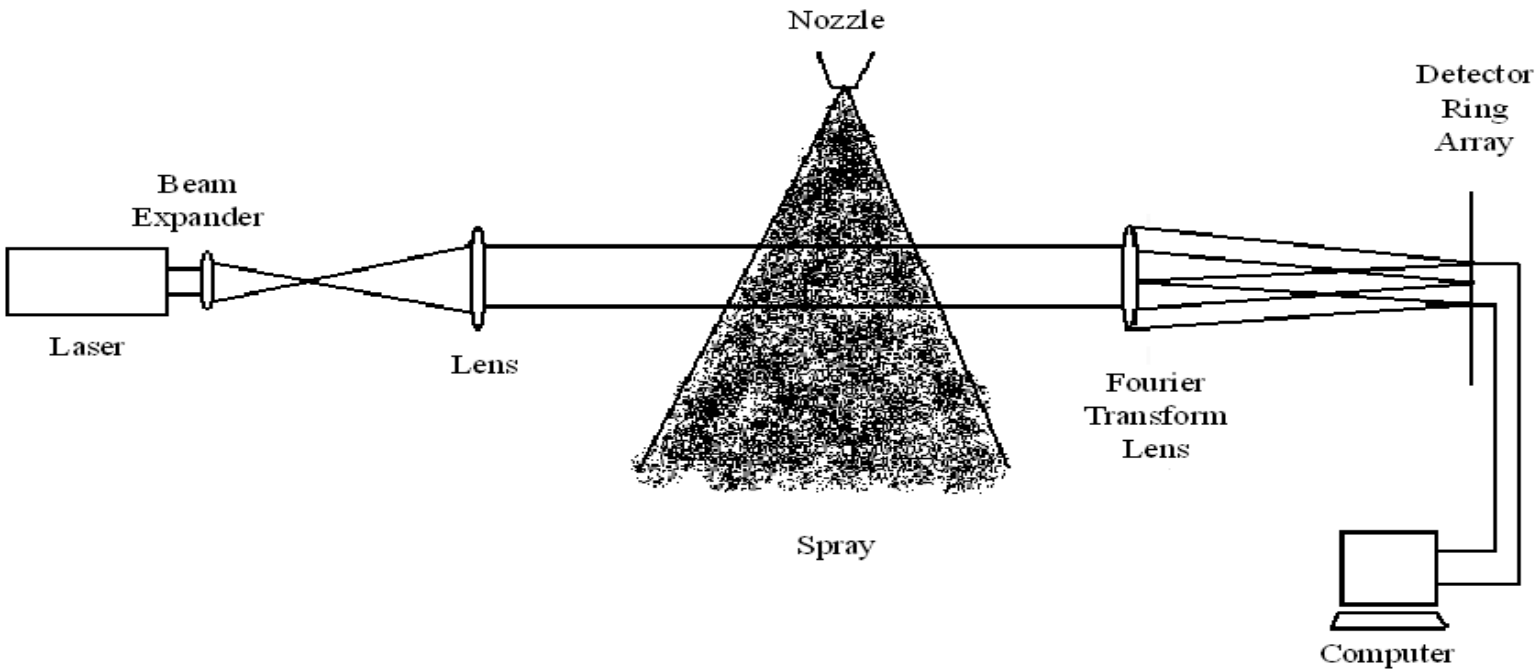

Fig. 3.7: Diagram of Malvern/INSITEC In-Line Ensemble Particle Concentration and Size (EPCS) system.

3.2.4 Particle Image Velocimetry System

The Particle Image Velocimetry (PIV) technique was utilized in this study to visualize the velocity profile of the controlling liquid fuel droplets in this two-phase flow field.

Unlike conventional time consuming velocity measurement techniques such as hot-wire anemometry (HWA) or laser-doppler anemometry (LDA) that only measure single.point velocity and cannot capture instantaneous flow fields, the PIV system is able to measure the whole flow field simutaneously. Moreover the PIV technique is a non-intrusive method, so it can better reflect the real flowfield compared to an intrusive methods like HWA.

The typical Particle Image Velocimetry set-up includes a light source, light-sheet optics, seeding particles, and a camera for two-dimenisonal measurements or two cameras for three-Dimensional measurements. In this study only the two-dimensional PIV was used to measure the liquid fuel droplets velocities.

The set up of the two-dimensional PIV system from Integrated Design Tools Inc. is shown in Fig. 3.8. A compact, dual Nd: YAG laser-head Solo PIV system made by New-Wave Research and planar optics were used to generate a laser sheet at 532 nm. The timing signals to trigger the illumination laser were provided by the IDT Timing Control Module. This Timing Control Module also managed and distributed the trigger timing signals to the SharpVISION^{TM} cameras. An additional port in this module was used to synchronize with external events like the pulsing of fuel injectors. A SharpVISION^{TM} model 1300DE Camera with Nikon-standard 50 mm lens and progressive scan interline CCD sensor was utilized to capture two images in a very short interval to reflect the

movement of the illuminated particles when working in a double exposures mode. High-density cable was used to connect the camera and transmit data to the computer. SharpVision's ProVISION^{TM} software provided a graphic interface for image acquisition and data processing. This software was also fully integrated with the Tecplot data visualization package that made the velocity field data able to be displayed and presented in a more flexible way.

Seeding particles are the most important component for the PIV measurements. It is impossible to observe the fluid motion directly, so seeding particles should be added to allow for flow velocity measurements. Ideal seeding particles follow exactly the local fluid motion and should not alter the flow or the fluid properties. The images of the seeding particles are recorded continously at very small time intervals. In that way the motion of the flow can be represented as the displacement of the seeding particles. In other words, flow velocity can be measured indirectly by measuring the velocity of the seeding particles. In this study, since only the liquid fuel droplet velocity profile was needed in this study, no additional seeding particles were added, and the liquid fuel droplet velocity was directly measured.

Two major steps are required to characterize the flow field velocity using PIV techniques. First, the pixels of images taken by the camera must be correlated to the physical size in order to calculate the actual velocity later. This is done by placing a target with calibration markers in known positions in the same plane in which the velocity profile is going to be measured. The camera captures the image and transfers it to the PIV system for later comparison with the real flow images. Then, the camera acquires two consecutive flow field images in a very short interval. Each image is

analyzed by subdividing it into small interrogation regions and statistical methods are used to find the particle-image displacement. As long as the seeding particles follow the flow closely, these displacements can precisely represent the flow velocities.

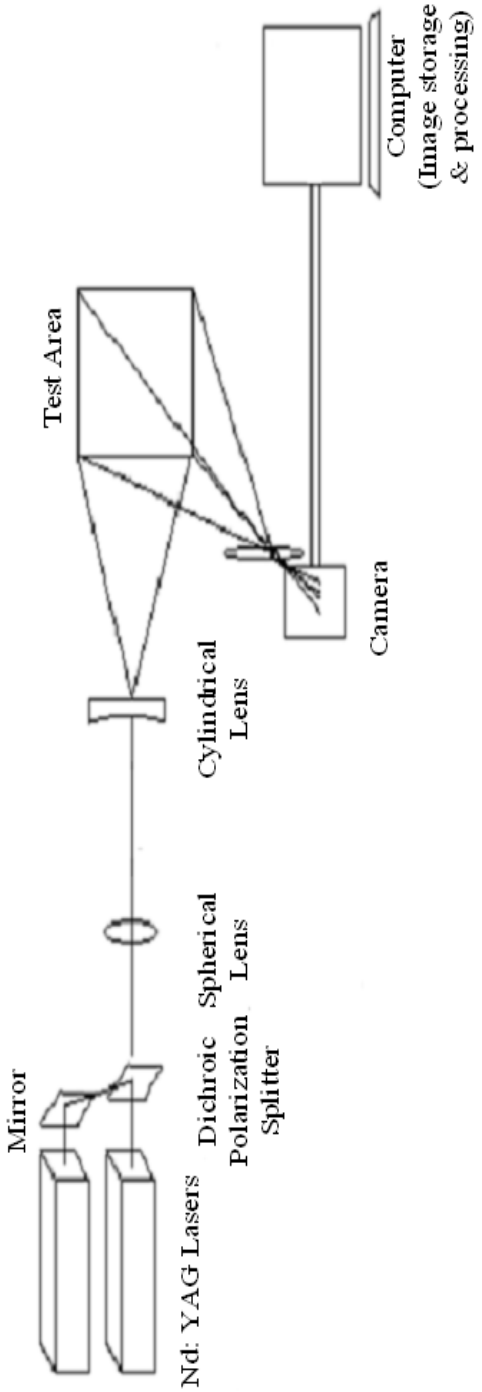

Fig. 3.8: Diagram of a 2.Dimensional Particle Image Velocimetry system.

3.3 Sensors and Actuators

Sensors and actuators are two key components in suppressing combustion instabilities. Sensors are critical to continuously monitor the combustor performance, and to provide in situ information to control systems. Without the data fed to the control system, the controller cannot generate the correct signals for the actuator. The actuators usually need to convert the input signal from the control unit into mechanical or some other form of output quantity, and to control the elements that they govern. Regulation of combustor performance relies on actuators that control elements' responses to commands from the control systems; they form a complete loop to fulfill the control purpose.

Numerous varieties of sensors and actuators have been used in both laboratory and industrial settings. A brief summary of sensors and actuators is presented in the following paragraphs.

The main requirement for sensors is that they must be able to detect important variations in combustor performance so that the control systems can respond in a timely fashion.

The most widely applied sensor has been the easily available and inexpensive dynamic pressure transducer [2], [45-49]. When combustion instability occurs, the pressure inside the combustor oscillates significantly. Thus, the dynamic pressure transducer is perhaps the simplest way to reflect the combustion instabilities. Microphones can also sense the pressure fluctuations and provide signal to the controller for control purposes. In addition to the pressure oscillation inside the combustor, heat releases also exhibit extreme fluctuations. In this way heat release can be another ideal variable to monitor combustor performance. Because of difficulties in measuring the heat

release directly, the chemiluminescence of combustion radical species such as CH* and OH*, which correlate to heat release variation, are often monitored to provide a temporal and spatial distribution of the heat release during the combustion process [50]. Optical methods have to be engaged in monitoring the heat release variations. Flame locations also change drastically when combustion instability occurs, leading to the employment of the photodiode technique in several studies [31], [38], [48]. Electrochemical based gas analyzers [51-52] were incorporated as a sensing device to monitor the variation of the chemical composition of the combustion products. Diode-laser sensors [53-57] were also demonstrated in the past. Although Micro-Electro-Mechanical-systems are not practical to be used in combustors now, they are still considered as potential sensors and actuators [58-61].

Typical actuators consist of a transformer and a final-control element. Signals from the control unit must be converted to some form of mechanical movement or other action to respond with appropriate output.

Some actuators that have been used to date in combustion instability suppressions include compression drivers [1], [62-64], mass flux modulation equipment [2], [4], [45], [51], [65-70], mechanical devices [29], [71-72] electric facilities [40], [73], heat release modulation instruments [74-75] and secondary fuel injection apparatus [46], [76-82]. Recent developments include the utilization of materials with piezoelectric [83] or magnetostrictive characteristics [84]. In addition, other physical phenomena such as microexplosions [78] have been explored for actuator consideration. However, due to practical limits, most of these actuators were confined to lab research programs and were rarely encountered outside the research laboratories.

A practical approach to control combustion instability is presented in this study. A Kistler 211B5 voltage mode dynamic pressure transducer with a measuring range of 0 to 100 psi was flush mounted on the combustor wall to continuously sense the pressure fluctuation inside the dump combustor. This Piezotron miniature pressure sensor is ideally suited for fast transient measurement under extreme environmental conditions. With the water-cooling adaptor 228P from the same company, this Kistler pressure sensor can easily withstand the harsh combustion environment. For space and power considerations, Bosch 2-18519 fuel injectors were used as actuators to modulate the controller fuel flux at high frequencies. Electrical signals determined the injector's starting point and the amount of fuel discharge. Without further atomization, the liquid would come out as a liquid stream, which is a problem because large droplets are unable to respond to the dynamics of flow field quickly [85-91]. A Coolmist brass/stainless steel mist nozzle was coupled downstream with each fuel injector to reduce the liquid droplet size to appropriate ranges for combustion control purposes [92]. In this way, the automotive fuel injector actually acted as a valve to control and modulate the controlling liquid fuel flow rate with a capability of fast response frequency up to 1000 Hz.

By analyzing the pressure oscillation inside the dump combustor sensed by the high-bandwidth Kistler dynamic pressure transducer, the controller can, then, generate an appropriate control signal to the automotive fuel injector and pressure-swirl atomizer combination. This actuator system then modulates the controlling liquid fuel with proper frequency and timing to create desired heat release oscillations that damp the pressure oscillations inside the combustor. In this way, a complete closed control loop was formed.

Chapter 4: Dynamics of Two-phase Flow Field

4.1 Introduction

Liquid fuel injection and combustion has been widely used in many practical combustion systems. However, using liquid fuel to suppress large amplitude pressure oscillation inside combustion chambers has been proven to be difficult because of the complicated burning process within the flow field.

Liquid fuel injectors coupled with a swirl atomizer were employed as an actuator in this study to suppress the combustion instability inside the combustion chamber. To better understand the function of liquid fuel droplet control in the suppression of combustion instabilities, detailed measurements of liquid fuel droplets were investigated [93-94]. Droplet size distribution and velocity characterization were focused on, since these two components directly affect spatial and temporal heat release.

In the current study, the Malvern/INSITEC In-Line Ensemble Particle Concentration and Size (EPCS) system was utilized to characterize instantaneous liquid fuel droplet size distributions. Droplet combustion was analyzed to discover the corresponding burning characteristics. Particle Image Velocimetry (PIV) technique was utilized to visualize the dispersion of the controlling liquid fuel droplets in the two-phase flow field.

4.2 Transient Characteristics of Controlling Liquid Fuel

4.2.1 Liquid Fuel Droplet Size Distribution as a Function of Injection Phase

Previous studies have shown that fuel droplet size plays a critical role in the effectiveness of combustion instability control with a liquid-fuel injection control strategy [46], [76], [95-96]. Because both the combustion time delay and the instantaneous

amplitude of heat release are related to the droplet size, a non-intrusive, laser based Malvern droplet analyzer was used to characterize the instantaneous size distribution of fuel droplets originating from the actuators.

Before characterizing the controlled fuel droplet size, the mass flow rate was calibrated using a measuring glass cylinder and a stopwatch. Since the automotive fuel injector was controlled by a pre-determined electrical pulse signal, either varying the duty cycle of the pulse wave or changing the forcing frequency could adjust the total ethanol injection amount. As shown in Fig. 4.1, the flow rate increased significantly with longer pulse durations.

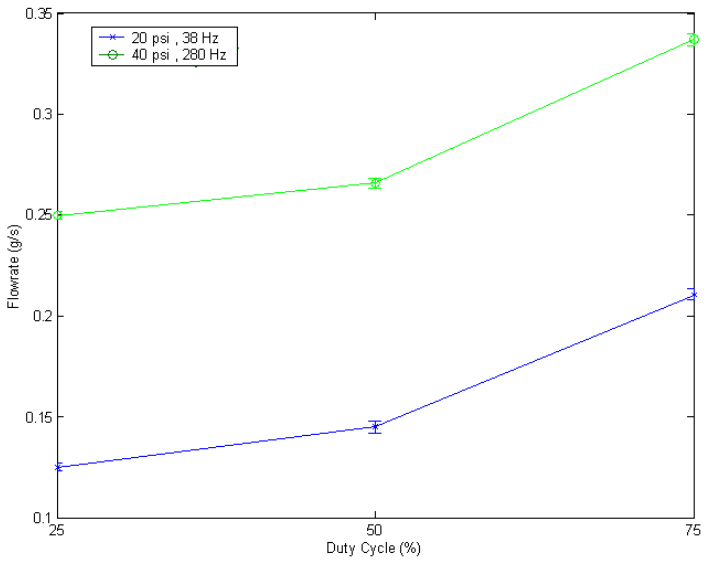

Fig. 4.1: Controlling liquid fuel flow rate vs. duty cycle.

The total amount of fuel (ethanol) also varied with forcing frequency, as shown in Fig. 4.2. At the same duty cycle of 50% conditions, the flow rate increases with the forcing frequency.

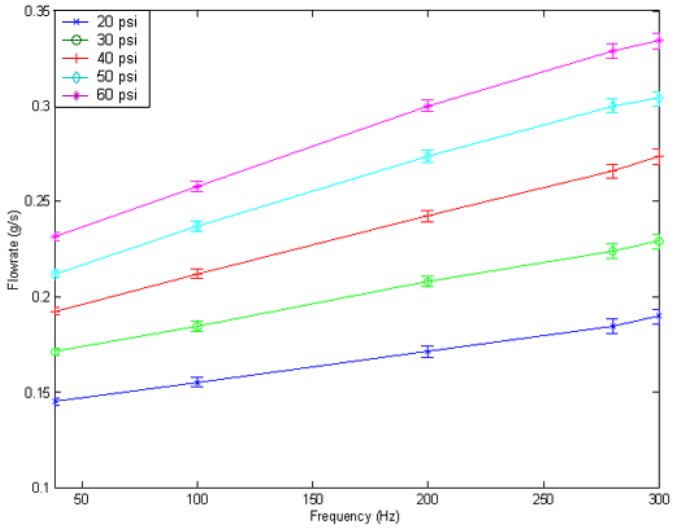

Fig. 4.2: Controlling liquid fuel flow rate .vs. forcing frequency.

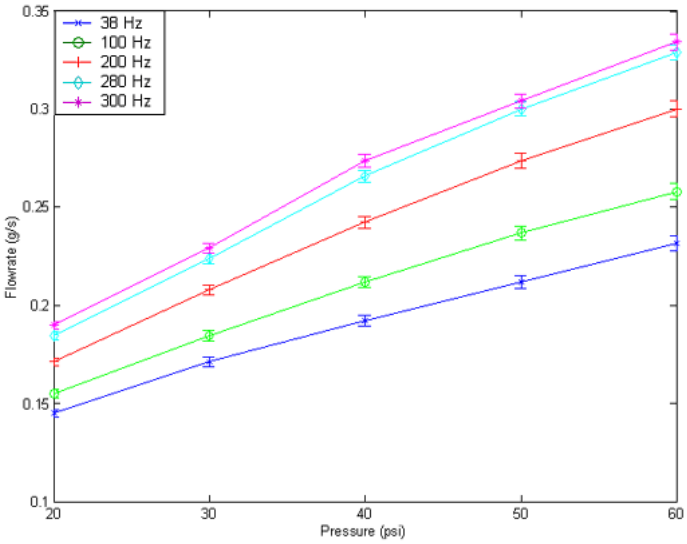

Fig. 4.3: Controlling liquid fuel flow rate .vs. forcing pressure.

Increasing the upstream pressure also increase the injected liquid fuel amount, as shown in Fig. 4.3. The duty cycle was kept at 50% for all test conditions.

A contour map of time-averaged ethanol flow rate per injector, varying with pressure and forcing frequency, is shown in Fig. 4.4. Based on previous studies, the desired flow rate was chosen in such a way that the power output delivered through the

dynamically controlled ethanol injection was about 10~15 % of the total thermal power output to suppress the large amplitude pressure inside the combustor.

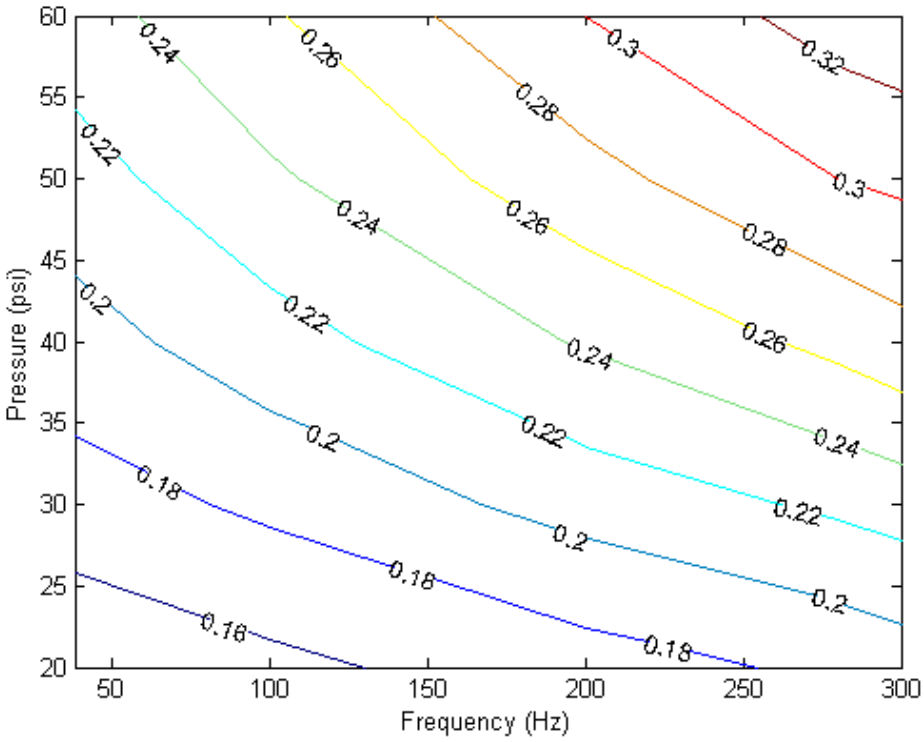

Fig. 4.4: Contour map of fuel flow rate changes with frequency and pressure.

Comprehensive droplet size measurements were conducted to analyze the transient behaviors of the pulsed sprays. Droplet size distribution information at all test conditions were acquired through the given probe volume as specified in Fig. 4.5.

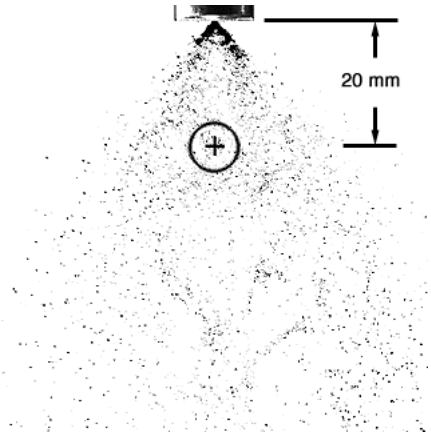

Fig. 4.5: Planar Mie-scattering image of a typical fuel spray with the probe area marked for Malvern droplet sizing measurements.

Time-averaged droplet size distributions at different injection conditions are illustrated in Appendix A. A typical droplet size distribution is shown in Fig. 4.6. The droplet sizes containing most of the flow mass extended over about 3 orders of magnitude, ranging from a few micros up to around a millimeter. The volume fraction of the spray corresponding to a pre-defined range of drop sizes was plotted as a histogram in Fig. 4.6, including the frequency distribution curve representing spray characteristics.

Unlike most droplet size distributions that follow the log-normal distribution law, this spray presented a bimodal mode of droplet size distribution in some cases. This suggested that large droplets existed during some transient period. Before liquid fuel spray forms, ethanol must pass through a small volume between the automotive fuel injector and the atomizer. While this volume was periodically pressurized and drained by the opening and closing of the fuel injector valve, the inside pressure value altered continuously between a minimum and a maximum value, depending on the state of the fuel injector. When the pressure behind the atomizer was low, the droplet size would become larger. This was also confirmed by close examination of the planar Mie-

scattering images of fuel sprays. Large droplets were presented during the transient phases when the fuel injector was just switched open.

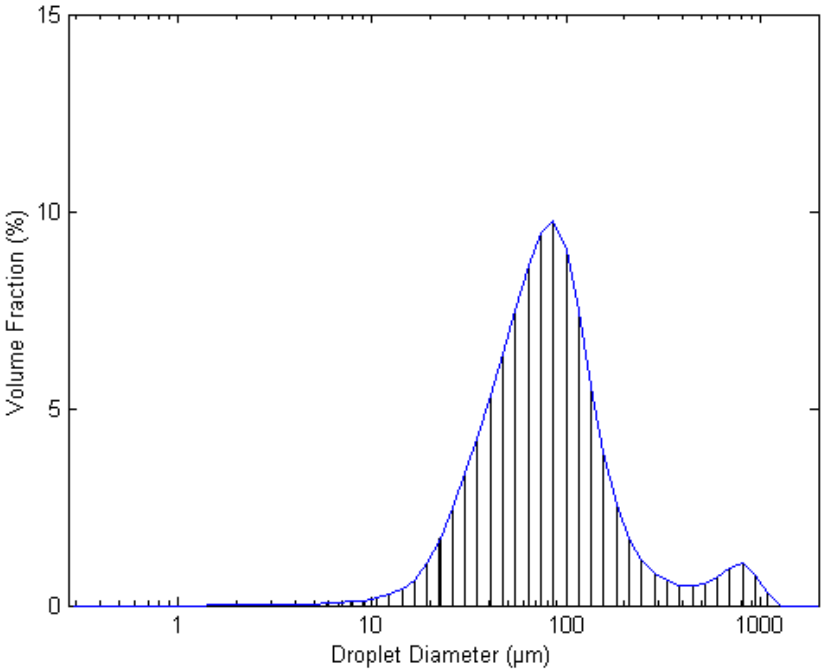

Fig. 4.6: Ethanol droplet size distribution at pressure 20 psi, forcing frequency 125 Hz and 50% duty cycle.

The effect of duty cycle on liquid fuel droplet size distribution is shown in Fig. 4.7. Except for different pulse durations, all these four measurements were taken at a forcing frequency of 38 Hz and a pressure of 20 psi. It was clearly shown that the volume fraction for larger droplets became smaller as the duty cycle increased. This was because of the delays that occurred before the ethanol entrapped in that small volume reached its maximum desired pressure. Large droplets were created when the pressure before the atomizer was low. With longer duty cycles, this delay time became less significant compared to the whole time period that the fuel injector was open. In this way, more ethanol could be fully pressurized before going through the atomizer and thus more small droplets were generated.

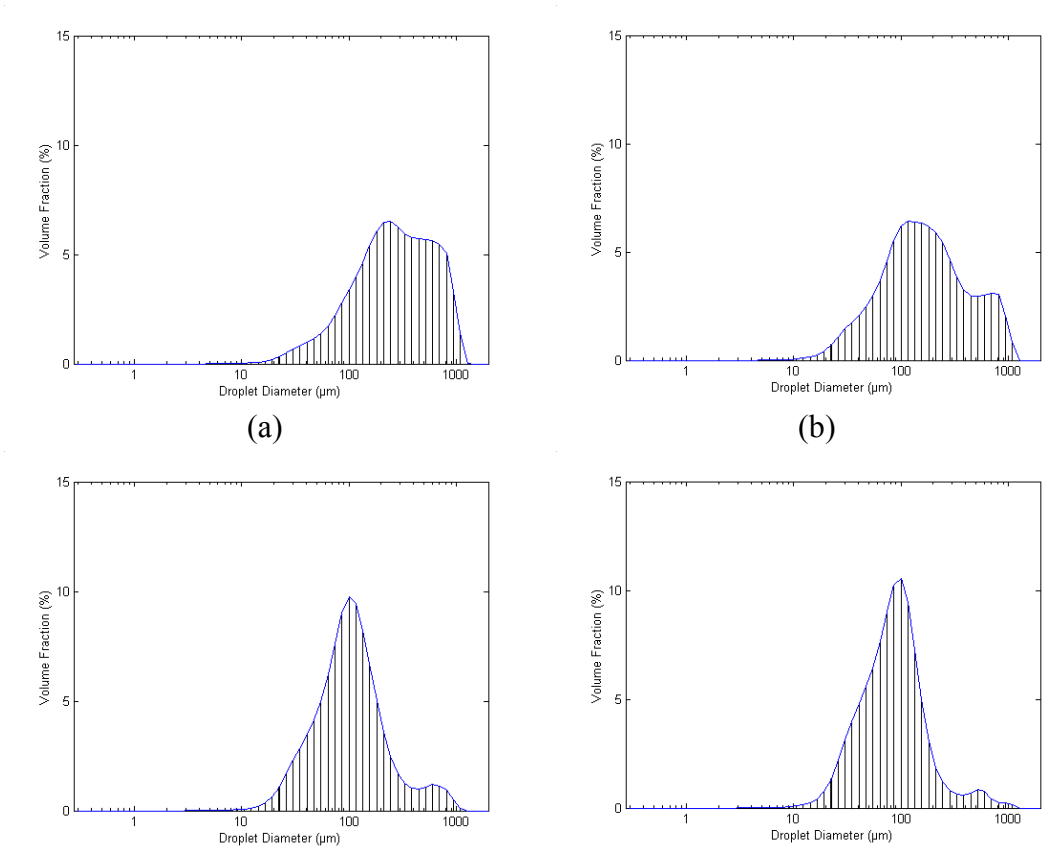

Fig. 4.7: Ethanol droplet size distribution at pressure 20 psi, frequency 38 Hz and duty cycle: (a) 25%, (b) 50%, (c) 75%, (d) 100%.

Fig. 4.8 demonstrates that with higher forcing frequencies, the volume fraction for small droplets becomes larger. This can be explained by the fact that at higher frequencies, the time duration between two continuous pulses becomes shortened. The fuel injector was opened before the liquid fuel that was trapped in the small volume was completely drained. High pressure fuel was held inside the volume at all times with high frequency forcing, regardless of whether or not the fuel injector was on. This was also confirmed with the planar Mie-scattering images of the liquid fuel sprays. With higher frequency, it became harder to detect when the fuel injector is on or off by just observing the fuel spray. Because the pressure behind the atomizer never actually reaches zero at

higher frequencies, large droplet formation at the beginning of the pressurization phase can be avoided.

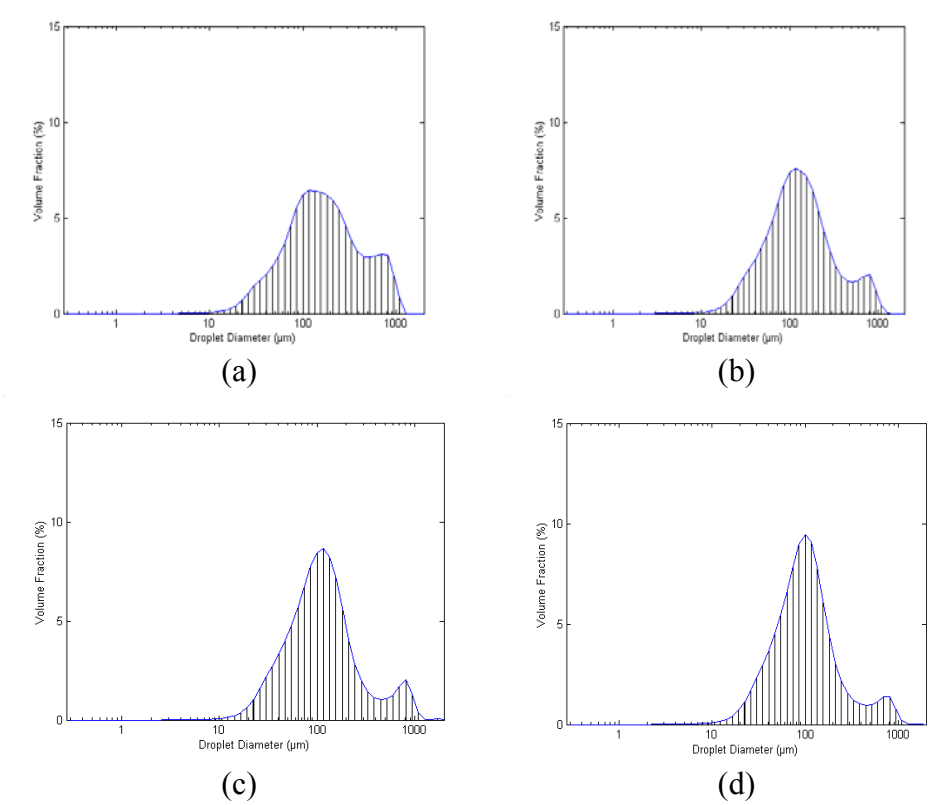

Fig. 4.8: Ethanol droplet size distribution at pressure 20 psi, 50% duty cycle, and forcing frequency: (a) 38 Hz (b) 100 Hz (c) 200 Hz (d) 300 Hz.

Upstream pressure also plays an important role in determining the droplet size. As illustrated in Fig. 4.9, the number of small droplets increased significantly as the pressure increased. At higher pressures, the swirl atomizer could achieve a much larger relative velocity between the liquid and the surrounding gas by converting the pressure into kinetic energy, thus making the break down of liquid spray into smaller droplets much easier.

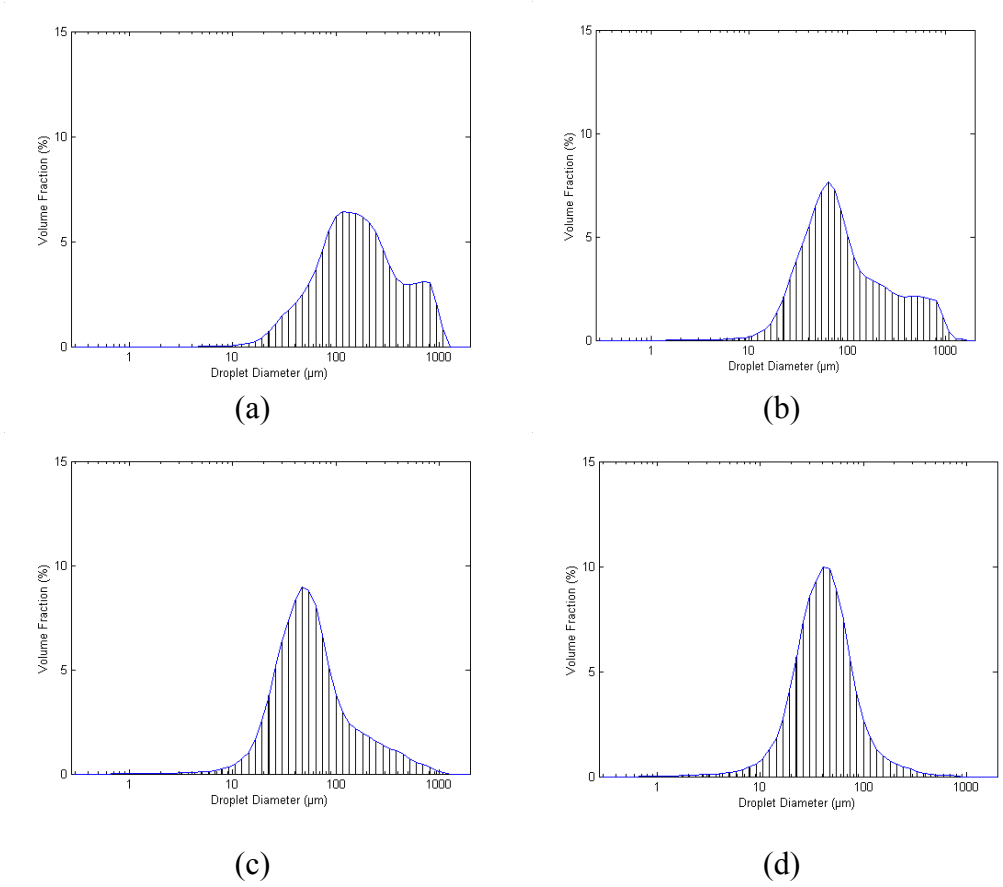

Fig. 4.9: Ethanol droplet size distribution at forcing frequency 38 Hz, 50% duty cycle, and injection pressure: (a) 20 psi (b) 30 psi (c) 40 psi (d) 50 psi.

A contour map of average diameter at different injection conditions is shown in Fig. 4.10. Sauter-Mean-Diameter was used as the representative parameter to depict the liquid fuel spray in all cases. As expected, the droplet size decreased with increasing injection pressure at fixed forcing frequencies. Additionally, droplet size decreased with increasing forcing frequency at fixed injection pressure. It was also noted that the injection pressure played a more important role in determining the average Sauter-Mean-Diameter that did the forcing frequency.

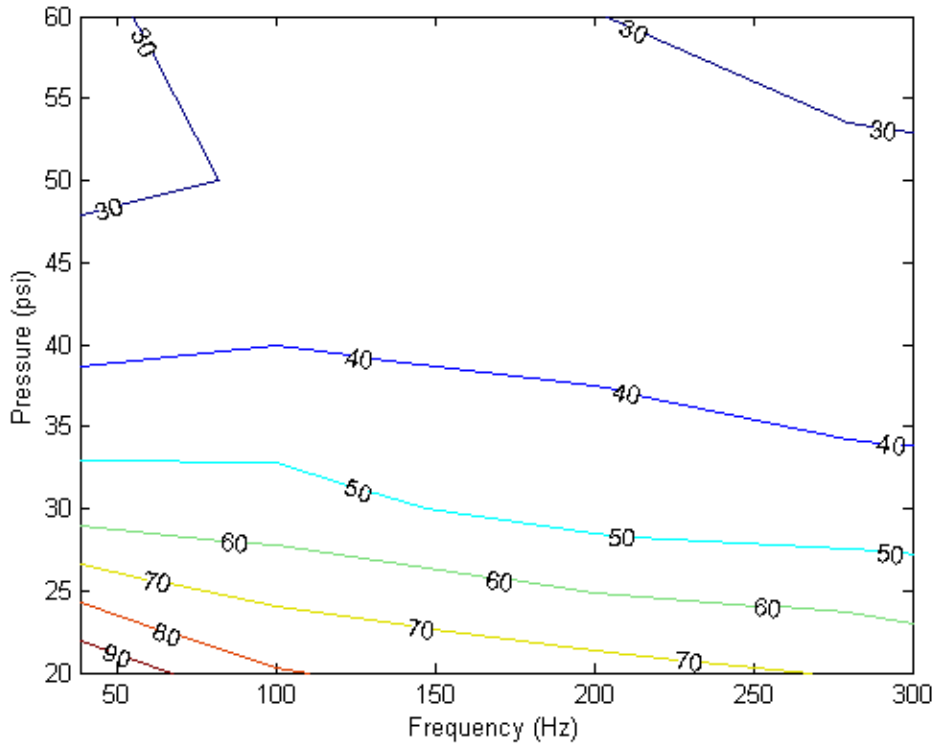

Fig. 4.10: Average Sauter-Mean-Diameter as a function of forcing frequency and injection pressure.

Six cases were selected to reveal time-evolution of droplet size distributions. Fig. 4.11 displays a typical variation in the droplet size distribution taken at four different phases when the liquid fuel was forced at 20 psi, 125 Hz and 50% duty cycle. It was evident that the droplet size distributions went through a periodical variation as expected. At a phase angle of 0 degree, the size distribution exhibits a bimodal nature, corresponding to the initial pressurization process. As the pressure inside the trapped volume became larger, more small droplets were formed, causing the volume fraction for small droplets to increase. At phase 180º, the distributions appeared as a log-normal mode, similar to typical steady-state sprays. After the fuel injector was closed at phase 180º, the trapped liquid fuel pressure decreased and the number of larger droplets was increased. Similar behavior was observed at other conditions. The rest of the data is

shown in Appendix B detailing the measured droplet size distribution at every 45º intervals.

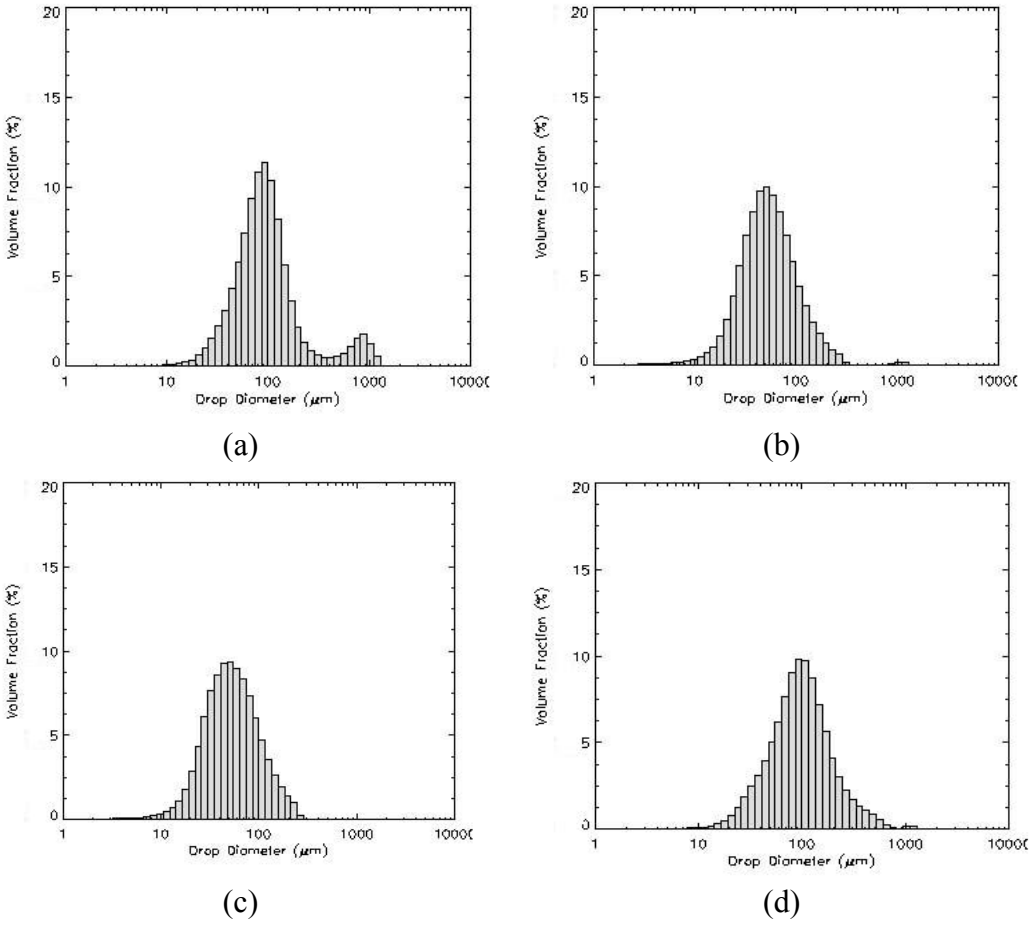

Fig. 4.11: Phase-locked ethanol droplets size distribution at pressure 20 psi, forcing frequency 125 Hz, 50% duty cycle, phase angle (a) 0˚ (b) 90˚ (c) 180˚ (d) 270˚.

The phase-lock-averaged Sauter-Mean-Diameter at various conditions are illustrated in Fig. 4.12. The results show that the droplet size went through a cyclic variation. This finding has an important implication for combustion control because the droplet size modulation is expected to significantly affect the transient heat release behavior.

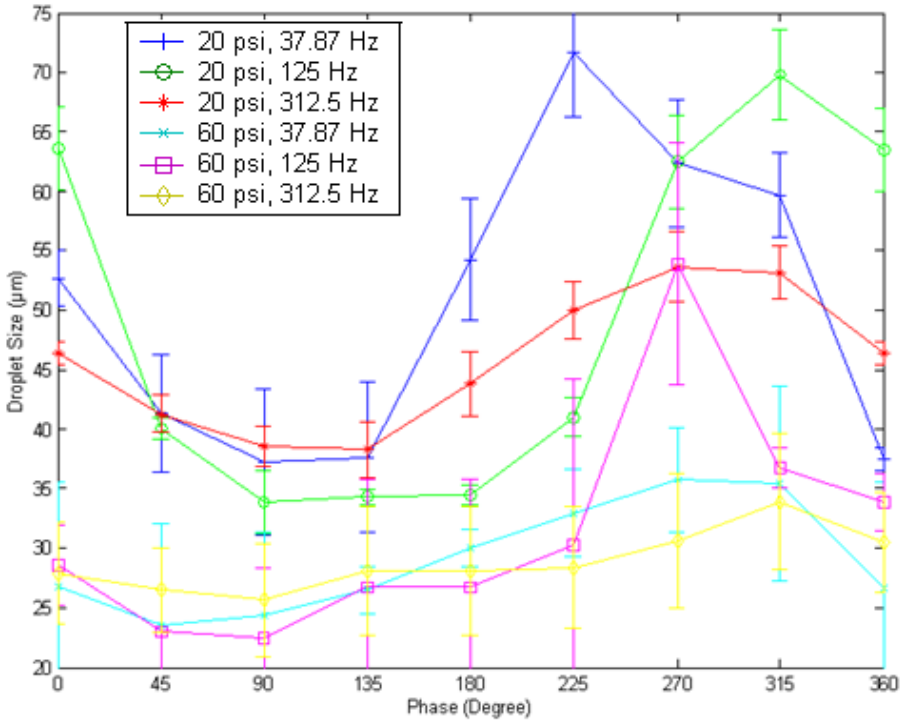

Fig. 4.12: Phase-lock-averaged Sauter-Mean-Diameter variation at different injection conditions.

4.2.2 Corresponding Variation in Liquid Fuel Heat Release Fluctuation

According to Rayleigh's criterion, one strategy to suppress the combustion instability could be to control the timing of heat release fluctuation q' with respect to the pressure oscillation p'. That is to say, that the large amplitude pressure oscillation inside the chamber could be suppressed if the heat release fluctuation q' occurs out of phase with respect to pressure oscillation p'.

To demonstrate the effectiveness of active suppression of vortex-driven combustion instability using a controlled liquid-fuel injection strategy, the heat release

characteristic of the controlling fuel must be analyzed. A simple heat release model of a fuel droplet was built to fulfill the above analysis.

In this model, a droplet is assumed to burn in a two-step process. First the droplet is heated to the boiling point when it begins to vaporize and burn. The vaporization timing during the heat-up process is assumed negligible so that the initial droplet size remains constant until the droplet reaches its boiling point. As burning proceeds, the induced flow recirculation within the droplet soon creates a fairly uniform temperature distribution, so that throughout its volume, the droplet temperature is assumed to be fairly close to the surface temperature.

It is also assumed that the heat flux absorbed by the droplet is used to vaporize the droplet first, so

$$h\left(\pi D^2\right)\left(T_\infty - T_f\right)dt = \rho_f h_{fg} dV \tag{4.1}$$

Here, h is the convective heat transfer coefficient, D is the fuel droplet diameter, T_∞ is the free stream temperature, T_f is the fuel droplet temperature, ρ_f is the fuel droplet density, h_{fg} is the latent heat of formation, t is the time and V is the fuel droplet volume.

Rearranging Equation (4.1):

$$\frac{dV}{dt} = \frac{h\left(\pi D^2\right)\left(T_\infty - T_f\right)}{\rho_f h_{fg}} \tag{4.2}$$

Droplet vaporization is often modeled after the D^2 law

$$D(t) = D_0\left(1 - \frac{t}{\tau}\right)^{0.5} \qquad \text{for } 0 \le t \le \tau \tag{4.3}$$

Where τ represents the characteristic fuel droplet vaporization time, and D_0 is the initial fuel droplet diameter.

Rate of change of heat release of a fuel droplet with diameter $D(t)$ can be written as:

$$\dot{Q}(t) = -\rho_f h_{RP} \frac{dV}{dt} = -\rho_f h_{RP} \frac{d}{dt}[\frac{\pi D^3}{6}(1-\frac{t}{\tau})^{\frac{3}{2}}] = \rho_f h_{RP} \frac{\pi D^3}{4\tau}(1-\frac{t}{\tau})^{\frac{1}{2}} \quad (4.4)$$

Maximum instantaneous heat release occurs when t = 0 and can be given as:

$$\dot{Q}_{\max} = \frac{\pi \rho_f h_{RP} D_0^3}{4\tau} \quad (4.5)$$

By combing Eqn. (4.2) and Eqn. (4.4), the result for τ can be determined as:

$$\tau = \frac{\rho_f h_{fg} D_0}{4h(T_\infty - T_f)} \quad (4.6)$$

This would mean that the maximum instantaneous heat release of a droplet occurs when the droplet size is biggest and the quantitative value is given by:

$$\dot{Q}_{\max} = -\rho_f h_{RP} \frac{h(\pi D_0^2)(T_\infty - T_f)}{\rho_f h_{fg}} = \frac{h h_{RP}(\pi D_0^2)(T_\infty - T_f)}{h_{fg}} \quad (4.7)$$

Here, h, the convective heat transfer coefficient can be estimated from the following equation using the Nusselt number.

$$Nu = hD_0 / k \quad (4.8)$$

An empirical equation to calculate the Nusselt number for a droplet burning in a forced convection environment is given by Faeth [97] as follows:

$$Nu = 2 + \frac{0.555\,\mathrm{Re}^{1/2}\,\mathrm{Pr}^{1/3}}{\left[1 + 1.232 \Big/ \left(\mathrm{Re}\,\mathrm{Pr}^{4/3}\right)\right]^{1/2}} \tag{4.9}$$

Here Re is the Reynolds number that can be estimated based on the fuel droplet diameter and velocity, Pr is Prandtl number (for an atmospheric convection condition *Pr* is set to a constant value of 0.7).

The fuel droplet temperature T_f in Equation 4.7 can be estimated as the average value of the fuel droplet boiling point temperature T_{fb} and the gas temperature T_g inside the combustor. That is to say:

$$T_f = \frac{T_{fb} + T_g}{2} \tag{4.10}$$

Based on the above liquid fuel droplet combustion model, the heat release variation at different phases of a cycle was analyzed using the acquired droplet size data. It is expected that with higher injection pressure, which means more small droplets, the instantaneous heat release rate will be larger. Since for equal amounts of liquid fuel more small droplets indicate larger fuel-oxygen surface area, the fuel can be burned much faster and more energy can be released.

The instantaneous heat release of different phases of a cycle was normalized by the averaged heat release of the complete cycle and illustrated in Fig. 4.13. It was noted that with higher frequencies, the heat release rate variation was much smoother compared to the lower injection frequency conditions. This was because with high injection frequency, the liquid fuel trapped between the fuel injector and atomizer cannot be drained as completely as it can in low frequency injection conditions. Therefore the

droplet size variation in high frequencies was not as well defined as in low frequency situations. The resulting change in heat release fluctuation was not as acute as in low frequency circumstances. This finding suggested that if this liquid-fuel injection strategy were used to suppress high frequency combustion instabilities, setting the injection frequency as a sub-harmonic of the dominant peak frequency and utilizing its higher harmonics could be a possible strategy.

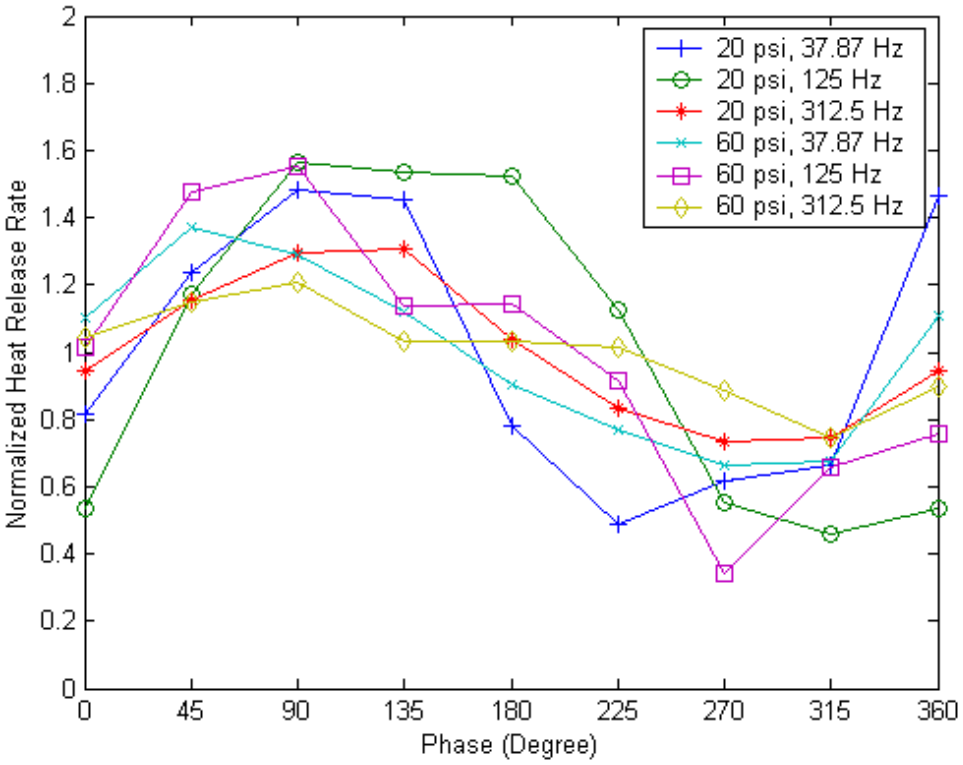

Fig. 4.13: Phase-locked heat release rate variation at different injection conditions.

Analysis of the instantaneous heat release with a liquid-fuel injection strategy showed without doubt that this strategy was feasible in suppressing combustion instabilities because heat release fluctuation could be created with droplets of different sizes. If the heat release fluctuation q' was added to the combustion system in such a

way that it was always out of phase with respect to the pressure oscillation p', large amplitude pressure oscillations could be suppressed according to Rayleigh's criterion.

4.3 Velocity Profile of Controlled Liquid Fuel Droplets

The droplet velocity is another important parameter in the characterization of liquid fuel sprays. The velocity profile can determine how the droplets will be deployed before they are completely burned. To acquire the fuel droplet velocity profile, the PIV technique was employed in this dissertation work. Planar Mie-scattering images were also obtained in the meantime for qualitative characterization purposes.

First, liquid fuel droplet spray in a quasi-quiescent environment was investigated. A complete cycle of phase-lock-averaged planar Mie-scattering images of pulsed sprays forced at 20 psi, 38 Hz and 50% duty cycle is shown in Fig. 4.14. Forty instantaneous images were averaged at each phase. The pulsed nature of the liquid fuel sprays is clearly illustrated in this figure. Since the duty cycle of the injector control signal was set to 50%, no fuel was expected immediately after the 180 degree phase. However, as implied previously, the fuel injector was not completely off, at least until phase 210º according to Fig. 4.14. This was the result of the trapped liquid fuel being released. Though the fuel injector was switched off, there was a delay in the complete release of the pressure upstream of the atomizer and the draining of all the liquid fuel. Therefore, the volume between the fuel injector and the atomizer needs to be as small as possible to precisely control the liquid fuel sprays.

Depending on the forcing frequency and pressure, the liquid fuel spray dynamics appeared to be quite different in the quasi-quiescent environment. As illustrated in Fig. 4.15, for the same injection pressure at lower forcing frequency conditions, the spray

clearly went through a completely "on" and completely "off" phases as in (a) and (c). But at the higher frequency as in (b) and (d), it was difficult to distinguish the complete "off" phases of the fuel flow. This suggested that for higher frequency actuation, the spray shape was simply modulated at the driving frequency instead of going through a complete "on" and "off" transition due to the trapped volume between the fuel injector and the atomizer. The injection pressure also played an important role in the liquid fuel spray. Also shown in Fig. 4.15, the spray angle increased as the forcing pressure increased at the same forcing frequency conditions.

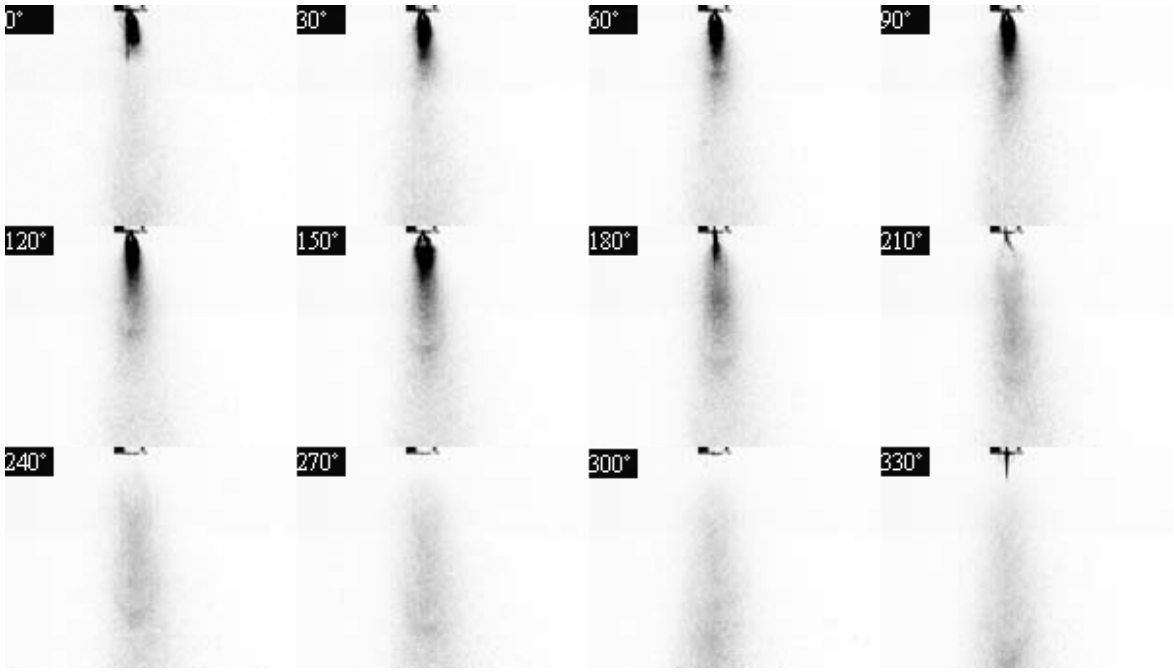

Fig. 4.14: A complete cycle of planar Mie-scattering images at forcing frequency 38 Hz, 20 psi and 50% duty cycle.

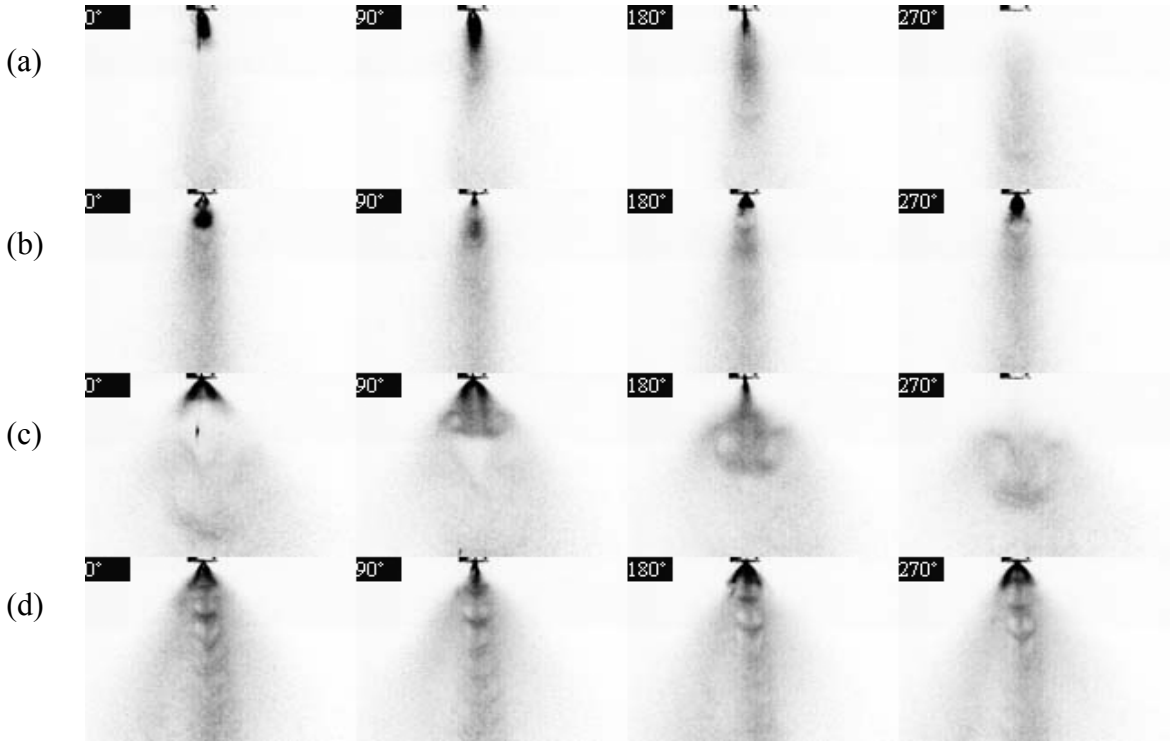

Fig. 4.15: Planar Mie-scattering images at different forcing conditions: (a) 20 psi, 38 Hz; (b) 20 psi, 280 Hz; (c) 60 psi, 38 Hz; (d) 60 psi, 280 Hz

The droplet velocities under the quasi-quiescent environment were directly measured with a PIV instrument. Fig. 4.16 represents a sequence of phase-locked average velocity profiles of droplets when pulsed at 38 Hz and 20 psi. The velocity unit in these figures was in m/sec. Both the vector length and the gray scale manifested the magnitude of the velocity. From these phase-lock-averaged PIV results, it was revealed that droplet velocities were highest at around 6.5 m/sec when they were just coming off the atomizer tip, but eventually slowed down due to the drag force. As the fuel injector was periodically pulsed, droplet velocities were also modulated at the same frequency. This was demonstrated as the large velocity droplets moved down stream at increased phase angles. This finding was also observed at the "off" stages of the fuel injectors. Residual

droplets up to 12 mm downstream of the nozzle exit area still showed small magnitude vectors in the velocity profile images.

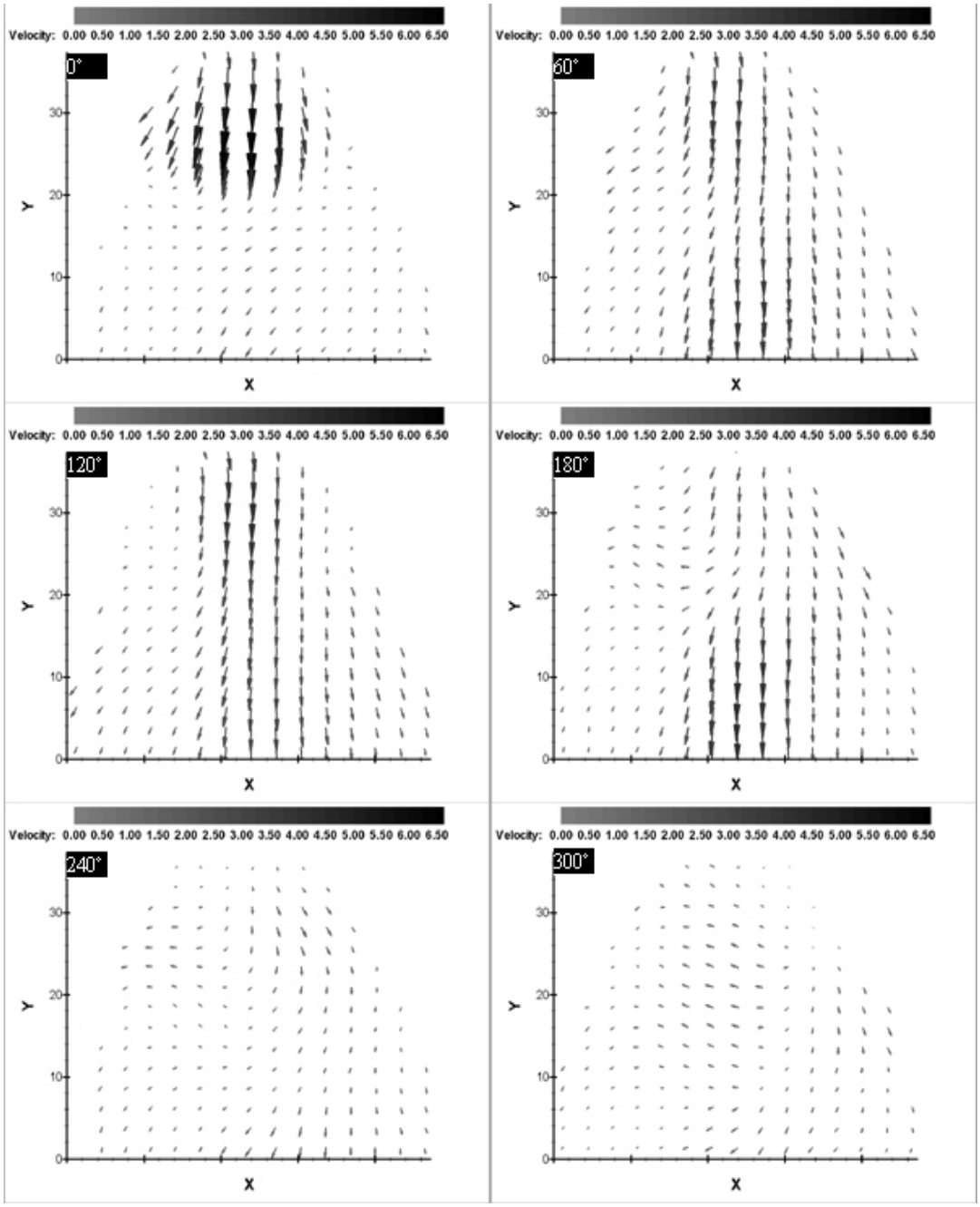

Fig. 4.16: A sequence of phase-lock-averaged velocity profile images at forcing frequency 38 Hz and injection pressure 20 psi.

(a)

(b)

(c)

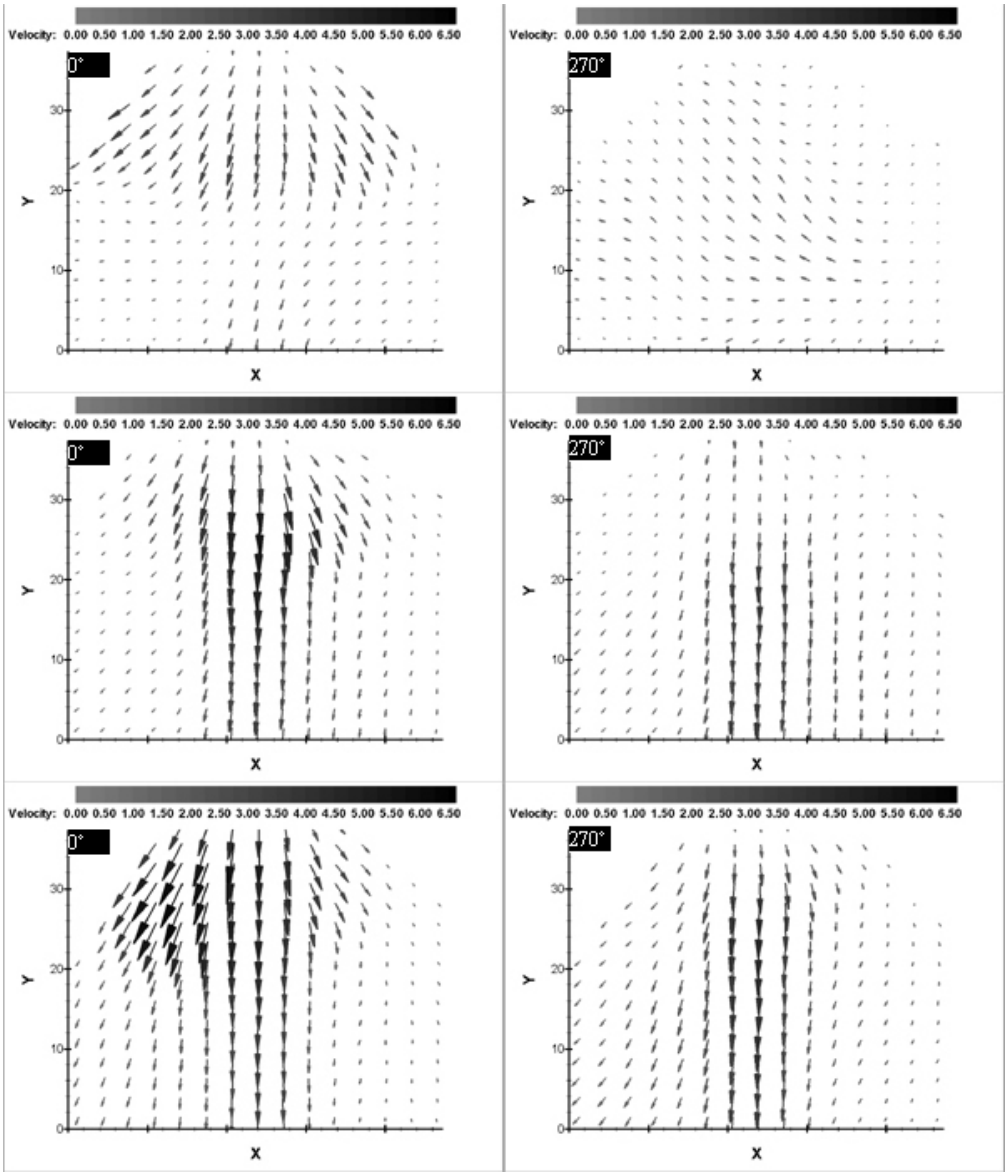

Fig. 4.17: Phase-lock-averaged velocity profile at same injection pressure 40 psi, same duty cycle 50%, but with different forcing frequency: (a) 38 Hz, (b) 150 Hz, (c) 280 Hz.

Phase-lock-averaged velocity profiles at an injection pressure of 40 psi and duty cycle of 50%, with varying forcing frequencies, are compared in Fig. 4.17. Two phases of three different forcing frequency conditions: 38 Hz, 150 Hz, and 280 Hz are shown in this figure. With higher frequencies, the droplets moved faster due to the residual pressure that was caused by trapped liquid fuel between the fuel injector and the atomizer.

Fig. 4.18 compares the phase-lock-averaged velocity profiles at the same forcing frequency of 280 Hz and duty cycle of 50% with varying injection pressures: 20 psi, 40 psi, and 60 psi. It was clearly illustrated that with higher pressure, the droplets exited the nozzle much faster.

(a)

(b)

(c)

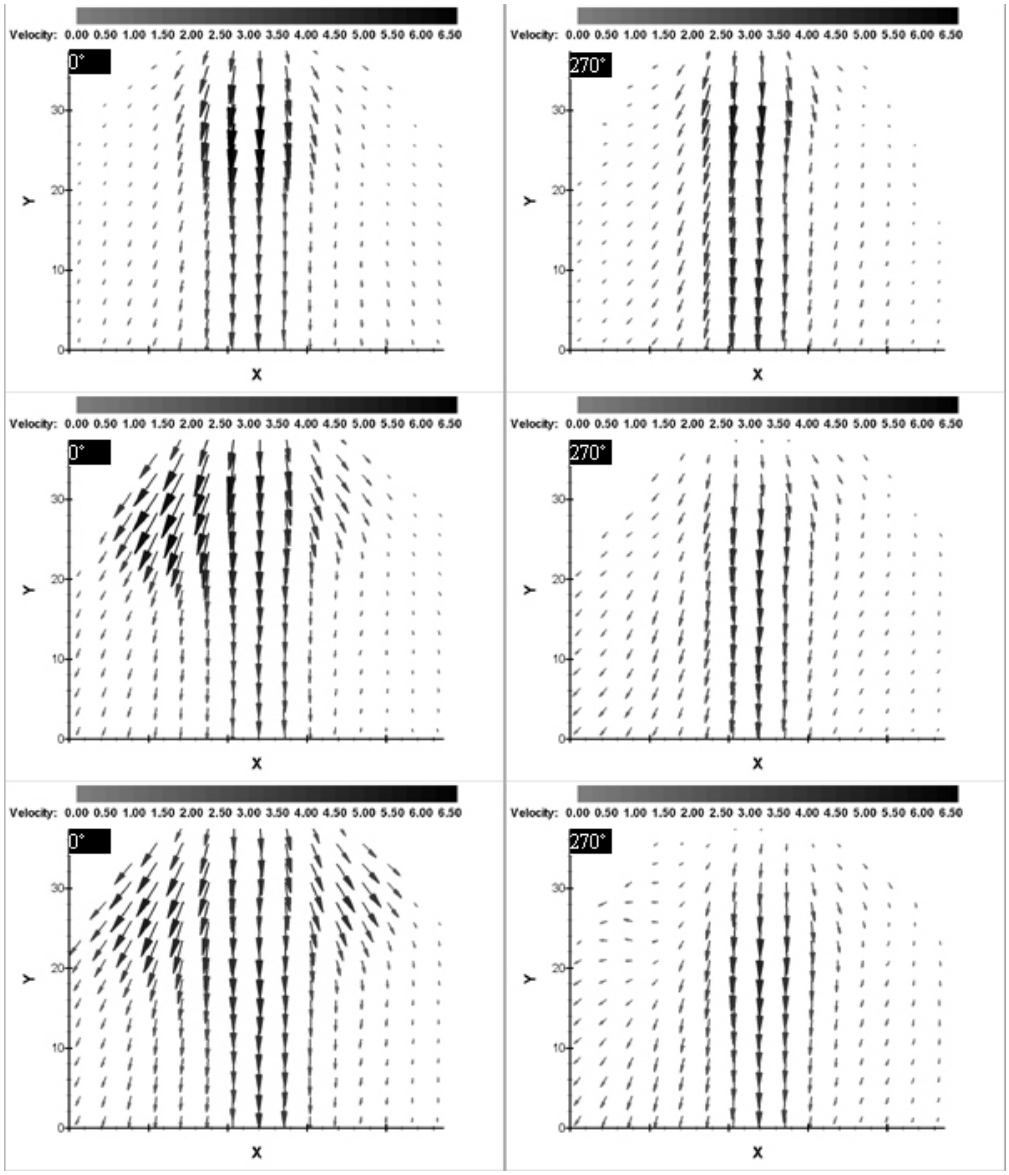

Fig. 4.18: Phase-lock-averaged velocity profile at same forcing frequency 280 Hz, same duty cycle 50%, but with different injection pressure: (a) 20 psi, (b) 40 psi, (c) 60 psi.

PIV measurements were also extended to the reacting flow fields to study fuel droplet behaviors under combustion conditions. For comparison purposes, fuel droplet dispersion into nonreacting environment was also investigated at the same inlet conditions.

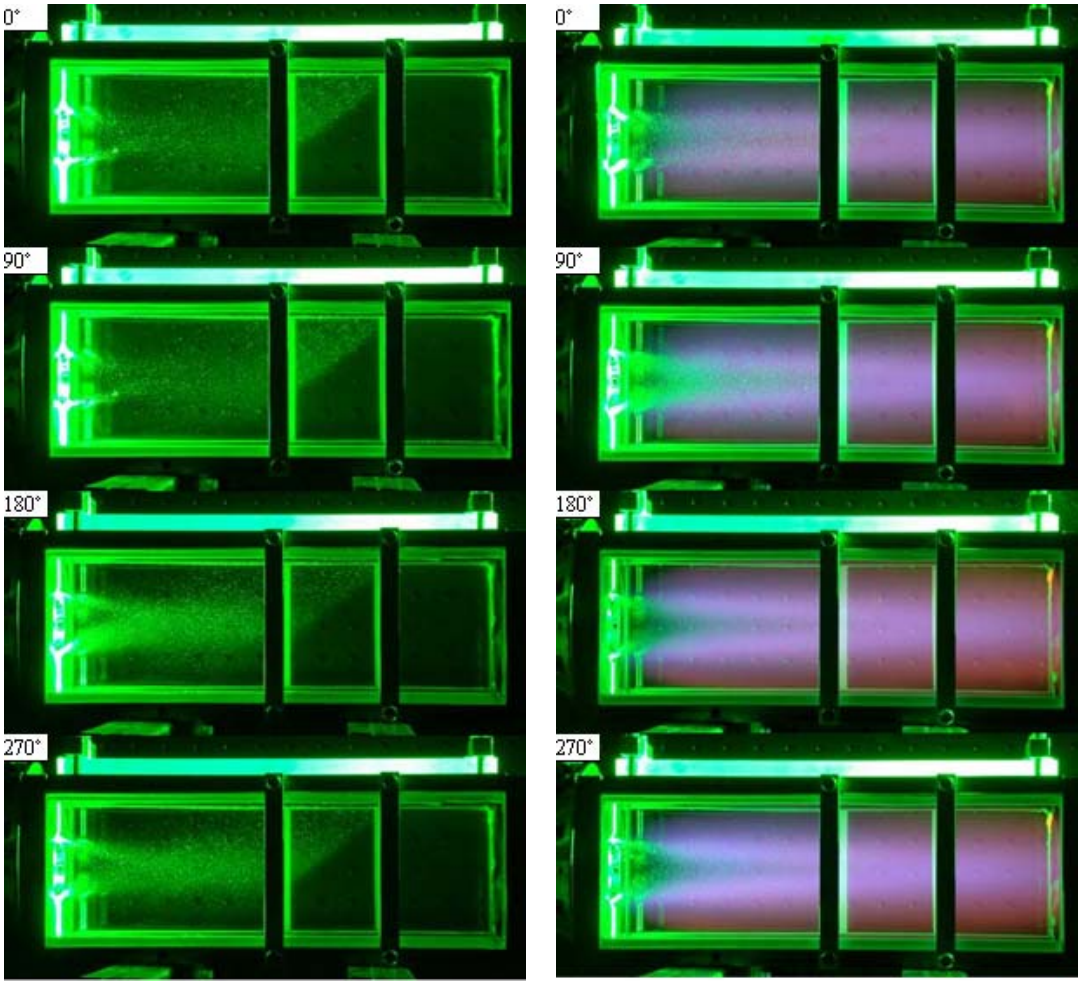

(a) (b)

Fig. 4.19: Sequence of phase-lock-averaged planar Mie-scattering spray images at different phases of a cycle (a) without combustion; (b) with combustion. Liquid fuel was forced at 38 Hz, 20 psi and 50% duty cycle.

Two sequences of phase-lock-averaged planar Mie-scattering fuel spray images at different cycle phases are illustrated in Fig. 4.19. The fuel spray images under

combustion conditions were compared to the images of corresponding phases with no combustion conditions. Forty instantaneous images were averaged to reduce the turbulent effect. As expected, a lesser number of liquid fuel droplets remained in the reacting flow field as smaller droplets were quickly vaporized and burned. However, enough droplets were still left in the reacting flow field to obtain statistically meaningful velocity measurements.

Fig. 4.20 shows two sets of phase-lock-averaged velocity profiles for the nonreacting and reacting cases respectively. To obtain meaningful droplet velocity measurements, 40 instantaneous velocity profiles were averaged to eliminate random droplet behaviors. In the near field, where the droplets just came into the dump combustor, the velocity magnitude fluctuated from 0 to 10 m/sec as the result of the interactions between the droplets and flow field. As the remaining droplets were carried downstream, they approached the dump plane reference velocity of 15 m/sec. Compared to the nonreacting case, the droplet velocities were generally higher under reacting situations.

Detailed comparison of fuel droplet velocities between reacting and nonreacting cases is shown in Fig. 4.21. Droplet velocities at four different phases under combustion conditions were contrasted with the corresponding phases of noncombustion circumstances. It was obvious that droplets moved faster when combustion occurred. Large-scale vortex structures were still observed periodically shedding at this fixed-frequency open-loop control condition. Therefore, this oscillation may have been the cause of the droplets speeding up.

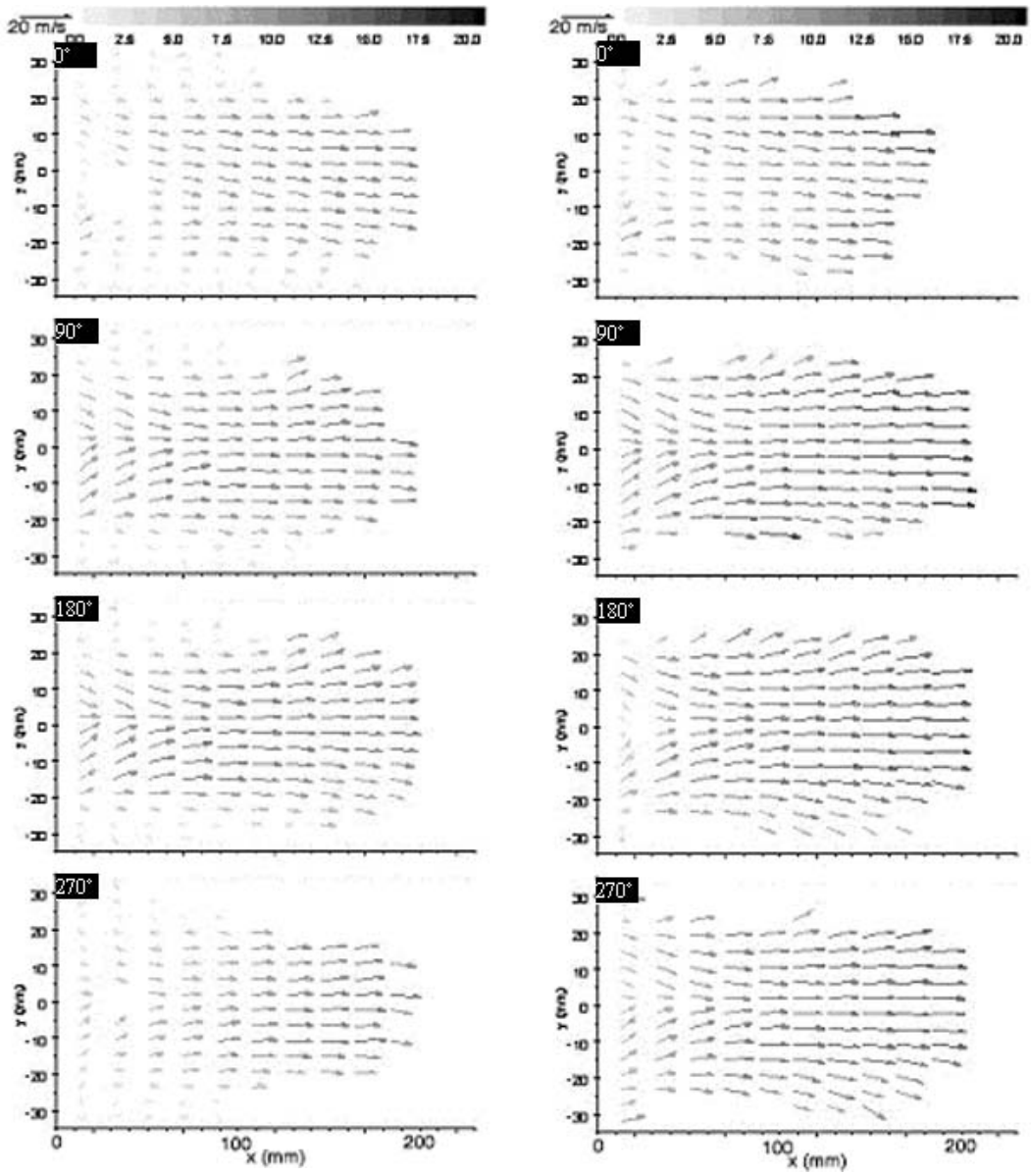

(a) (b)

Fig. 4.20: Phase-averaged velocity profiles of fuel droplets at different phase of a cycle (a) nonreacting case; (b) reacting case, liquid fuel was forced at 38 Hz, 20 psi and 50% duty cycle.

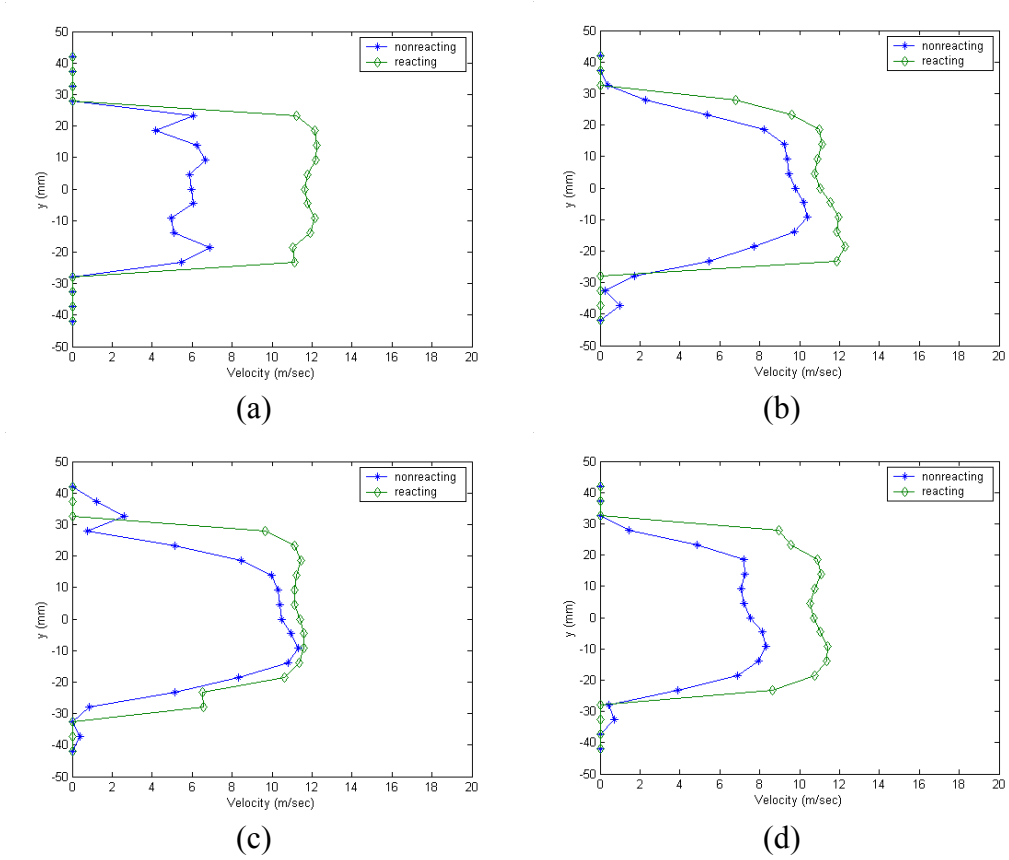

Fig. 4.21: Droplets velocity at x = 41.32 mm from dump plane at different phase angle (a) 0°; (b) 90°; (c) 180°; (d) 270°, liquid fuel was forced at 38 Hz, 20 psi and 50% duty cycle.

4.4 Summary and Discussion

This study characterized the dynamics of controlled pulse fuel sprays intended to suppress the large amplitude pressure oscillations. A Malvern instrument was used to investigate the initial size distribution of fuel droplets coming out of the actuators, and PIV was applied to visualize the fuel droplet dispersion into the reacting flow field.

The results showed that the fuel droplet distribution exhibited bimodal modes in pulsed sprays under certain situations. Both droplet size distribution and the Sauter-Mean-Diameter were oscillated at the frequency of fuel actuation as the fuel injectors were periodically pulsed. Droplet combustion analysis showed that this cyclic change in

size led to substantial changes in heat release characteristics, and that desired heat release fluctuations could be obtained using controlled liquid fuel injection techniques.

It was shown analytically in this chapter that transient heat release rate could be controlled by variation in fuel droplet size as well as the number of droplets. The droplet size was important because it determines not only the time delay associated with heat release but also its peak amplitude. This result implies that a minimum requirement for liquid-fuel actuator is an ability to control fuel droplet size and number as a function of time. Also important characteristics may be spatial distribution of fuel droplets, i.e., controlling where the fuel droplets are placed.

PIV measurements provided better insight into the rate and location of fuel droplet dispersion as well as the effect of heat release on fuel droplet distribution. For pulsed sprays, the droplets reached their maximum velocities of about 6.5 m/sec at the atomizer exit and then slowed down due to drag in quasi-quiescent environments. Under burning conditions inside the combustion chamber, the fuel droplets interacted with the flow field and gradually caught up with the flow velocity near the combustor centerline.

The characterization study in this chapter revealed that both droplet size and spatial distributions were affected by the present approach of pulsed fuel actuation.

Chapter 5: Heat Release Pattern .vs. Vortex Structures

5.1 Introduction

Rayleigh's criterion suggests that combustion instability is a result of heat release fluctuations coupled with pressure oscillation in a positive manner. Heat release fluctuation evidently plays a critical role in amplifying and sustaining the large amplitude pressure oscillation inside the combustion chamber.

This chapter presents a natural heat release pattern of a vortex-driven instability in a simple set up designed to control the transient processed. The specific objectives were to clarify the responsible physical mechanisms in vortex driven combustors and to understand the transient location where fuel should be added for suppressing combustion instabilities. Since large-scale vortex structures play an important role in combustion instabilities in those types of vortex-driven combustors [23], [50], [98-108], this research work investigated the relationship of heat release fluctuation relative to the large-scale vortex structures [109].

Large-scale vortex structures were visualized with Schlieren techniques and information on heat release fluctuations with respect to vortex structures was obtained using CH* chemiluminescence measurements. These two qualitative results were compared at their corresponding phases to determine their relationship.

5.2 Experimental Setup and Instrumentation

To focus on investigating how heat release fluctuations associate with the large-scale vortex structures, Sanming electronics S-75A loudspeakers with a frequency response range from 125 Hz to 8500 Hz were employed to periodically force the inlet

flow at a desired frequency to simulate the natural oscillation of inlet flow. As a result of the excitation, large coherent structures were created and propagated downstream periodically. However, this acoustic driver was not powerful enough to affect the inlet conditions of the previous dump combustor facilities. As a result, a much smaller scale rig was built to control the vortex shedding process with the incorporated loudspeaker.

First, a simple vortex-stabilized jet flame model was built to characterize the heat release changes with respect to the flow structures, as shown in Fig. 5.1. Air and propane gas were then introduced separately through choked orifices into a circular tube with an inner diameter of 25.4 mm. The choked orifices were placed at the same axial location but at the opposite side of the circumference to increase the mixing of the reactants. To simulate the natural oscillation inside the vortex-driven combustors, this gas mixture was periodically surged downstream by acoustic excitation at pre-defined frequencies by a loudspeaker along a 250 mm long aluminum pipe. Sine wave with preset frequency and amplitude was used to activate the acoustic driver. A Bogen C-100 amplifier was used to amplify the signal created by the signal generator. In this unconfined turbulent flame jet model, a short circular extension of 32.3 mm length and 30.0 mm inner diameter was added to the open-end of the inlet pipe to stabilize the flame at the pipe exit. Without this short extension pipe the flames would be very unsteady and could not be maintained throughout the experiment.

The phase-locked Schlieren technique was employed to visualize the density gradient in the flow field, i.e., the interface between reactants and products. As expected, the visualization revealed the presence of large coherent structures that were shed periodically at the inlet exit. The local heat release was characterized with CH*

chemiluminescence. An Omega HH731 stroboscope was used as a light source and a Pulnix CCD camera was employed to obtain all the images.

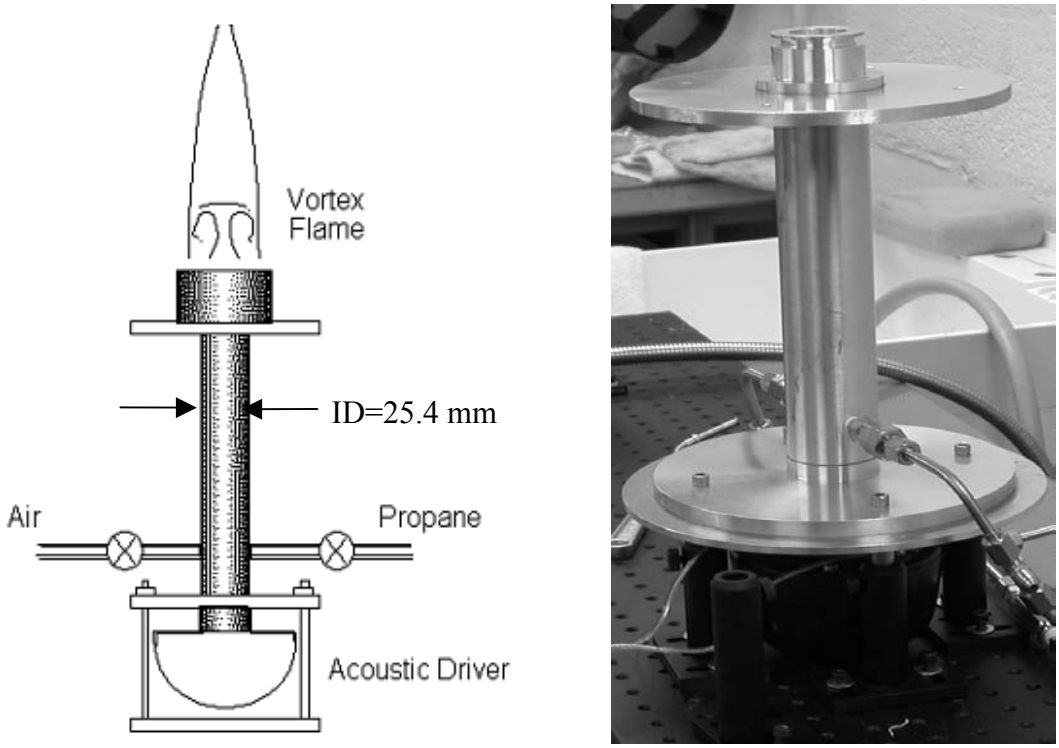

(a) (b)

Fig. 5.1: Vortex-stabilized jet flame model.

In this free turbulent jet flame model the equivalence ratio of the reacting gaseous mixture has to be kept near the stoichiometric condition so that the flame can be stabilized at the exit. To produce a recirculation region that can stabilize the combustion process near the inlet exit plane at lean combustion conditions, modifications were made to this free turbulent jet flame model and another combustor model was created.

A square combustor was put on top of the exit of the inlet pipe to cover all the desired equivalence ratio operating conditions. As illustrated in Fig. 5.2, a 305 mm long, and 102 mm wide stainless steel square combustor section was added for flame stabilization purposes at lean equivalence ratio test conditions. Same lengths of quartz

windows were put on both sides to provide full optical access for the flow and flame visualizations.

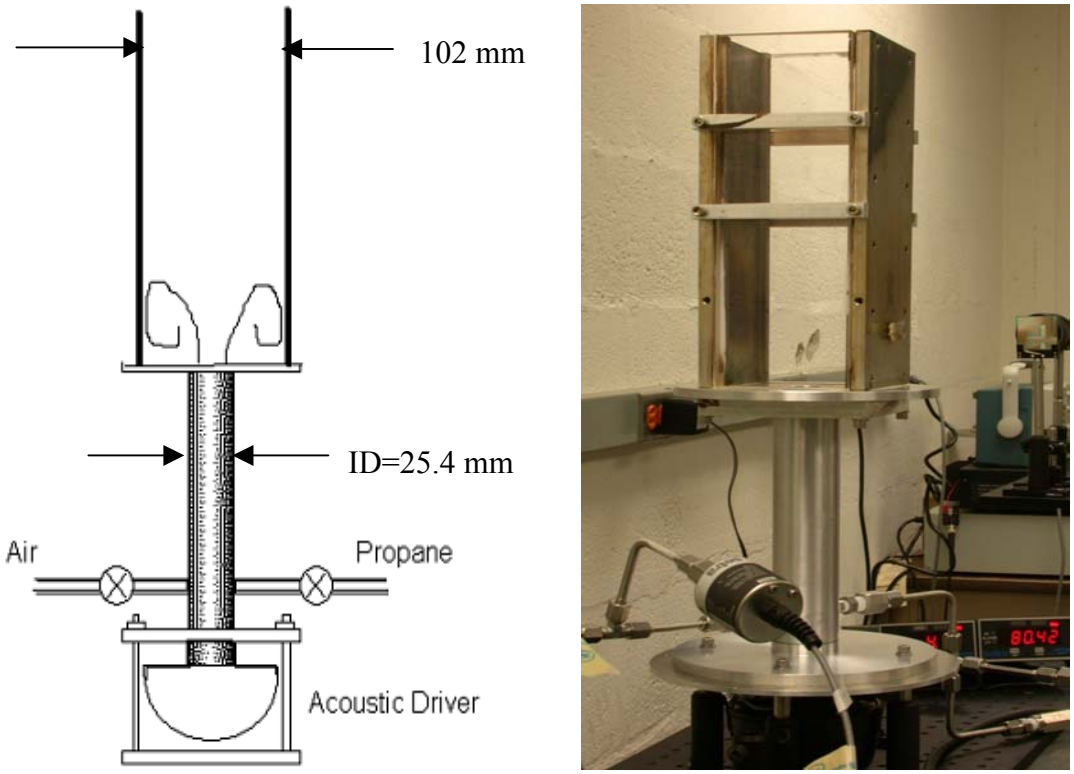

(a) (b)

Fig. 5.2: Combustor model.

5.3 Flame Model

Large-scale coherent structures play an important role in combustion and heat release processes by controlling the mixing between the fresh reactants and hot combustion products in premixed combustors. On one hand, large-scale structures could enhance combustion because of the increase of transport and vigorous fine-scale molecular mixing that take place upon eddy breakup. On the other hand, large-scale structures could stifle combustion by increasing entrainment of cold air into the potential reaction zone as well as by severely stretching the flames.

To identify the spatial and temporal distributions of heat release surplus and deficit with respect to the large-scale coherent structures, a vortex-driven turbulent jet flame model was built and systematically investigated in this study.

Because the vortex shedding frequency was controlled in this study, a regular CCD camera could be utilized for investigating the phase variation instead of using expensive high-speed equipment. The key to this phase-locked technique [110] was that the acoustic forcing frequency was set close to an integral multiple of imaging acquisition frequency. In this way, every continuous acquired single image reflected a slightly different phase of a cycle, and the images of a complete cycle were linked from different acoustic forcing periods. Turbulent effects were removed by averaging several same phase instantaneous images.

The experimental flow conditions of this flame model are summarized in Table 5.1. The forcing frequency and forcing amplitude of the acoustic driver were varied to identify the distributions of heat release fluctuations relative to the large-scale vortex structures. Due to the flame stability limitation in this rig, all the experiments were conducted near stoichiometric conditions.

Table 5.1: Experimental conditions for jet flame combustion model

Inlet Velocity (m/sec)	Equivalence Ratio	Forcing Frequency (Hz)	Inlet Diameter (mm)
8.4	0.97	180,240,300,360	15.0

While the forcing frequency was the only variable parameter in this arrangement there were two non-dimensional parameters of interest in this study. They were Strouhal number, *St*, and Damköhler number, *Da*. They are defined as:

$$St = \frac{fD}{u} \tag{5.1}$$

$$Da = \frac{\tau_{chem}}{\tau_{flow}} \tag{5.2}$$

Here D is the diameter of the exit, u is the exit mean velocity, f is the driven frequency of the acoustic driver, τ_{flow} is the fluid dynamic time, and τ_{chem} is the chemistry time.

In this experiment, τ_{flow} was taken as the period of forced oscillations and thus inversely proportional to the forcing frequency of the loudspeaker as shown in Fig. 5.3(a). While the chemistry time τ_{chem} was estimated from the chemical ignition data involving hydrocarbon fuels [111] as in Fig. 5.3(b), the equation τ_{chem} is a steep function of the equivalence ratio, which is particularly crucial near the blowoff limits. It is near minimum when equivalence ratio ϕ is near the stoichiometry point and increases exponentially as the equivalence ratio decreases.

The corresponding non-dimensional parameters of the experimental conditions are shown as in Fig. 5.4.

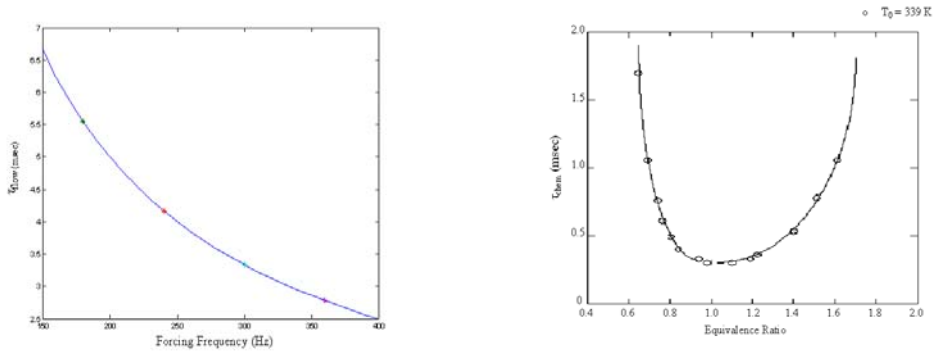

(a) (b)

Fig. 5.3: (a) Flow dynamic time; (b) Chemistry time.

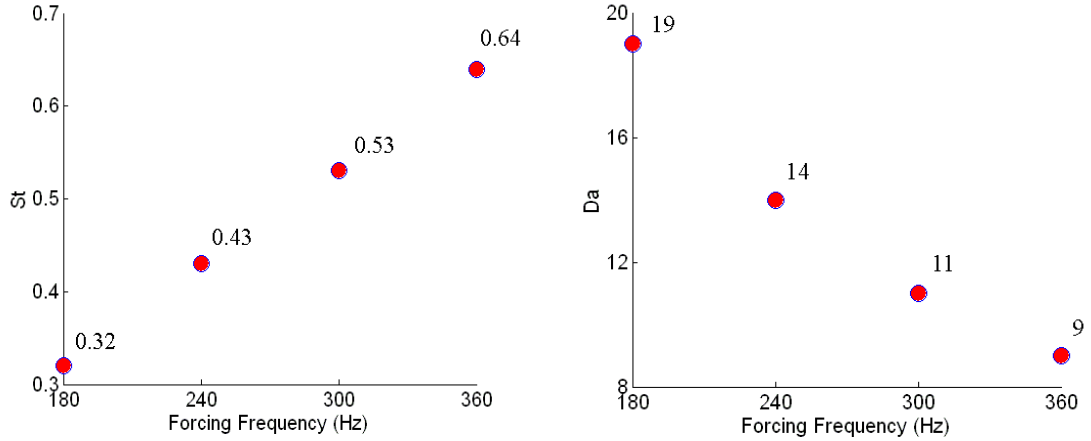

(a) (b)

Fig. 5.4: (a) Strouhal number; (b) Damköhler number.

The Strouhal number increased from 0.32 to 0.64 as the driving frequency of the loudspeaker increased from 180 Hz to 360 Hz. To stabilize the flame at the exit plane, this jet flame model must be operated at near fuel rich conditions. Thus the only parameter that affected the Damköhler number is the flow dynamic time, which is inversely proportional to the forcing frequency. For all the investigated condition in this study, the Damköhler number varied from 9 to 19. The range was still fairly high suggesting chemistry was extremely "fast" compared to flow time scale.

This research work used Schlieren techniques to visualize the interface between cool reactants and hot products. As expected, large-scale vortex structures were shed periodically at the inlet exit. A typical sequence of phase-locked spark Schlieren images is shown in Fig. 5.5. Large coherent structures were observed to generate and propagate down stream due to the periodic forcing of the acoustic driver.

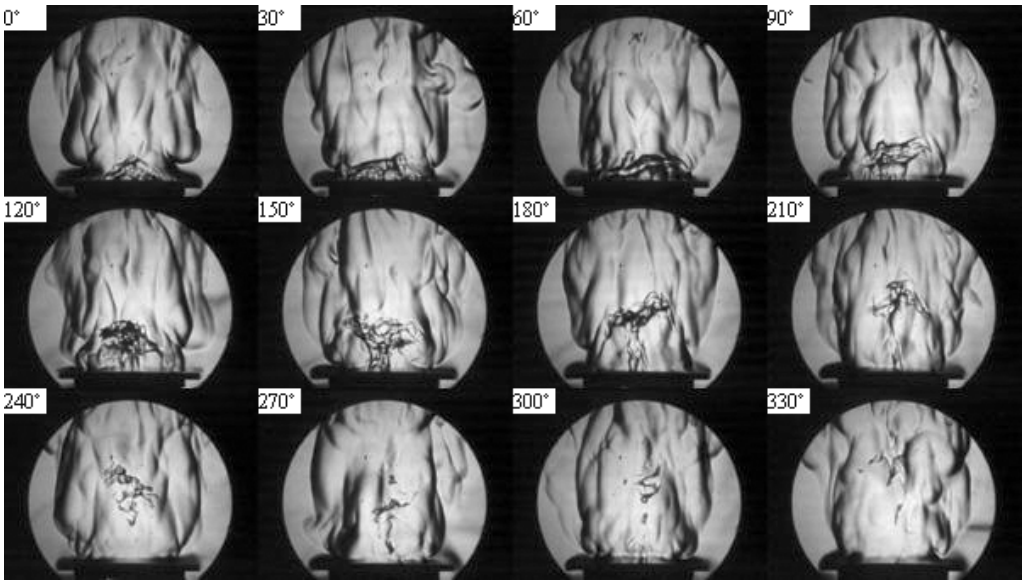

Fig. 5.5: Phase-locked instantaneous Schlieren images of a cycle at forcing amplitude 20V and forcing frequency 240 Hz.

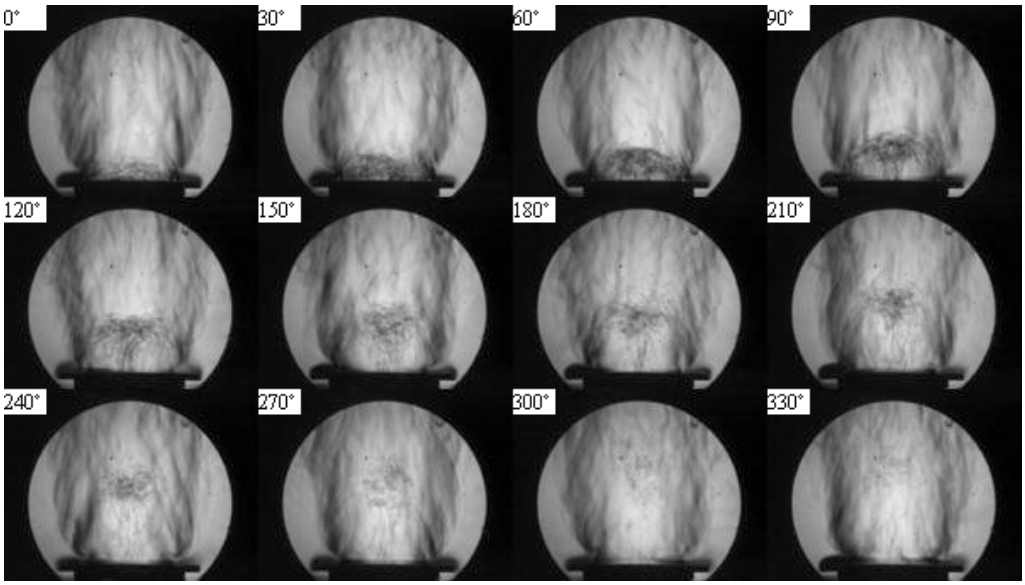

Fig. 5.6: Phase-lock-averaged Schlieren images of a cycle at forcing amplitude 20V and forcing frequency 240 Hz.

Nine instantaneous Schlieren images that were obtained at same phase were averaged into a single image to filter out the turbulent part of the flow movement. The

vortex structures in these averaged images were more symmetrical, as shown in Fig. 5.6, which depicts a complete cycle of the phase-lock-averaged Schlieren images.

Local heat release was characterized using the CH* chemiluminescence technique. Fig. 5.7 illustrates a sequence of phase-locked CH* chemiluminescence oscillation images of a cycle at a forcing amplitude of 20V and forcing frequency of 240 Hz. Only the fluctuation component was shown in these figures because it was this fluctuation component that could couple with the pressure oscillations and cause combustion instabilities. The way to get these images was to subtract the time-averaged CH* chemiluminescence amplitudes from the instantaneous CH* chemiluminescence at each spatial location. This would result in only the oscillating part of heat release, for example, q' . In these CH* chemiluminescence oscillation images, the white color represented the hot spot, where heat release was higher than the local average. The black color represented the cool spot, where heat release was lower than the local average. The local average heat release value was represented by the gray color. From Fig. 5.7 it can be observed that the heat release fluctuations also went through a phase variation process as the acoustic driver forced the inlet mixture to flow periodically.

The instantaneous Schlieren and CH* chemiluminescence oscillation images were combined together to disclose the relationship between the heat release fluctuations and the large coherent structures, as shown in Fig. 5.8. The color of CH* chemiluminescence images was adjusted to differentiate with the Schlieren images. The white color still represented the hot spots, while the red color represented the cool areas and the pink represented local average heat release. In this case, heat release fluctuations were

observed closely following the large vortex structures. The Schlieren and CH* chemiluminescence images of all experimental conditions are illustrated in Appendix C.

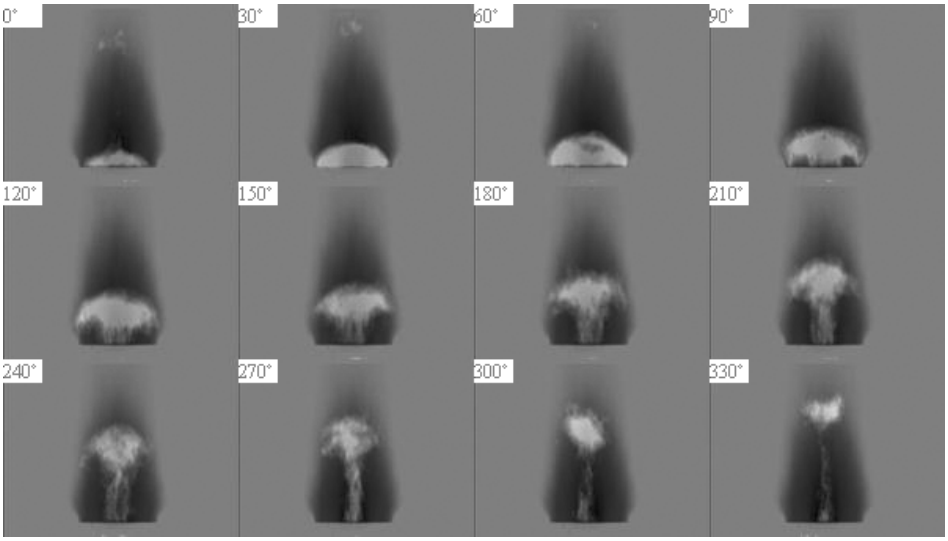

Fig. 5.7: Phase-locked CH* chemiluminescence oscillation images of a cycle at forcing amplitude 20V and forcing frequency 240 Hz.

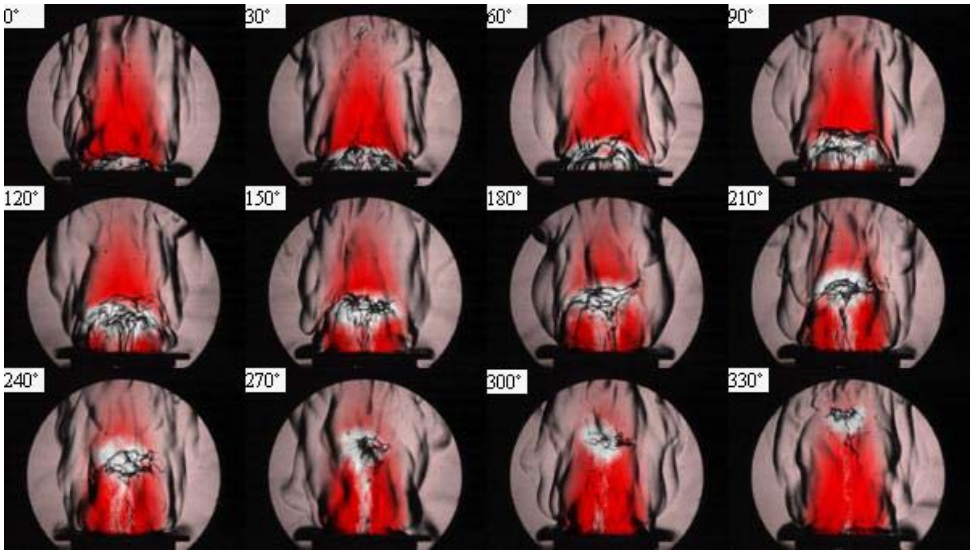

Fig. 5.8: Phase-resolved visualization of instantaneous Schlieren and CH* chemiluminescence images of a cycle at forcing amplitude 20V and forcing frequency 240 Hz.

The effect of forcing amplitude on the relationship between heat release fluctuations and vortex structures is shown in Fig. 5.9. Each column represents a different

forcing amplitude condition. With increasing forcing amplitude, (meaning more forcing power), the vortices became more organized. However, regardless of forcing amplitude condition, the hot spot of heat release oscillation closely followed the vortex front.

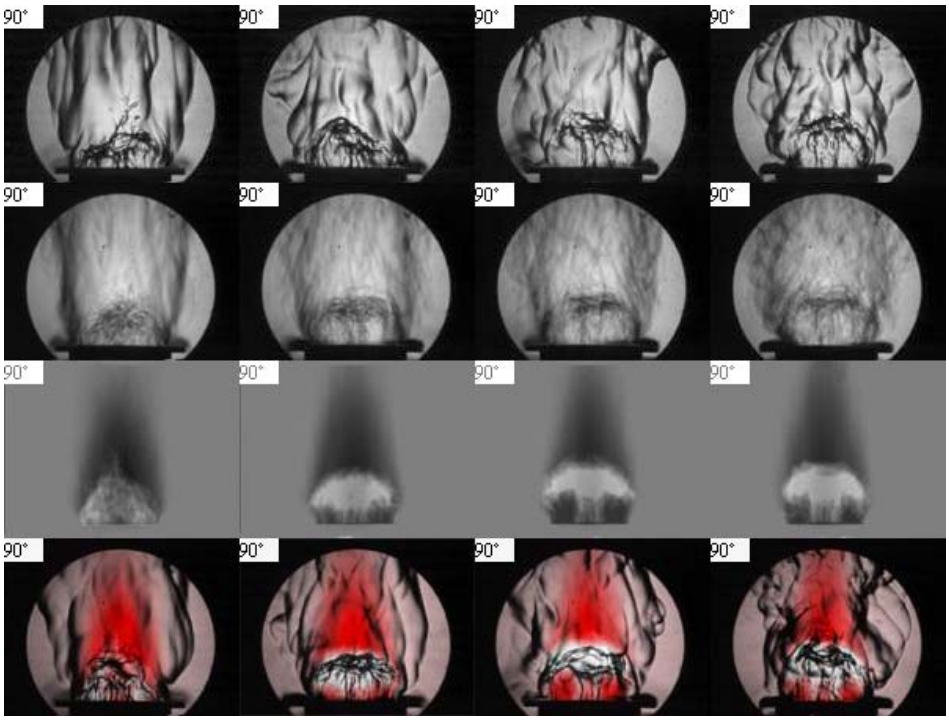

(a) (b) (c) (d)

Fig. 5.9: Effect of forcing amplitude at 180 Hz (a) 5V, (b) 10V, (c) 15V, (d) 20V from top to bottom: spark Schlieren images, averaged Schlieren images, CH* chemiluminescence oscillations images, superimposed composite images.

Fig. 5.10 demonstrates the effect of the forcing frequency. Each column represents a different forcing frequency case. The vortex structures shrank as the forcing frequency increased. However, in all test conditions the heat release oscillation still closely followed the vortex structure regardless of forcing frequency, as shown in the superimposed composite images in Fig. 5.10.

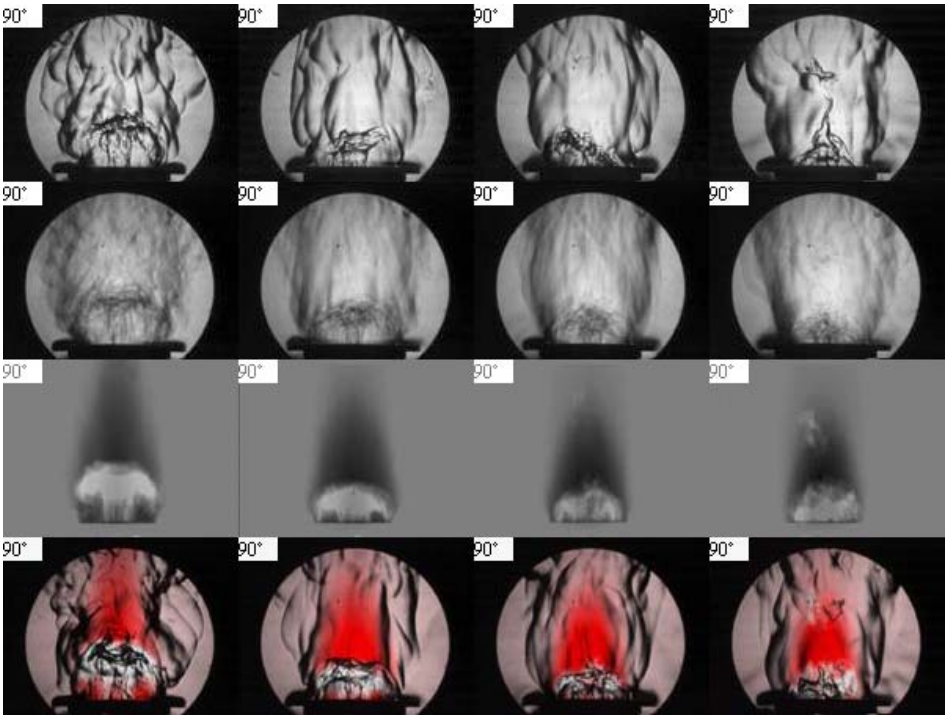

(a) (b) (c) (d)

Fig. 5.10: Effect of forcing frequency at 20V (a) 180 Hz, (b) 240 Hz, (c) 300 Hz, (d) 360 Hz from top to bottom: spark Schlieren images, averaged Schlieren images, CH* chemiluminescence oscillations images, superimposed composite images.

5.4 Combustor Model

For the previous flame model experiment conditions, the equivalence ratio of gas mixture was kept near stoichiometric to stabilize the flame at the pipe exit. To simulate more practical operating conditions associated with combustion instabilities, a combustor was placed downstream of the premixed jet that discharged from the inlet, as shown in Fig. 5.2, to stabilize the flames at lower equivalence ratios.

The experimental flow conditions for this combustor model are summarized in Table 5.2. Similar experiments, such as those completed in the flame model, were repeated at much lower equivalence ratio conditions to reveal the relationship between heat release fluctuations and large-scale vortex structures.

Table 5.2: Experimental conditions for combustor model

Inlet Velocity (m/sec)	Equivalence Ratio	Forcing Frequency (Hz)	Inlet Diameter (mm)
7.7	0.60. 0.65, 0.70	180	25.4

Because the chemistry time scale increased as the equivalence ration decreased, the Damköhler number was effectively reduced to as low as 2.3 in this study. The reduced parameters for combustor experiments are shown in Fig. 5.11.

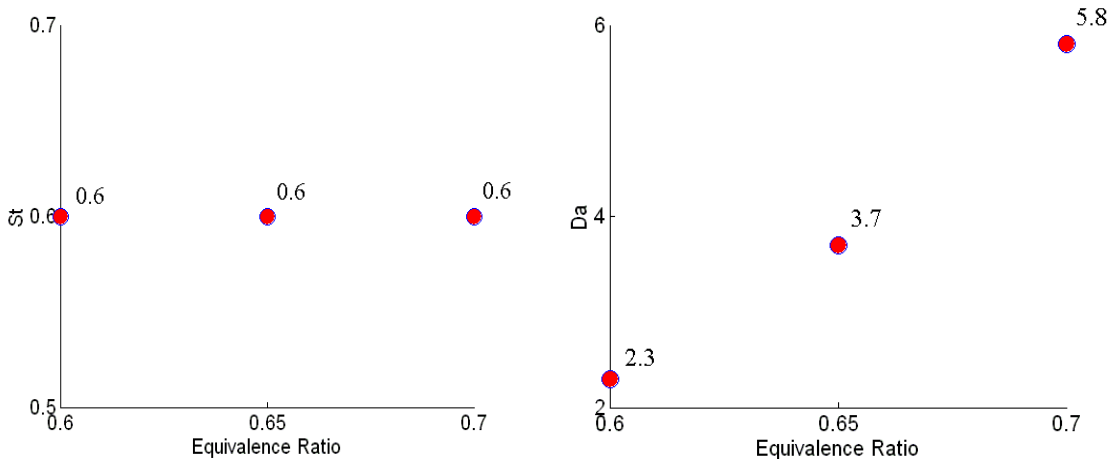

Fig. 5.11: (a) Strouhal number, (b) Damköhler number.

For the combustor experiments, the reacting flows became much more turbulent as a result of an increased Reynolds number. This caused the excited vortex structures to become more distorted and asymmetric. Moreover, the attachment of the flame to the quartz windows caused uneven heating of the windows, contributing to additional measurement difficulties and negatively affecting the image qualities. Nevertheless, an interesting trend was clearly observed.

Fig. 5.12 shows the results of an equivalence ratio of 0.7 for the combustor experiments. Spark Schlieren images are shown on the top and the processed CH*

chemiluminescence data for the corresponding phase on the bottom. Again, the light color represents local hot spots and the red represents regions of heat release intensity deficit. At this equivalence ratio, the Damköhler number is still fairly high. It appears that the hot spots again closely follow the propagation of vortex development. The overall results for this case were quite similar to those in the flame experiments.

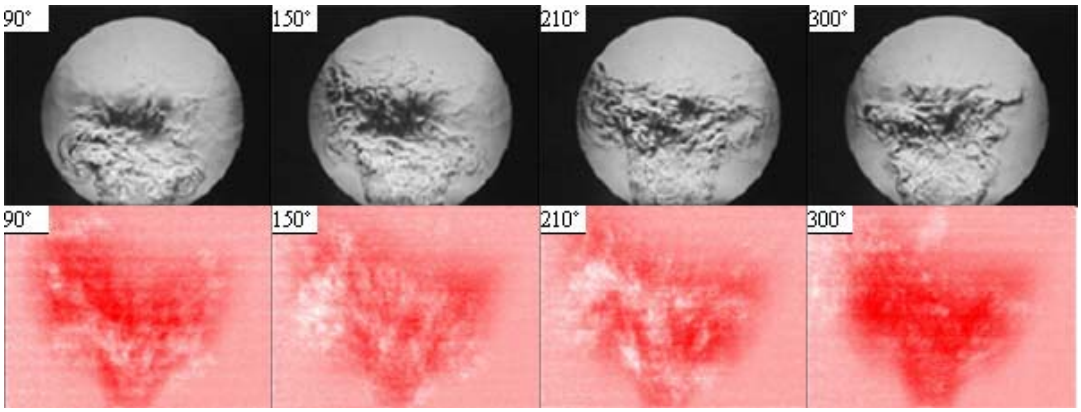

Fig. 5.12: Schlieren images and CH* chemiluminescence oscillations images at equivalence ratio of 0.7 test conditions.

However, when the combustor was running with at an equivalence ratio of 0.6, the relationship between heat release fluctuation and vortex structure development significantly changed. The spark Schlieren images and corresponding processed CH* chemiluminescence images at this low equivalence ratio condition are shown in Fig. 5.13. The vortex development can still be observed clearly in a sequence of spark Schlieren images, but the corresponding hot spot evolution, as observed at high equivalence ratio conditions, was not found in the processed CH* chemiluminescence oscillation images. At this low equivalence ratio running condition, heat release oscillation no longer followed the large coherent structures.

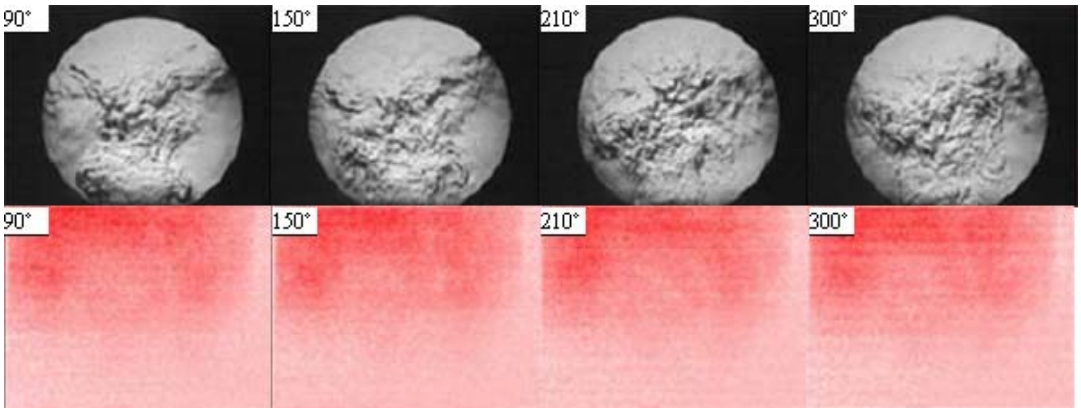

Fig. 5.13: Schlieren images and CH* chemiluminescence oscillations images at equivalence ratio of 0.6 test conditions.

Since chemistry time scale τ_{chem} increases exponentially as the equivalence ratio decreases, the ratio between fluid dynamic time τ_{flow} and chemistry time τ_{chem}, i.e., the Damköhler number was reduced to the order of unity at this low equivalence ratio condition. Thus, these two time scales became comparable at low equivalence ratio conditions.

Flame luminescence images at different equivalence ratio conditions were also recorded in this study. It was observed that at an equivalence ratio of 0.6, the flame was completely detached from the dump plane. This explained why there were no hot spots at the exit plane of the corresponding CH* chemiluminescence oscillation images; most of the combustion did not occur in the near field.

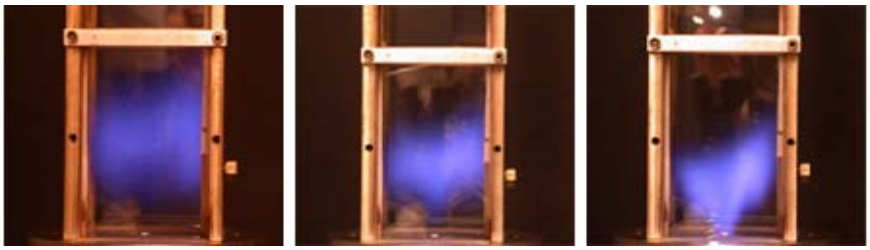

(a) (b) (c)

Fig. 5.14: Luminescence images at equivalence ratio: (a) 0.6, (b) 0.65, (c) 0.7.

5.5 Summary and Discussion

This chapter characterized heat release patterns in vortex-driven combustors. An acoustic driver was employed to acoustically force the premixed reactants in both the flame model and combustor model to simulate natural vortex-driven combustor conditions. Large-scale vortex structures were visualized with Schlieren techniques and heat release fluctuation data was obtained through CH* chemiluminescence measurements. By comparing the corresponding phases of the Schlieren and CH* chemiluminescence data, the relationship between the heat release fluctuation and the large-scale vortex structures was obtained.

The experimental results are as follows:

1) The size and strength of large-scale vortex structures and heat release fluctuations were affected by the Strouhal number. However, the relationship of oscillating heat release patterns with respect to the shed vortices was unaffected by the change in Strouhal number.

2) When the chemistry time scale is much smaller than the flow dynamic time scale, i.e., a high Damköhler number, the heat release fluctuation follows the large-scale vortex structure closely.

3) When the chemistry time scale becomes the same order as the flow dynamic time scale, i.e., a Damköhler number near unity, the fluctuation in heat release no longer follows the large vortex structure. A local heat release deficit area was observed in low Damköhler number conditions. This could be due to excessive stretching of vortex action that caused local flame reduction.

Chapter 6: Self-sustained Vortex-driven Combustion Instability Control

6.1 Introduction

This chapter discusses the experimental results performed on the dump combustor rig with the measurement methods described in chapter 3. The pressure oscillation inside the combustion chamber was characterized with a Kistler 211 B5 voltage mode dynamic pressure transducer. Flow structures were visualized using the high-speed Schlieren technique and flame configurations were directly observed with a high-speed camera [38], [112].

First, systematical experiments were conducted at low speed combustion operation conditions. Then, both open loop control and closed-loop control strategies were employed to a selected case to suppress the violent pressure fluctuations inside the dump combustor. Flow structure and flame development were visualized and compared at three conditions: open-loop control, closed-loop control, and no control.

Next, the reference speed at the dump plane was increased to Mach 0.3 to simulate real ramjet combustion chamber inlet conditions. Again, the combustion instability was found under certain circumstances; a large amplitude pressure oscillation case was picked to test the feasibility of using the liquid fuel injection control strategy. Both open loop control and closed-loop control methods were used. As a result of the harsh running environment and the limitations of the high-speed camera, only the dynamic pressure signals inside the chamber were monitored.

Based on the above experimental results, it was shown unequivocally that active suppression of vortex-driven combustion instabilities using controlled liquid-fuel

injection was not only a feasible technology for reducing the large amplitude pressure oscillations, but also that this approach could be scaled up to real industrial rigs.

6.2 Low Mach number Experimental Results

6.2.1 Dump Combustor without Control

6.2.1.1 Pressure Spectra

To reveal the possible physical mechanisms that drive the pressure oscillations in the combustion chamber, the characteristics of the dump combustor were systematically investigated by monitoring its fluctuating pressure component.

A Kistler 211B5 Piezotron miniature dynamic pressure transducer was flush mounted on the bottom plate of the dump combustor at 50 mm downstream from the dump plane to continuously measure the pressure oscillation inside the combustion chamber. The signal from this dynamic pressure transducer was then fed into a Kistler 5010B dual mode charge amplifier and provided to a TDS3014B Digital Phosphor Oscilloscope that had a bandwidth of 100 MHz and a maximum sampling rate of 1.25 GHz on each of its 4 channels. Fast Fourier Transform was carried on the fluctuating pressure signal to mathematically convert the time-domain pressure signal into its frequency components to reveal the dominant combustion instability frequency. To cover the significant range of frequencies that may occur during the combustion instability process, a sampling rate was chosen according to the Nyquist criteria. The highest frequency that any digital oscilloscope can measure without errors, which is called the Nyquist frequency, is one-half of the sample rate. The FFT waveform can display the input signal frequency components from DC to the Nyquist frequency. That is to say, to accurately represent the dynamic pressure frequency spectrum without aliasing or

distortion, a sampling rate must be chosen that is at lease twice the dominant frequency in the FFT spectrum. In this study, the sampling rate was chosen to be 5,000 samples/sec to cover a frequency range of 0 to 2,500 Hz. Since longitudinal mode combustion instabilities are usually within a low frequency range, this sampling rate was able to cover all the frequency points of interest.

A typical dynamic pressure trace when the dump combustor changed from stable combustion to unstable combustion is shown in Fig. 6.1. The amplitudes of dynamic pressure inside the chamber were relatively small with stable combustion conditions, usually less than 5 percent of the mean pressure value. In this study, since the combustor exit was directly open to the atmosphere environment, the mean pressure inside the combustion chamber was about the same as atmosphere pressure. When combustion instability occurred - the conversion of heat release to mechanical energy - very large amplitude pressure oscillations took place, as illustrated in Fig. 6.1.

Dump combustor tests showed that the amplitudes of pressure oscillation were substantially greater under certain operating conditions. As shown in Fig. 6.2, the amplitude of the pressure fluctuation was still within 5 percent of the mean pressure value when burning at the equivalence ratio of 0.525 and dump plane velocity of 10 m/s. No dominant peak frequency was shown in the corresponding FFT spectrum diagram, shown in Fig. 6.3, during this stable combustion process.

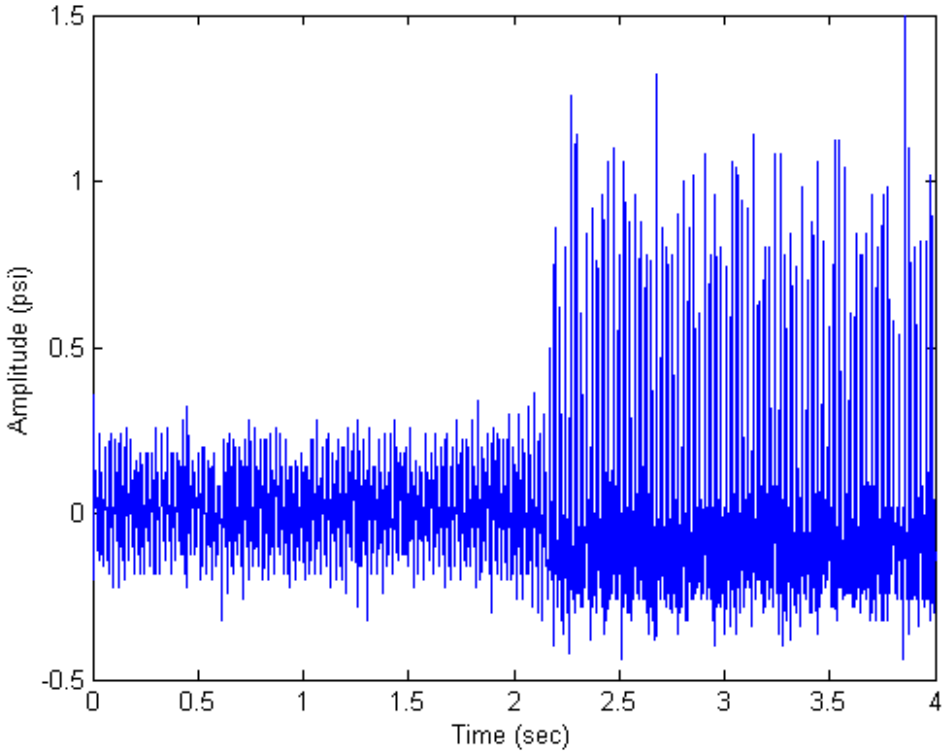

Fig. 6.1: Typical pressure oscillation when combustion instability occurs.

It is customary to describe the sound pressures and the intensities using logarithmic scales known as sound levels. One reason is that the very wide range of sound pressures and intensities encountered in the acoustic environment. Using a logarithmic scale compresses the range of numbers required to describe this wide range of intensities. Since the pressure oscillation in this study was within a small dynamic range, using the Linear Root-Mean-Square scale to display FFT waveform was more suitable for directly comparing components with similar magnitude values. When the combustor was operating at equivalence 0.6 and reference velocity 15 m/s, signals changed significantly as shown in Fig. 6.4. Large periodic pressure fluctuation up to ± 14% of the mean value occurred inside the dump combustor. A peak frequency of 38 Hz with several higher harmonics was exhibited in the FFT diagram, as shown in Fig. 6.5.

This dominant frequency coincided with the frequency of the acoustic quarter wave mode of the combustor inlet pipe. Combustion instability happened due to the unsteady heat release coupled with the natural acoustic modes of the combustor inlet, which excited the natural pressure oscillation inside the chamber.

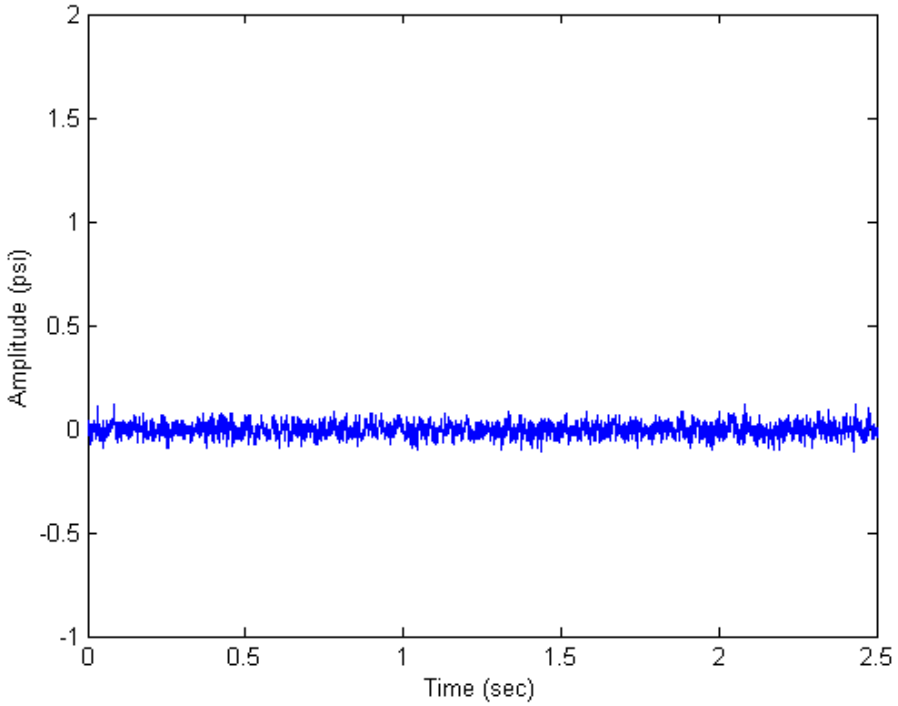

Fig. 6.2: Dynamic pressure signal in the chamber during stable combustion.

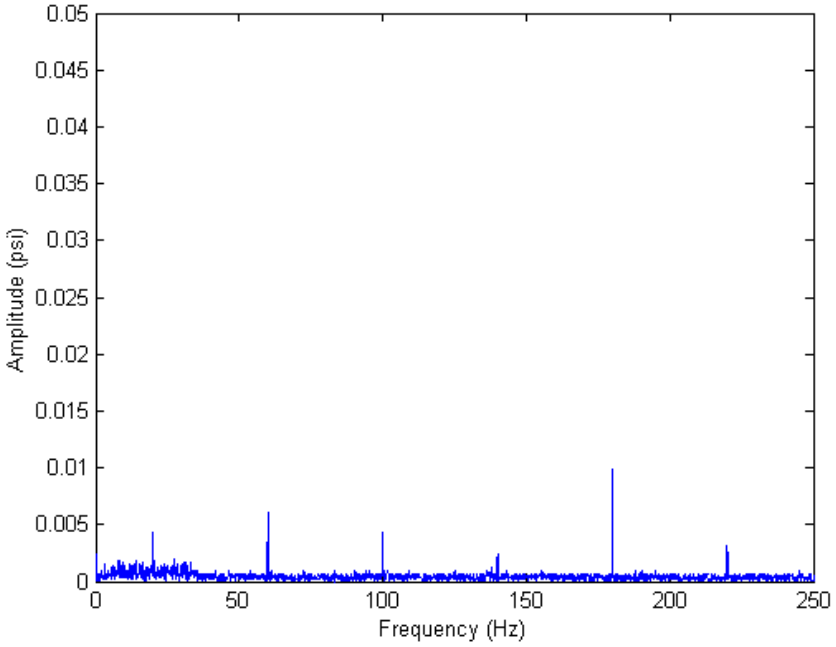

Fig. 6.3: FFT of dynamic pressure signal inside the chamber during stable combustion.

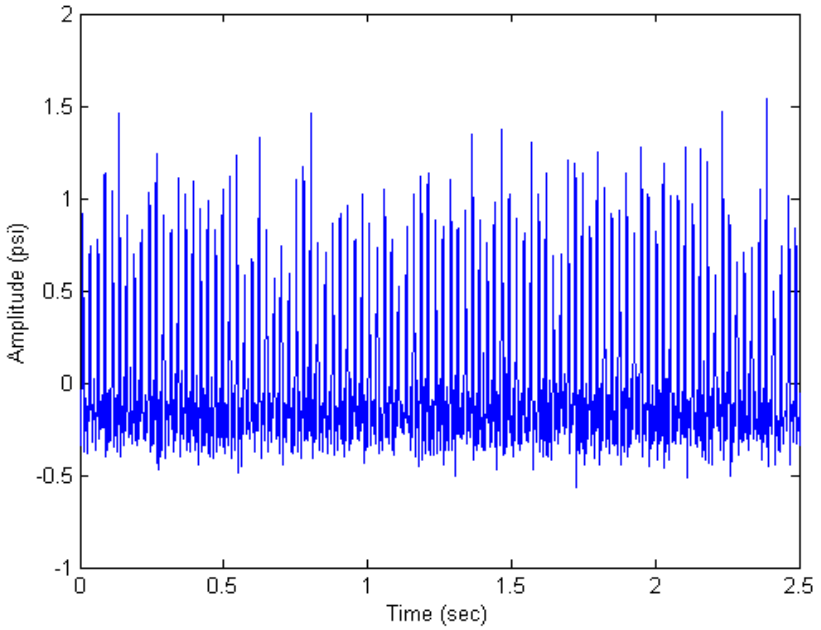

Fig. 6.4: Dynamic pressure signal inside the chamber during unstable combustion.

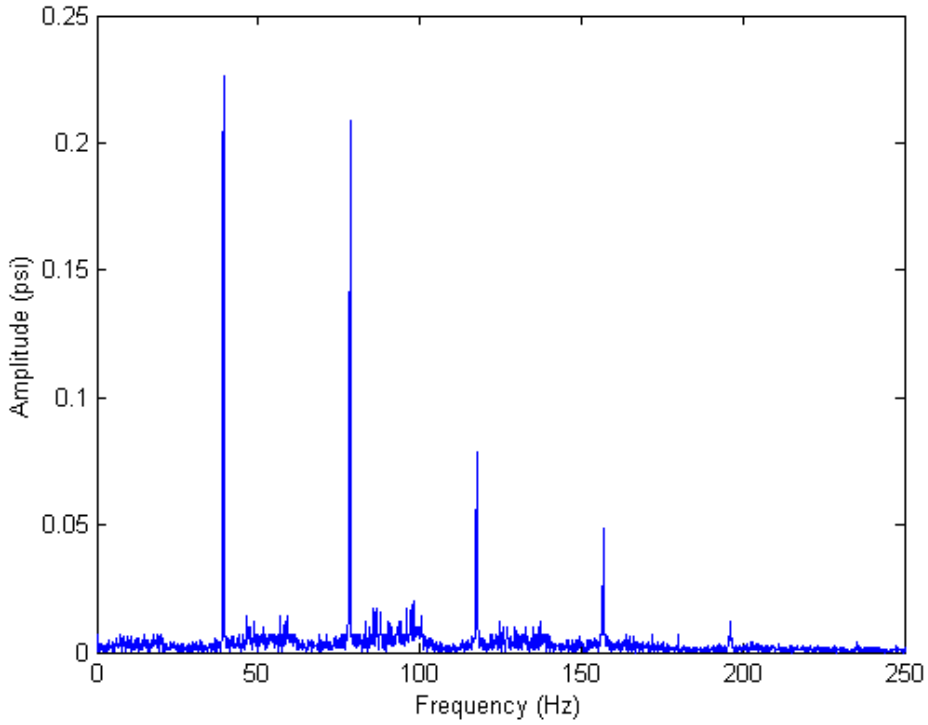

Fig. 6.5: FFT of dynamic pressure signal inside the chamber during unstable combustion.

Comprehensive experiments covering equivalence ratios from 0.5 to 0.7 and reference velocity from 10 m/s to 20 m/s, as shown in Table 6.1, were conducted systematically to characterize the dump combustor. The maximum Root-Mean-Square values of the dynamic pressure at 38 Hz are presented in this table. Detailed pressure trace and spectra at covered experimental conditions are illustrated in Appendix D.

A contour map for the characterization of this low speed dump combustor was generated, as shown in Fig. 6.6. The most violent pressure oscillation inside the combustor occurred when the equivalence ratio was 0.6 and reference velocity was 15 m/s. The total thermal output power was 44 kW. The operating condition that resulted in large-amplitude, self-excited oscillations was chosen as a baseline case. Later on, all

detailed characterizations and control experiments were performed with the same averaged equivalence ratio and reference velocity.

Table 6.1 Maximum RMS value of the dynamic pressure at 38 Hz of different experimental conditions:

Φ	U_{ref} = 10 m/s	U_{ref} = 15 m/s	U_{ref} = 20 m/s
0.500	0.001	0.001	N/A
0.525	0.001	0.075	0.024
0.550	0.027	0.159	0.068
0.575	0.045	0.198	0.067
0.600	0.074	0.226	0.060
0.650	0.023	0.116	0.039
0.700	0.001	0.082	N/A

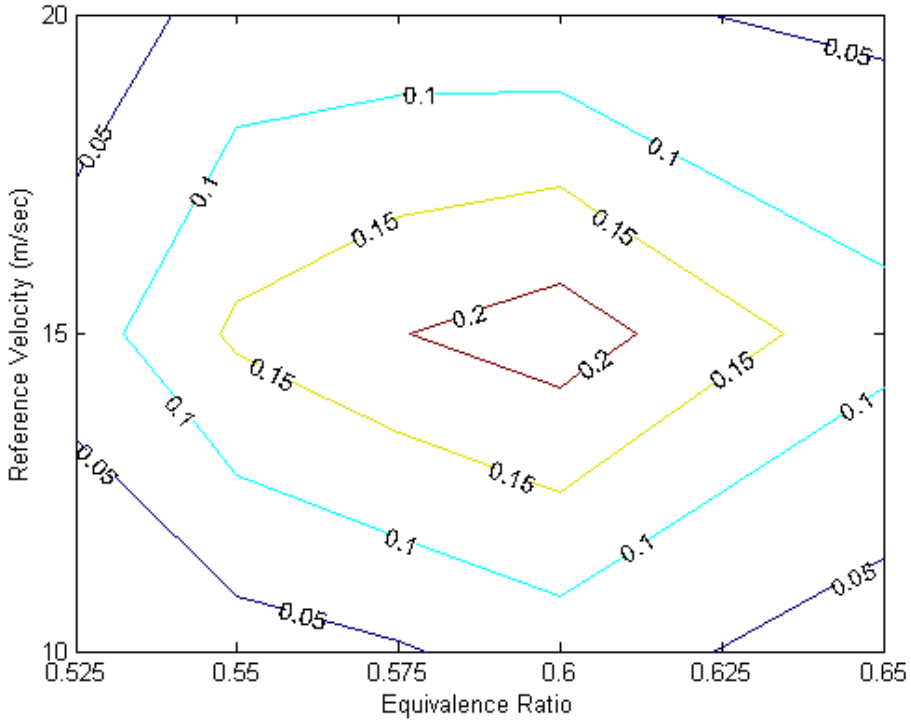

Fig. 6.6: Contour map of the dynamic RMS pressure at 38 Hz of different experimental conditions.

6.2.1.2 Schlieren Images

The flow field was characterized with the high-speed spark Schlieren imaging technique to identify important physical processes that might account for the driving and sustaining of the excited large amplitude pressure oscillations inside the dump combustor.

The optical arrangement is shown in Fig. 3.3. Two converging lens, with a diameter of 76 mm light path area were put on each side of the dump combustor to observe the flow field that was illuminated by a point light source. The total observable area for the combustion chamber was 102 x 305 mm. To cover all significant combustion process details, this set of lenses was placed at four different positions, moving from the location near the dump plane to points downstream. Because this combustion instability was a periodical phenomenon, these four sets of high-speed spark Schlieren images could be combined later with the aid of the pressure signals.

A high-speed camera ran at 1000 frames per second to continuously capture the flow field images. A sequence of high-speed Schlieren images were taken from the unstable combustion case at eight different phases and is shown as in Fig. 6.7. The complete set of 26 spark Schlieren images at different phases of the cycle are shown in the Appendix E. In this case, the reference velocity at the dump plane was 15 m/s and the equivalence ratio was 0.6. The fundamental mode of the oscillating pressure is 38 Hz, so twenty-six complete cycles were obtained at every location. With the pressure trace as a reference, these spark Schlieren images at four different locations were connected. From these images, it was evident that large-scale vortex structures were periodically shed from the dump plane and marked downstream.

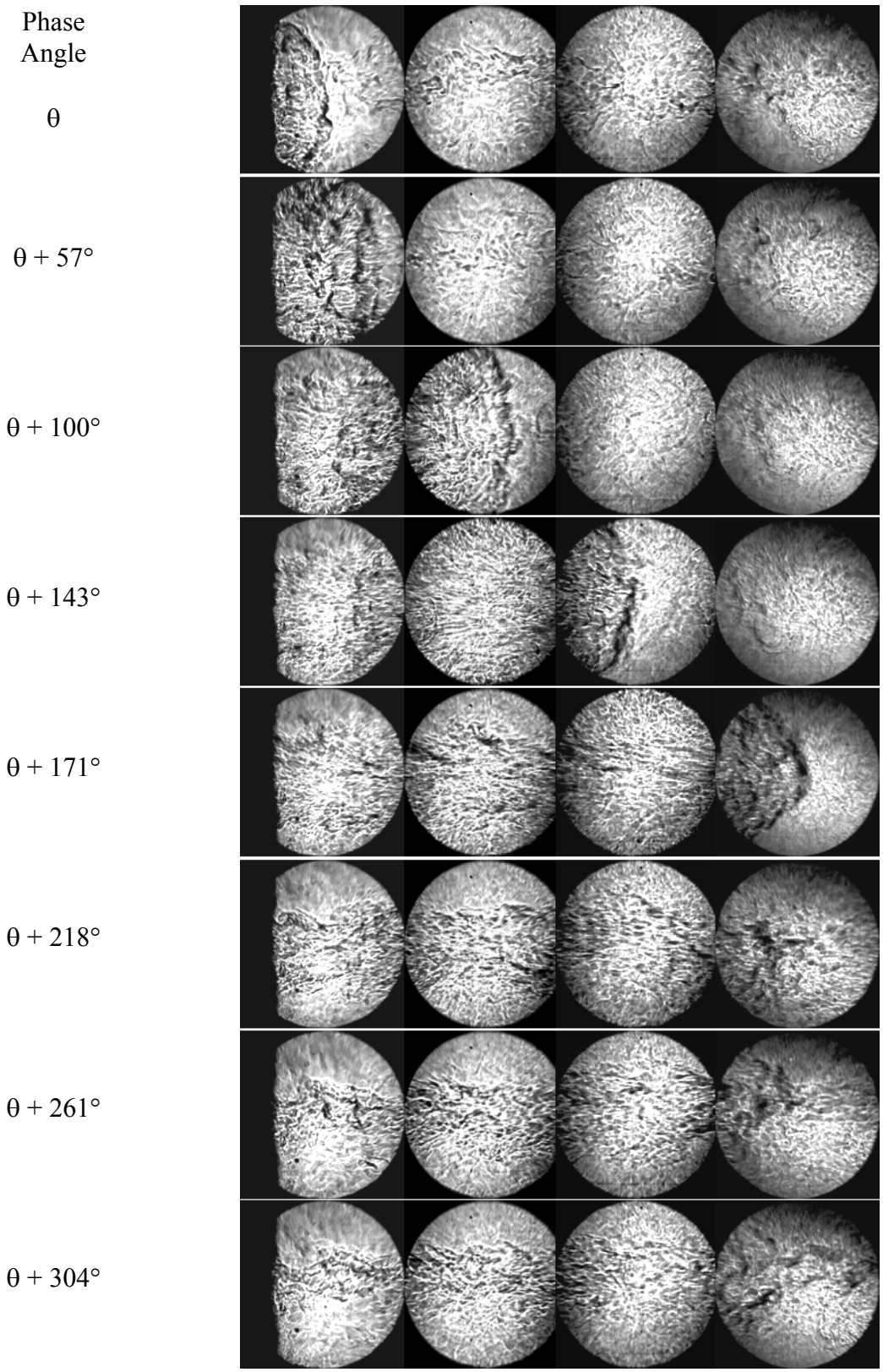

Fig. 6.7: A sequence of Schlieren images taken for the uncontrolled case.

6.2.1.3 Flame Images

Since it was known that the vortex movements might cause periodic entrainment of unburnt reactants and subsequently periodic combustions and extinctions, the luminous portion of the flame was captured by a high-speed camera through the quartz window at a speed of 1000 frames per second. Fig. 6.8 shows flame structures at twelve different phases of an unstable combustion cycle, with flow direction moving from left to right. It is clearly illustrated that the flame was periodically detached from the dump plane and the recirculation zone, and that most of the combustion occurred downstream of the recirculation zone. Similar results regarding large-scale vortex structures and unsteady flame were also revealed by other researchers in the past [50], [102], [106], [113-117].

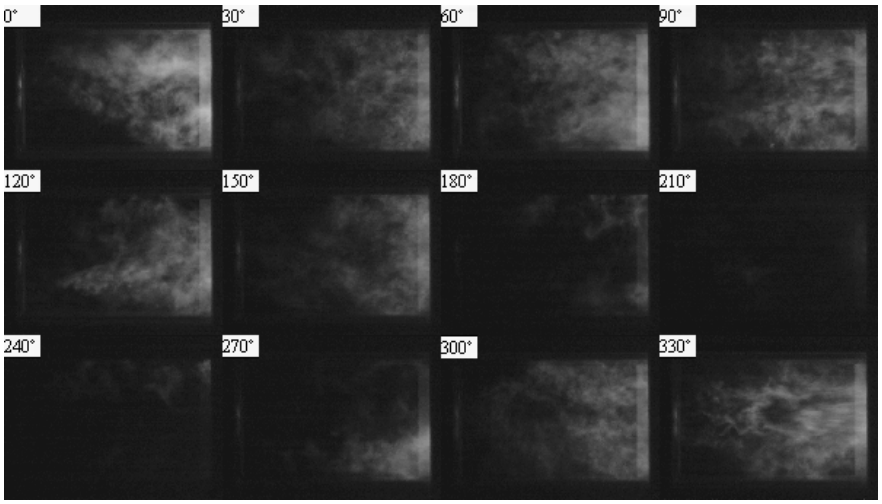

Fig. 6.8: Flame structure of no combustion control case.

6.2.2 Dump Combustor with Open-loop Control

6.2.2.1 Pressure Spectra

Open loop control strategies were applied to the previous baseline case to examine its effectiveness in suppressing the large pressure fluctuation inside the combustion chamber. Differing from the uncontrolled case, for which all the energy was provided by the main fuel ethylene, the open loop control method diverted part of the power supply by burning controlled liquid fuel ethanol. Automotive fuel injectors were pulsed at the fundamental mode of the instability: 38 Hz and 50% duty cycle. The driving pressure for the ethanol was set at 20 psi. Steady injection of ethylene constituted 82% of the total thermal output, and the remaining 18% was provided by controlled fuel ethanol.

Two kinds of open loop methods were investigated. One was a fixed frequency 38 Hz injection and the other was a variable frequency injection. The variable frequency injection utilized exactly the same signal to pulse the fuel injectors as in the later closed-loop control method. In other words, the fuel injector control signal that was used in the close-loop control system was recorded and played back in a open-loop fashion. The only difference between the variable frequency open-loop control and close-loop control was the existence of the feedback signal.

For the open loop control method, the resulting pressure signals and the power spectra were the same for both fixed frequency and variable frequency control, as shown in Fig. 6.9 and Fig. 6.10. While the fundamental frequency of combustion instability remained unchanged in both open loop control cases, the pressure trace showed a certain reduction in amplitude compared to the uncontrolled case. Fig. 6.11 shows the pressure

fluctuation trace in comparison to the baseline case. Fig. 6.12 is the corresponding FFT spectra diagram.

Although a direct injection of controlling liquid fuel into the combustor without feedback signals reduced the amplitude of pressure fluctuations by almost 50%, open-loop control approaches were still not effective enough to suppress the instability. The fundamental frequency that coincided with the quarter wave acoustic mode of the inlet pipe still existed in the FFT diagrams.

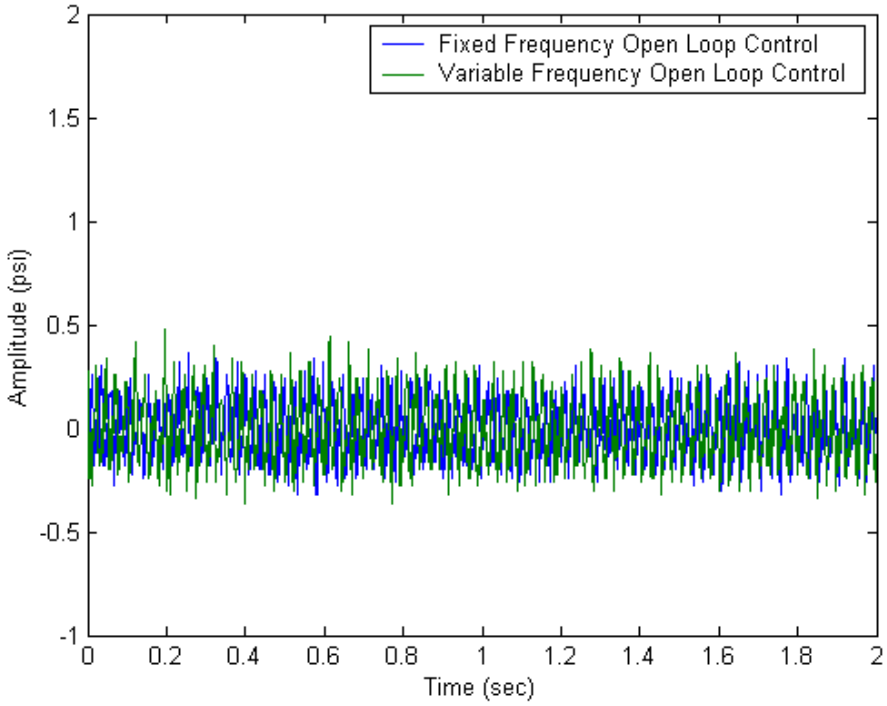

Fig. 6.9: Dynamic pressure signal inside the chamber for open-loop control methods.

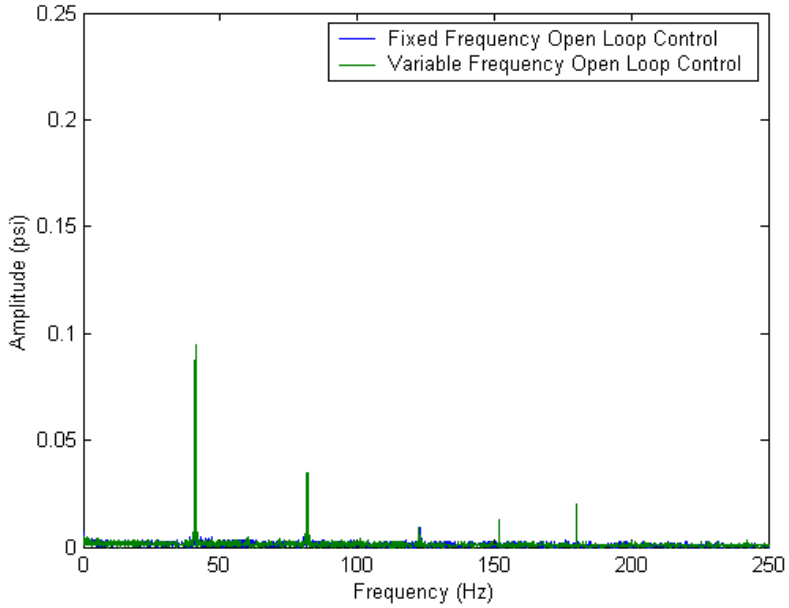

Fig. 6.10: FFT of dynamic pressure signal inside the chamber for open-loop control methods.

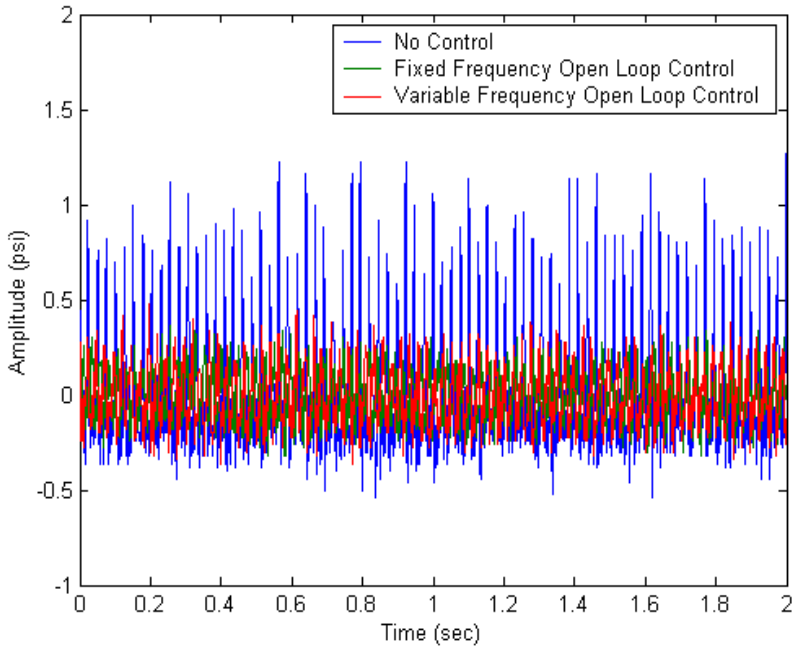

Fig. 6.11: Dynamic pressure signal inside the chamber for different conditions.

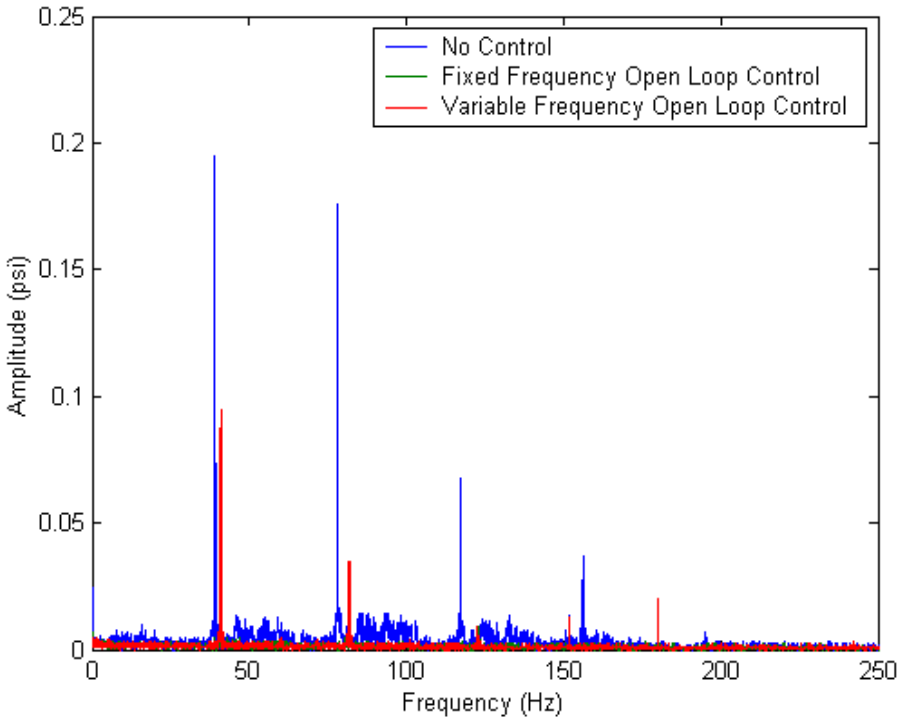

Fig. 6.12: FFT of dynamic pressure signal inside the chamber for different conditions.

6.2.2.2 Schlieren Images

High-speed spark Schlieren imaging was also applied to the open loop control experiments. The same high-speed camera operating at 1000 frames per second was used to capture the observable area. The difference in Schlieren images between the two open loop control strategies, both for fixed-frequency injection and variable frequency injection, was almost indistinguishable. A complete cycle of spark Schlieren images at 26 different phases was illustrated in the Appendix E. Fig. 6.13 shows a sequence of High-speed Schlieren images at eight different phases, taken for the fixed frequency open loop control case. Large vortex structures still periodically shed from the dump plane and moved downstream. Compared to the uncontrolled case, these vortices were less organized.

The convection velocity of the vortex front was tracked based on the obtained Schlieren images, and the results are shown in Fig. 6.14. For both the uncontrolled case and open loop controlled case, the vortex velocity increased slightly as it convected downstream from the dump plane. The average propagation velocity for the uncontrolled case was estimated to be about 13.2 m/s, while for the open-loop control case it was about 11.7 m/s. Both speeds were close to the average inlet flow velocity of 10 m/s. The slightly higher propagation velocity in the uncontrolled case could be a result of the higher amplitude pressure oscillation in rougher combustion conditions.

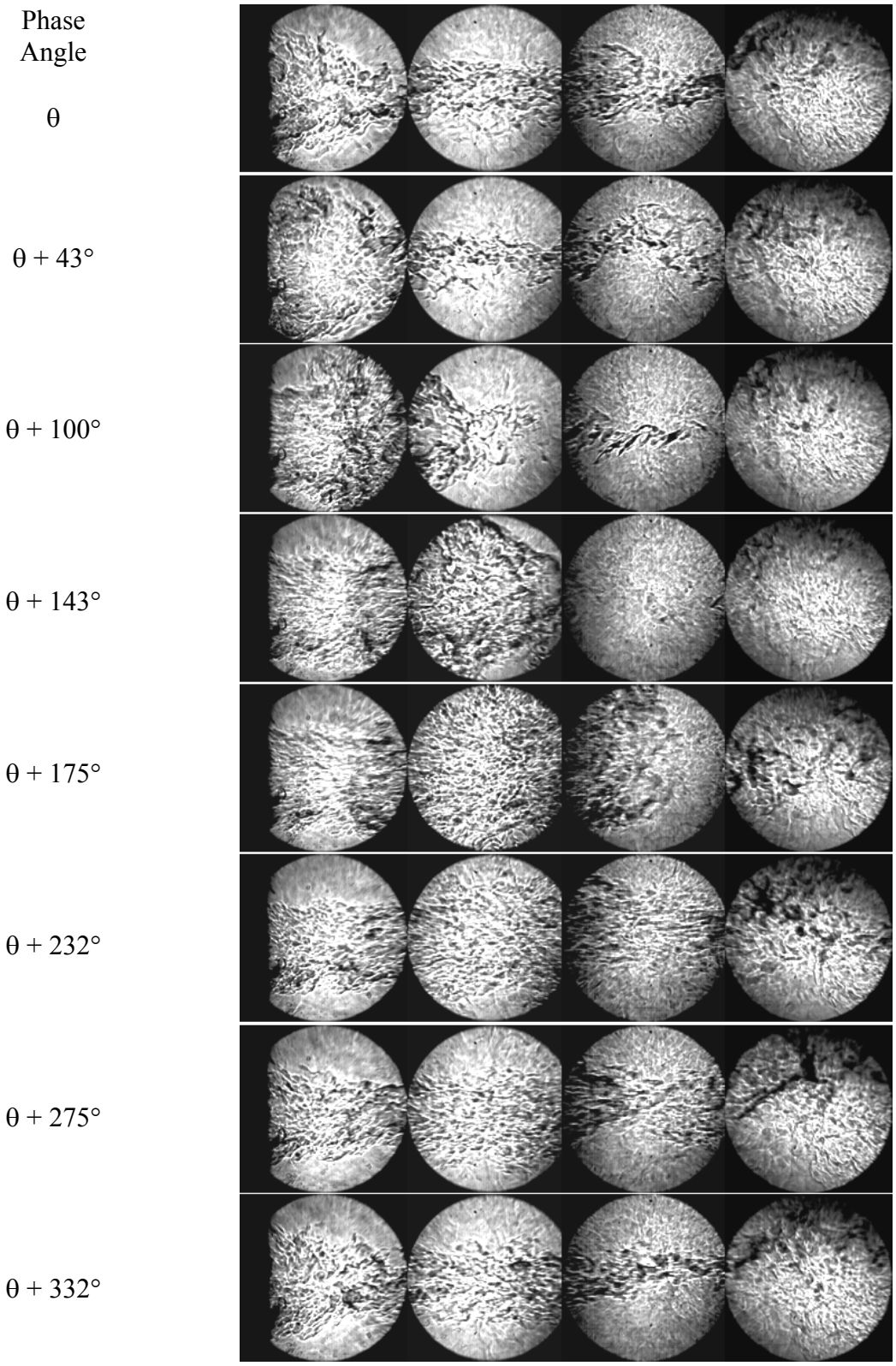

Fig. 6.13: A sequence Schlieren images taken for theopen-loop control case.

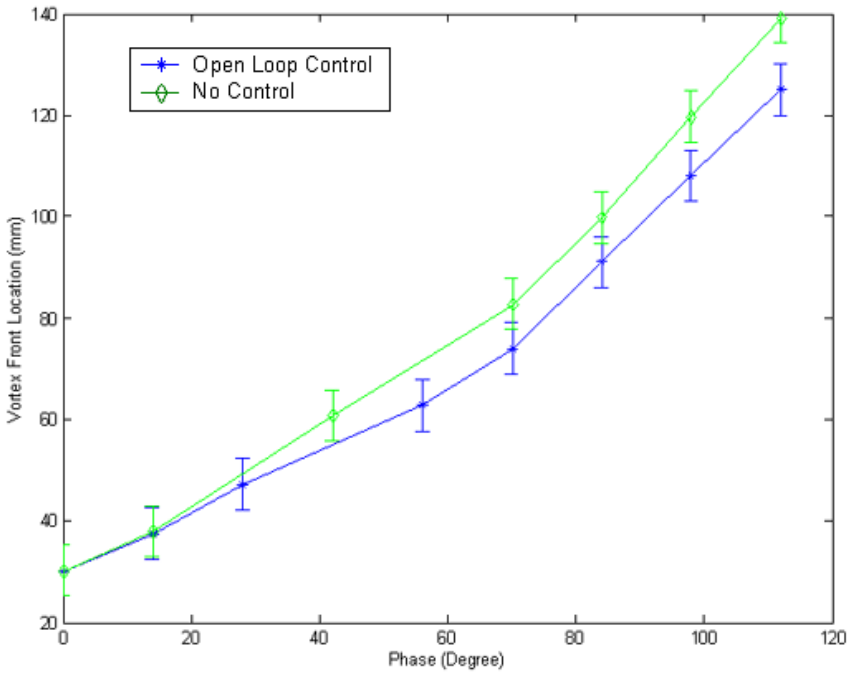

Fig. 6.14: Vortex convection velocity at different test conditions.

6.2.2.3 Flame Images

A high-speed camera was employed to visualize the flame shape under open-loop control conditions. Both fixed frequency open loop control and variable frequency open loop control showed similar behavior. Significant flame characteristic changes were observed in both cases due to the redistribution of thermal power providers. With the controlling liquid fuel ethanol, the flame became attached to the dump plane and stopped moving back and forth, as shown in Fig. 6.15 and Fig. 6.16. However, the periodically changing shape of the flame core area still indicates the existence of large-scale vortex structures in both open-loop control cases.

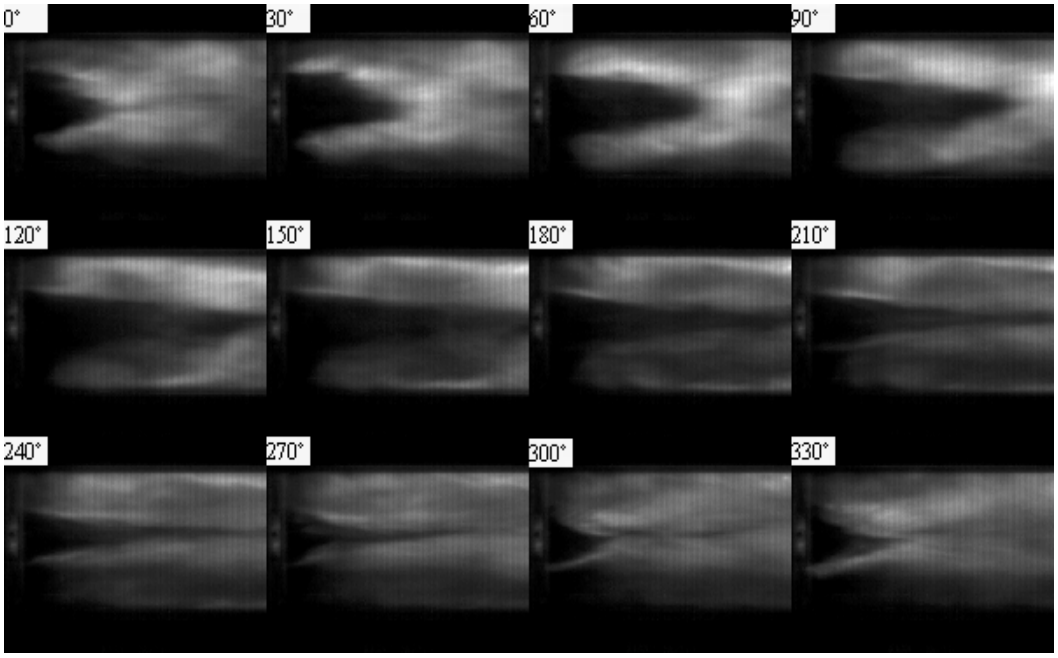

Fig. 6.15: Flame structure of open loop control case.

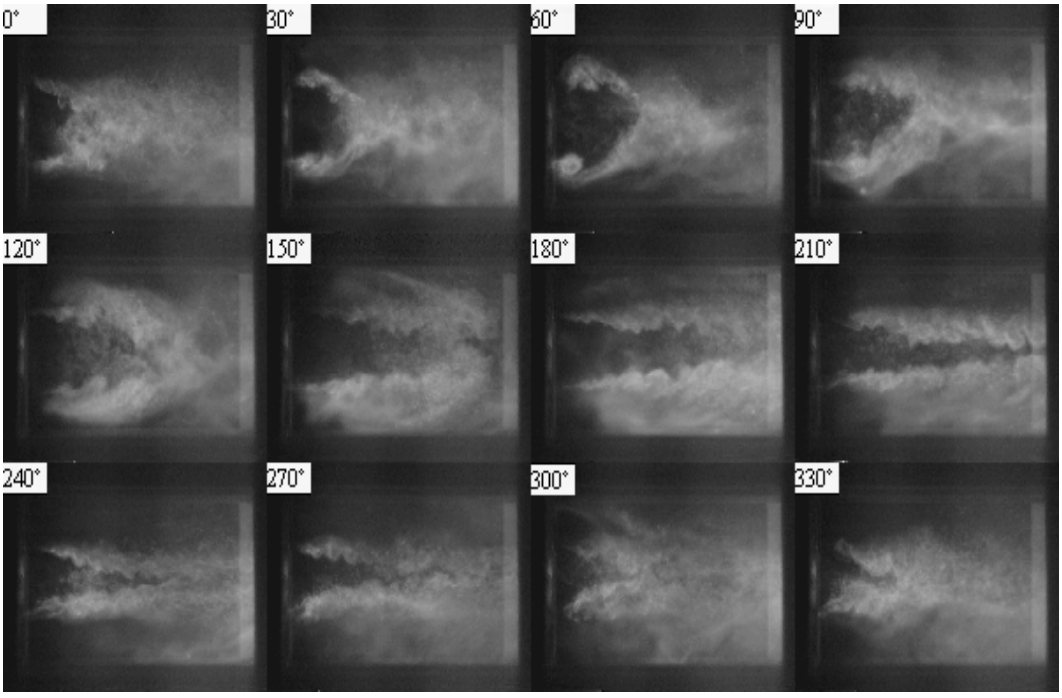

Fig. 6.16: Flame structure of open loop control case.

6.2.3 Dump Combustor with Closed-loop Control

6.2.3.1 Pressure Spectra

To further suppress the large amplitude self-sustained pressure oscillation inside the dump combustor, a MIT Posicast controller [118-120] was applied to the uncontrolled case in a closed-loop manner. As with the open-loop control cases, the controller liquid fuel ethanol was pressurized at 20 psi. Main fuel ethylene provided 82% of the total thermal output while controlling liquid fuel ethanol provided the rest. The injection timing of the controller fuel was determined by the feedback signal. For this study, the dynamic pressure signal measured inside the combustion chamber was fed into the controller to command the on/off and duration timing of the fuel injectors. Although the control signal added to the fuel injectors was no longer at a fixed frequency since it was adjusted according to the combustor pressure signal, the average operating condition was still identical to the uncontrolled and open-loop controlled experimental conditions.

The pressure traces of the uncontrolled case, two open-loop controlled cases, and closed-loop controlled case were compared as shown in Fig. 6.17. The corresponding pressure spectra diagram is shown in Fig. 6.18. These four cases were conducted under the same operating conditions in a time-averaged sense. The only difference was in the way the controlling fuel was managed.

It was found that the timing of the controller fuel was very important. Although the variable frequency open loop control and closed-loop control used the same signals to activate the actuator system, the results were quite different. With closed-loop control, the pressure fluctuation was completely suppressed to the noise level and there was no significant peak in frequency, according to the FFT diagram as in Fig. 6.18.

By comparing these four different set of experiments, it became clear that in order to attain maximum attenuation benefit, the controlling fuel injection should retain the correct phasing so that the heat release fluctuation is always out-of-phase with the local pressure oscillations.

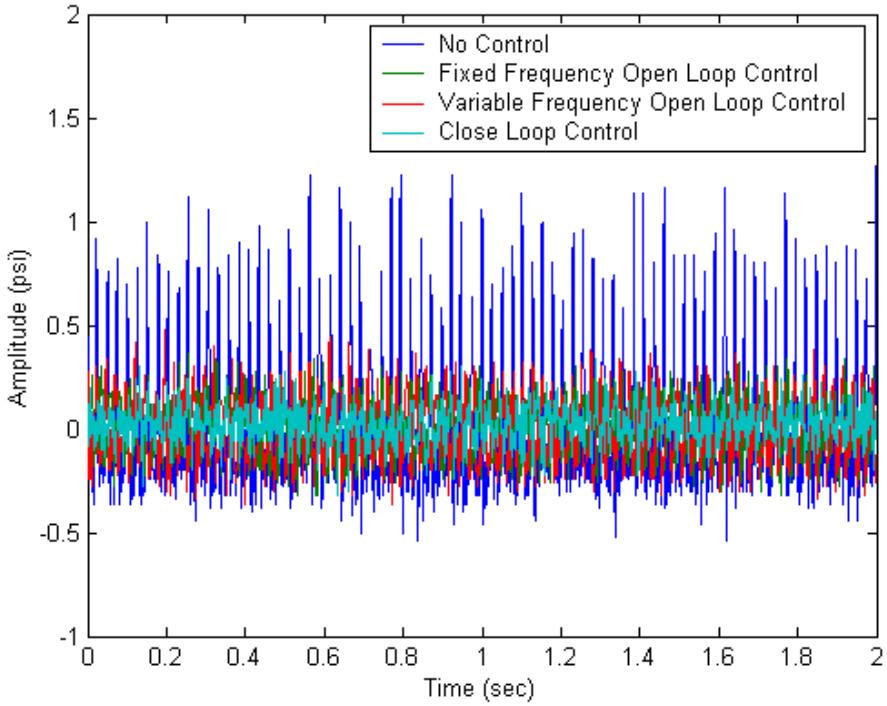

Fig. 6.17: Dynamic pressure signal inside the chamber for different test conditions.

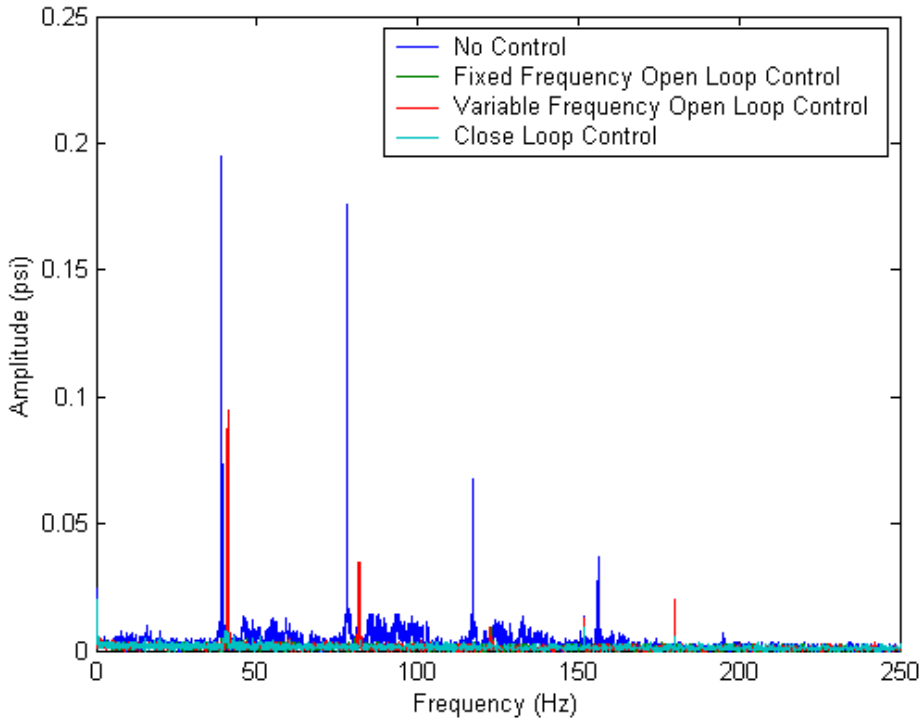

Fig. 6.18: FFT of dynamic pressure signal inside the chamber for different test conditions.

6.2.3.2 Schlieren Images

Unlike the uncontrolled case and open-loop control case, high-speed Schlieren images of the close-loop controlled case showed no sign of periodical vortex shedding from the dump plane. Fig. 6.19 is a sequence of eight different phase Schlieren images under closed-loop control conditions. This result confirmed that the periodic vortex shedding played an important role in vortex-driven combustion instabilities. It provided a vital link between the natural pressure oscillation and unsteady heat release inside the combustion chamber. Effective combustion instability control in vortex-driven combustors requires the complete suppression of these large-scale vortex structures.

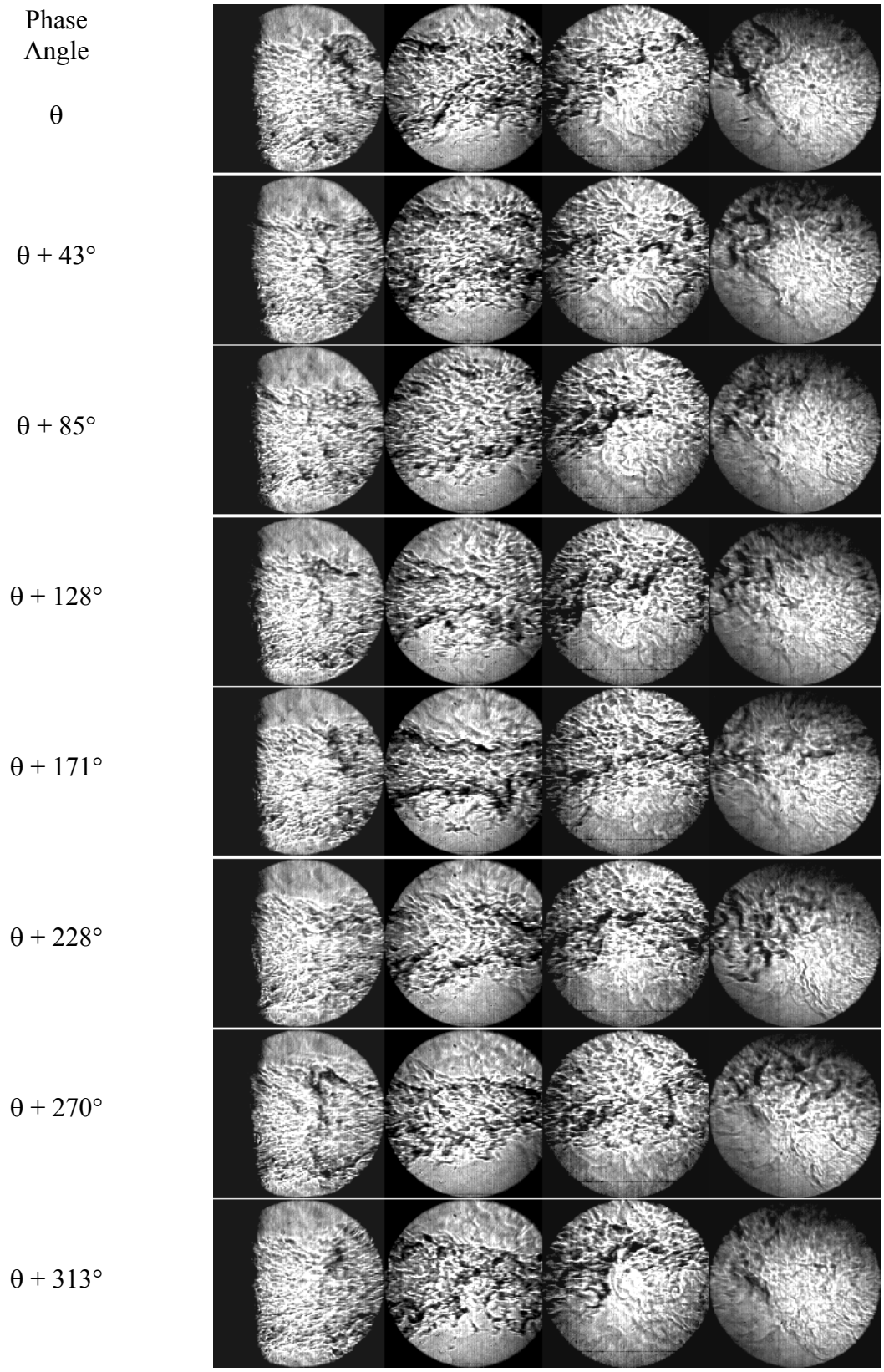

Fig. 6.19: A sequence of Schlieren images for the close-loop control case.

6.2.3.3 Flame Images

Flame configurations under closed-loop control conditions also were observed with the high-speed camera. There were no significant differences among flame shapes at different phases, as shown in Fig. 6.20. In this case, the flame core area remained at the same shape and size because the periodic vortex shedding was completely suppressed.

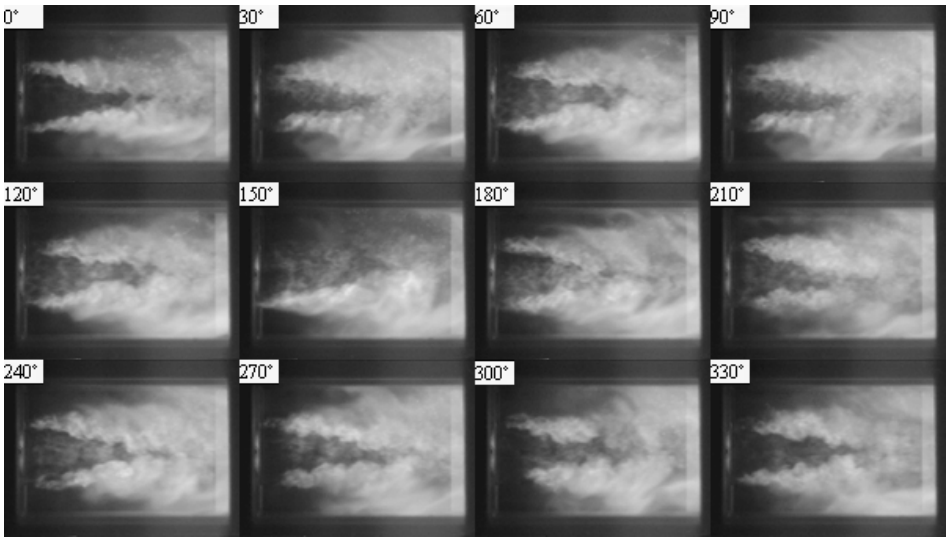

Fig. 6.20: A sequence of flame images for the close-loop control case.

6.3 High Mach number Experimental Results

To simulate an actual ramjet combustor with high velocity at the reference dump plane, both the air flow rate and fuel flow rate were increased significantly to achieve the required operating conditions with the same dump combustor rig. The power output of this model ramjet combustor under high-speed conditions was raised to 364 kW and the velocity at the dump plane was increased to 96 m/s. Combustion instability still took place when the air and ethylene mixed at equivalence ratio around 0.8. As shown in Fig. 6.21, up to $\pm$ 5psi pressure oscillations were exhibited during this unstable combustion process. The dominant frequency of the dynamic pressure signal was about 250 Hz, which coincided with the quarter wave acoustic mode of the dump combustor.

When using the Ultima 1024 high-speed camera from Photron^{TM} USA Inc, in order to increase the frame capture rate, the viewing area has to be sacrificed. To capture the whole square combustor viewing area, the maximum frame rate has to be kept at or below 1000 frames per second. With a dominant frequency of 250 Hz, at most four complete cycles can be captured. Using four instantaneous images is not enough to acquire significant statistical meaning, especially for this kind of high turbulent combustion exercise. Therefore, no visualizations were carried out for this higher speed/higher power case. Only the dynamic pressure signal inside the dump combustor was monitored to check the effectiveness of the same actuator system. In the mean time, to keep the same controlling fuel flux amount relative to the total fuel flux, two more automotive fuel injector and atomizer combinations were added to the actuator system. The pressure forced on the liquid fuel ethanol was also increased from 20 psi to 60 psi. The pulse frequency of the fuel injector was changed to the dominant frequency as shown in the FFT diagram of the uncontrolled case as Fig. 6.22.

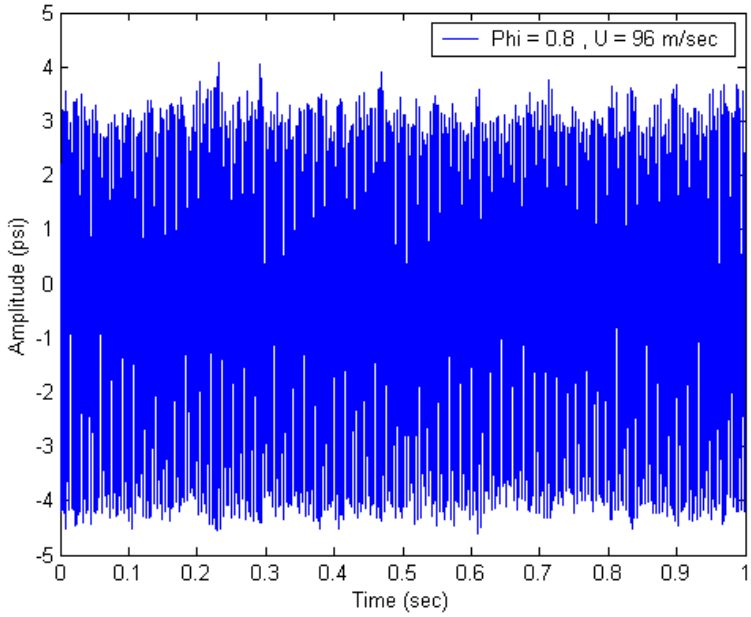

Fig. 6.21: Dynamic pressure signal inside the chamber with no control condition.

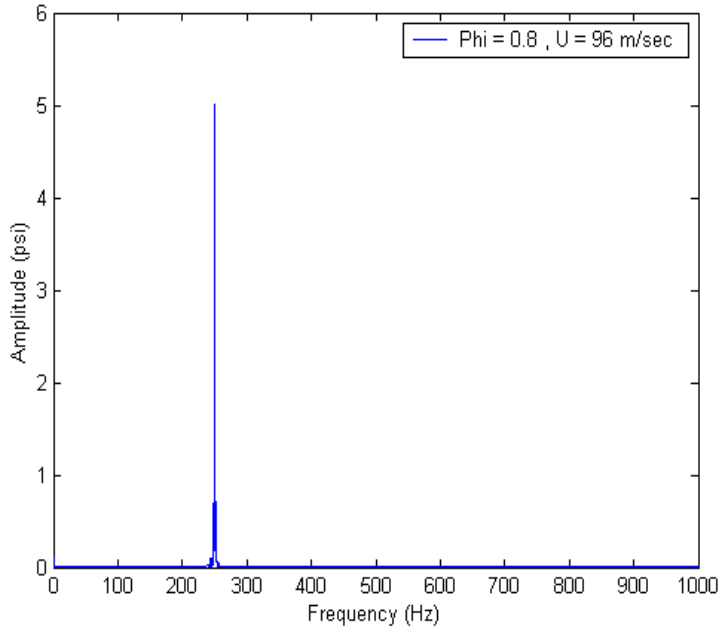

Fig. 6.22: FFT of dynamic pressure signal inside the chamber with no control condition.

Both open loop control and closed-loop control strategies were applied to suppress the large amplitude pressure oscillations inside the chamber. The flow conditions were kept identical in a time-averaged sense; when liquid fuel ethanol was added for controlling purposes, the flow rate of the main fuel ethylene was reduced correspondingly to maintain the same average total equivalence ratio inside the dump combustor. Fig. 6.23 shows the pressure trace with open-loop control strategy using four fuel injectors forced at 250 Hz. Although no peak was shown in the FFT diagram, as shown in Fig. 6.24, the dump combustor still displayed large pressure fluctuations up to ± 7% of its mean value, as shown in Fig. 6.23. Compared with the open-loop control case, the closed-loop control method completely suppressed the pressure oscillation inside the dump combustor to the noise level as shown in Fig. 6.25. No peak frequency was observed in the corresponding FFT diagram, as shown in Fig. 6.26.

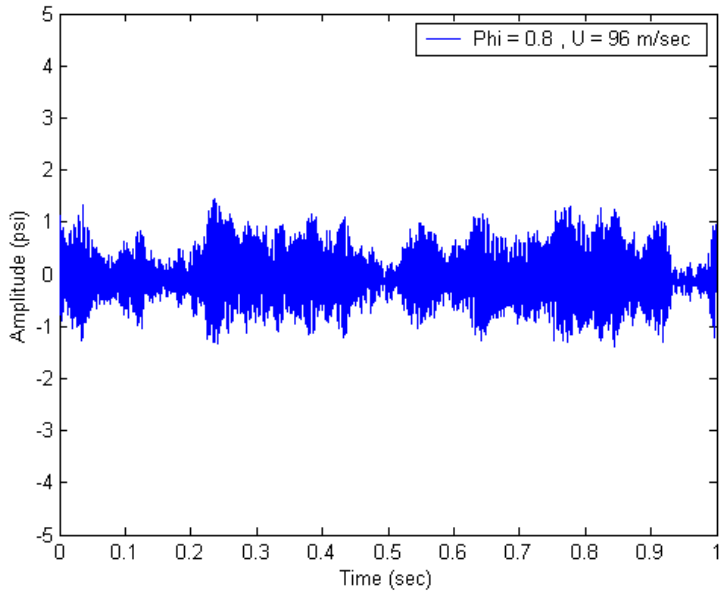

Fig. 6.23: Dynamic pressure signal inside the chamber with open-loop control condition.

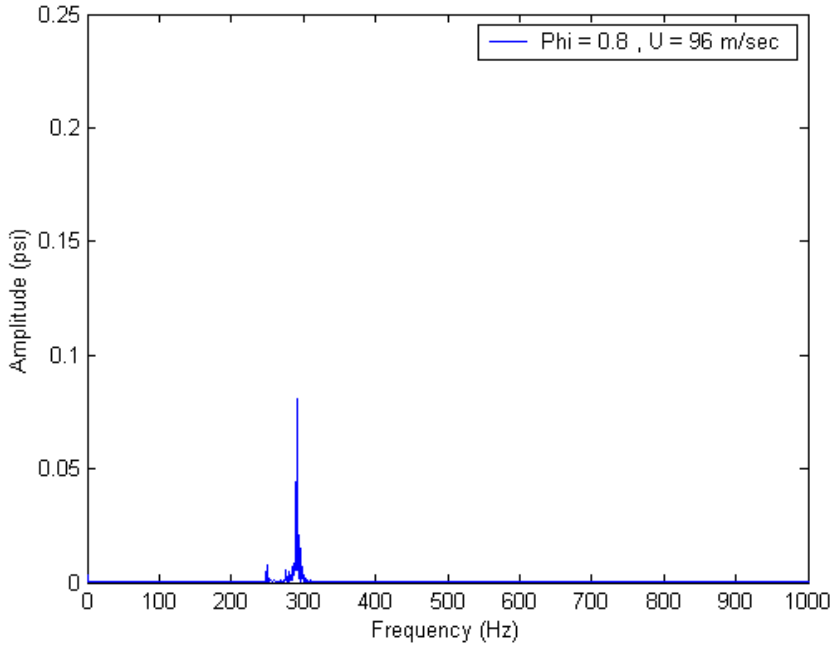

Fig. 6.24: FFT of dynamic pressure signal inside the chamber with open-loop control condition.

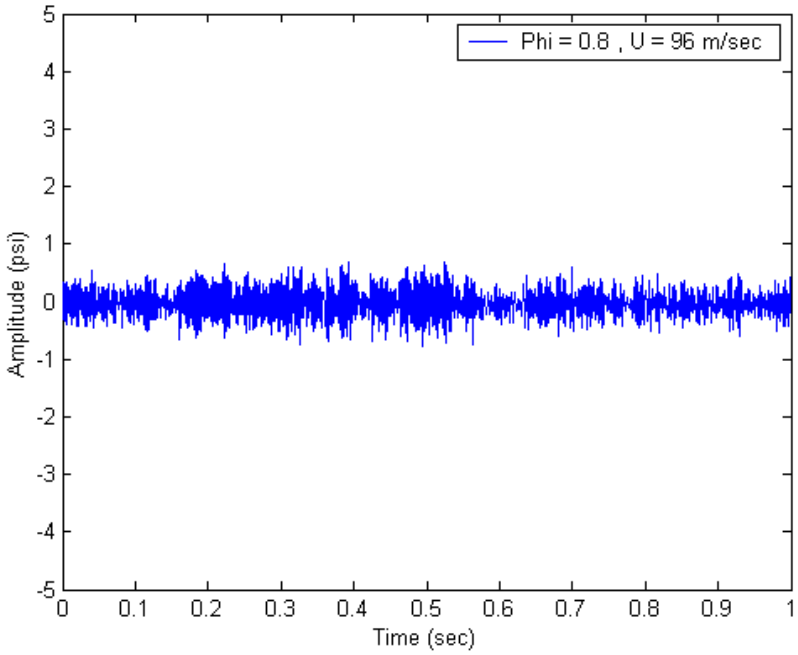

Fig. 6.25: Dynamic pressure signal inside the chamber with close-loop control condition.

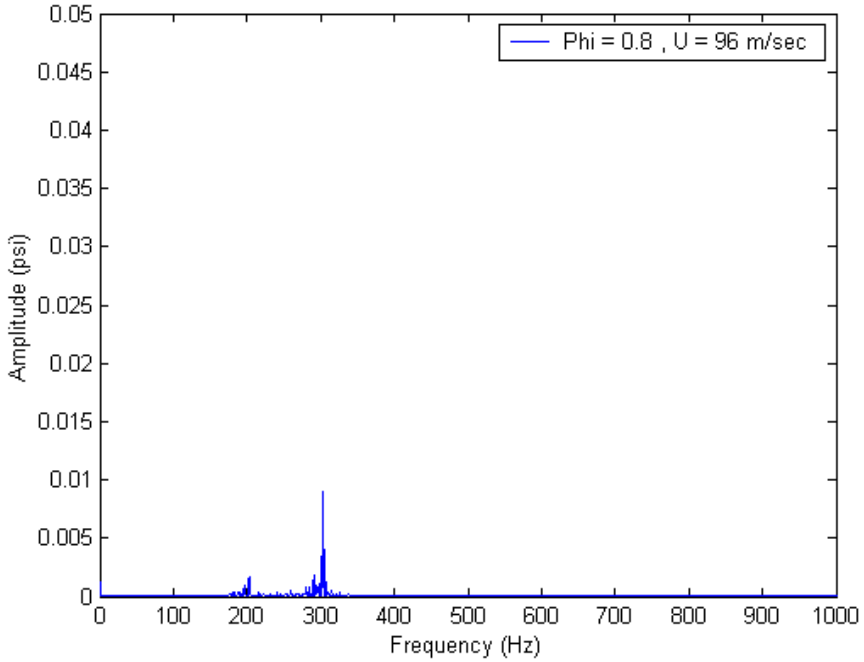

Fig. 6.26: FFT of dynamic pressure signal inside the chamber with close-loop control condition.

Another way to test the effectiveness of controlling combustion instability using a liquid fuel injection strategy was to determine the onset conditions of large amplitude pressure oscillation with different control methods. To do this, the reference velocity at the dump plane was held constant at Mach number 0.3, and the equivalence ratio was kept changing by adjusting the total pressure of the main fuel ethylene. As shown in Fig. 6.27, without any control arrangement, large pressure oscillation occurred around the equivalence ratio of 0.77. With open-loop forcing at 250 Hz, the pressure fluctuation was postponed until the equivalence ratio of 0.8. However, with the closed-loop control strategy, no large amplitude pressure oscillations occurred within the test region. It was evident that the operating range of the model dump combustor could be extended with the liquid fuel injection control strategy.

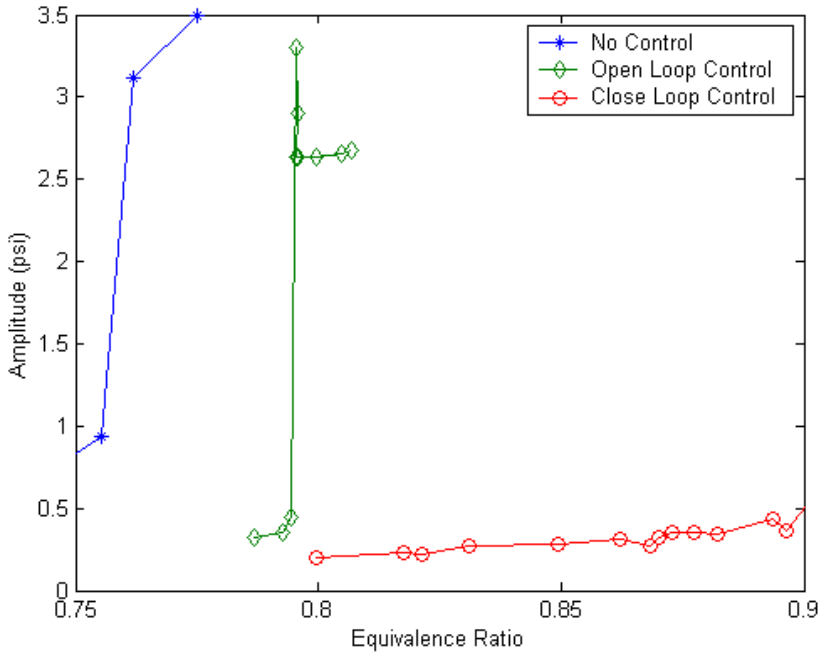

Fig. 6.27: Onset of the combustion instability with different control strategies.

6.4 Summary and Discussion

Active suppression of combustion instabilities using controlled liquid fuel injection strategies were conducted at both low speed and high-speed operation conditions in a laboratory scale dump combustor.

For the low speed experimental conditions with closed-loop controlled pulsed fuel injection, the amplitude of dominant frequency instability was reduced by 13 dB as compared to the open-loop control case, and by 26 dB as compared to the uncontrolled case. High-speed visualization revealed that the large-scale vortex structures played an important role in sustaining large amplitude pressure oscillations in this dump combustor. In a reacting flow, these large-scale vortex structures might entrain fresh reactants and cause periodic heat release oscillation. If properly phased, these heat release fluctuations could couple with the natural pressure oscillations and transfer energy from heat to the

existing acoustic mode of the chamber, thereby causing combustion instabilities. When instability was suppressed, large-scale periodic vortices were no longer observed in the combustion chamber.

Experiments under high-speed conditions proved that using a liquid fuel injection control strategy to suppress combustion instability could be extended to more practical conditions. The operating range can also be widened with this practical control method.

Chapter 7: Conclusions and Future Work

7.1 Conclusions

Combustion instabilities due to resonant coupling of flames and acoustic waves remain as one of the most challenging problems in the development of modern propulsion and power systems. Large amplitude pressure oscillations, excited by unstable combustion processes, can cause serious problems such as structural damage, increased thermal loading, performance degradation or inlet unstart in ramjet.

Suppression of combustion instability may rely on passive or active methods. Passive combustion control methods achieve their goals in one of two ways: by increasing the energy losses from the oscillations, or by modifying the combustor design to avoid the most destructive instability modes, but these methods often are costly and time consuming. Moreover, passive methods are only applicable in very narrow frequency ranges.

As a more efficient technology to solve combustion instability problems, active combustion control strategy has gained significant interest since the 1980s. Numerous efforts have been put into this field in order to understand the physical mechanisms and deal with related technical issues of implementing active instability control techniques in combustion systems.

Most of previous active control studies utilized gaseous fuel to suppress combustion instabilities. However, using liquid fuel to suppress combustion instabilities is more realistic for propulsion applications. For example, it is not practical and safe for an aircraft to carry gaseous fuel on board. More studies need to be conducted focusing on the use of liquid fuel sources to suppress combustion instabilities.

The main focus of this dissertation work was to theoretically establish and experimentally demonstrate the active instability suppression with liquid fuel injection strategy in a vortex-driven combustor. The sequences of steps that are taken are as follows:

First, to better understand the function of pulsed fuel sprays in combustion instability suppression, detailed liquid fuel spray characterizations including droplet size distribution and velocity profiles were obtained with the Malvern instrument and PIV measurements, respectively. Heat release from droplet combustion was also analyzed in this study.

Additionally, to identify proper locations for the supply of secondary liquid fuel for combustion instability suppression purposes, the natural heat release pattern in a vortex-driven combustor was characterized in this research work. Temporally evolving heat release associated with periodic vortices was characterized using phase-resolved Schlieren images and CH* chemiluminescence measurement. The relationship between oscillatory heat release and large-scale coherent structures was systematically investigated in this study.

Next, comprehensive experiments were conducted on a dump combustor rig to reveal the physical mechanisms associated with combustion instabilities and control strategies. Dynamic pressure signals were recorded to monitor oscillations inside the dump combustor. High-speed Schlieren imaging was employed to visualize the changes of the flow field, both with and without additional liquid fuel injection.

Lastly, scale-up experiments of instability suppression with pulsed liquid fuel injection were accomplished.

The important findings of this research work are summarized below:

- The Sauter-Mean-Diameter of liquid fuel droplet oscillate from 38 μm to 73 μm as the result of the periodic pressurization and relief of pulsed liquid fuel injection.
- High amplitude heat release fluctuations up to ± 60% of its mean value can be generated due to the droplet size modulation with the pulsed liquid fuel injection strategy. Theoretically, it is feasible to suppress combustion instabilities with this control strategy.
- At high Damköhler number conditions, i.e., the chemistry time scale being much smaller than the flow dynamic time scale, the natural heat release oscillation in a premixed vortex-driven combustor closely followed the evolvement of the vortex front. But when the Damköhler number became close to unity, i.e., the chemistry time scale was on the same order of the flow dynamic time scale, natural heat release fluctuations in the vortex-driven combustor no longer coincided with large-scale coherent structures.
- Heat release deficit area was found near the dump plane when the combustor was operated at low Damköhler number conditions. Combustion instabilities can be suppressed if additional heat is added into this area.
- High-speed Schlieren results illustrated that vortex shedding plays an important role in maintaining self-sustained combustion instabilities. Complete combustion instability control requires total suppression of these large-scale coherent structures.

- The sound pressure level at the excited dominant frequency was reduced by more than 20 dB with controlled liquid fuel injection method at lower thermal power output conditions. The timing of liquid fuel injection is critical to achieve maximum oscillation reduction.
- Experiments on higher inlet Mach number conditions demonstrated that liquid fuel injection strategy could be extended to more realistic flow conditions. Up to ± 5psi high amplitude pressure oscillations at 364 kW power output condition were completely suppressed to background noise level and the operating range of this laboratory scale dump combustor was expanded.

7.2 Future Work

While the research on active combustion instability control with liquid fuel is certainly not complete, the direction of progress shown in this study is very promising and encouraging.

Further steps of active instability suppression research in vortex-driven combustors with the pulsed liquid-fuel injection strategy can be conducted in the following areas:

1) The relationship of heat release fluctuations with respect to large-scale vortex structures at low Damköhler number conditions is still not very clear. Since heat release information determines the changes of natural pressure oscillations inside the combustor, more study is needed to establish a general criterion to identify desired spatial locations of supplying controlled liquid fuel.

2) Although experiments on the laboratory scale dump combustor have indicated that applying a direct liquid fuel injection strategy at power output as high as 364 kW can reduce the amplitude of combustion instabilities, full-scale combustor experiments are still needed to test the applicability of this concept.

Appendix A – Averaged Droplets Sauter-Mean-Diameter

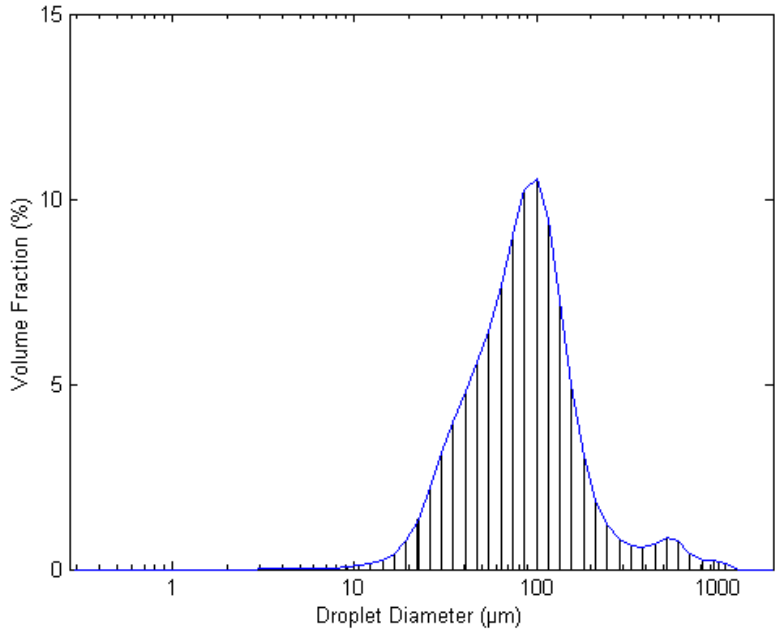

Fig. A.1: Ethanol droplets size distribution at pressure 20 psi and 100% duty cycle.

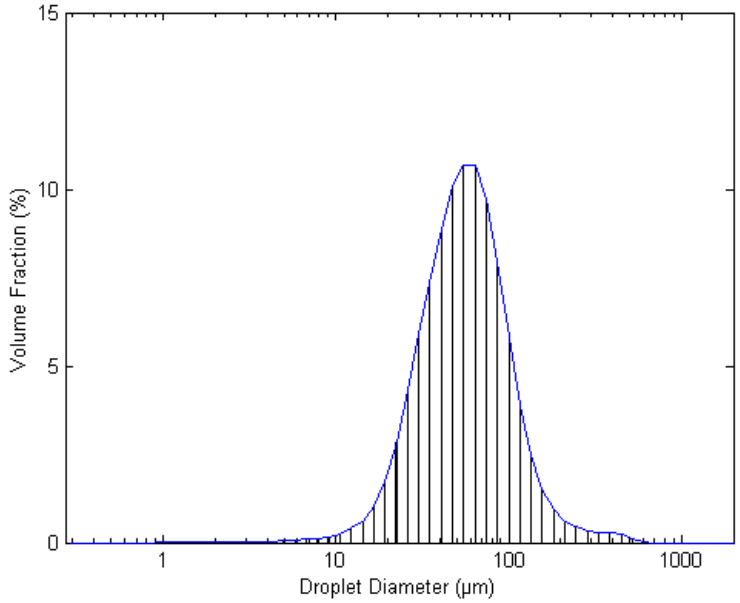

Fig. A.2: Ethanol droplets size distribution at pressure 30 psi and 100% duty cycle.

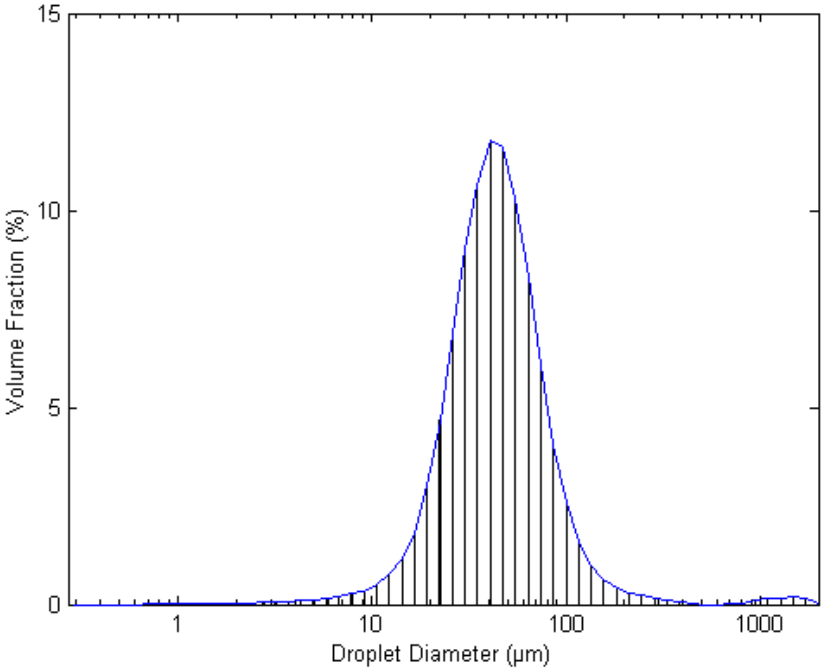

Fig. A.3: Ethanol droplets size distribution at pressure 40 psi and 100% duty cycle.

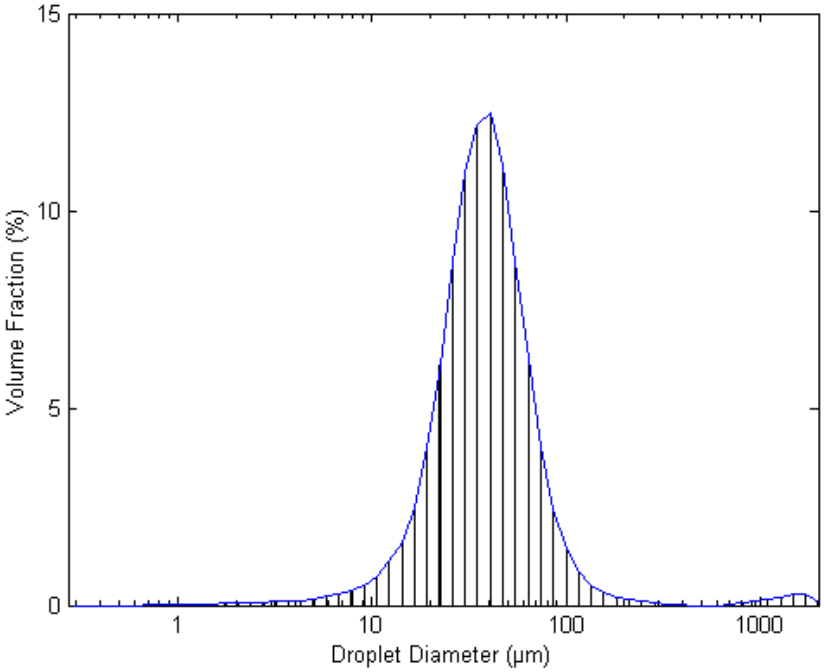

Fig. A.4: Ethanol droplets size distribution at pressure 50 psi and 100% duty cycle.

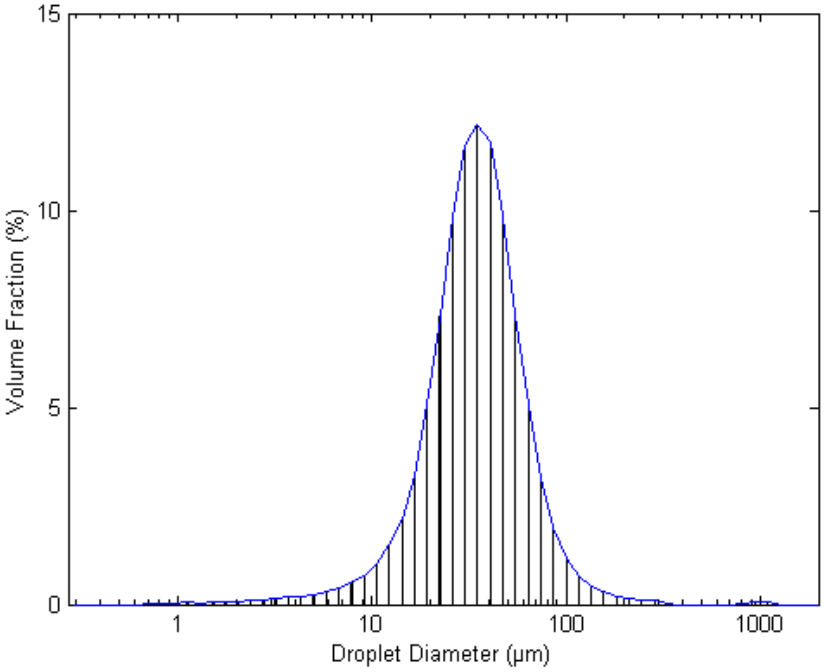

Fig. A.5: Ethanol droplets size distribution at pressure 60 psi and 100% duty cycle.

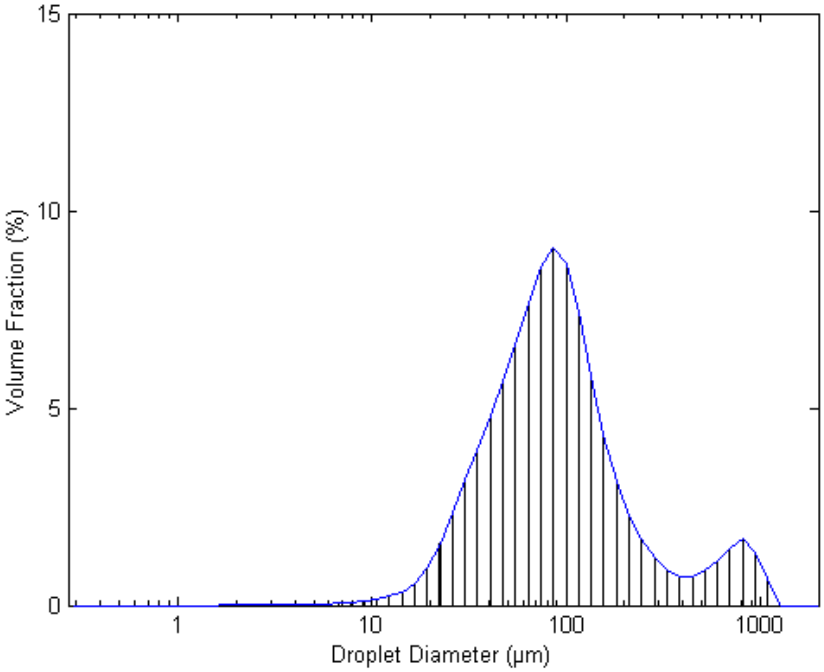

Fig. A.6: Ethanol droplets size distribution at pressure 20 psi, forcing frequency 37.87 Hz and 50% duty cycle.

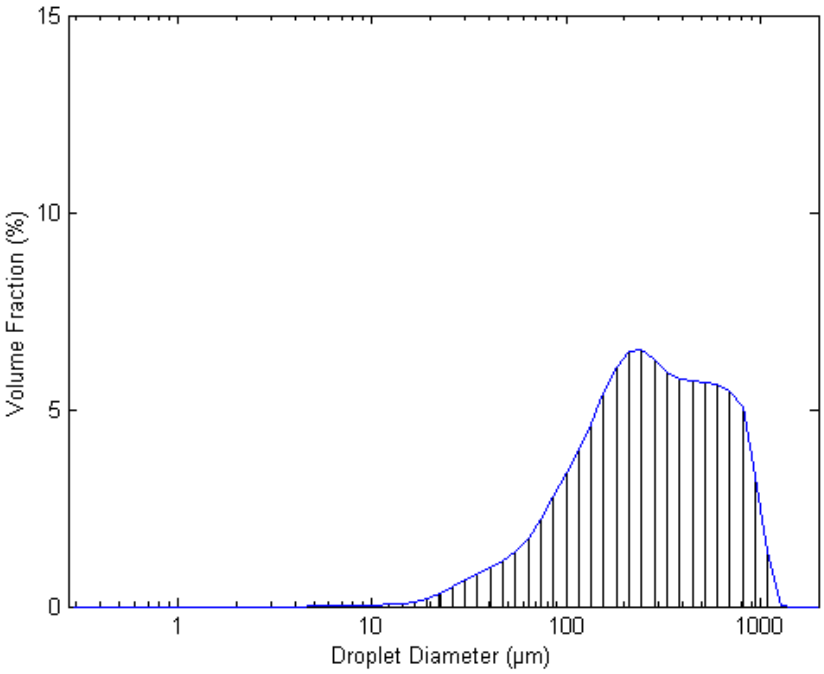

Fig. A.7: Ethanol droplets size distribution at pressure 20 psi, forcing frequency 38 Hz and 25% duty cycle.

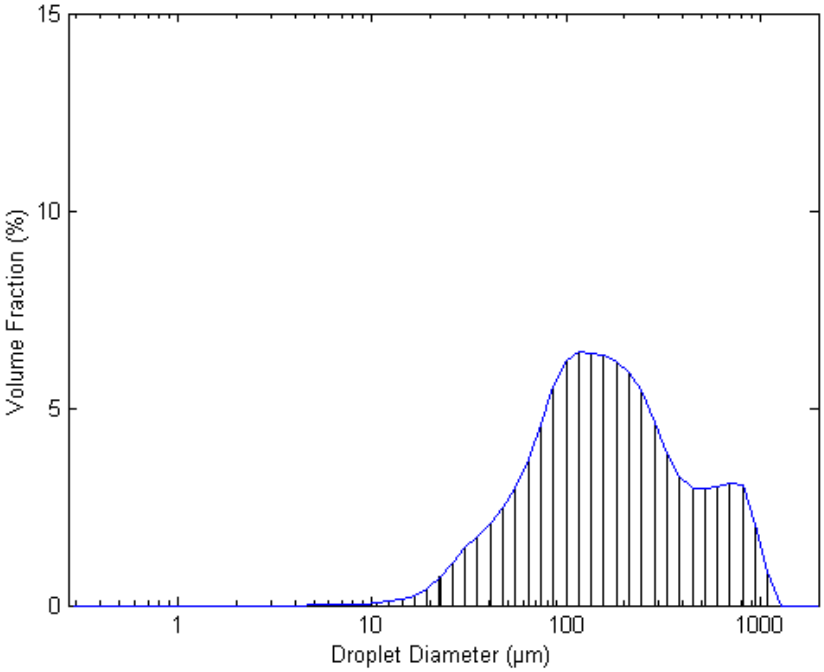

Fig. A.8: Ethanol droplets size distribution at pressure 20 psi, forcing frequency 38 Hz and 50% duty cycle.

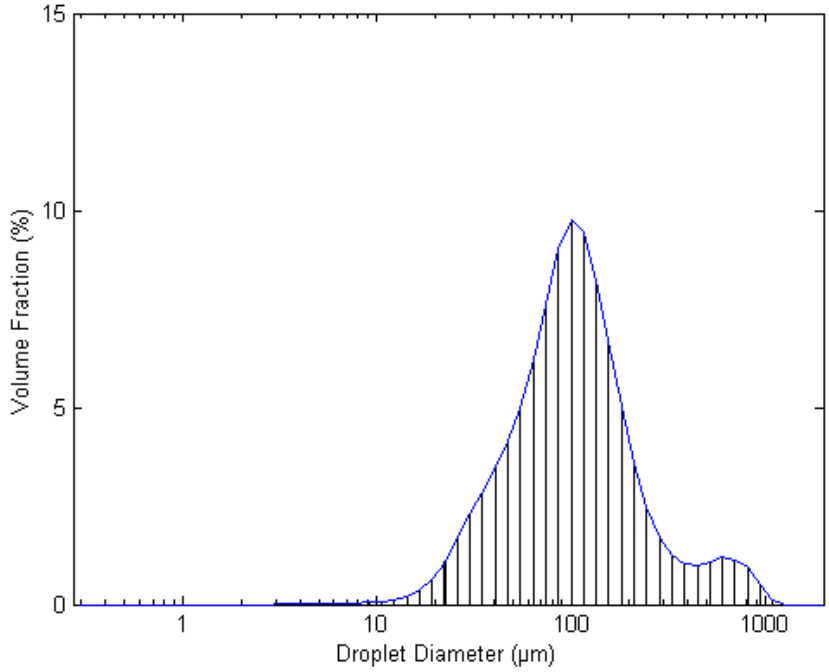

Fig. A.9: Ethanol droplets size distribution at pressure 20 psi, forcing frequency 38 Hz and 75% duty cycle.

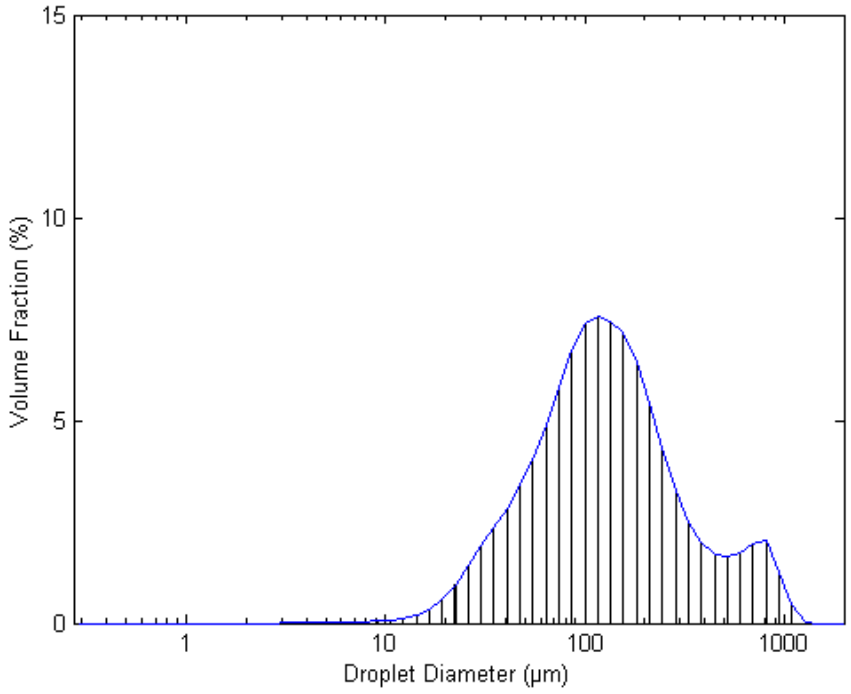

Fig. A.10: Ethanol droplets size distribution at pressure 20 psi, forcing frequency 100 Hz and 50% duty cycle.

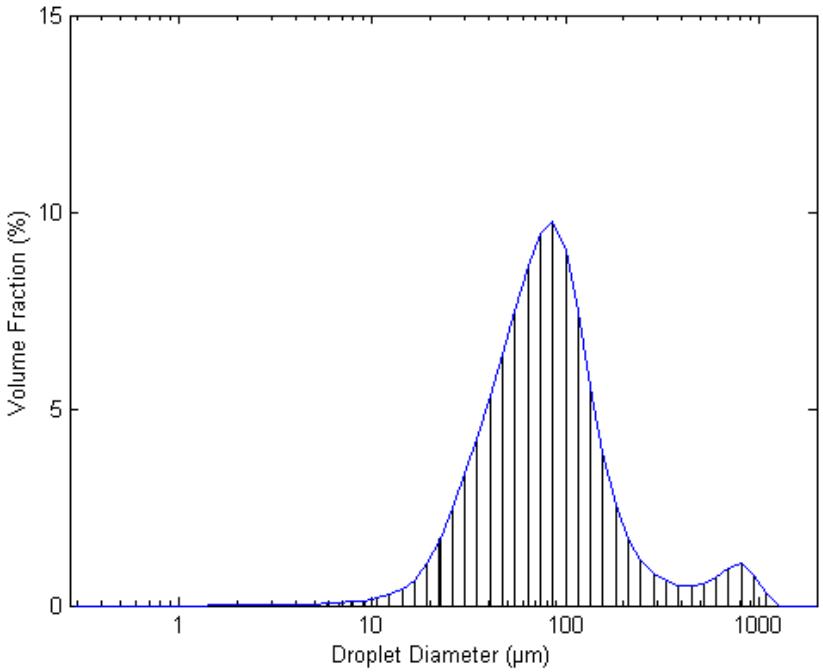

Fig. A.11: Ethanol droplets size distribution at pressure 20 psi, forcing frequency 125 Hz and 50% duty cycle.

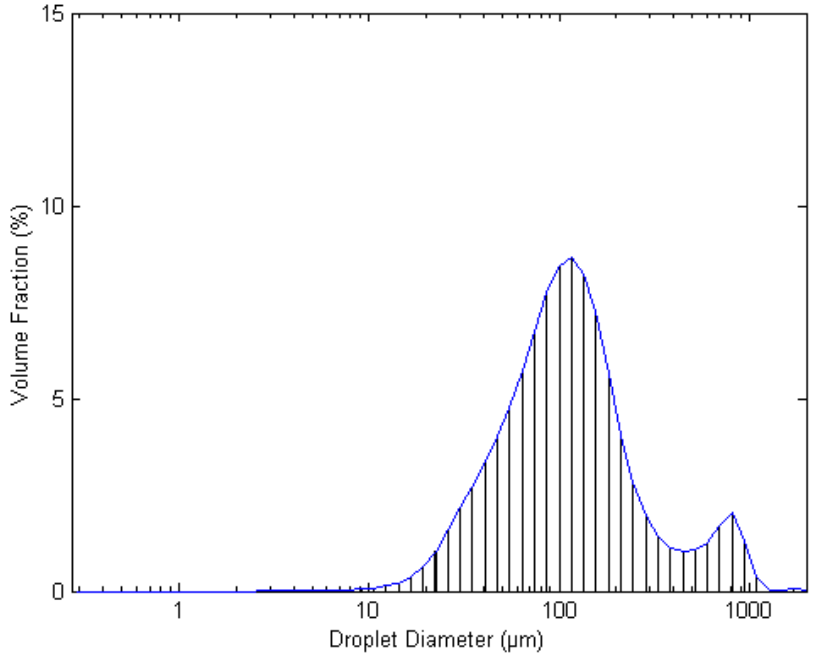

Fig. A.12: Ethanol droplets size distribution at pressure 20 psi, forcing frequency 200 Hz and 50% duty cycle.

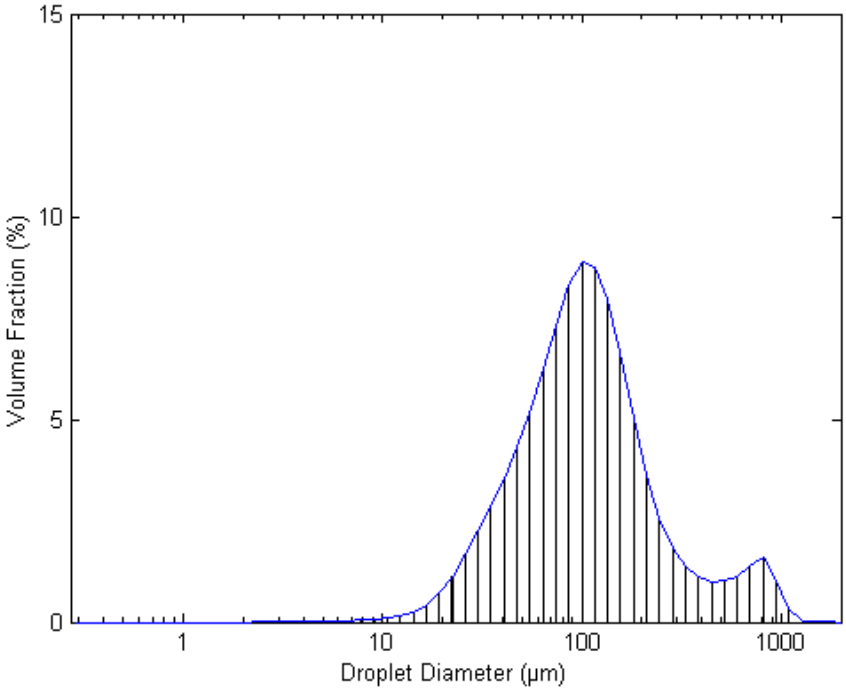

Fig. A.13: Ethanol droplets size distribution at pressure 20 psi, forcing frequency 280 Hz and 50% duty cycle.

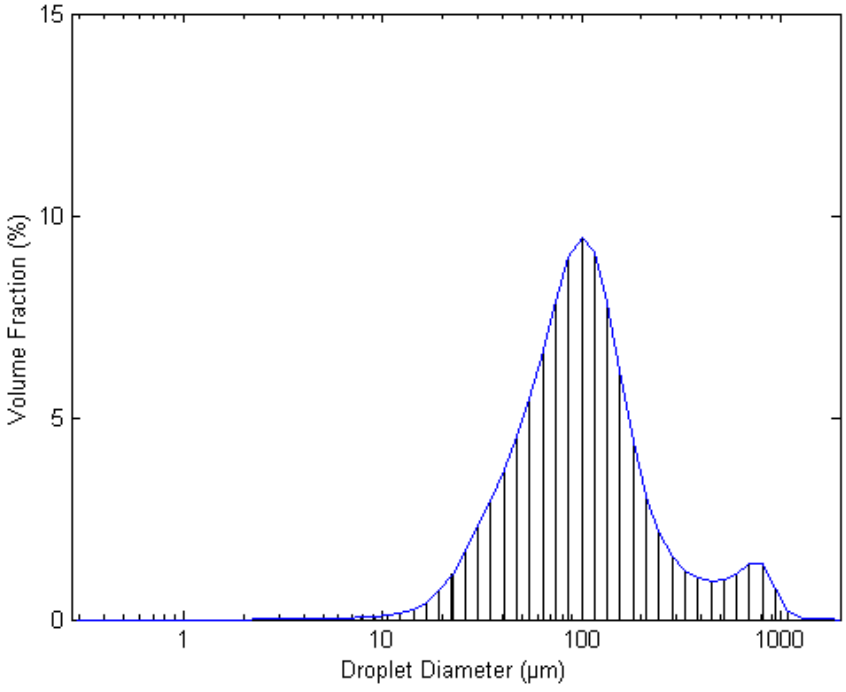

Fig. A.14: Ethanol droplets size distribution at pressure 20 psi, forcing frequency 300 Hz and 50% duty cycle.

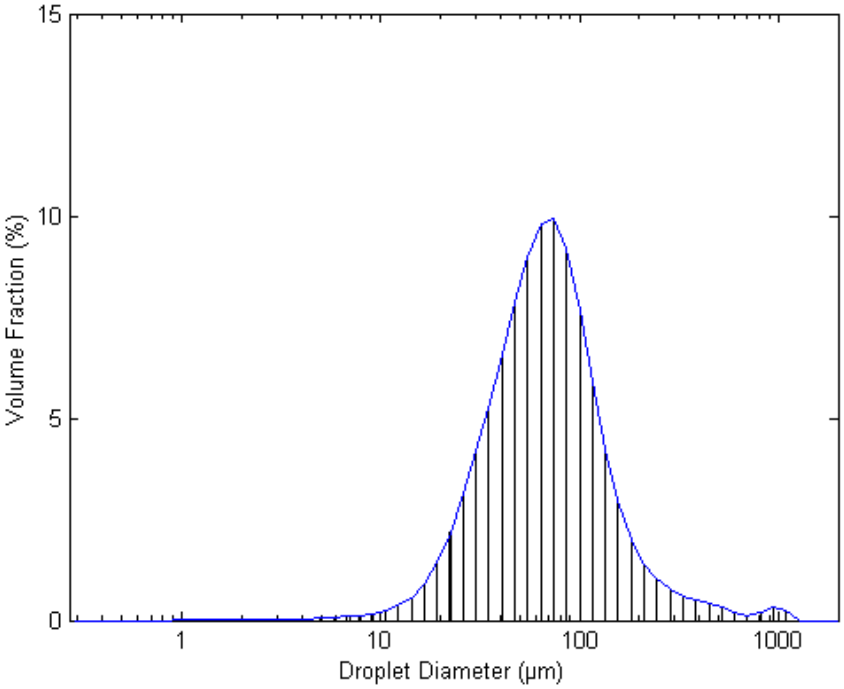

Fig. A.15: Ethanol droplets size distribution at pressure 20 psi, forcing frequency 312.5 Hz and 50% duty cycle.

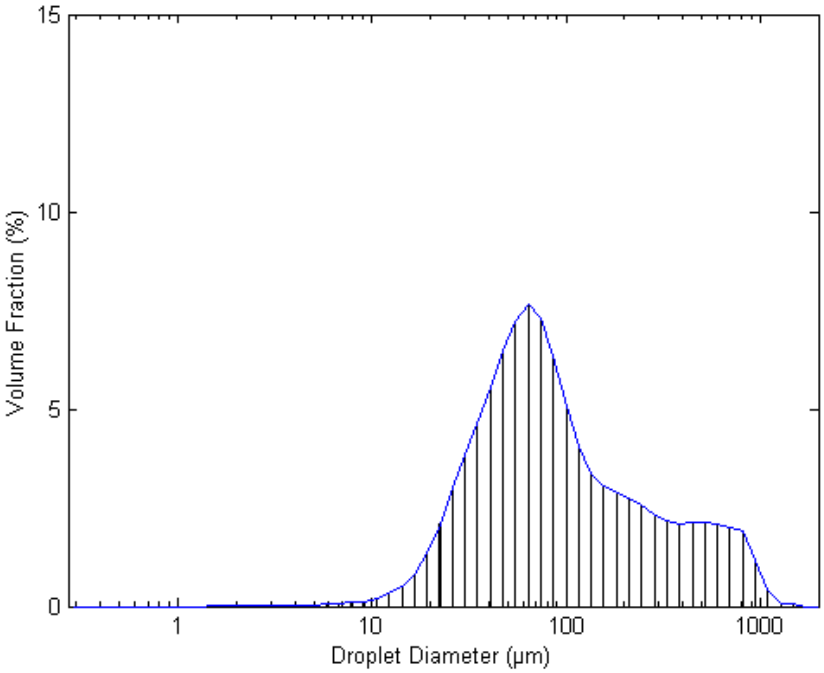

Fig. A.16: Ethanol droplets size distribution at pressure 30 psi, forcing frequency 38 Hz and 50% duty cycle.

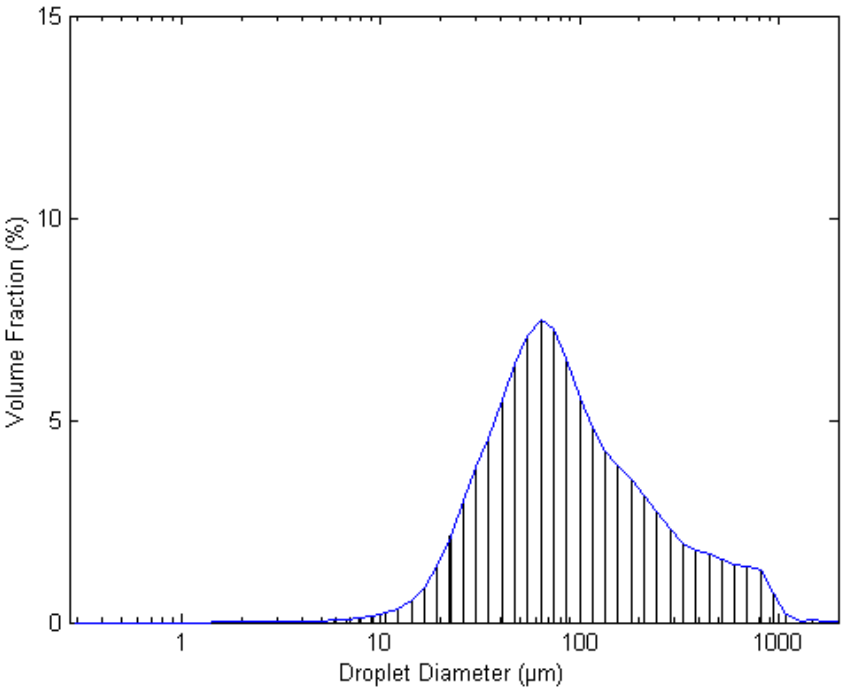

Fig. A.17: Ethanol droplets size distribution at pressure 30 psi, forcing frequency 100 Hz and 50% duty cycle.

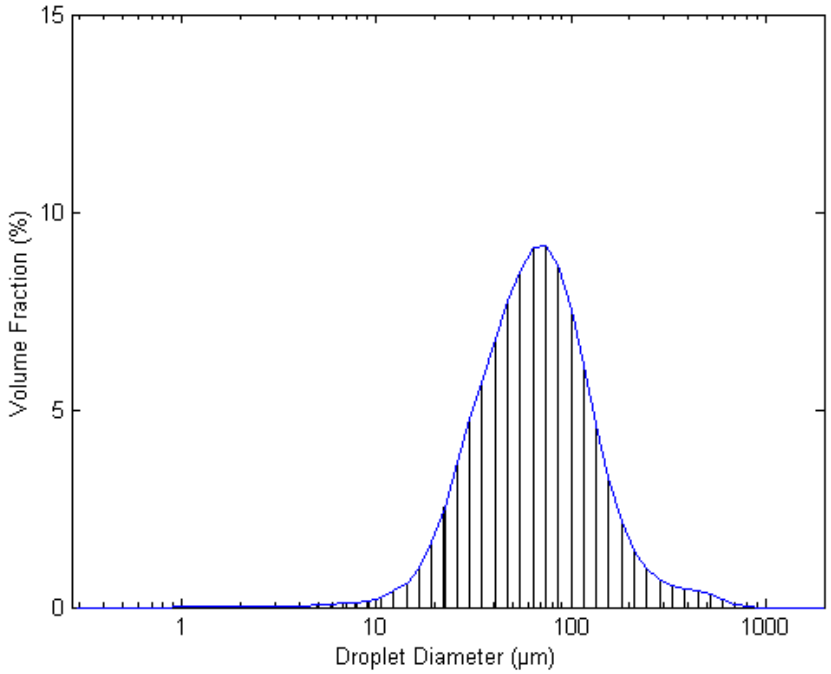

Fig. A.18: Ethanol droplets size distribution at pressure 30 psi, forcing frequency 200 Hz and 50% duty cycle.

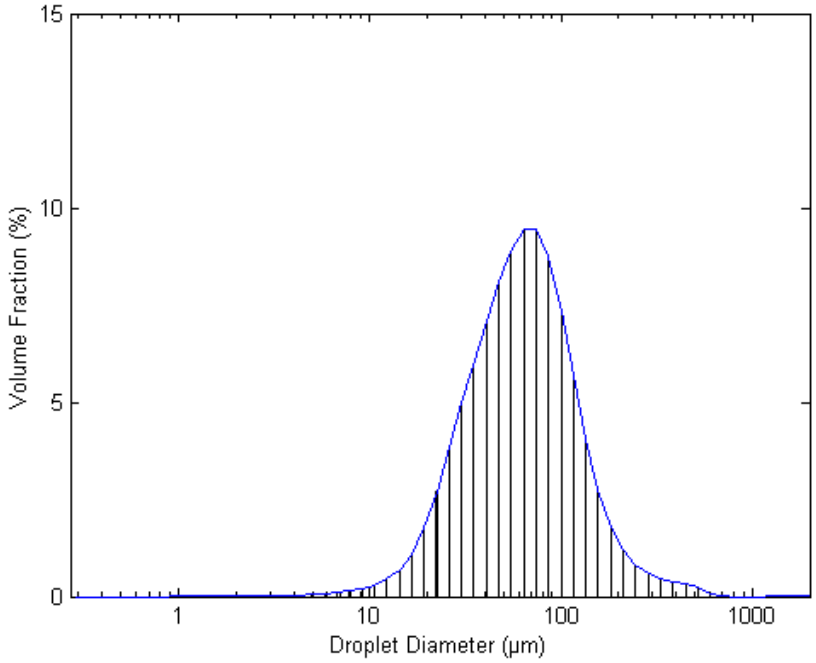

Fig. A.19: Ethanol droplets size distribution at pressure 30 psi, forcing frequency 280 Hz and 50% duty cycle.

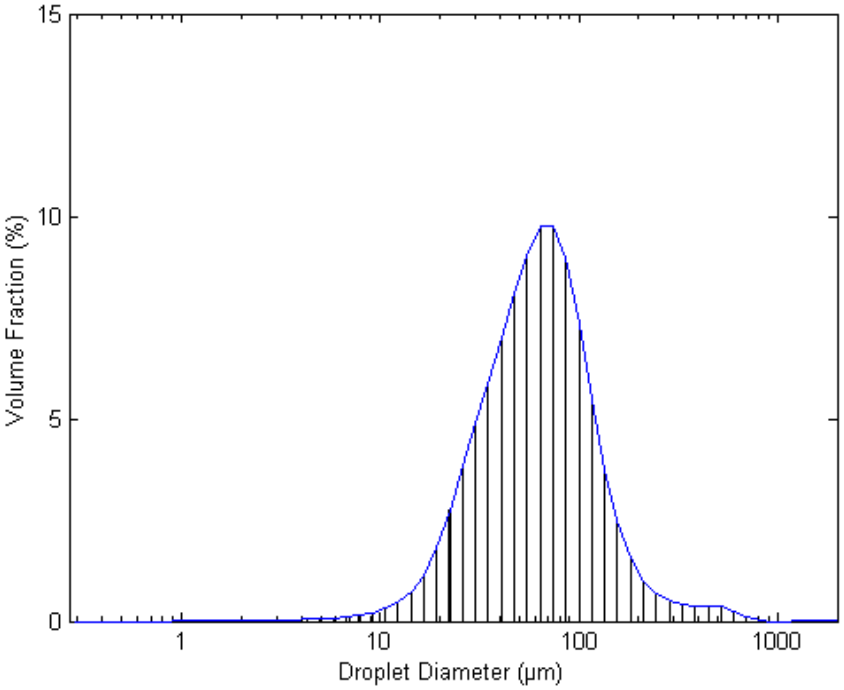

Fig. A.20: Ethanol droplets size distribution at pressure 30 psi, forcing frequency 300 Hz and 50% duty cycle.

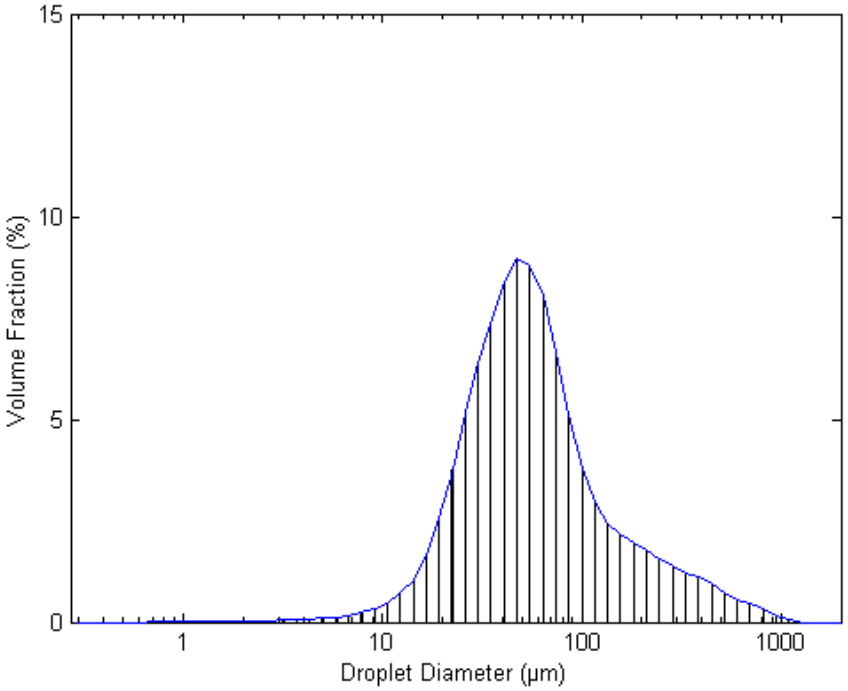

Fig. A.21: Ethanol droplets size distribution at pressure 40 psi, forcing frequency 38 Hz and 50% duty cycle.

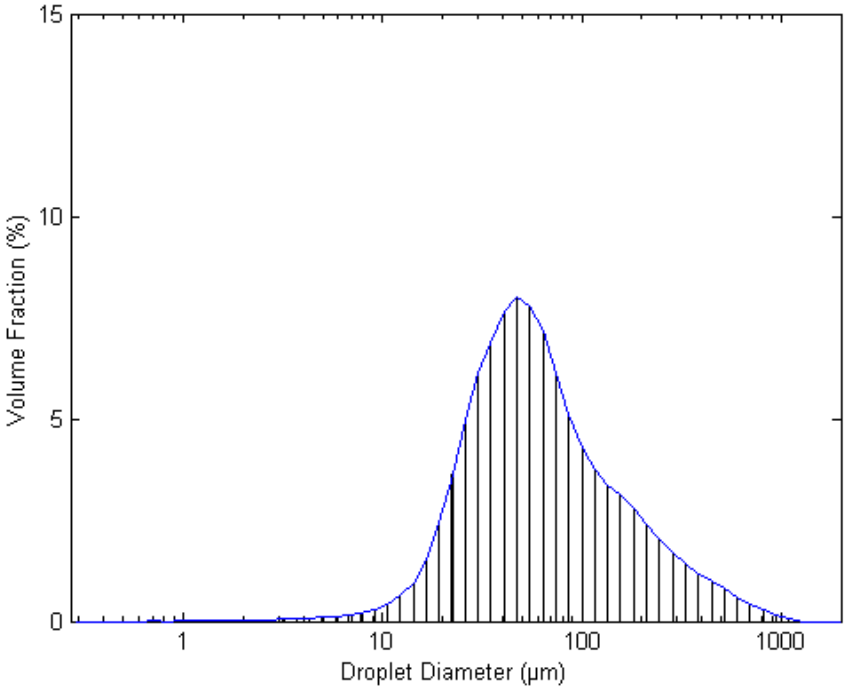

Fig. A.22: Ethanol droplets size distribution at pressure 40 psi, forcing frequency 100 Hz and 50% duty cycle.

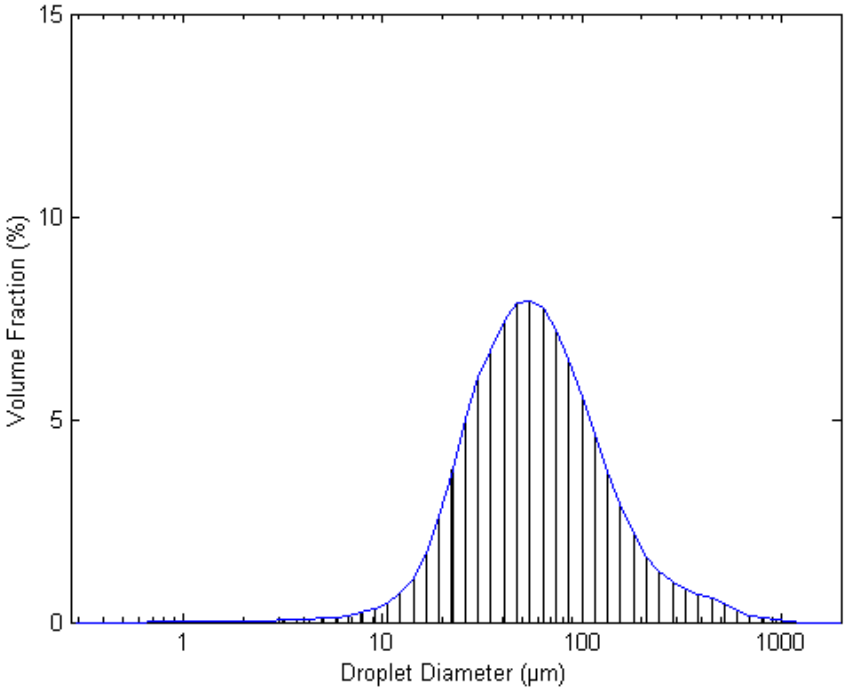

Fig. A.23: Ethanol droplets size distribution at pressure 40 psi, forcing frequency 200 Hz and 50% duty cycle.

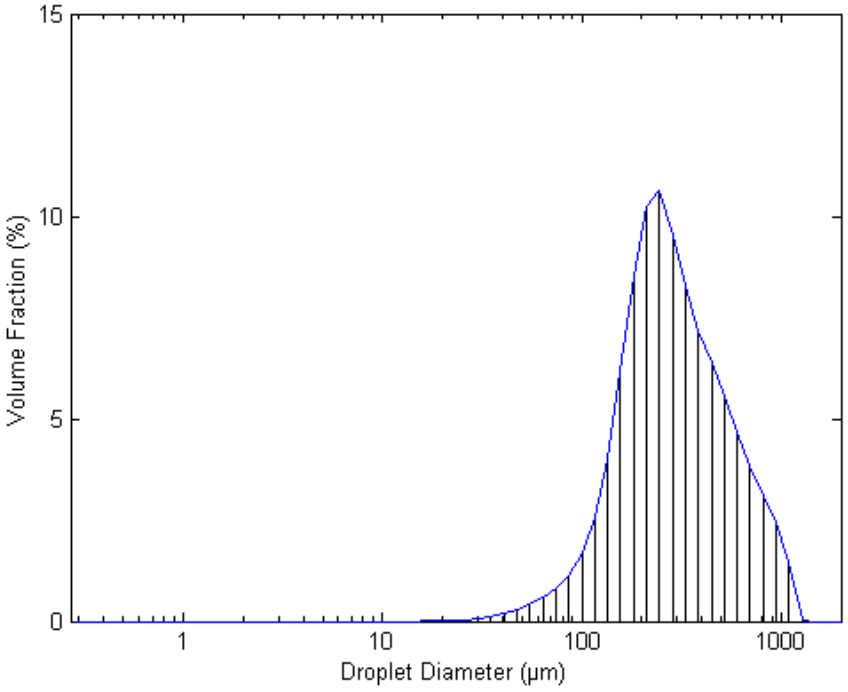

Fig. A.24: Ethanol droplets size distribution at pressure 40 psi, forcing frequency 280 Hz and 25% duty cycle.

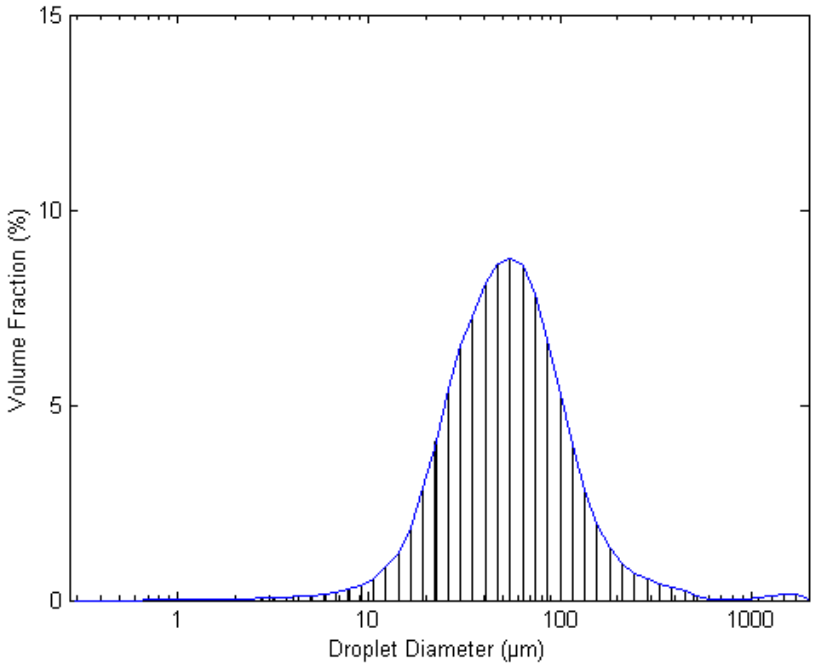

Fig. A.25: Ethanol droplets size distribution at pressure 40 psi, forcing frequency 280 Hz and 50% duty cycle.

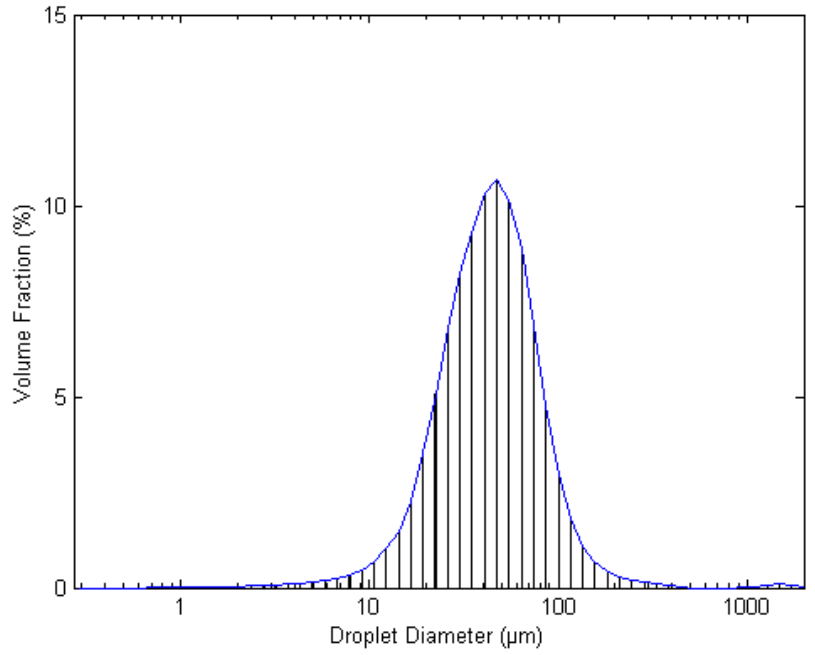

Fig. A.26: Ethanol droplets size distribution at pressure 40 psi, forcing frequency 280 Hz and 75% duty cycle.

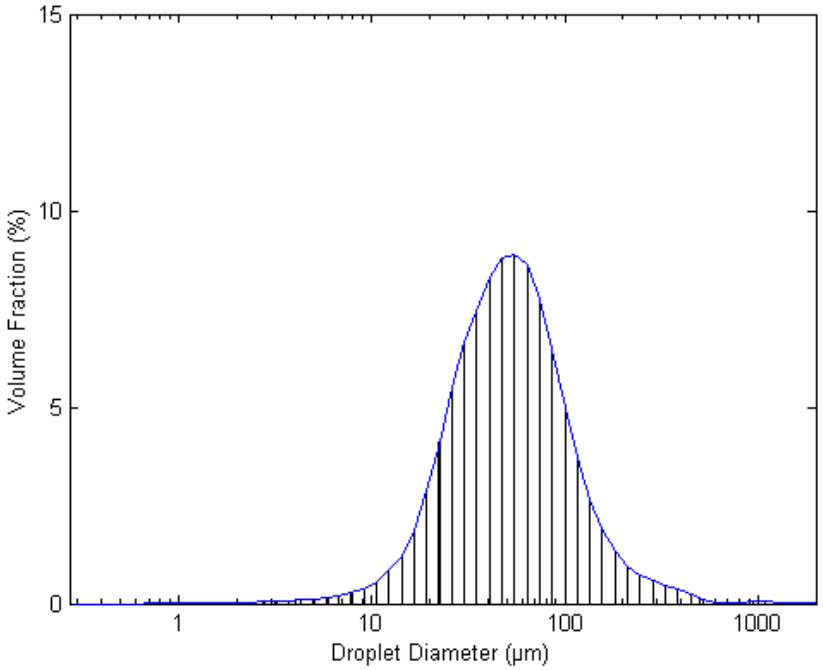

Fig. A.27: Ethanol droplets size distribution at pressure 40 psi, forcing frequency 300 Hz and 50% duty cycle.

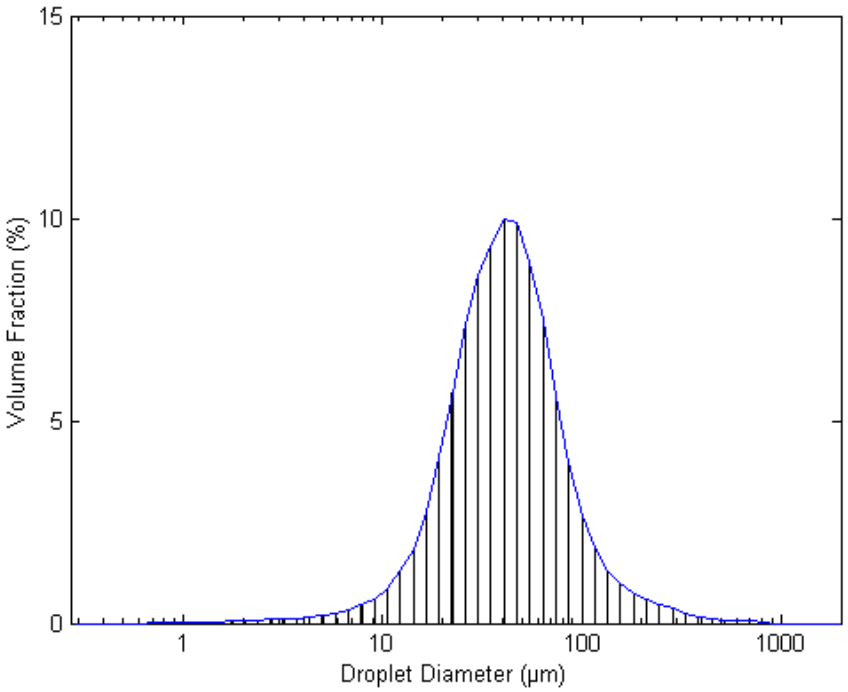

Fig. A.28: Ethanol droplets size distribution at pressure 50 psi, forcing frequency 38 Hz and 50% duty cycle.

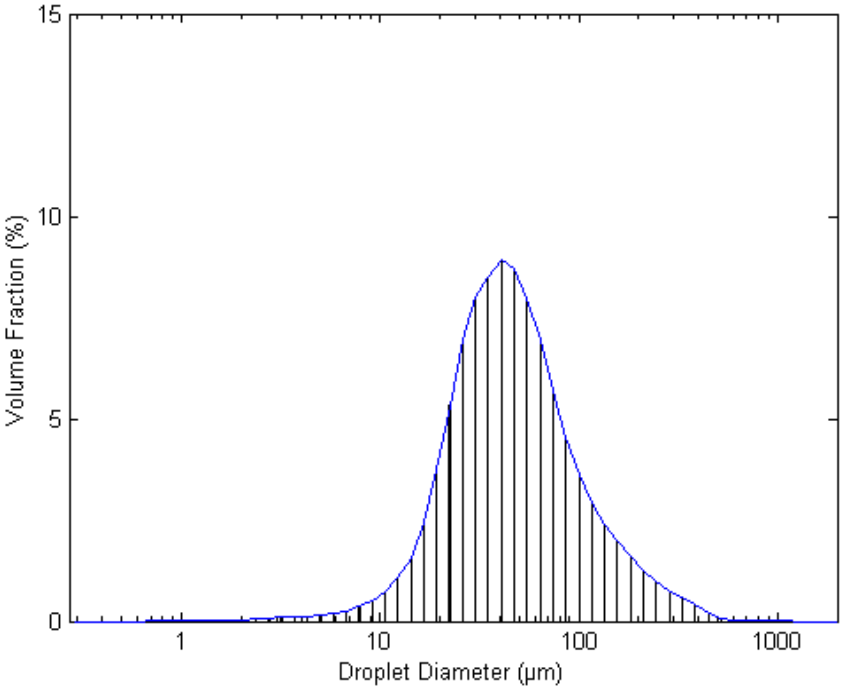

Fig. A.29: Ethanol droplets size distribution at pressure 50 psi, forcing frequency 100 Hz and 50% duty cycle.

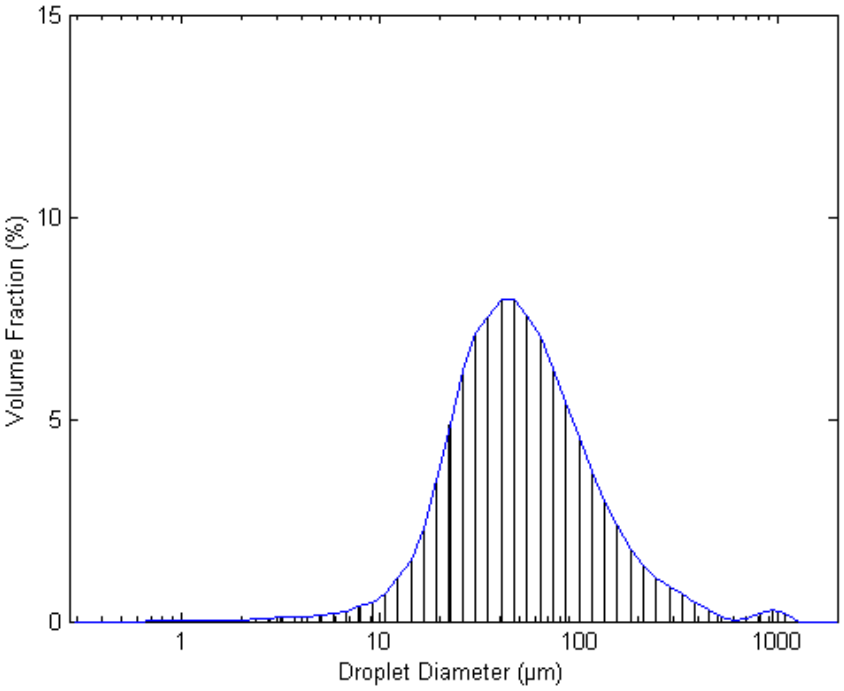

Fig. A.30: Ethanol droplets size distribution at pressure 50 psi, forcing frequency 200 Hz and 50% duty cycle.

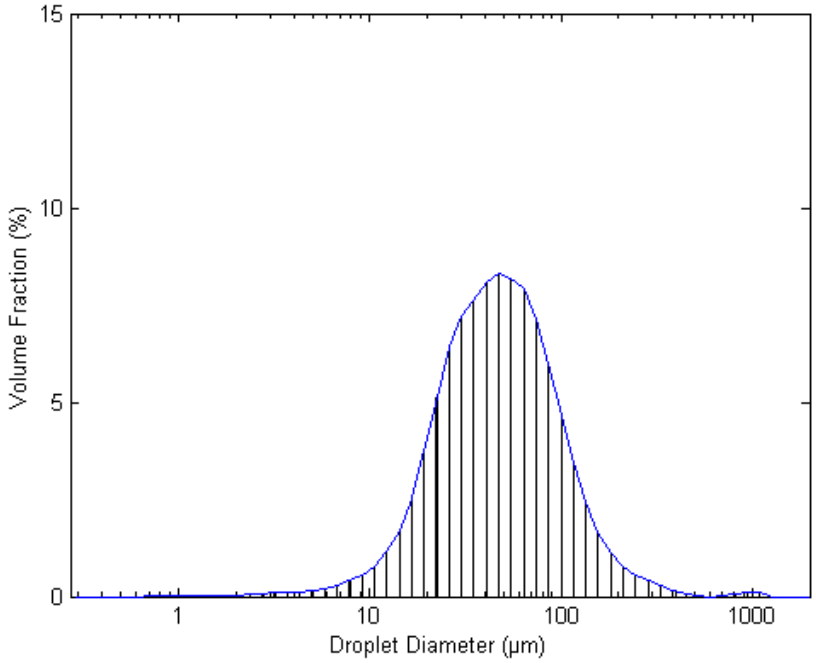

Fig. A.31: Ethanol droplets size distribution at pressure 50 psi, forcing frequency 280 Hz and 50% duty cycle.

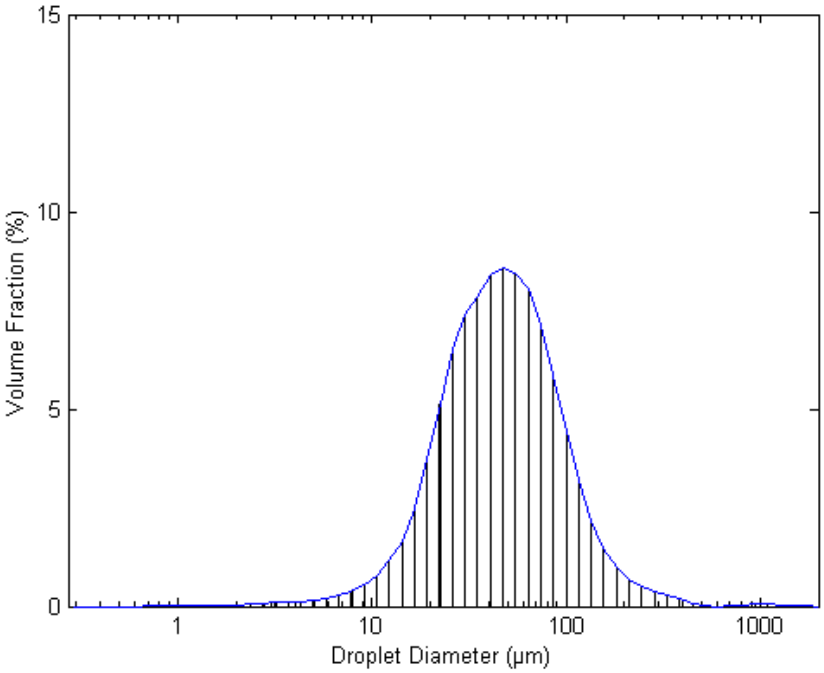

Fig. A.32: Ethanol droplets size distribution at pressure 50 psi, forcing frequency 300 Hz and 50% duty cycle.

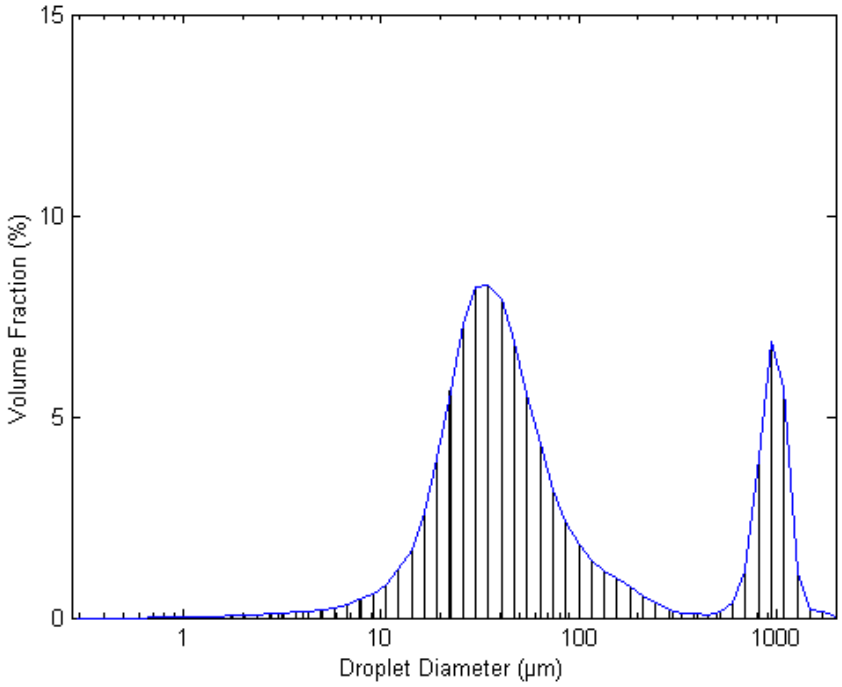

Fig. A.33: Ethanol droplets size distribution at pressure 60 psi, forcing frequency 37.87 Hz and 50% duty cycle.

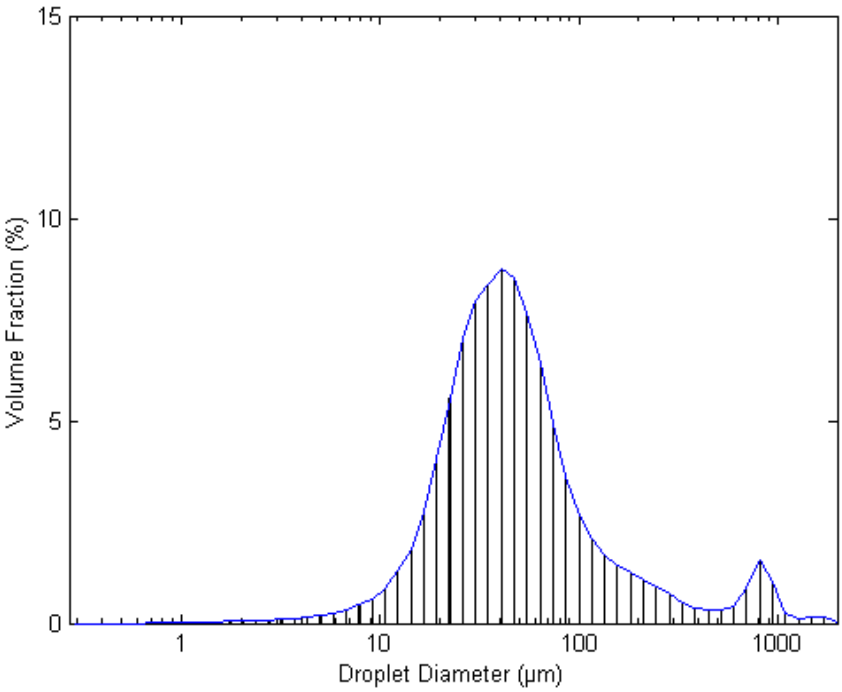

Fig. A.34: Ethanol droplets size distribution at pressure 60 psi, forcing frequency 38 Hz and 50% duty cycle.

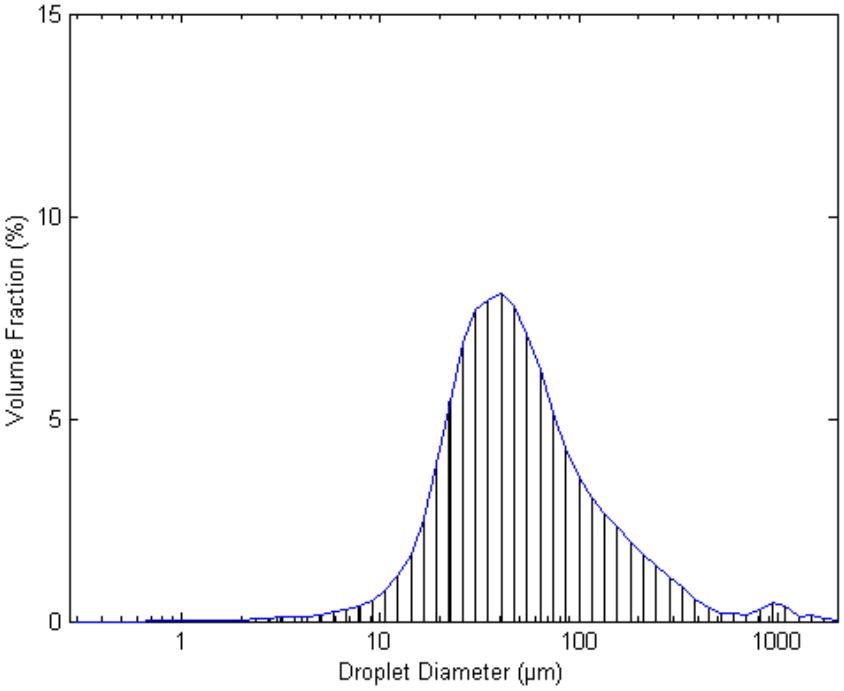

Fig. A.35: Ethanol droplets size distribution at pressure 60 psi, forcing frequency 100 Hz and 50% duty cycle.

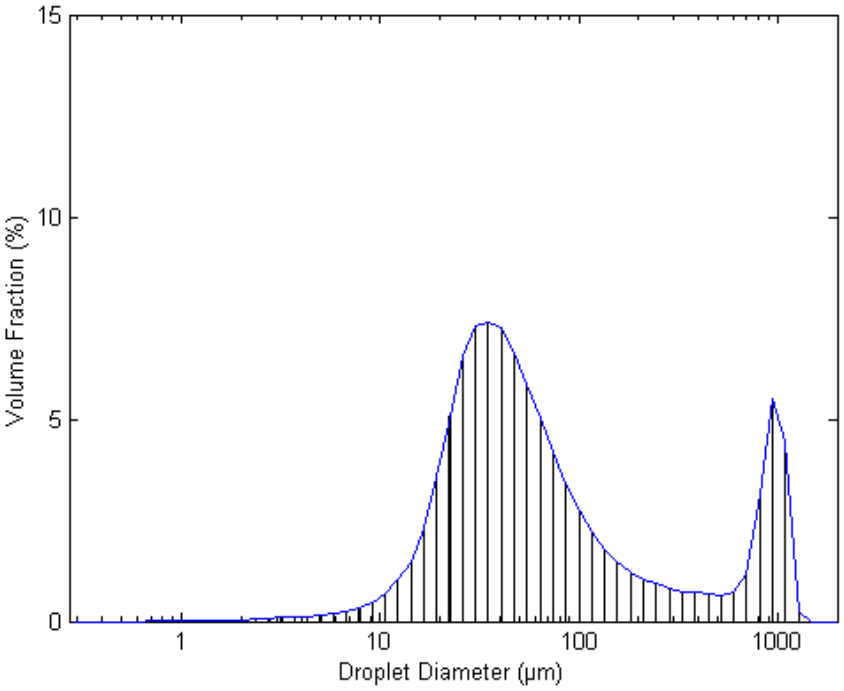

Fig. A.36: Ethanol droplets size distribution at pressure 60 psi, forcing frequency 125 Hz and 50% duty cycle.

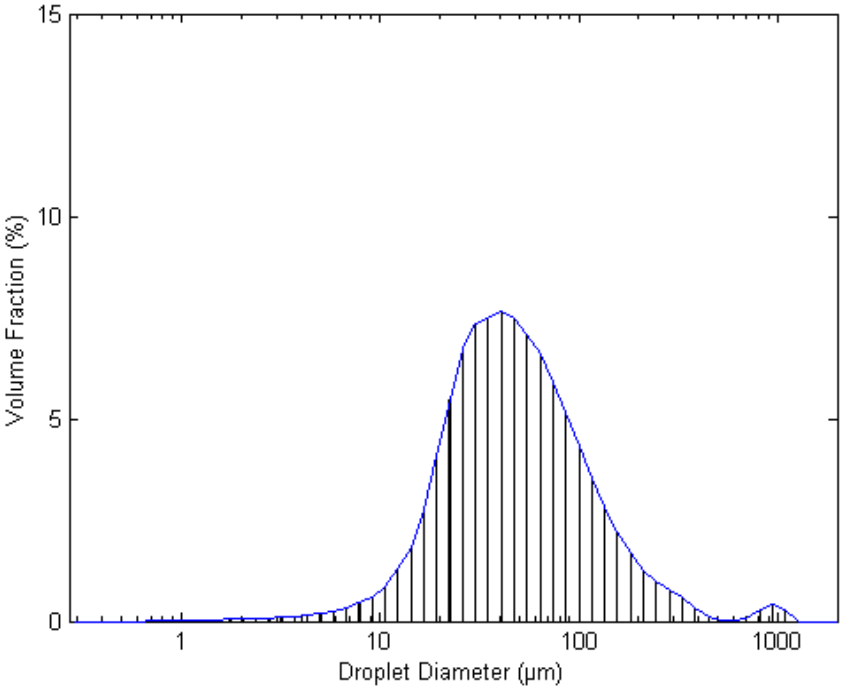

Fig. A.37: Ethanol droplets size distribution at pressure 60 psi, forcing frequency 200 Hz and 50% duty cycle.

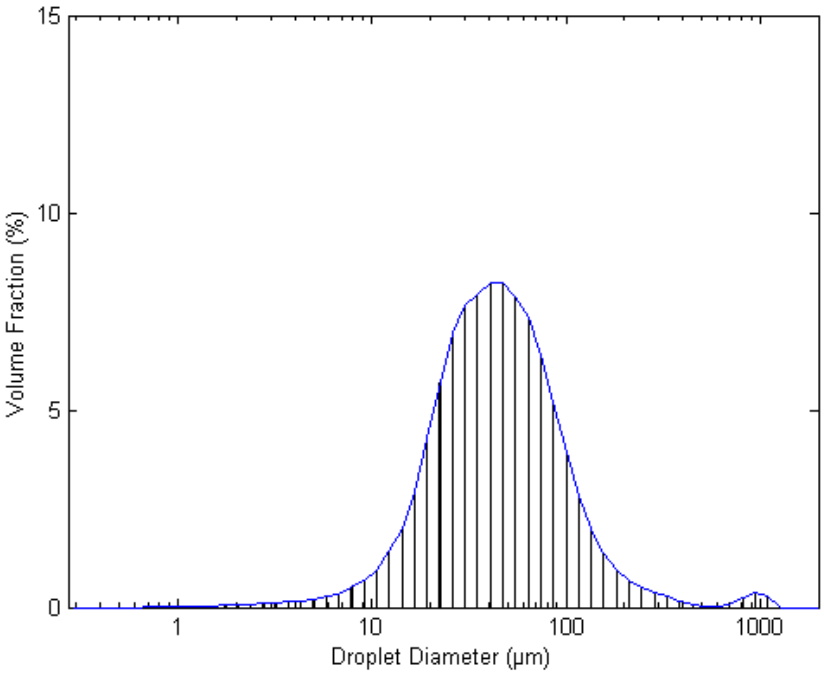

Fig. A.38: Ethanol droplets size distribution at pressure 60 psi, forcing frequency 280 Hz and 50% duty cycle.

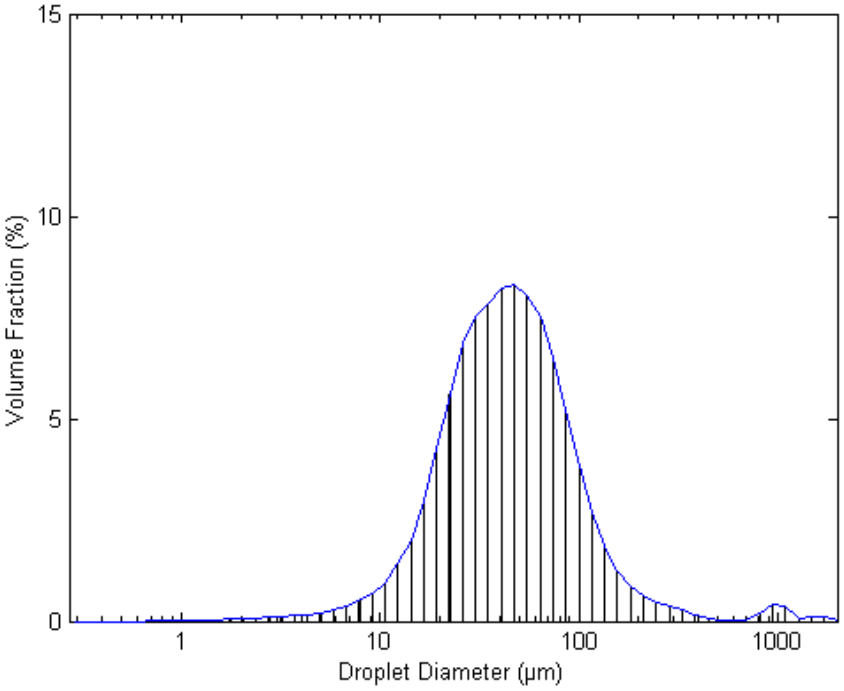

Fig. A.39: Ethanol droplets size distribution at pressure 60 psi, forcing frequency 300 Hz and 50% duty cycle.

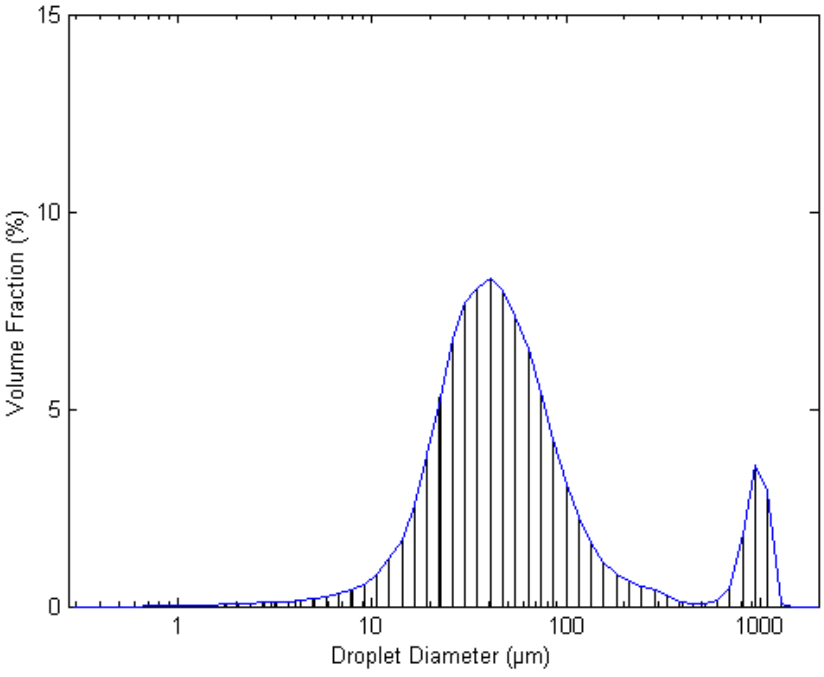

Fig. A.40: Ethanol droplets size distribution at pressure 60 psi, forcing frequency 312.5 Hz and 50% duty cycle.

Appendix B – Time-evolution of Droplets Sauter-Mean-Diameter

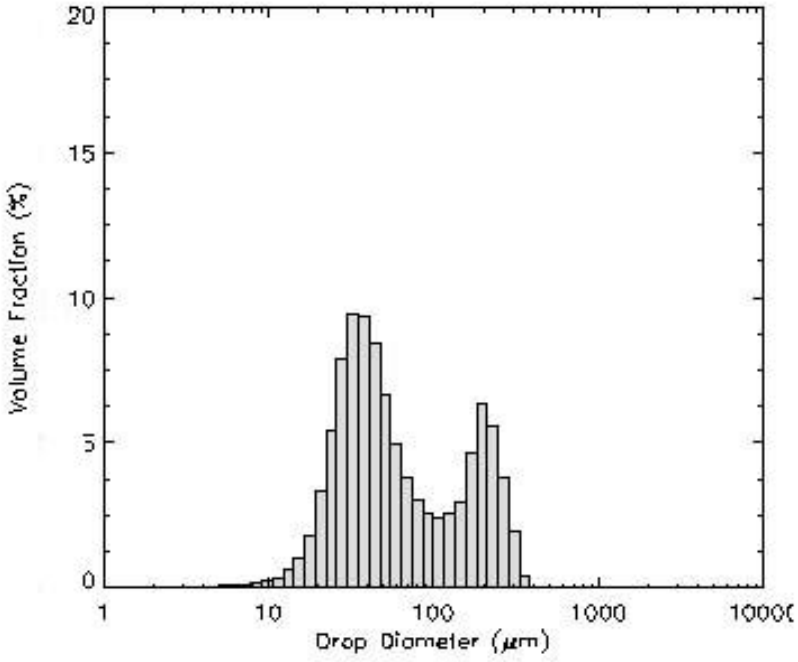

Fig. B1.1: Ethanol droplets size distribution at phase 0^{o}, pressure 20 psi forcing frequency 37.87 Hz and 50% duty cycle.

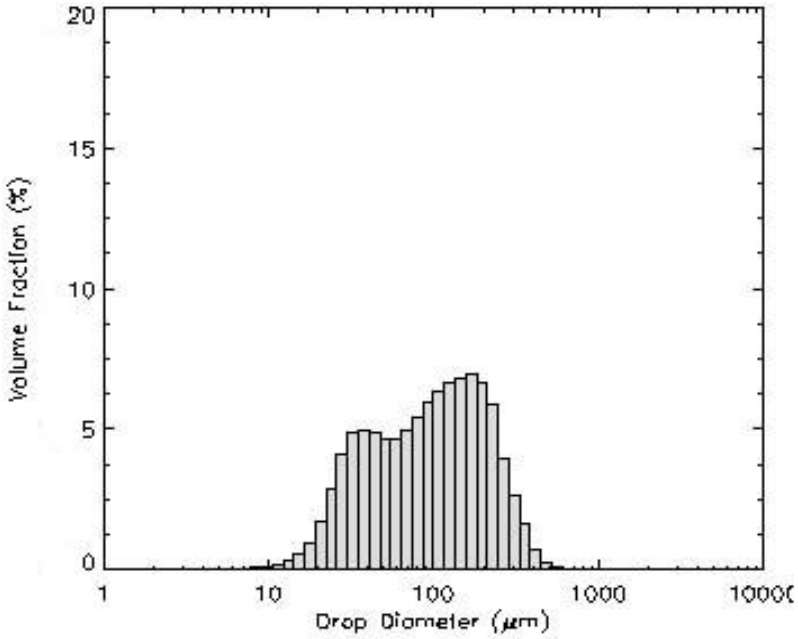

Fig. B1.2: Ethanol droplets size distribution at phase 45^{o}, pressure 20 psi, forcing frequency 37.87 Hz and 50% duty cycle.

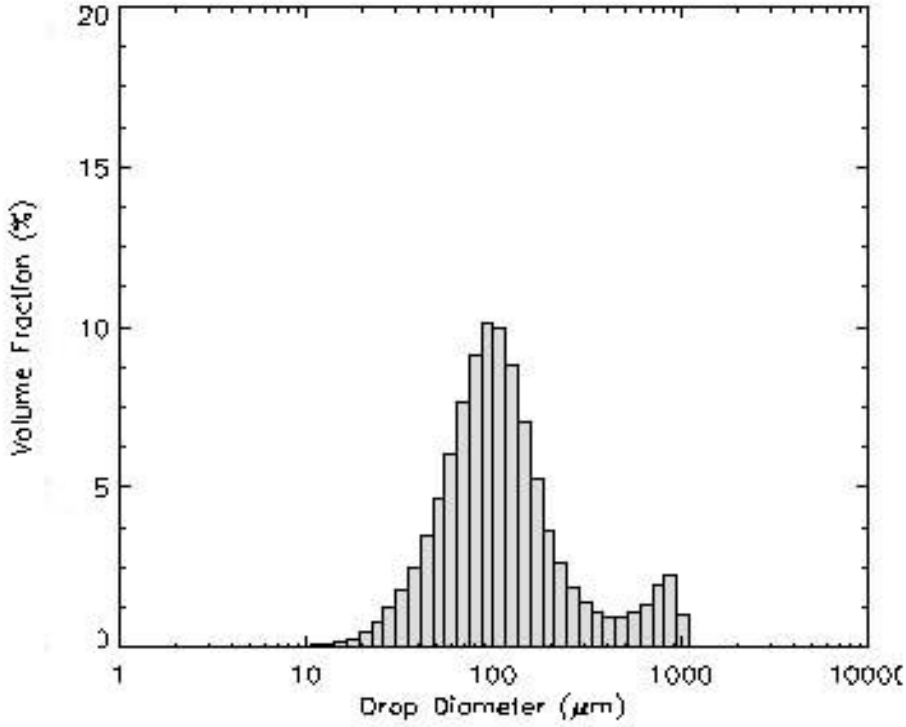

Fig. B1.3: Ethanol droplets size distribution at phase 90°, pressure 20 psi, forcing frequency 37.87 Hz and 50% duty cycle.

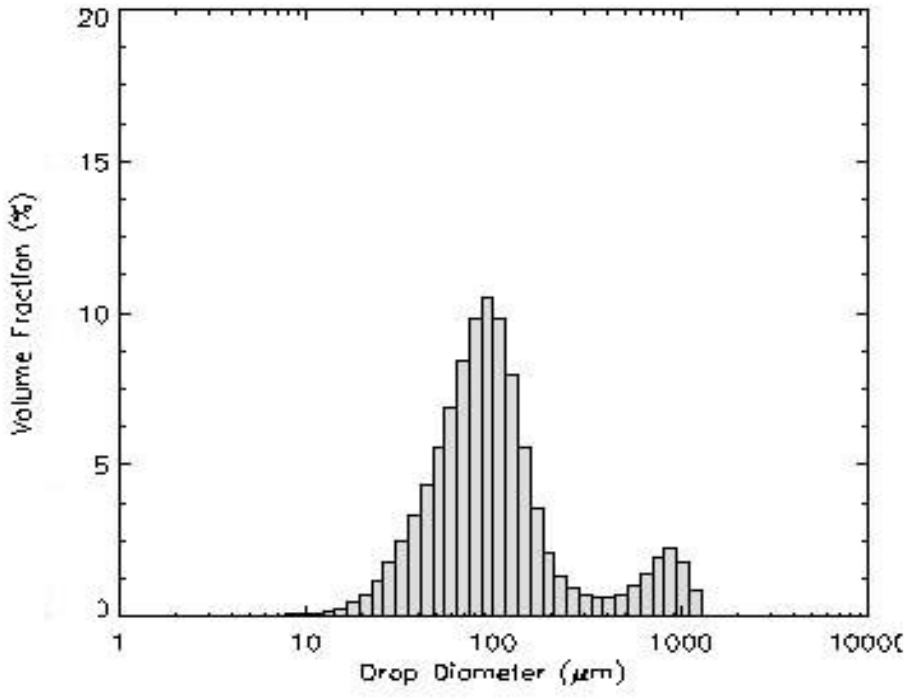

Fig. B1.4: Ethanol droplets size distribution at phase 135°, pressure 20 psi, forcing frequency 37.87 Hz and 50% duty cycle.

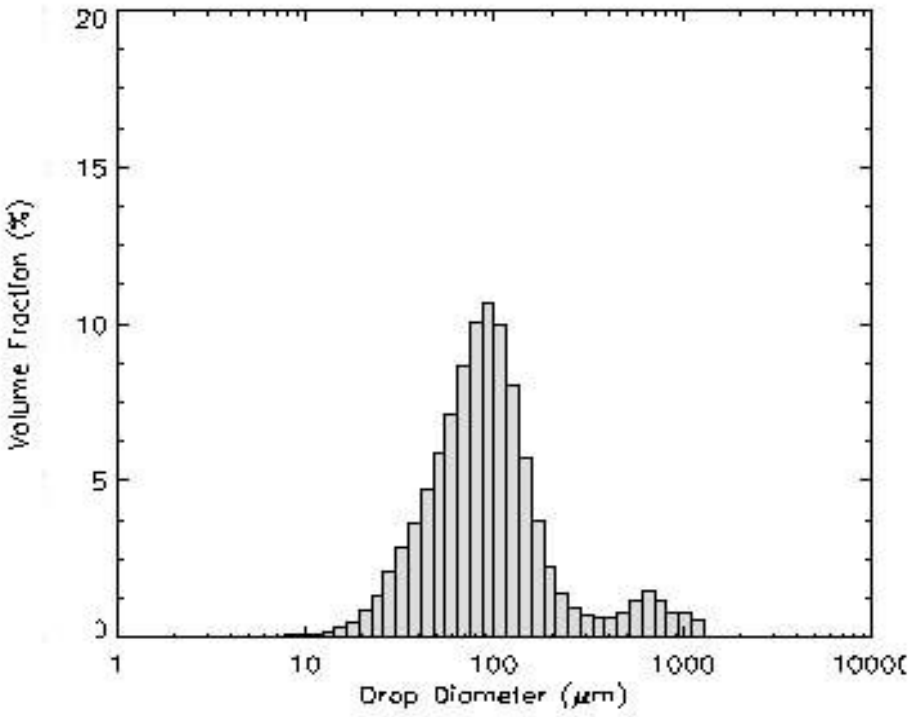

Fig. B1.5: Ethanol droplets size distribution at phase 180°, pressure 20 psi, forcing frequency 37.87 Hz and 50% duty cycle.

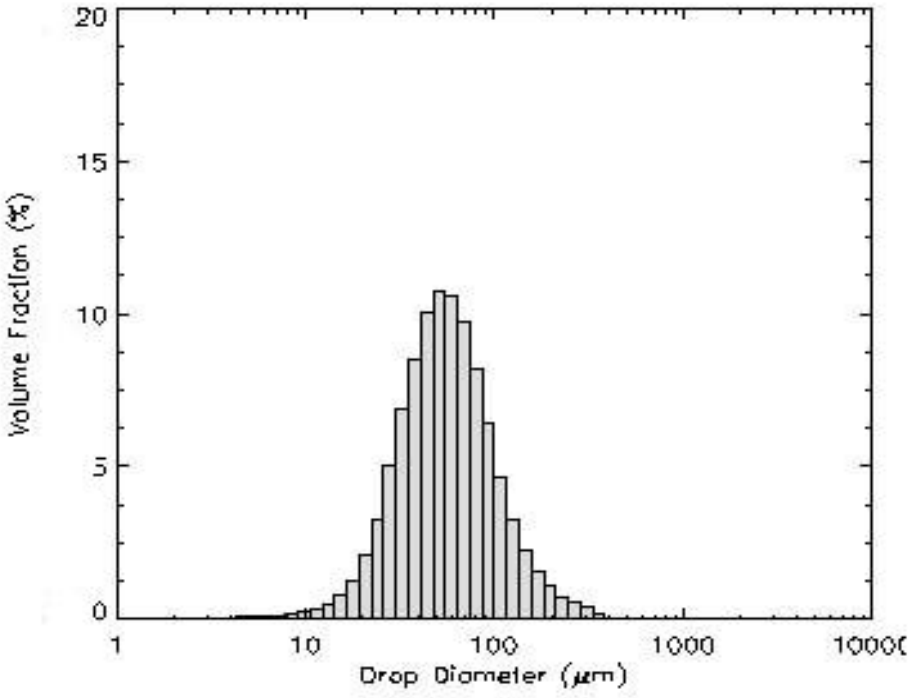

Fig. B1.6: Ethanol droplets size distribution at phase 225°, pressure 20 psi, forcing frequency 37.87 Hz and 50% duty cycle.

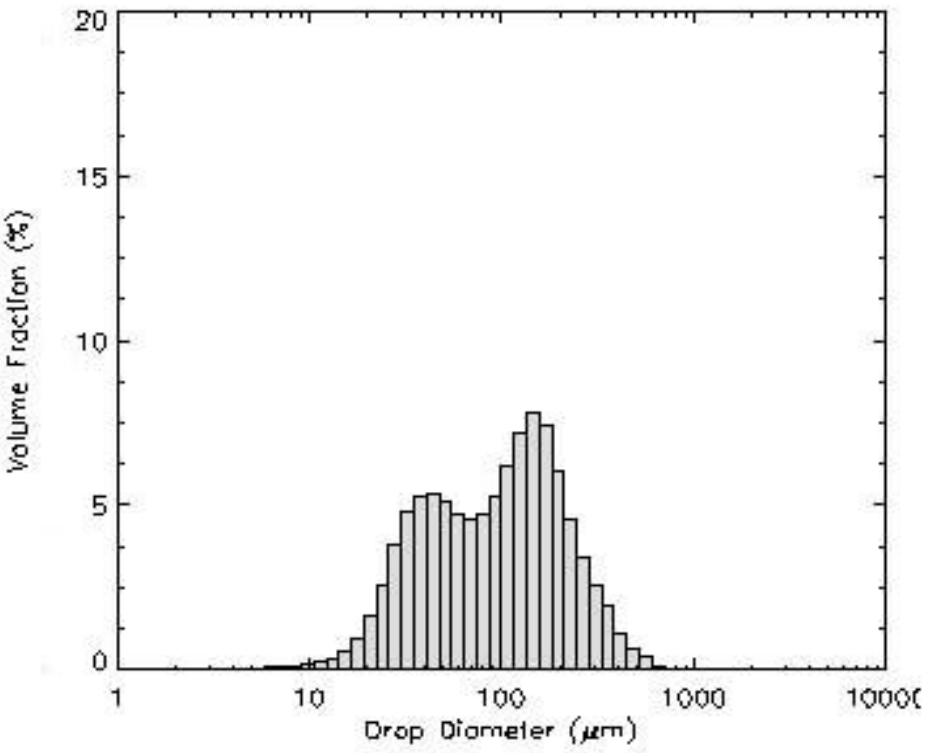

Fig. B1.7: Ethanol droplets size distribution at phase 270^{o}, pressure 20 psi, forcing frequency 37.87 Hz and 50% duty cycle.

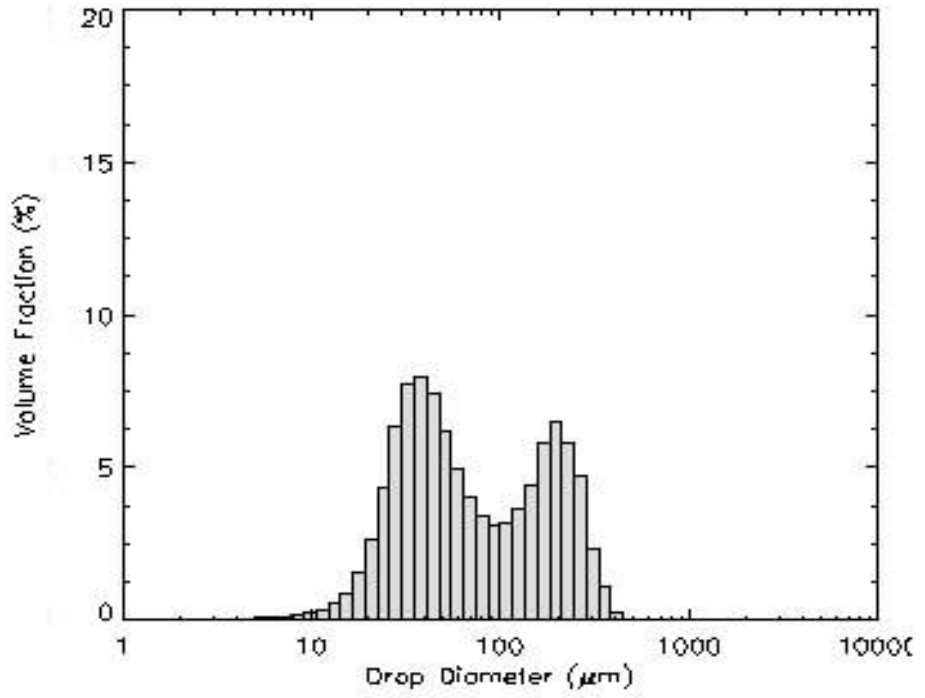

Fig. B1.8: Ethanol droplets size distribution at phase 315^{o}, pressure 20 psi, forcing frequency 37.87 Hz and 50% duty cycle.

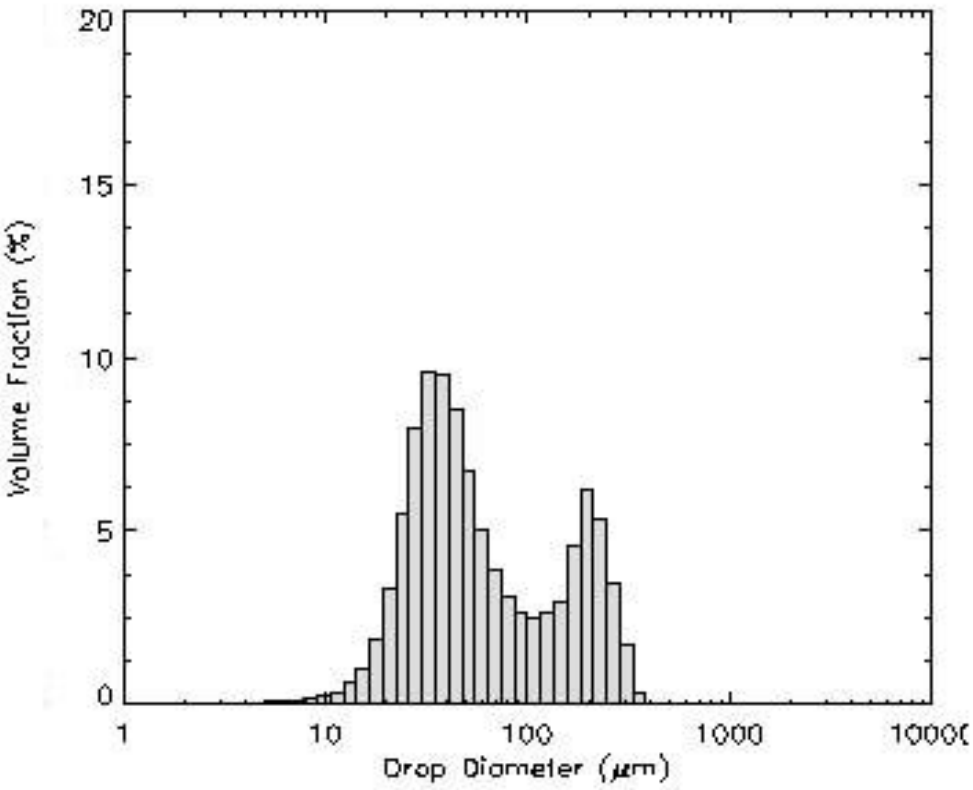

Fig. B1.9: Ethanol droplets size distribution at phase 360^{o}, pressure 20 psi, forcing frequency 37.87 Hz and 50% duty cycle.

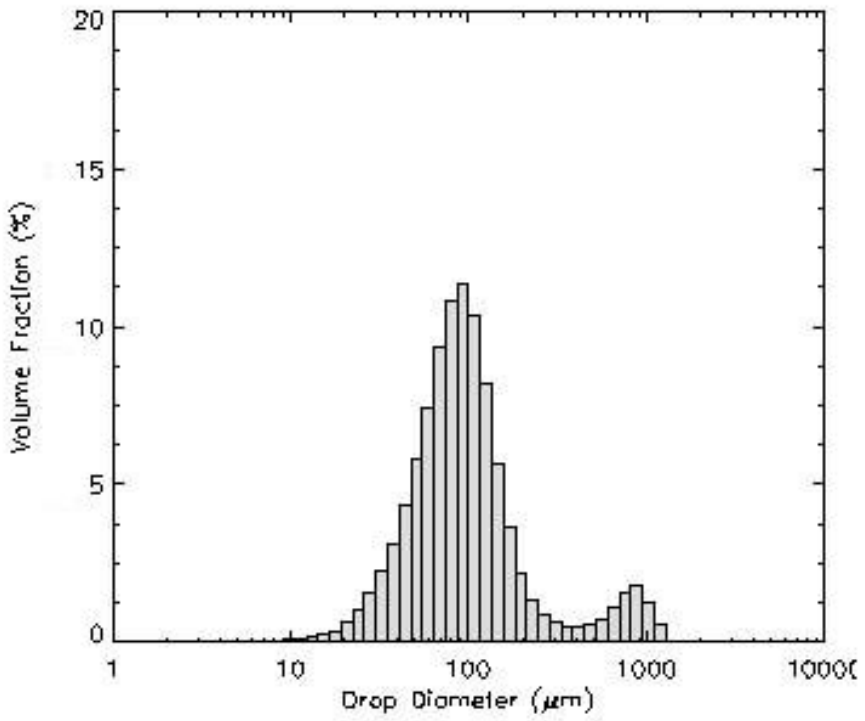

Fig. B2.1: Ethanol droplets size distribution at phase 0^{o}, pressure 20 psi, forcing frequency 125 Hz and 50% duty cycle.

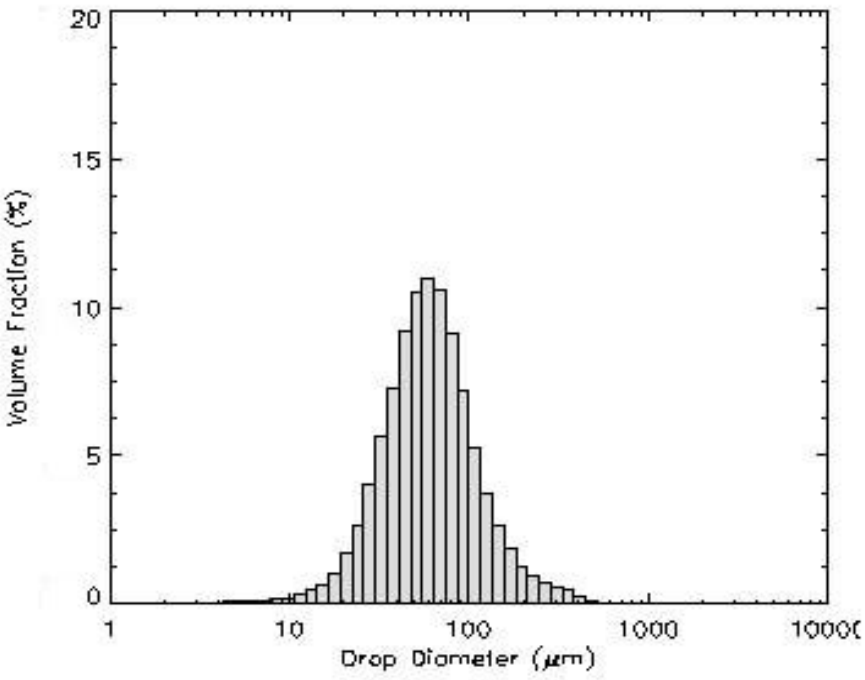

Fig. B2.2: Ethanol droplets size distribution at phase 45^{o}, pressure 20 psi, forcing frequency 125 Hz and 50% duty cycle.

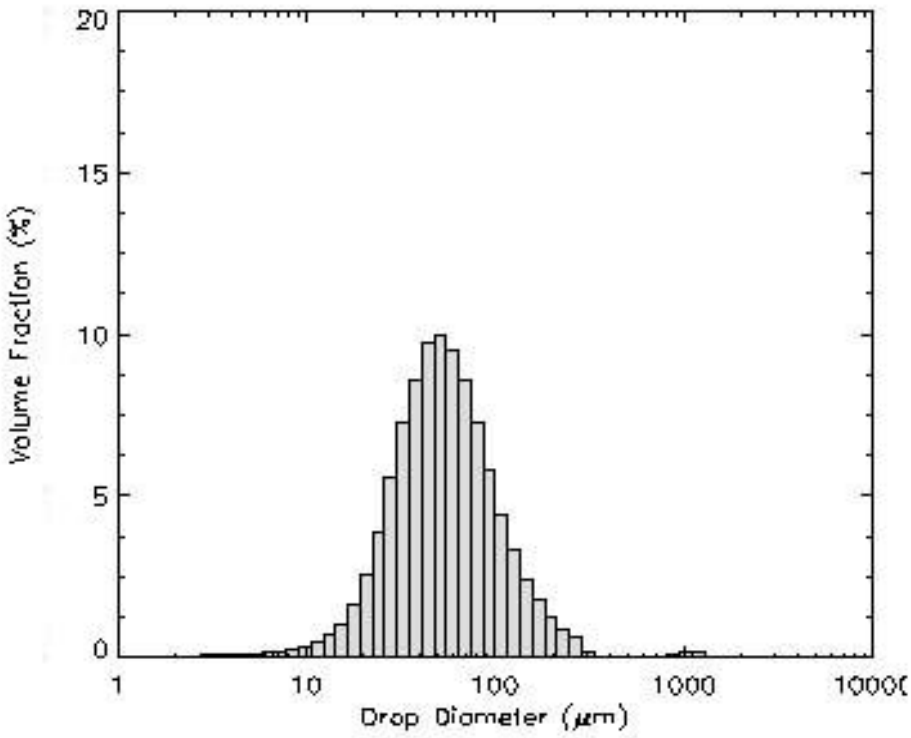

Fig. B2.3: Ethanol droplets size distribution at phase 90^{o}, pressure 20 psi, forcing frequency 125 Hz and 50% duty cycle.

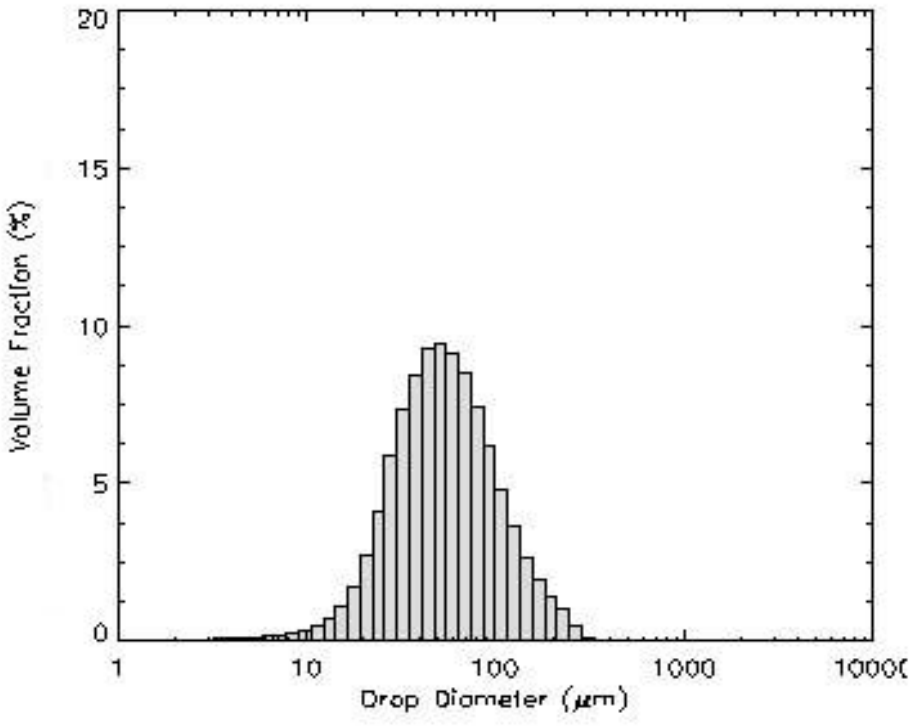

Fig. B2.4: Ethanol droplets size distribution at phase 135^{o}, pressure 20 psi, forcing frequency 125 Hz and 50% duty cycle.

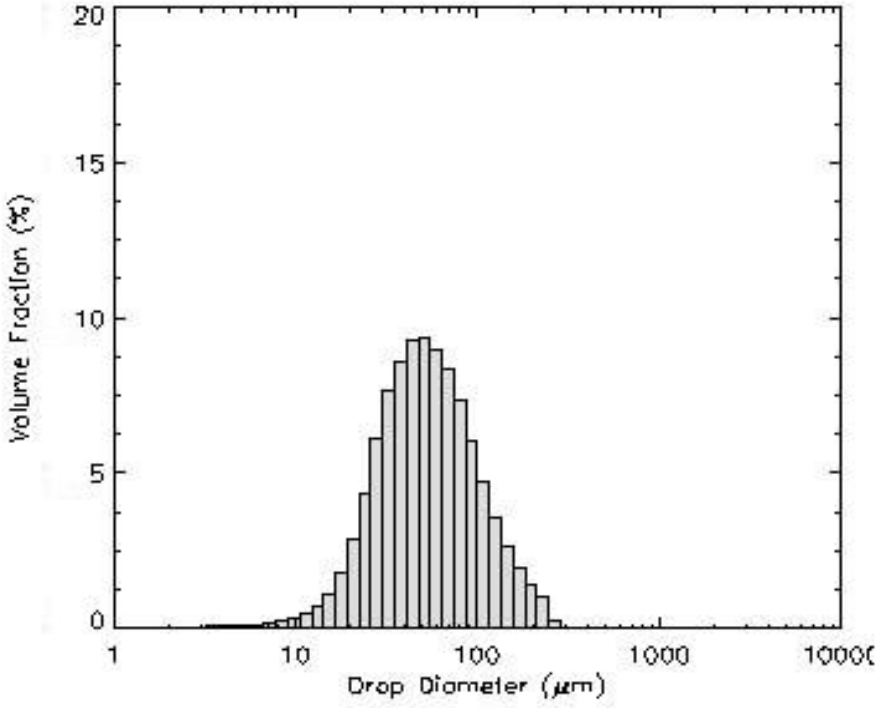

Fig. B2.5: Ethanol droplets size distribution at phase 180°, pressure 20 psi, forcing frequency 125 Hz and 50% duty cycle.

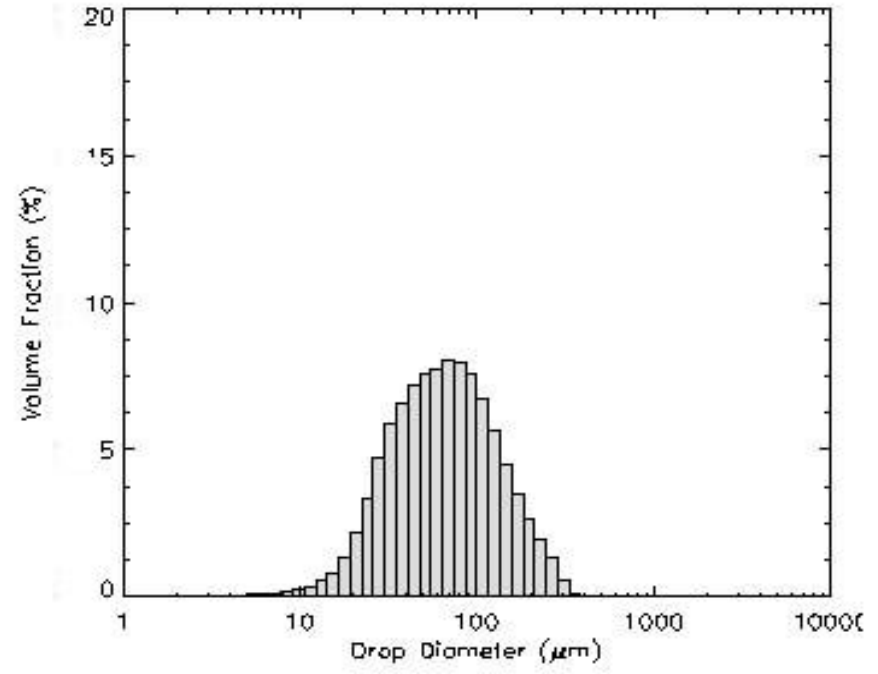

Fig. B2.6: Ethanol droplets size distribution at phase 225°, pressure 20 psi, forcing frequency 125 Hz and 50% duty cycle.

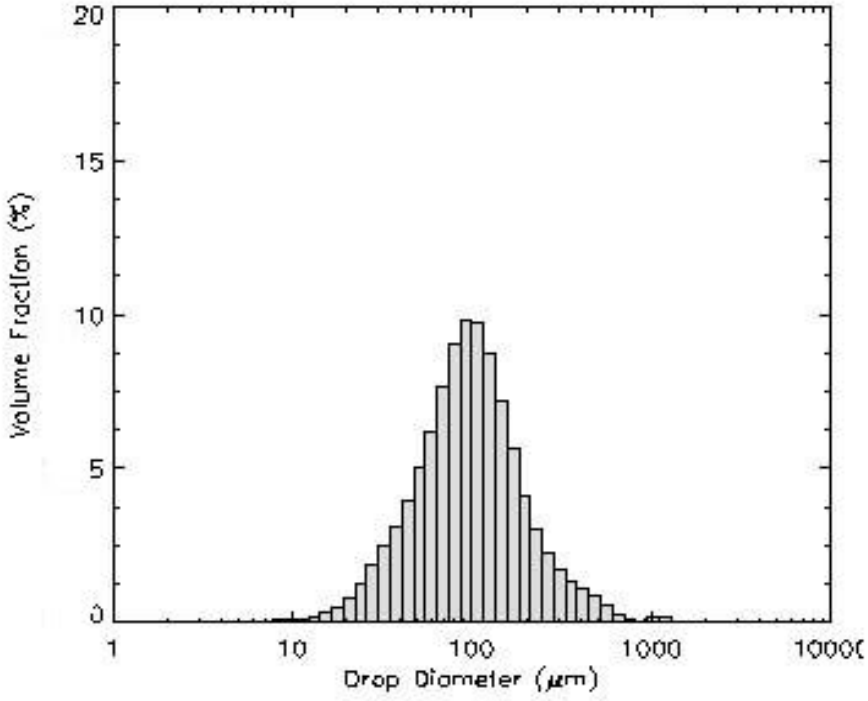

Fig. B2.7: Ethanol droplets size distribution at phase 270^{o}, pressure 20 psi, forcing frequency 125 Hz and 50% duty cycle.

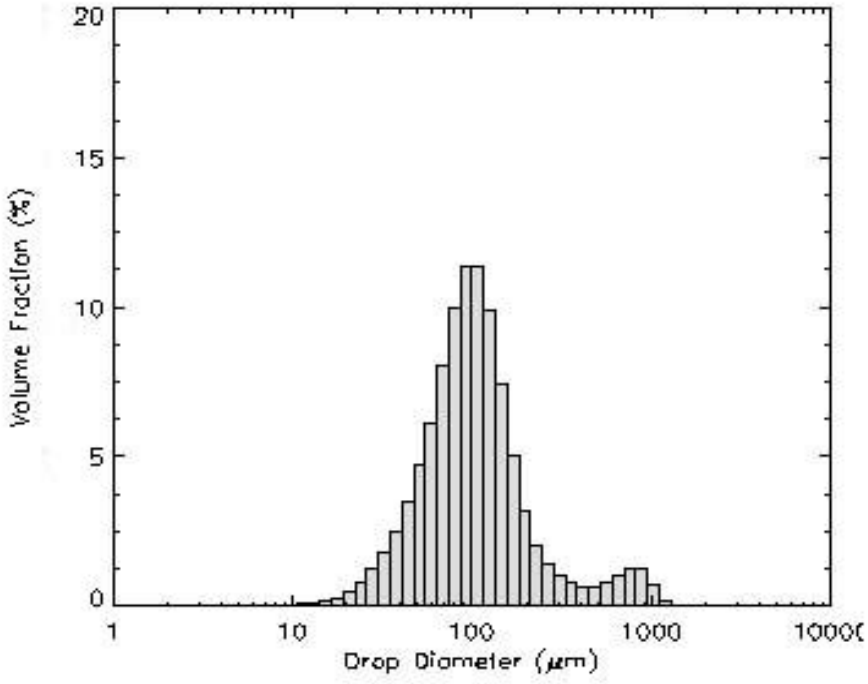

Fig. B2.8: Ethanol droplets size distribution at phase 315^{o}, pressure 20 psi, forcing frequency 125 Hz and 50% duty cycle.

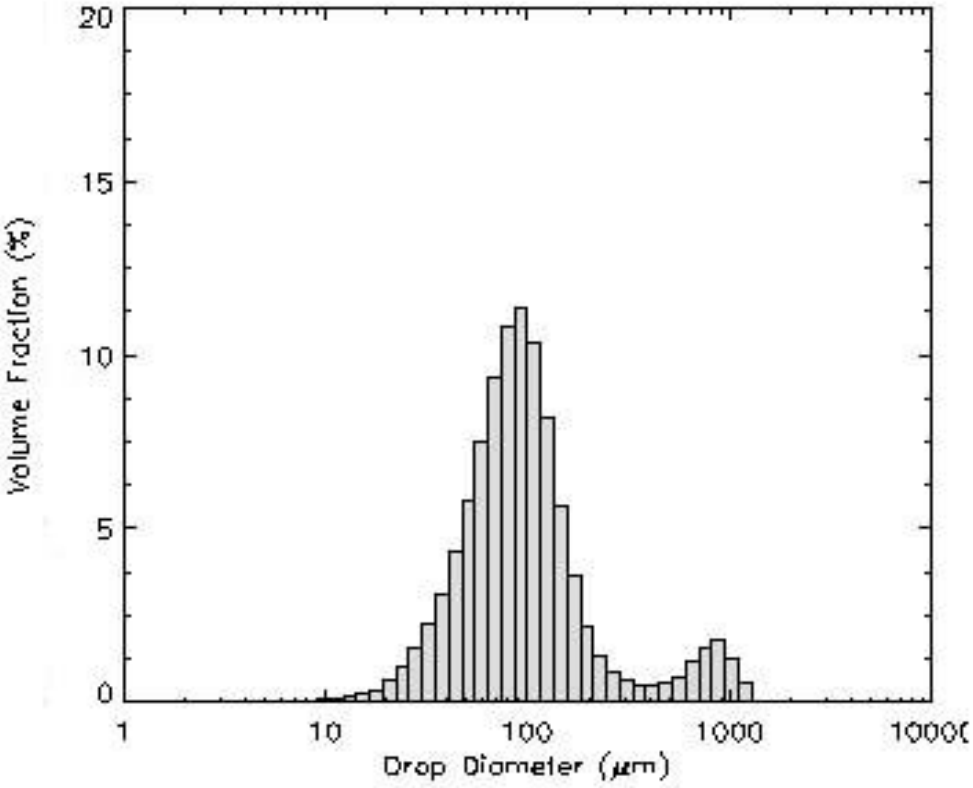

Fig. B2.9: Ethanol droplets size distribution at phase 360^{o}, pressure 20 psi, forcing frequency 125 Hz and 50% duty cycle.

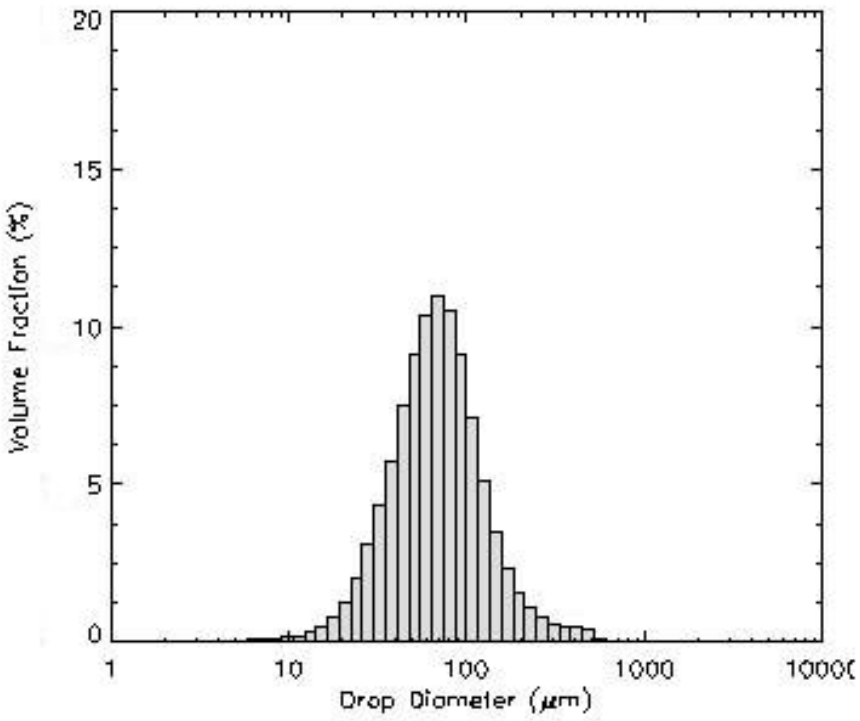

Fig. B3.1: Ethanol droplets size distribution at phase 0^{o}, pressure 20 psi, forcing frequency 312.5 Hz and 50% duty cycle.

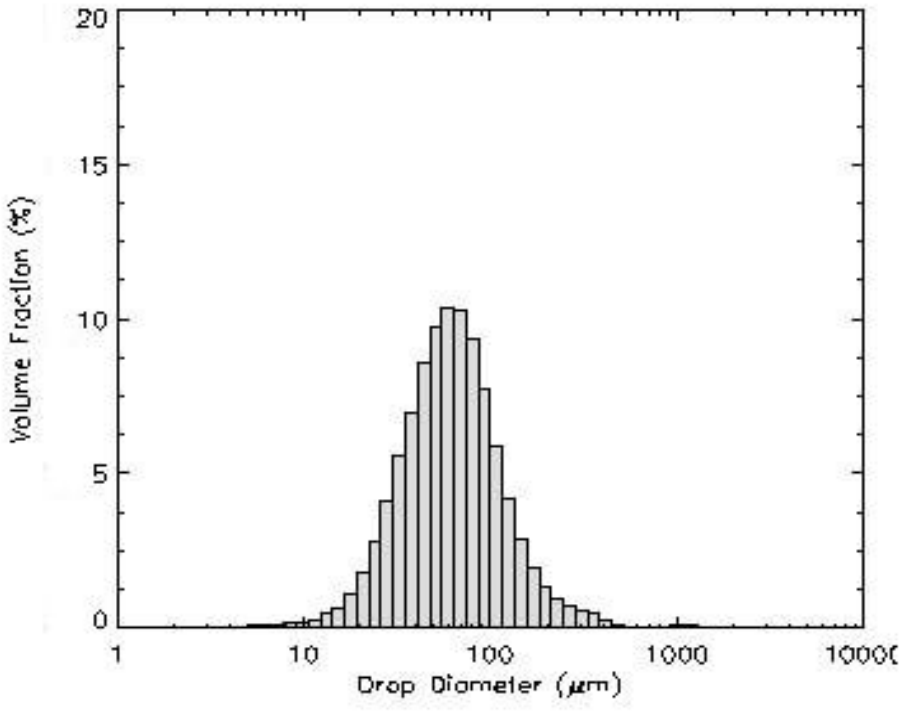

Fig. B3.2: Ethanol droplets size distribution at phase 45^{o}, pressure 20 psi, forcing frequency 312.5 Hz and 50% duty cycle.

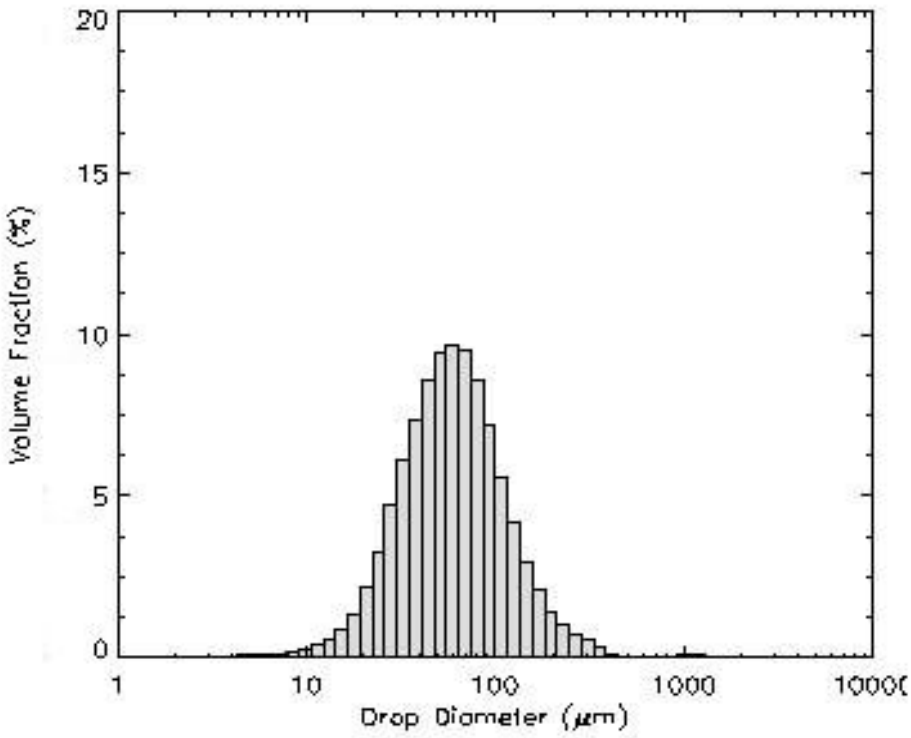

Fig. B3.3: Ethanol droplets size distribution at phase 90^{o}, pressure 20 psi, forcing frequency 312.5 Hz and 50% duty cycle.

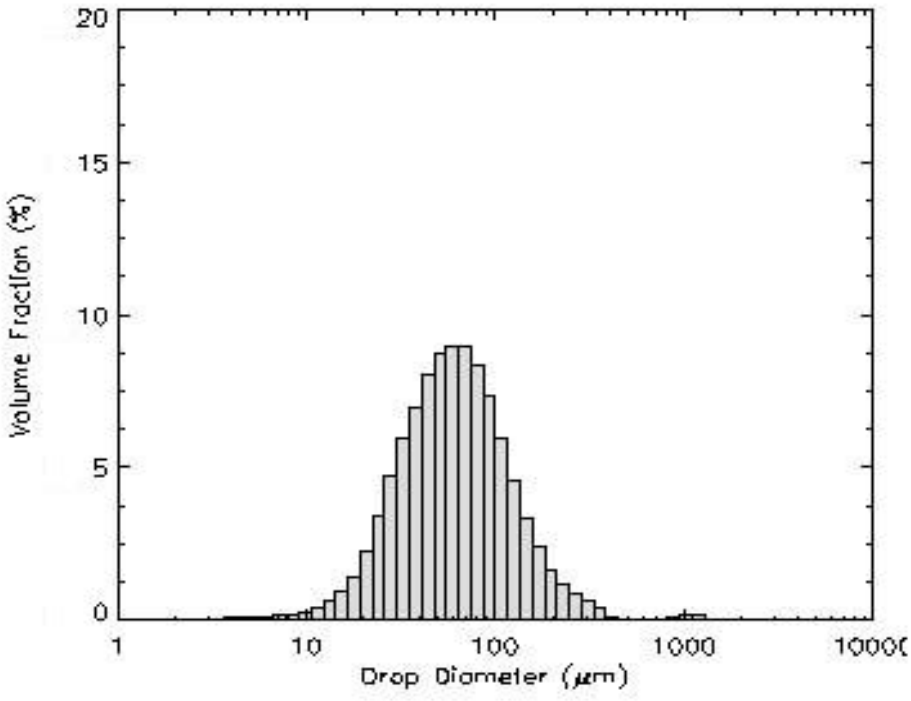

Fig. B3.4: Ethanol droplets size distribution at phase 135^{o}, pressure 20 psi, forcing frequency 312.5 Hz and 50% duty cycle.

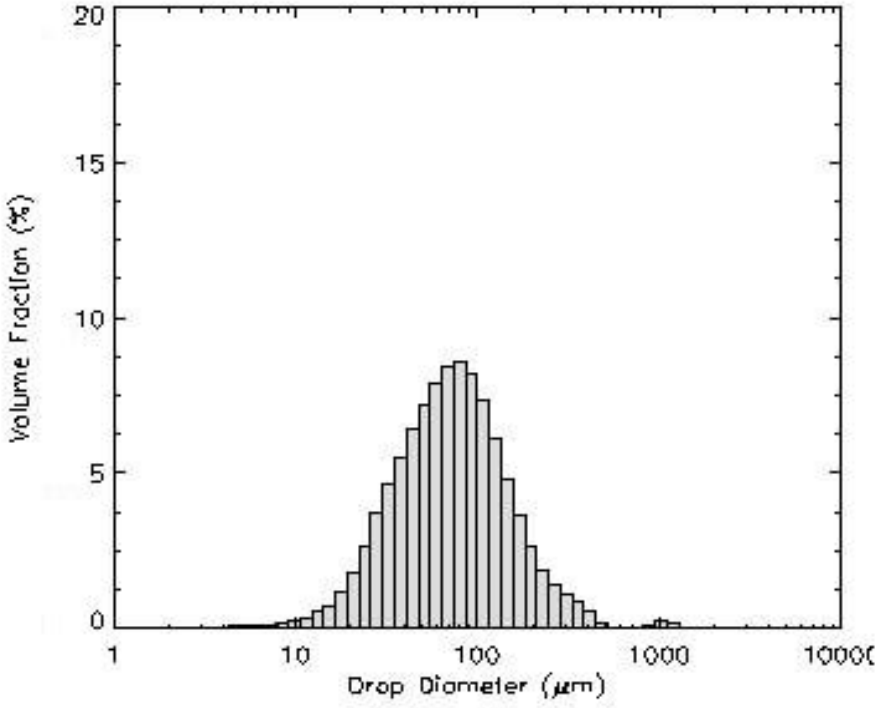

Fig. B3.5: Ethanol droplets size distribution at phase 180°, pressure 20 psi, forcing frequency 312.5 Hz and 50% duty cycle.

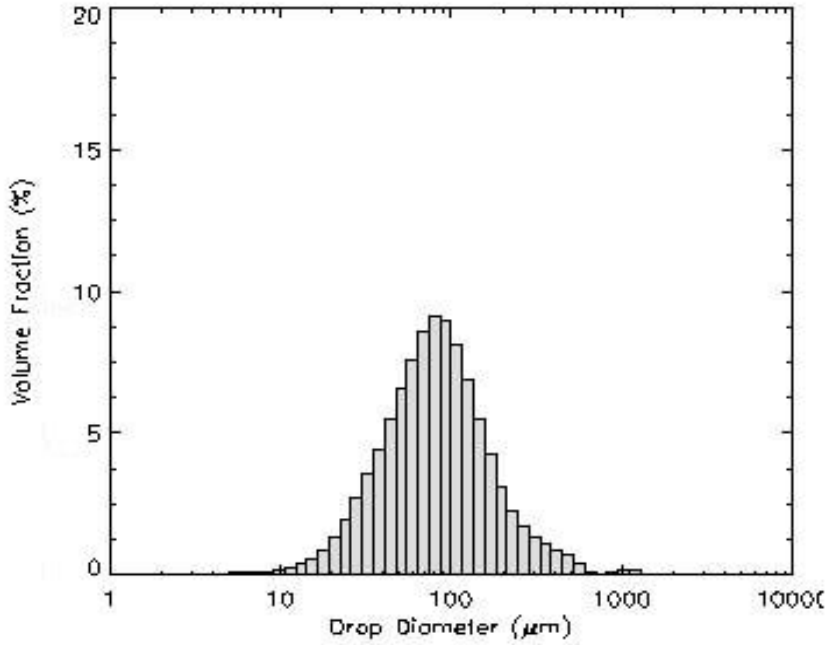

Fig. B3.6: Ethanol droplets size distribution at phase 225°, pressure 20 psi, forcing frequency 312.5 Hz and 50% duty cycle.

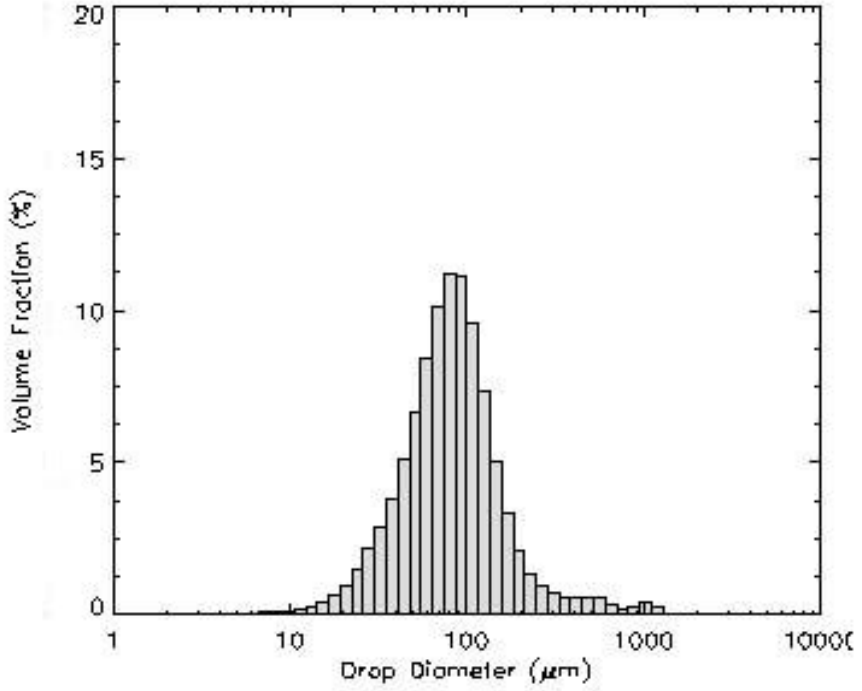

Fig. B3.7: Ethanol droplets size distribution at phase 270°, pressure 20 psi, forcing frequency 312.5 Hz and 50% duty cycle.

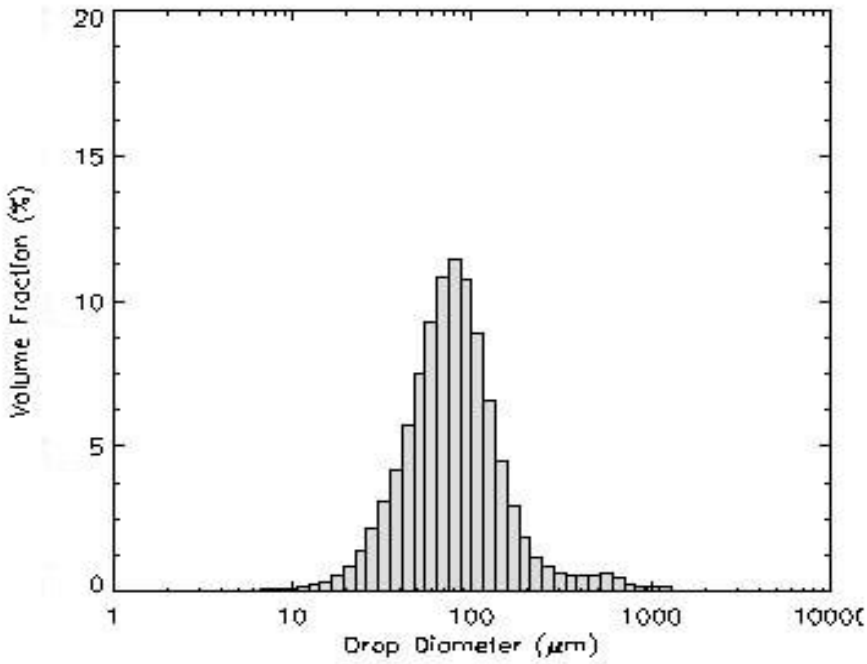

Fig. B3.8: Ethanol droplets size distribution at phase 315°, pressure 20 psi, forcing frequency 312.5 Hz and 50% duty cycle.

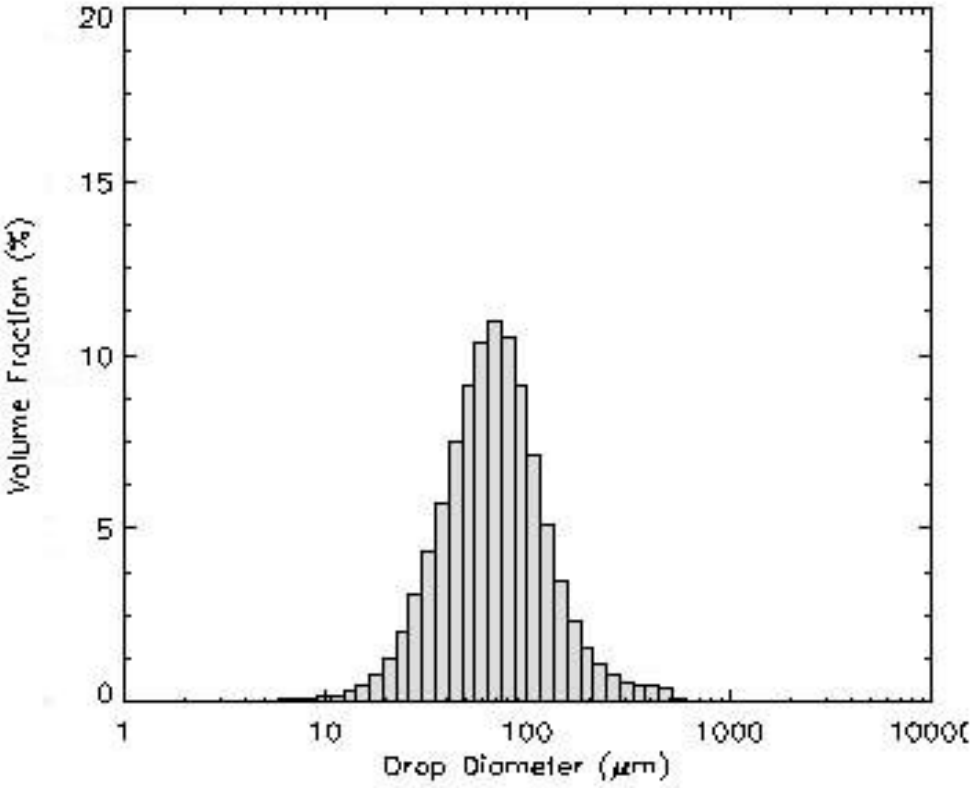

Fig. B3.9: Ethanol droplets size distribution at phase 360^{o}, pressure 20 psi, forcing frequency 312.5 Hz and 50% duty cycle.

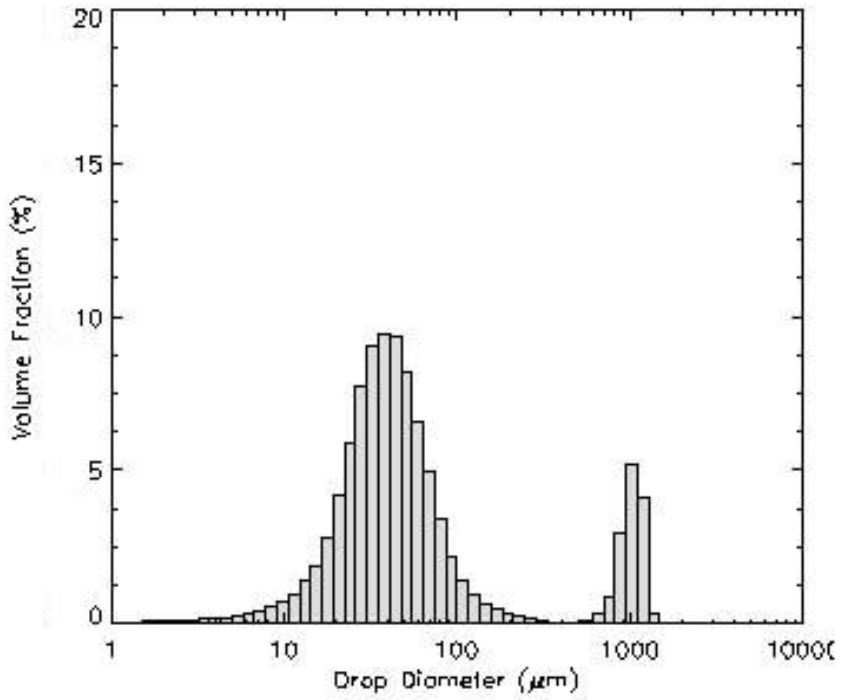

Fig. B4.1: Ethanol droplets size distribution at phase 0^{o}, pressure 60 psi, forcing frequency 37.87 Hz and 50% duty cycle.

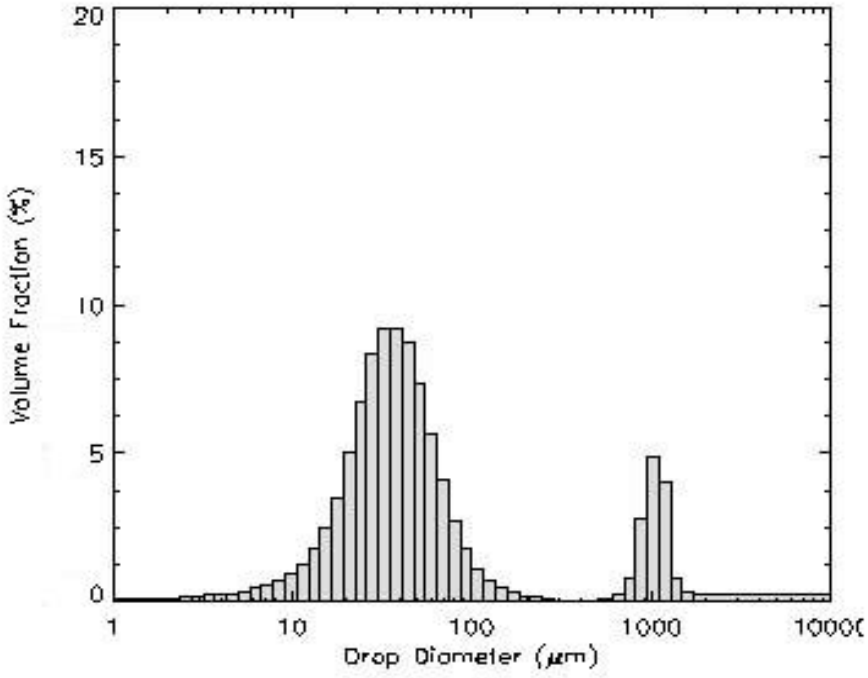

Fig. B4.2: Ethanol droplets size distribution at phase 45^{o}, pressure 60 psi, forcing frequency 37.87 Hz and 50% duty cycle.

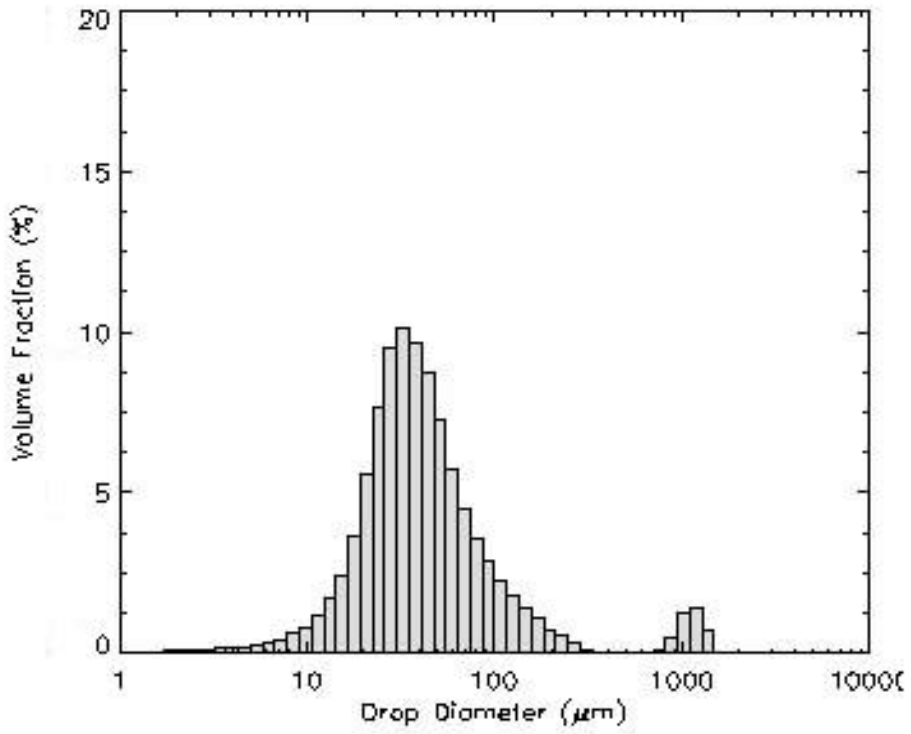

Fig. B4.3: Ethanol droplets size distribution at phase 90°, pressure 60 psi, forcing frequency 37.87 Hz and 50% duty cycle.

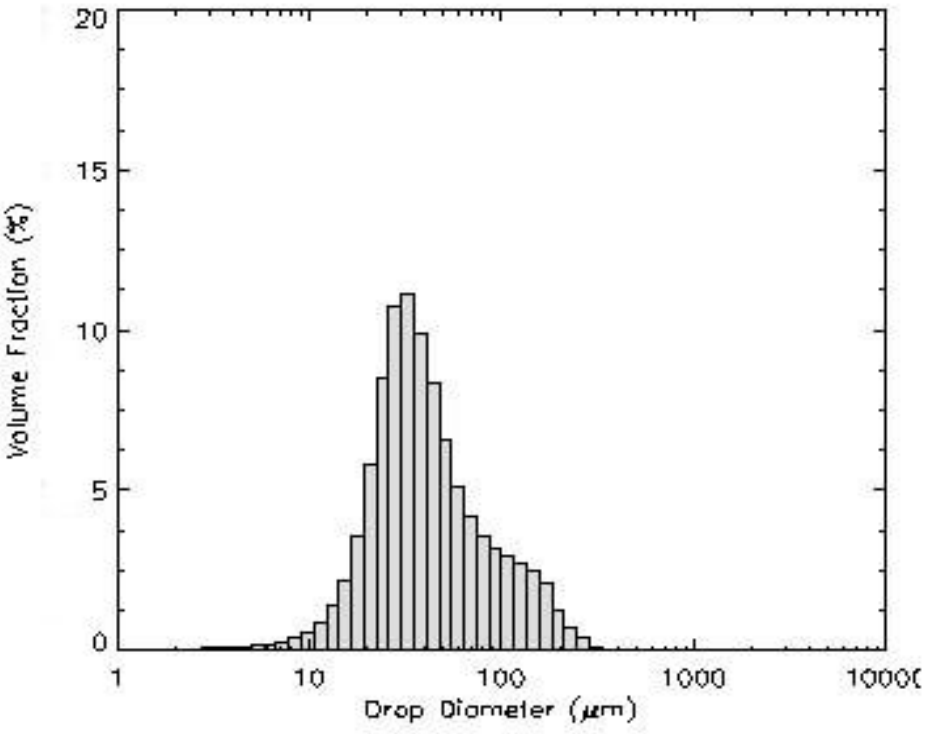

Fig. B4.4: Ethanol droplets size distribution at phase 135°, pressure 60 psi, forcing frequency 37.87 Hz and 50% duty cycle.

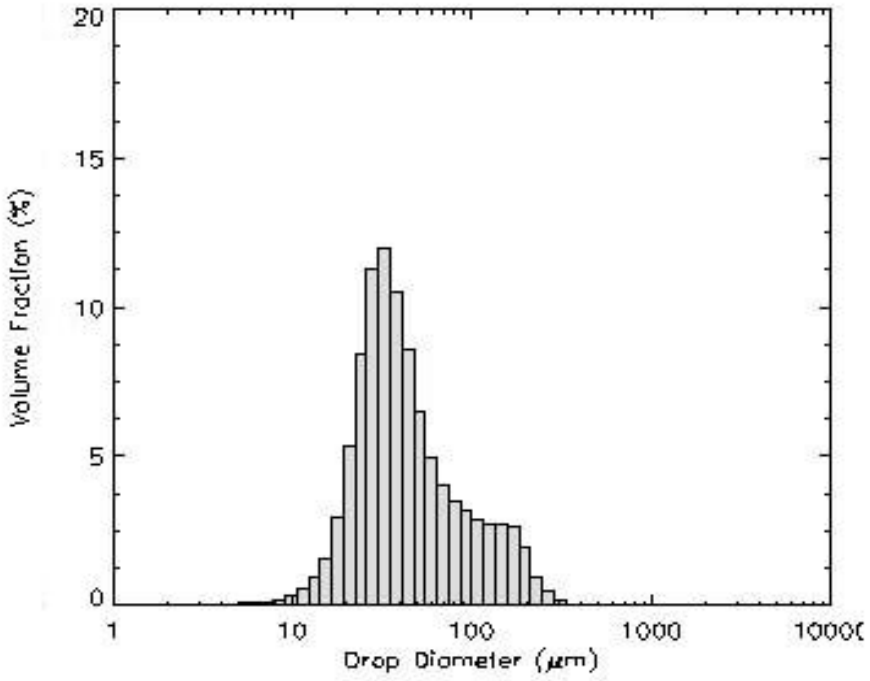

Fig. B4.5: Ethanol droplets size distribution at phase 180°, pressure 60 psi, forcing frequency 37.87 Hz and 50% duty cycle.

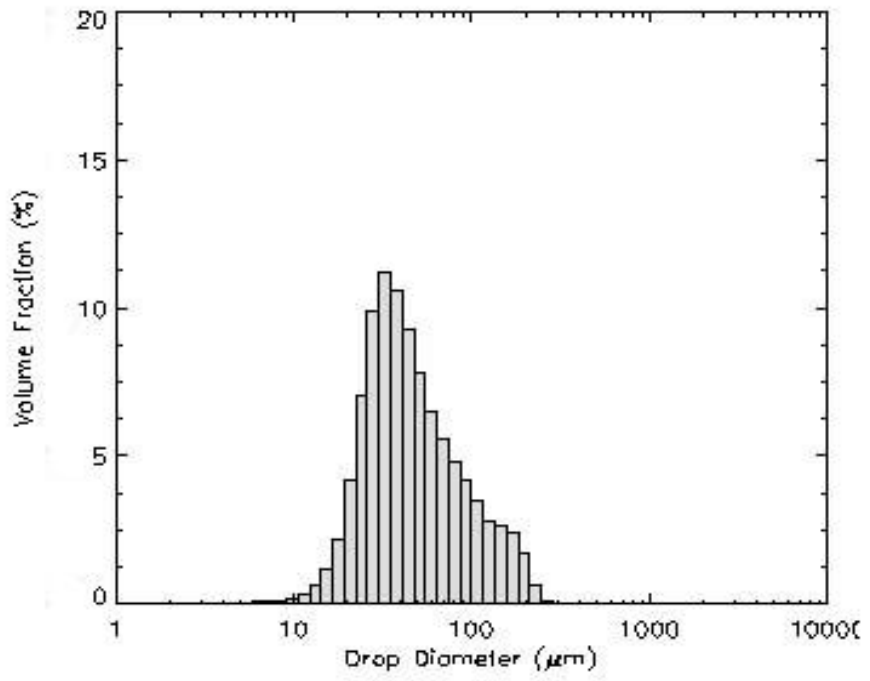

Fig. B4.6: Ethanol droplets size distribution at phase 225°, pressure 60 psi, forcing frequency 37.87 Hz and 50% duty cycle.

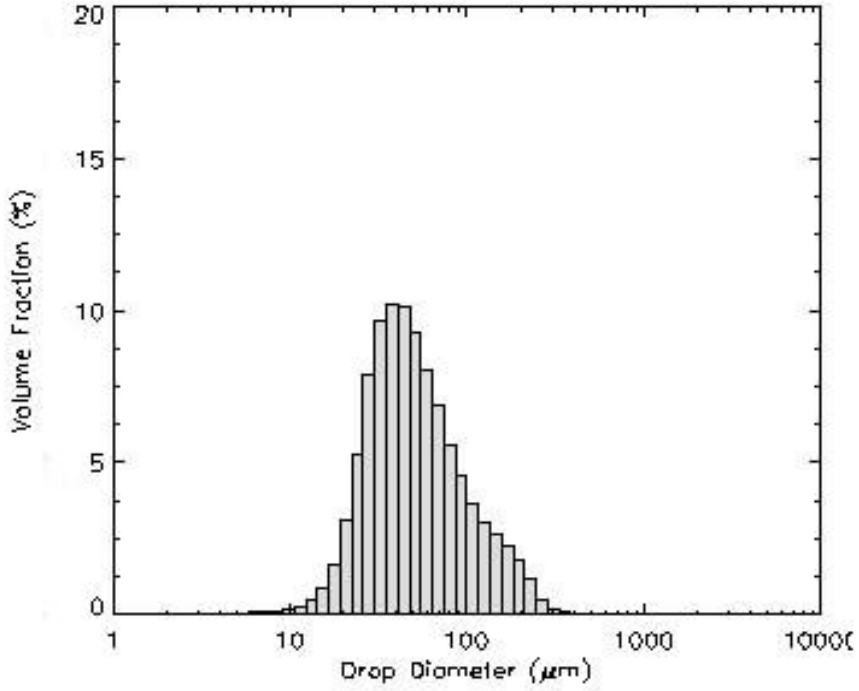

Fig. B4.7: Ethanol droplets size distribution at phase 270^{o}, pressure 60 psi, forcing frequency 37.87 Hz and 50% duty cycle.

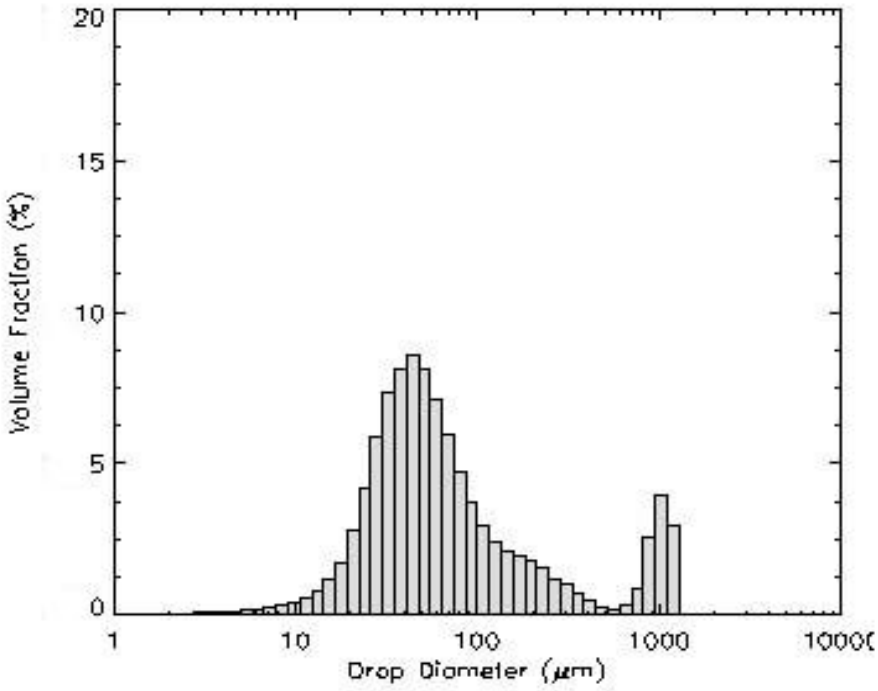

Fig. B4.8: Ethanol droplets size distribution at phase 315^{o}, pressure 60 psi, forcing frequency 37.87 Hz and 50% duty cycle.

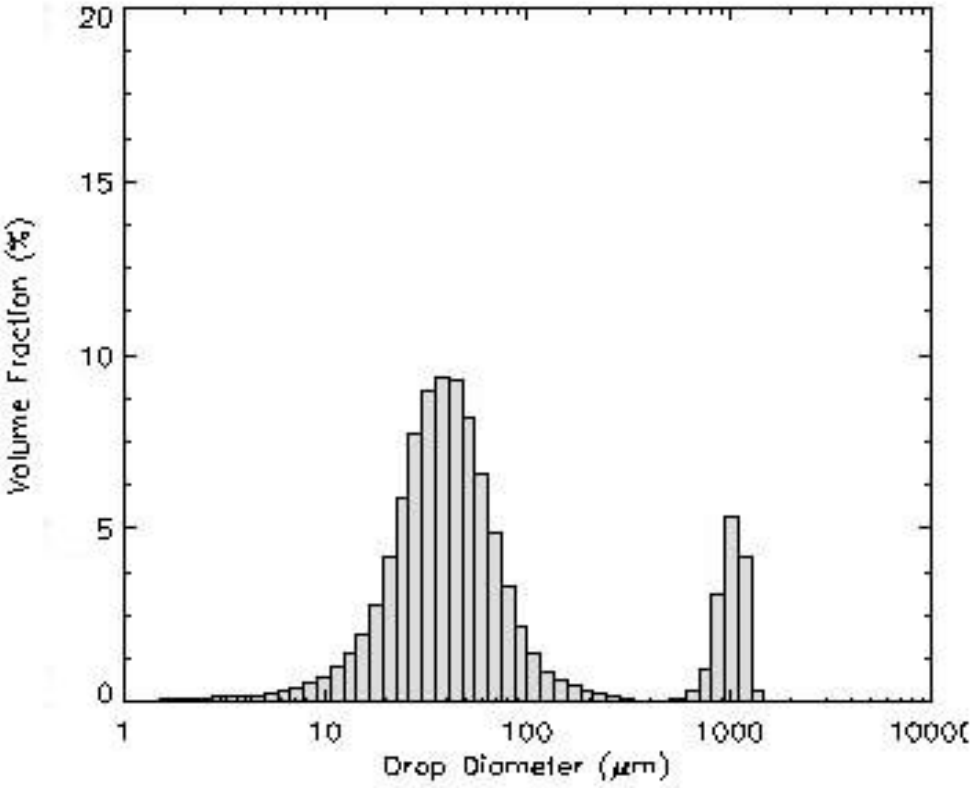

Fig. B4.9: Ethanol droplets size distribution at phase 360^{o}, pressure 60 psi, forcing frequency 37.87 Hz and 50% duty cycle.

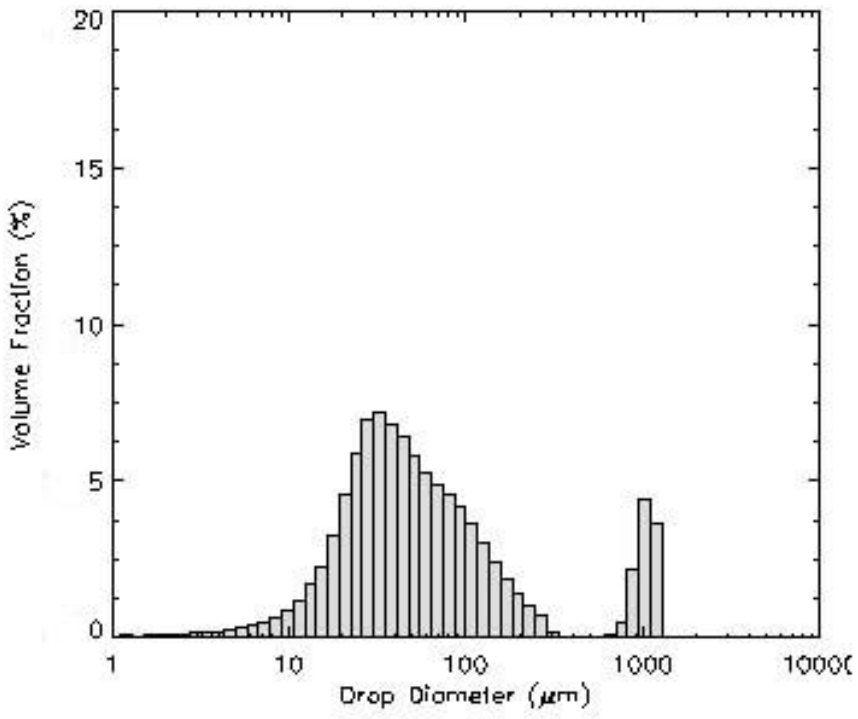

Fig. B5.1: Ethanol droplets size distribution at phase 0^{o}, pressure 60 psi, forcing frequency 125 Hz and 50% duty cycle.

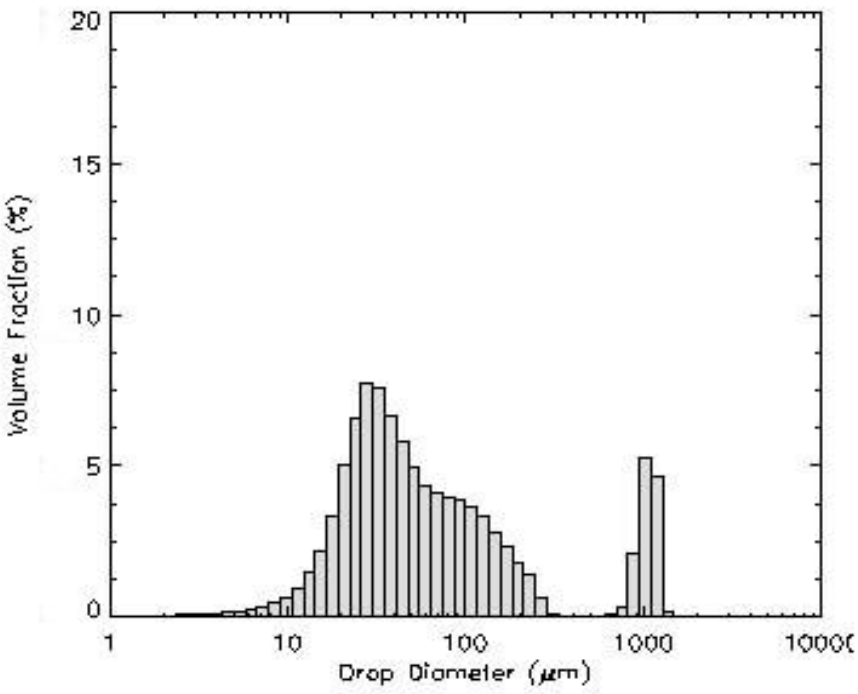

Fig. B5.2: Ethanol droplets size distribution at phase 45^{o}, pressure 60 psi, forcing frequency 125 Hz and 50% duty cycle.

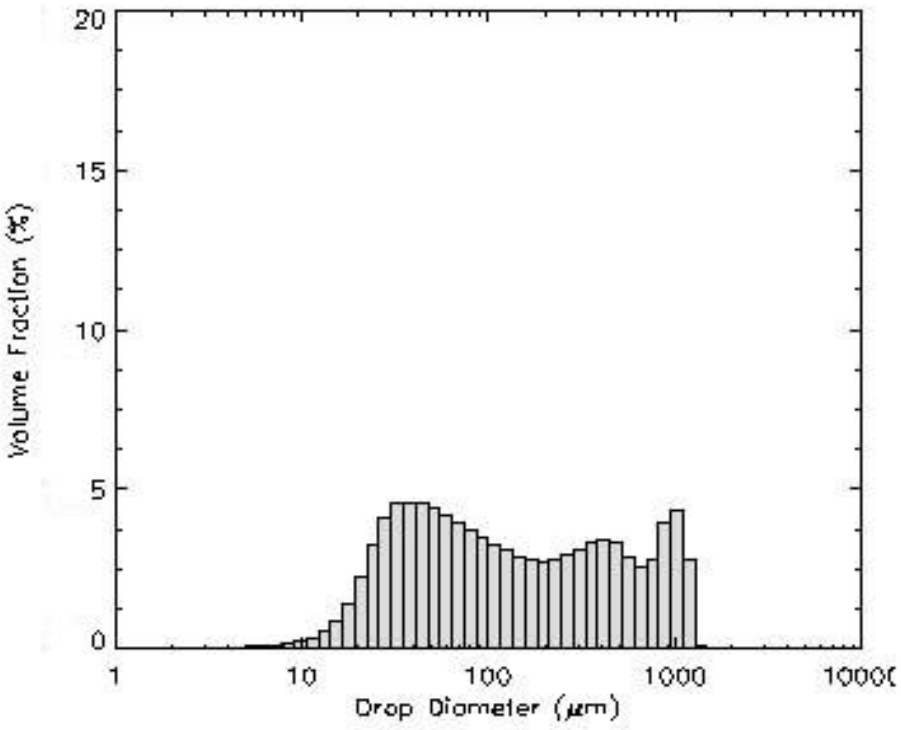

Fig. B5.3: Ethanol droplets size distribution at phase 90°, pressure 60 psi, forcing frequency 125 Hz and 50% duty cycle.

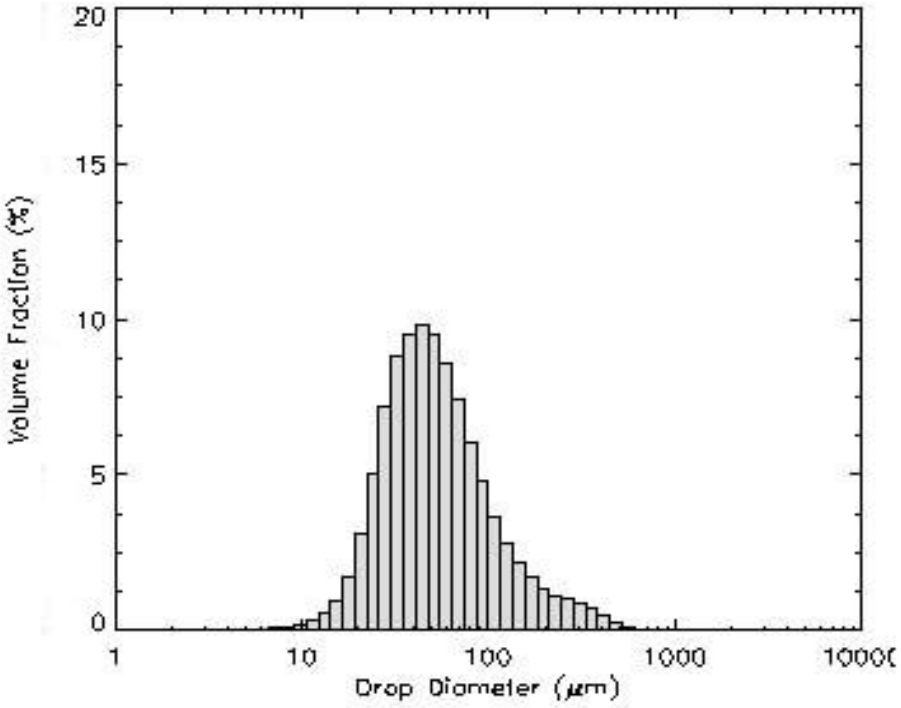

Fig. B5.4: Ethanol droplets size distribution at phase 135°, pressure 60 psi, forcing frequency 125 Hz and 50% duty cycle.

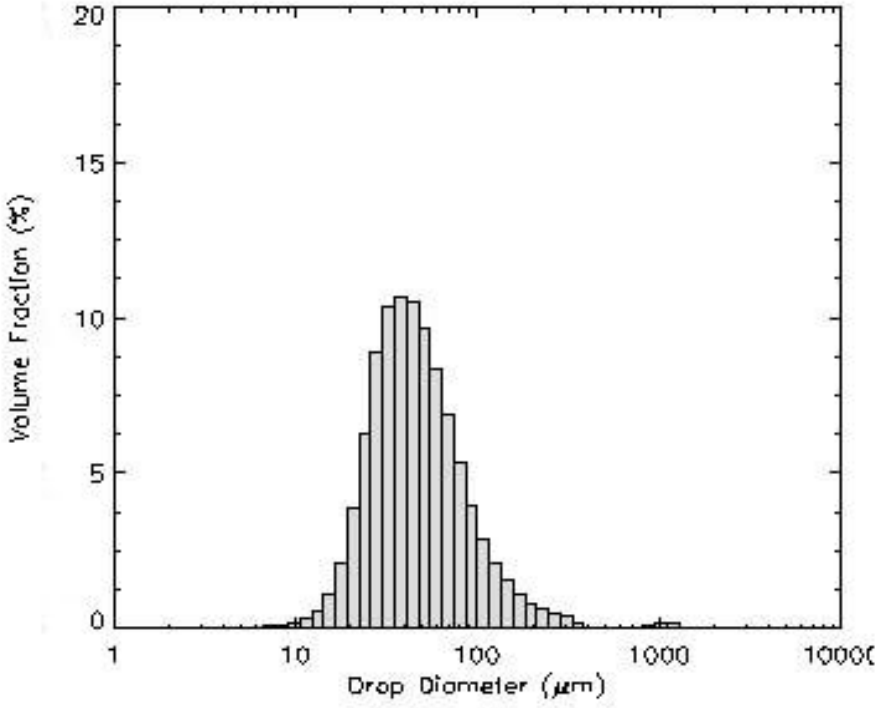

Fig. B5.5: Ethanol droplets size distribution at phase 180^{o}, pressure 60 psi, forcing frequency 125 Hz and 50% duty cycle.

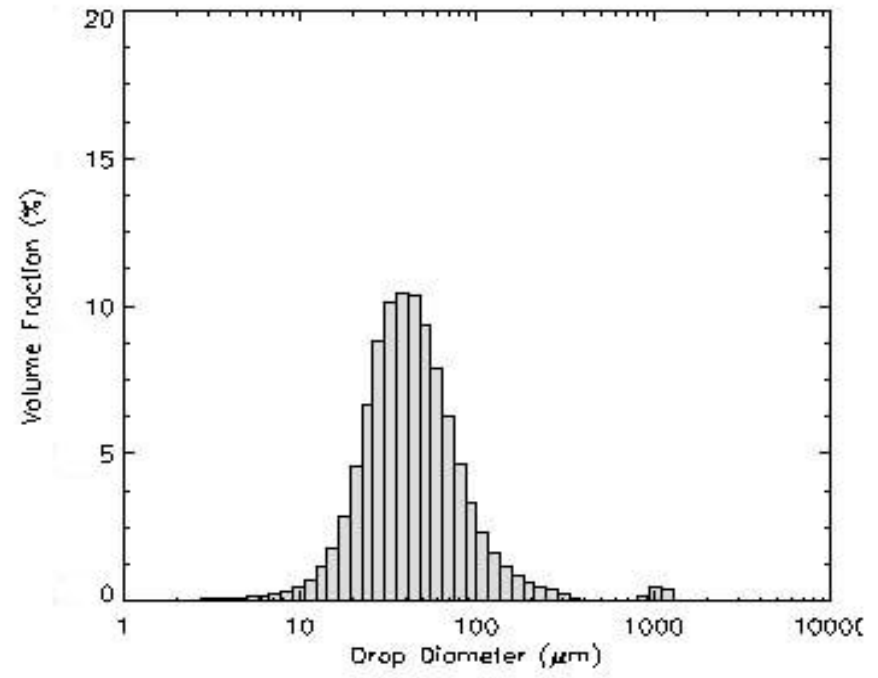

Fig. B5.6: Ethanol droplets size distribution at phase 225^{o}, pressure 60 psi, forcing frequency 125 Hz and 50% duty cycle.

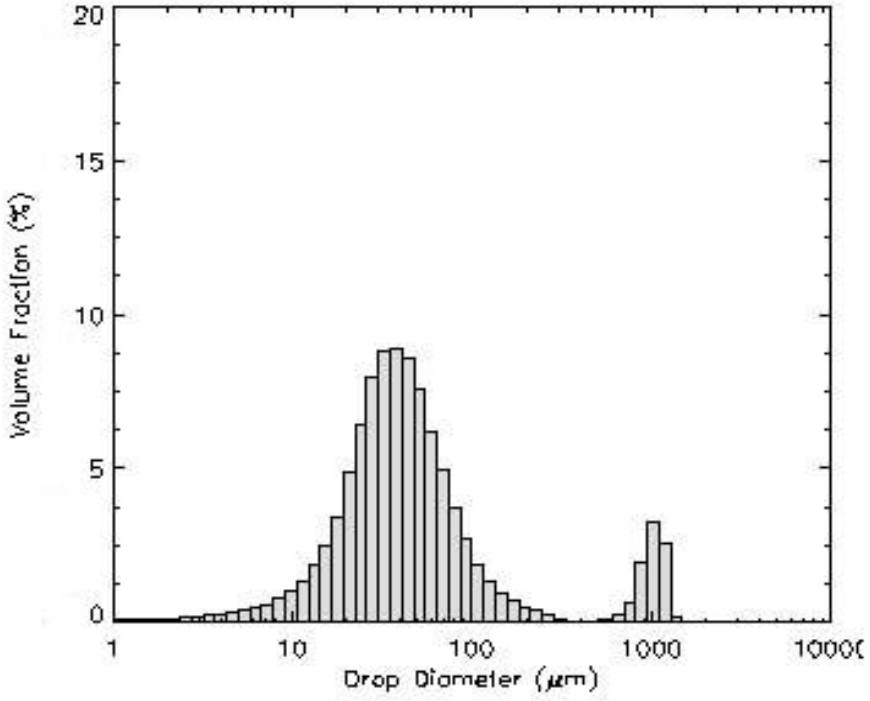

Fig. B5.7: Ethanol droplets size distribution at phase 270°, pressure 60 psi, forcing frequency 125 Hz and 50% duty cycle.

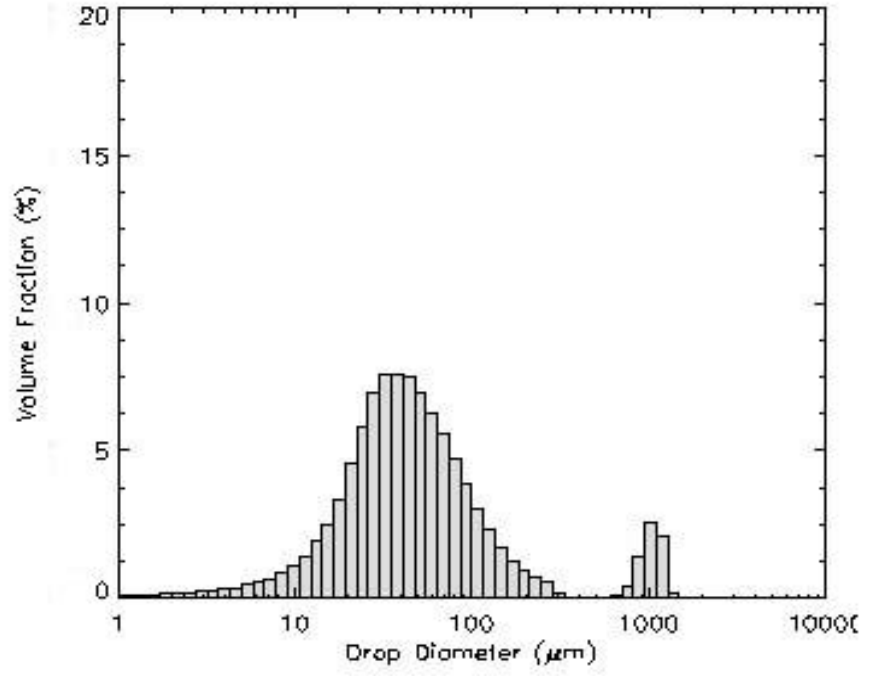

Fig. B5.8: Ethanol droplets size distribution at phase 315°, pressure 60 psi, forcing frequency 125 Hz and 50% duty cycle.

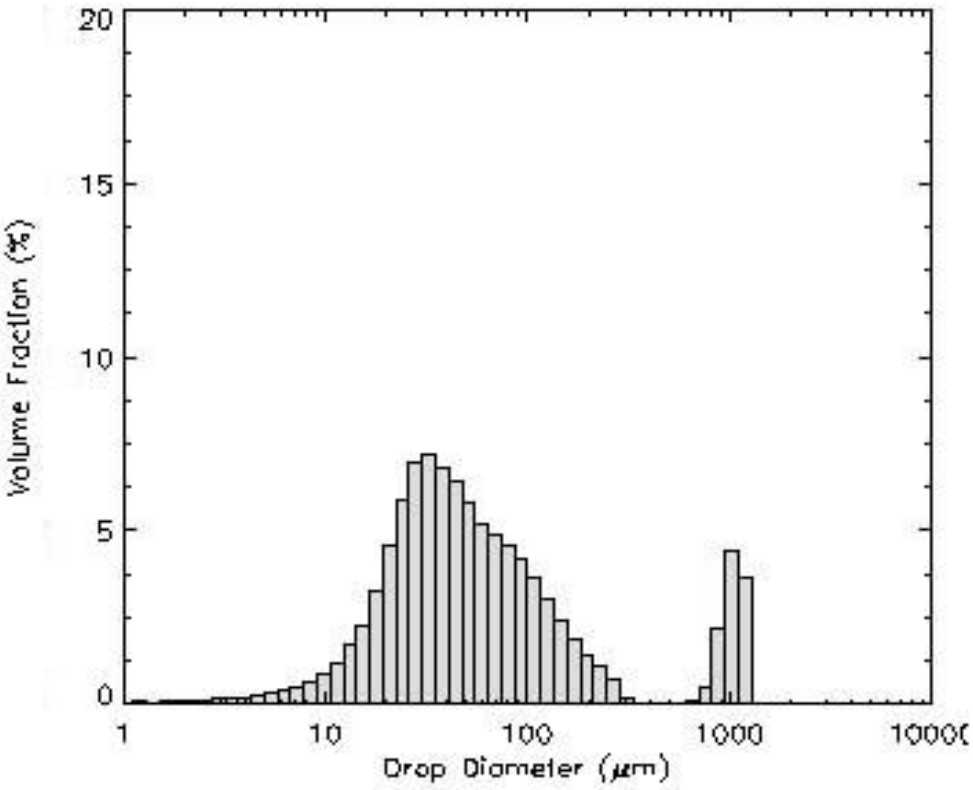

Fig. B5.9: Ethanol droplets size distribution at phase 360^{o}, pressure 60 psi, forcing frequency 125 Hz and 50% duty cycle.

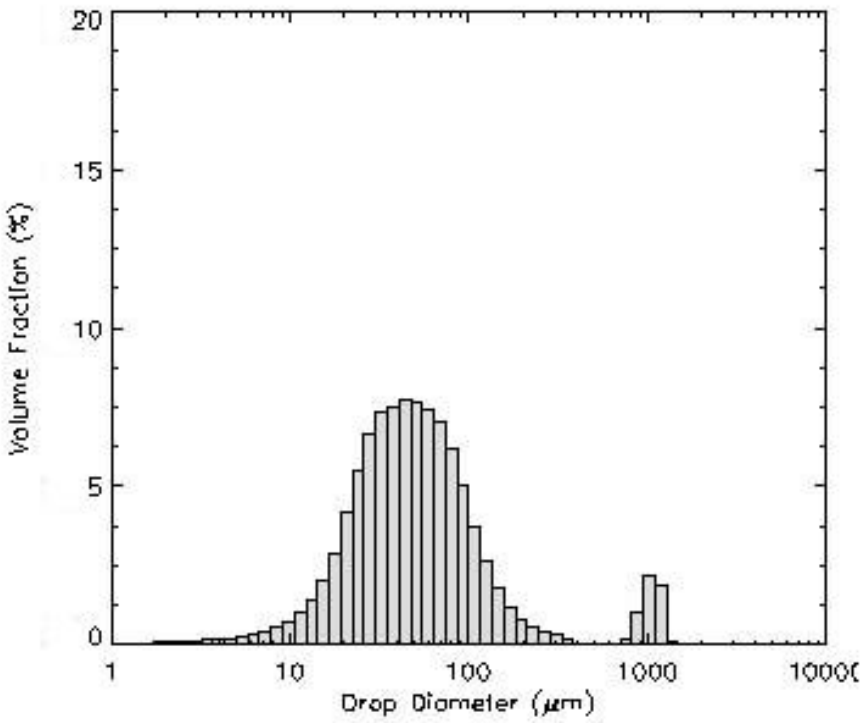

Fig. B6.1: Ethanol droplets size distribution at phase 0^{o}, pressure 60 psi, forcing frequency 312.5 Hz and 50% duty cycle.

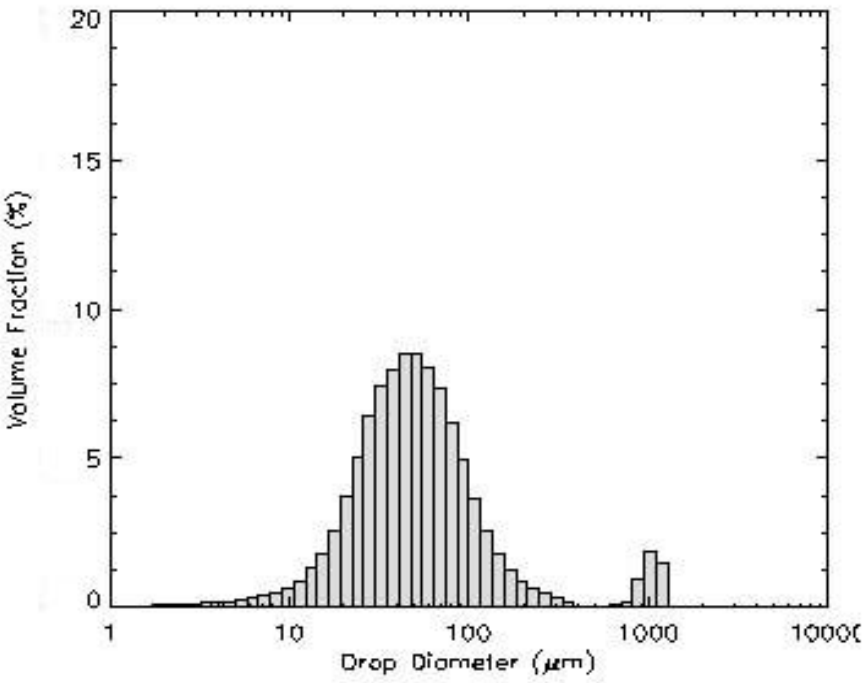

Fig. B6.2: Ethanol droplets size distribution at phase 45^{o}, pressure 60 psi, forcing frequency 312.5 Hz and 50% duty cycle.

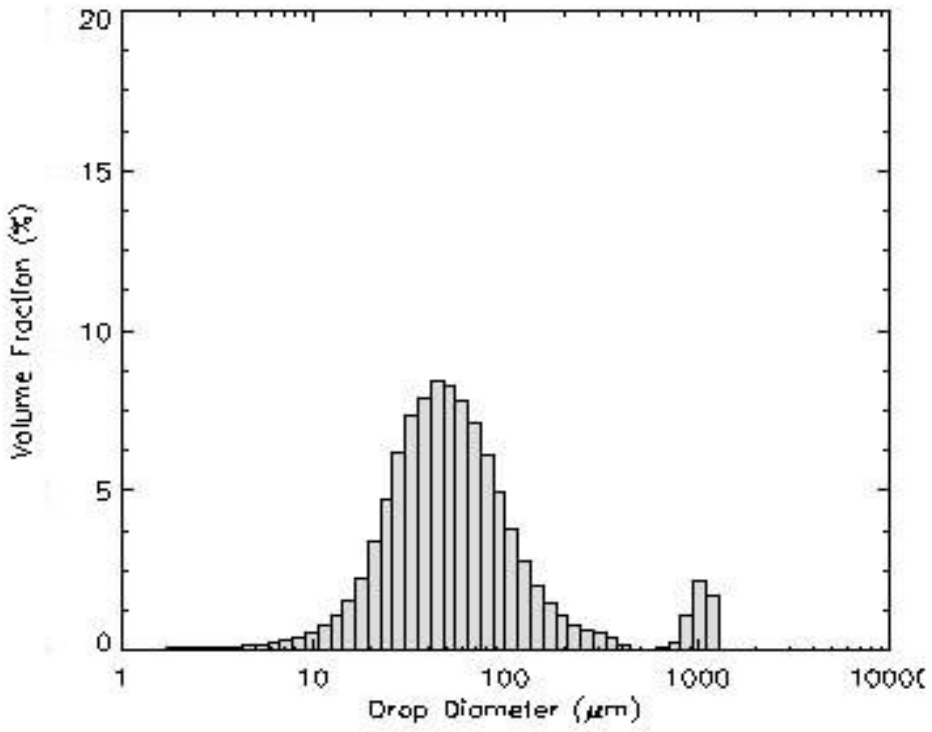

Fig. B6.3: Ethanol droplets size distribution at phase 90^{o}, pressure 60 psi, forcing frequency 312.5 Hz and 50% duty cycle.

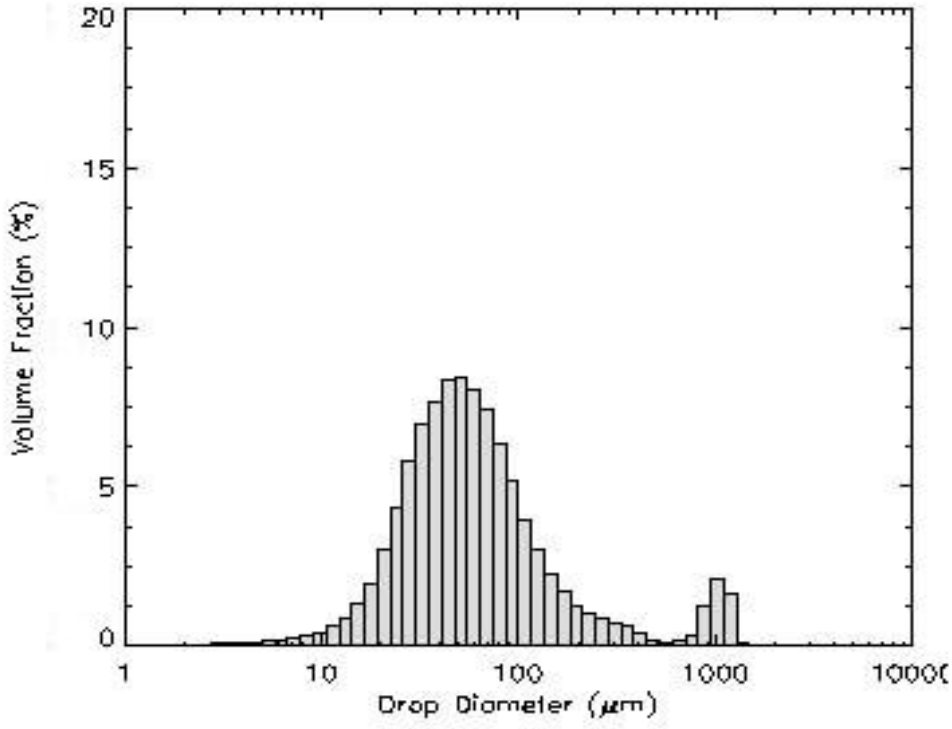

Fig. B6.4: Ethanol droplets size distribution at phase 135^{o}, pressure 60 psi, forcing frequency 312.5 Hz and 50% duty cycle.

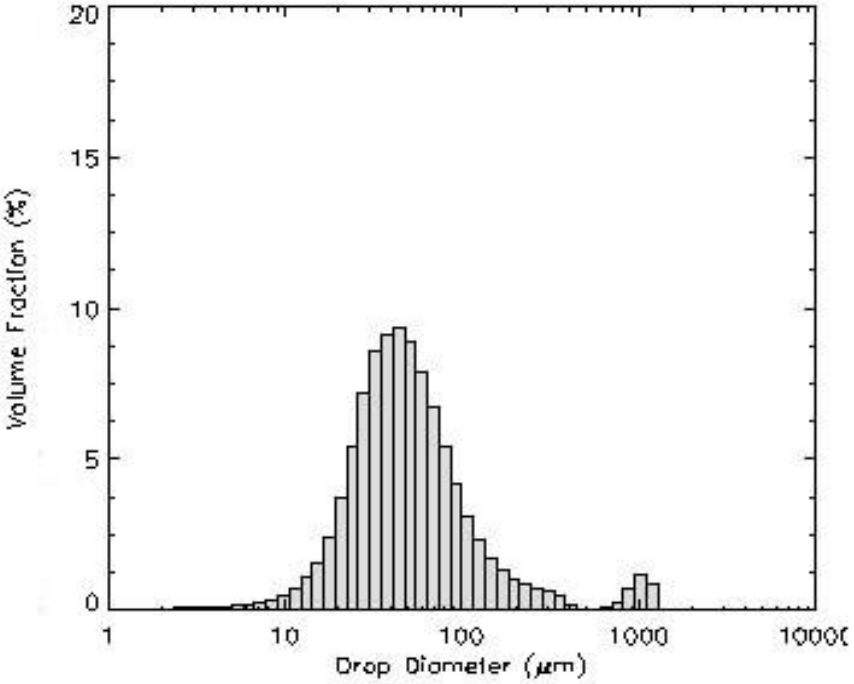

Fig. B6.5: Ethanol droplets size distribution at phase 180^{o}, pressure 60 psi, forcing frequency 312.5 Hz and 50% duty cycle.

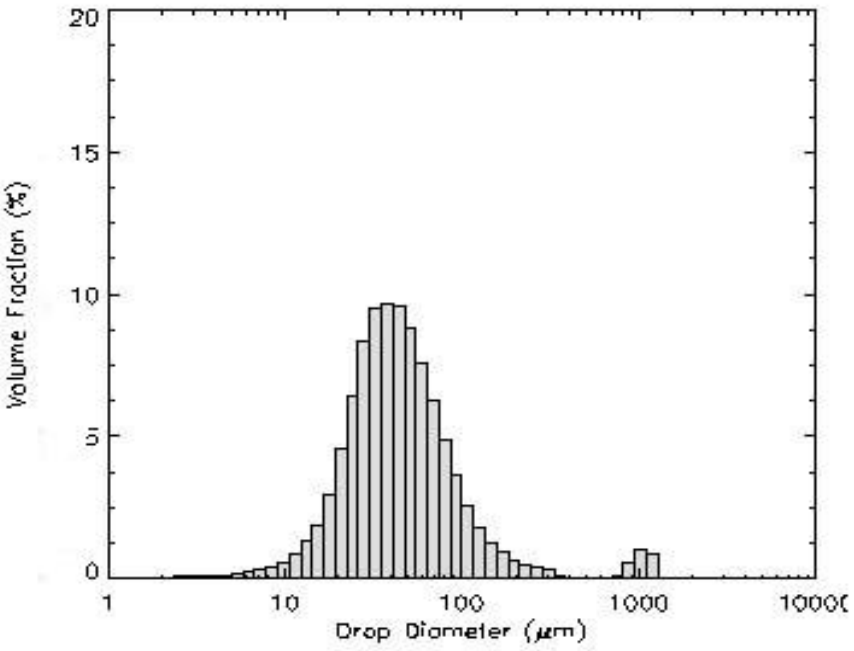

Fig. B6.6: Ethanol droplets size distribution at phase 225^{o}, pressure 60 psi, forcing frequency 312.5 Hz and 50% duty cycle.

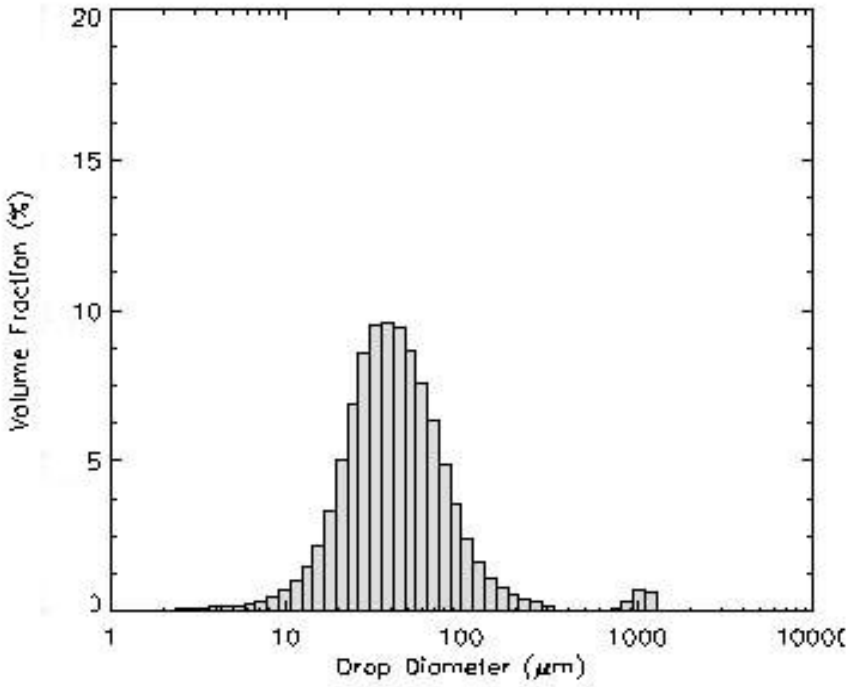

Fig. B6.7: Ethanol droplets size distribution at phase 270^{o}, pressure 60 psi, forcing frequency 312.5 Hz and 50% duty cycle.

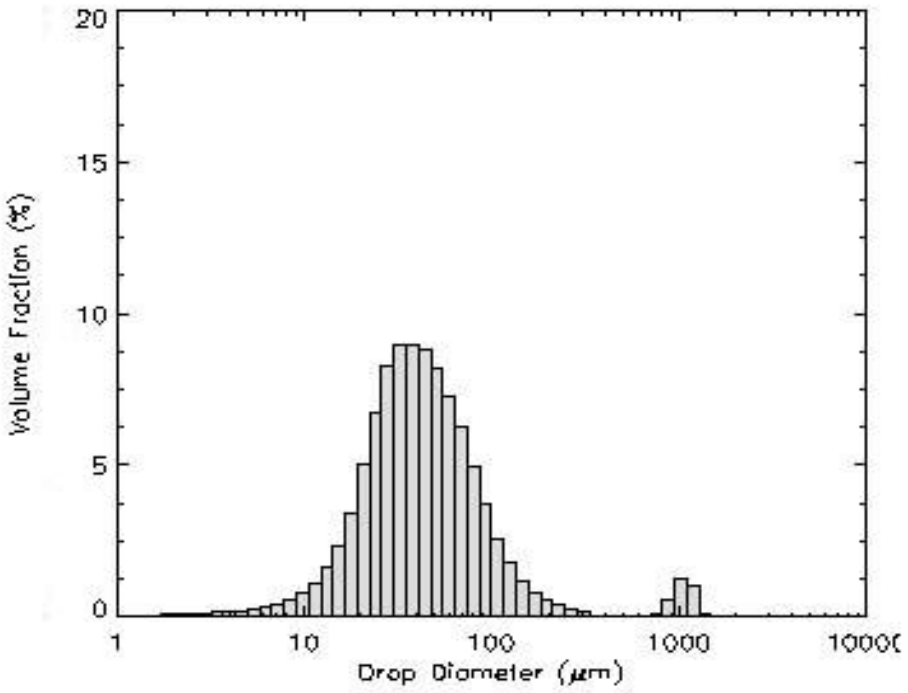

Fig. B6.8: Ethanol droplets size distribution at phase 315^{o}, pressure 60 psi, forcing frequency 312.5 Hz and 50% duty cycle.

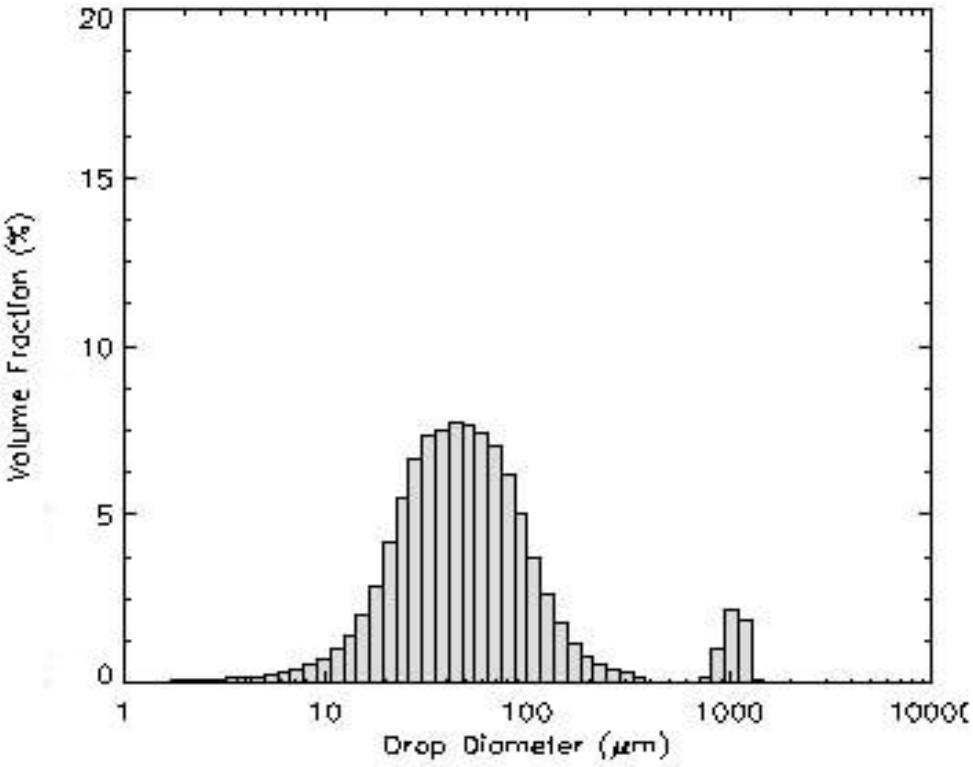

Fig. B6.9: Ethanol droplets size distribution at phase 360^{o}, pressure 60 psi, forcing frequency 312.5 Hz and 50% duty cycle.

Appendix C – Phase-locked Schlieren and CH* Image Sequence for Flame Model

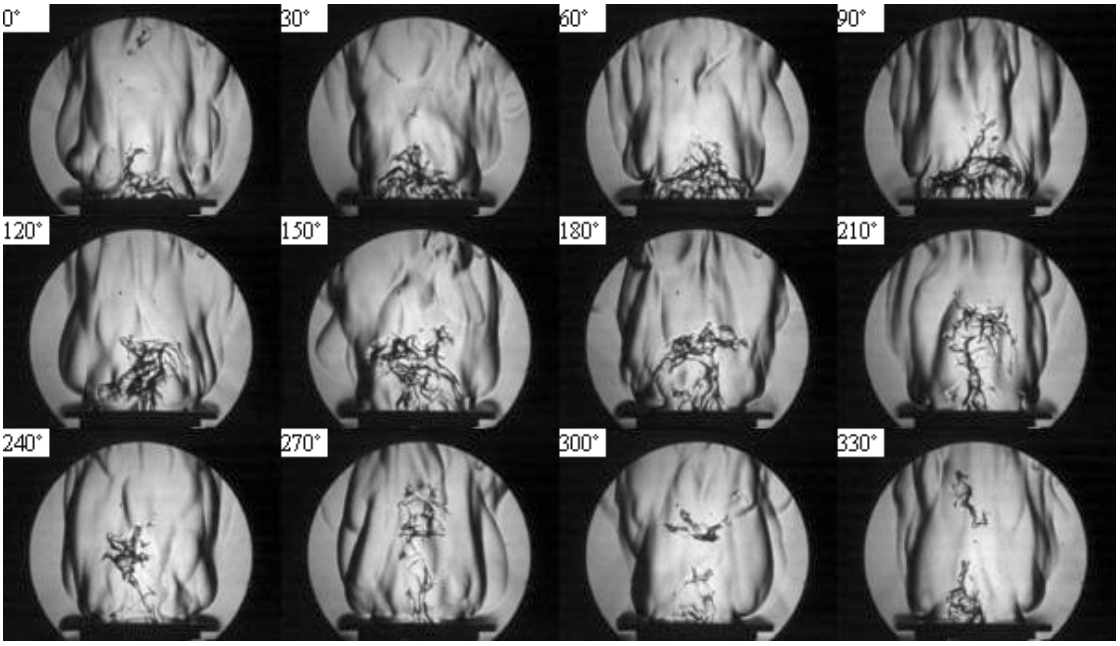

Fig. C.1: Phase-locked instantaneous Schlieren images of a cycle at forcing amplitude 5V and forcing frequency 180 Hz.

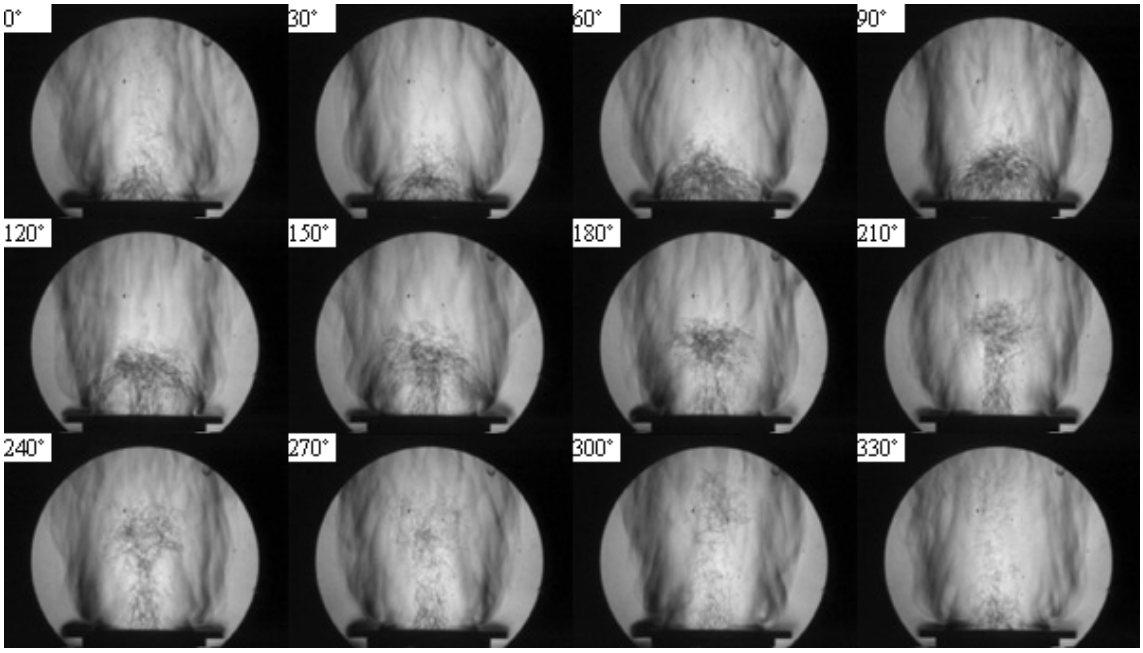

Fig. C.2: Phase-lock-averaged Schlieren images of a cycle at forcing amplitude 5V and forcing frequency 180 Hz.

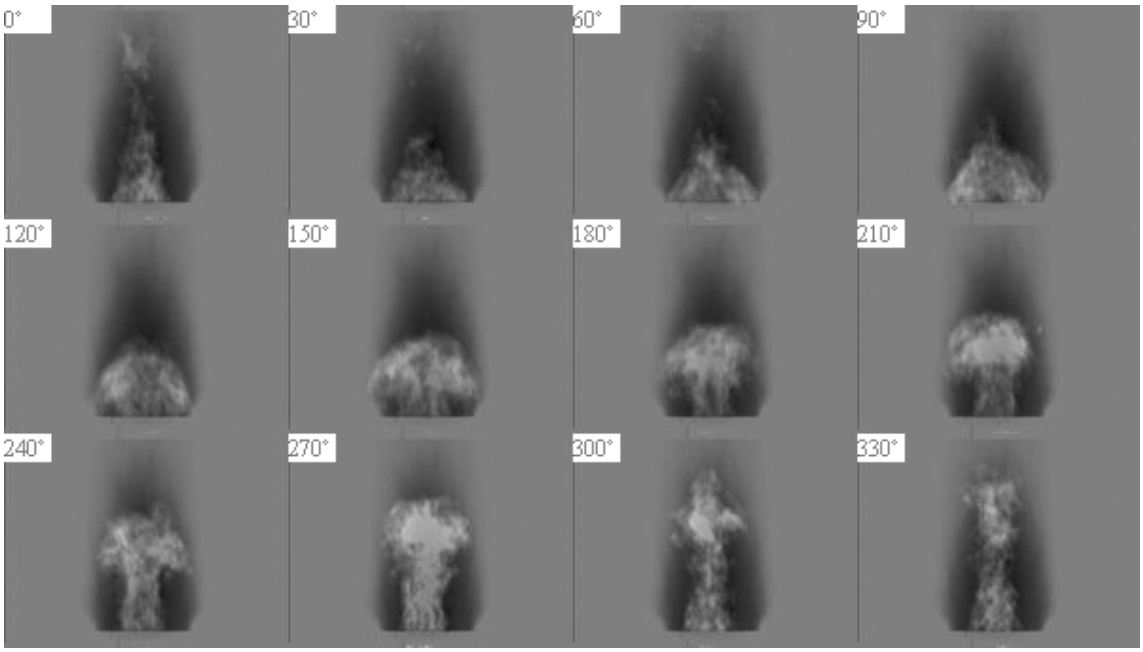

Fig. C.3: Phase-locked CH chemiluminescence oscillation images of a cycle at forcing amplitude 5V and forcing frequency 180 Hz.

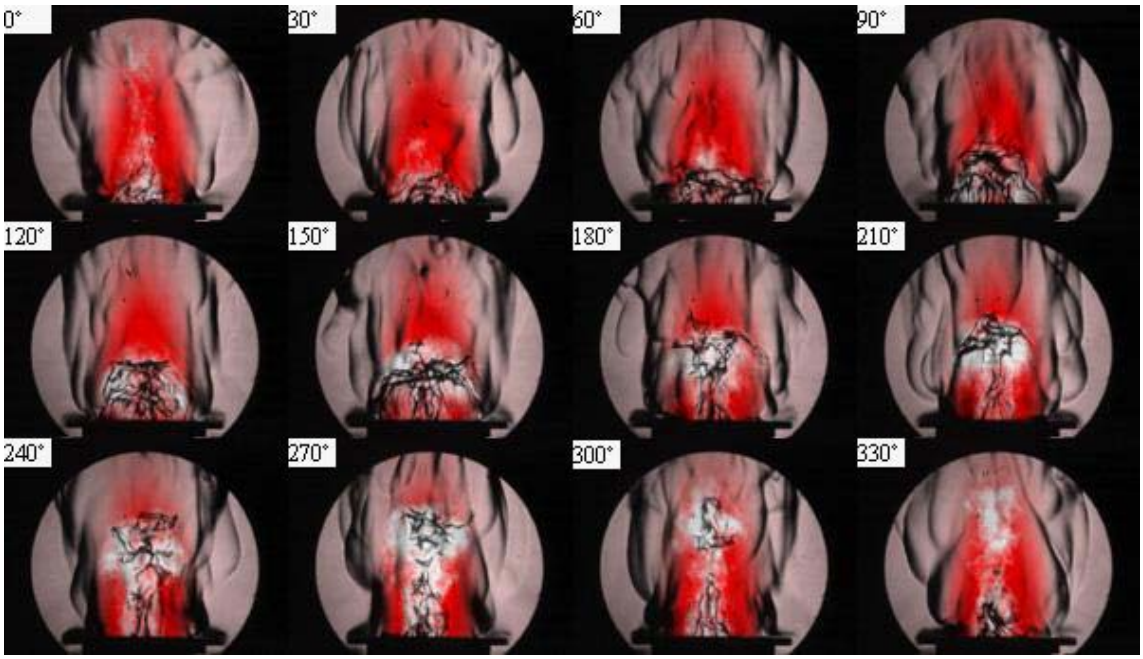

Fig. C.4: Phase-resolved visualization of instantaneous Schlieren and CH chemiluminescence images of a cycle at forcing amplitude 5V and forcing frequency 180 Hz.

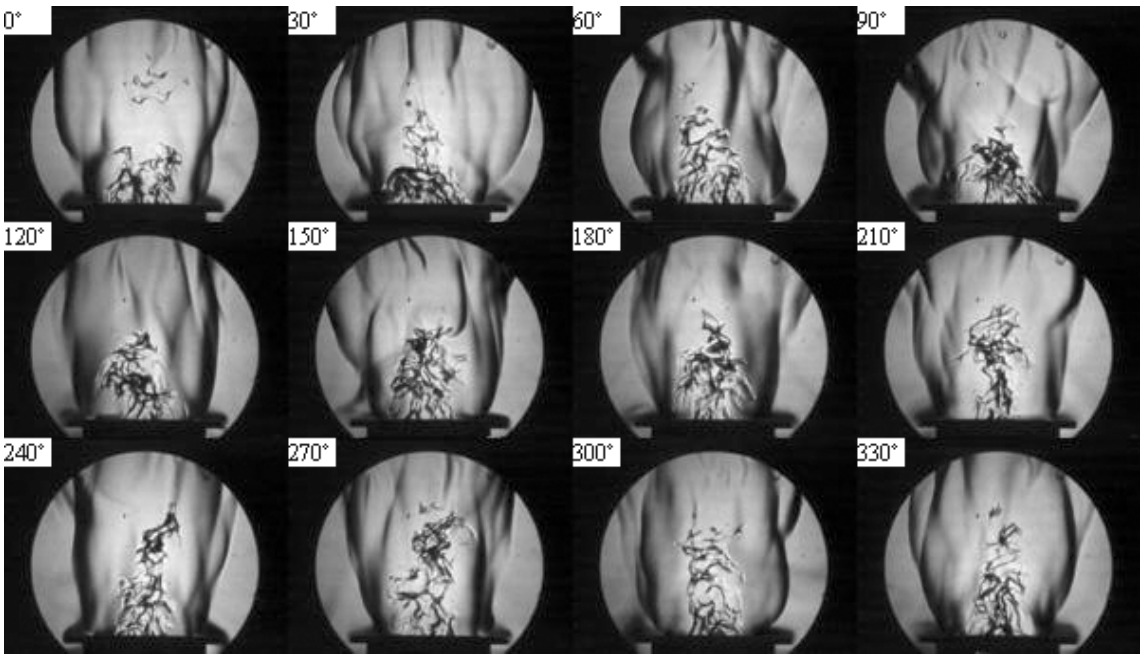

Fig. C.5: Phase-locked instantaneous Schlieren images of a cycle at forcing amplitude 5V and forcing frequency 240 Hz.

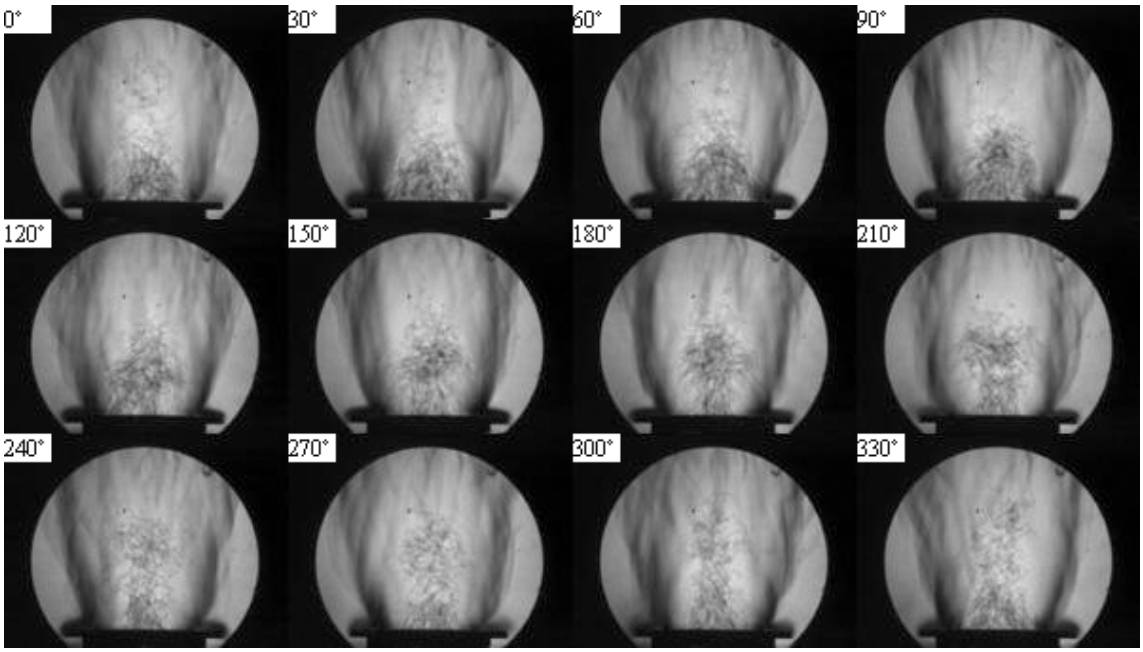

Fig. C.6: Phase-lock-averaged Schlieren images of a cycle at forcing amplitude 5V and forcing frequency 240 Hz.

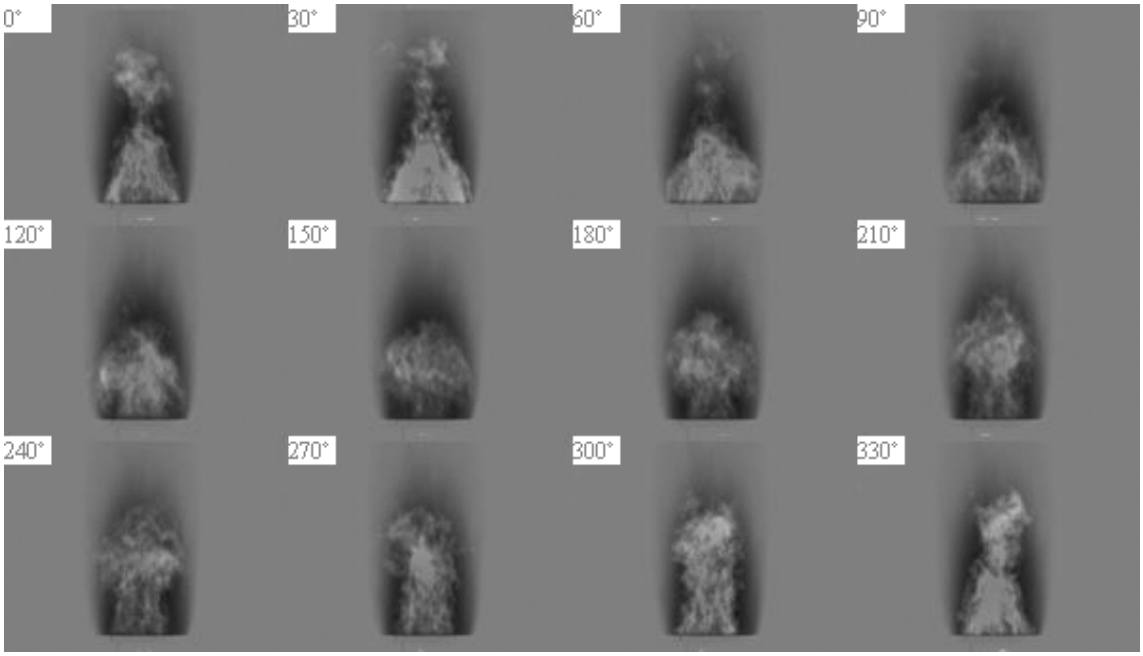

Fig. C.7: Phase-locked CH chemiluminescence oscillation images of a cycle at forcing amplitude 5V and forcing frequency 240 Hz.

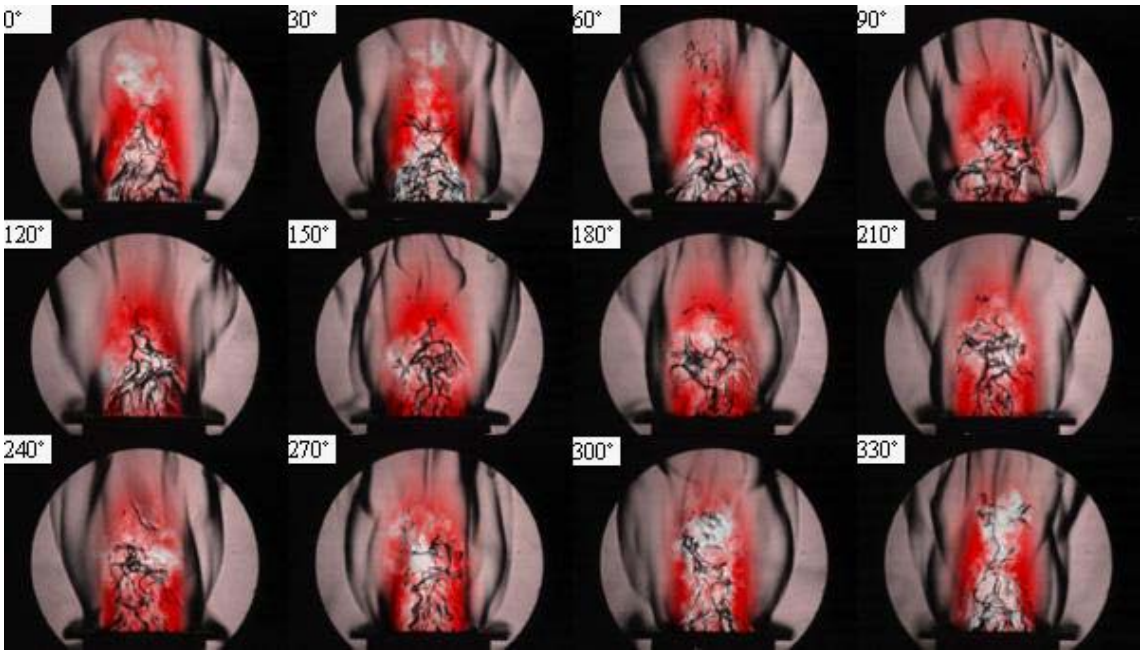

Fig. C.8: Phase-resolved visualization of instantaneous Schlieren and CH chemiluminescence images of a cycle at forcing amplitude 5V and forcing frequency 240 Hz

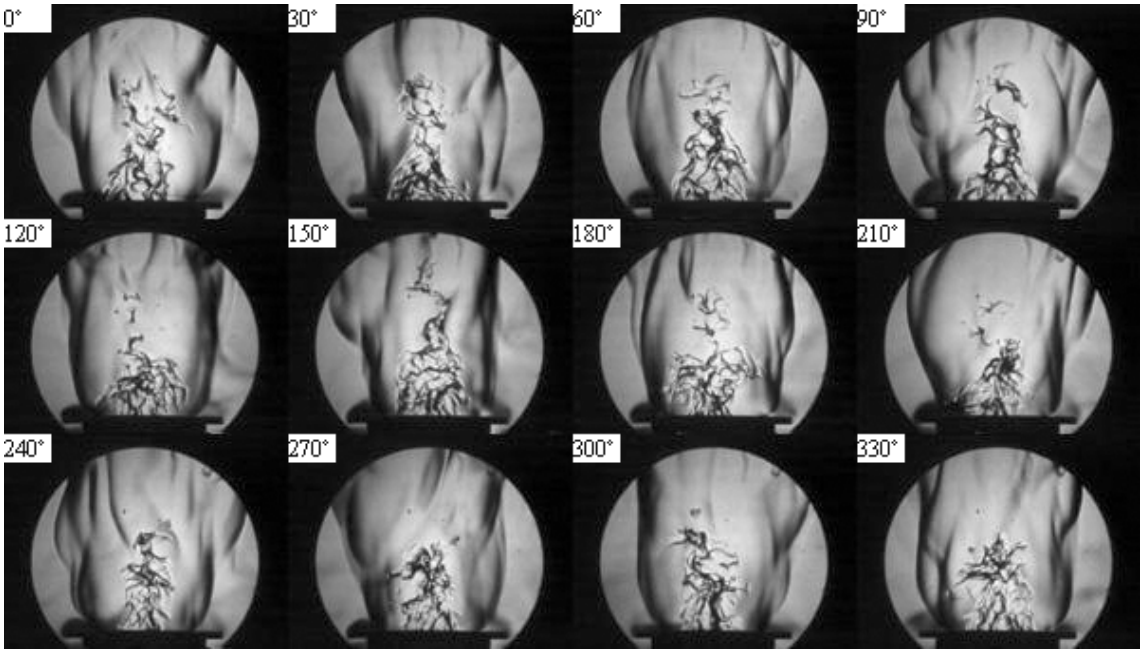

Fig. C.9: Phase-locked instantaneous Schlieren images of a cycle at forcing amplitude 5V and forcing frequency 300 Hz.

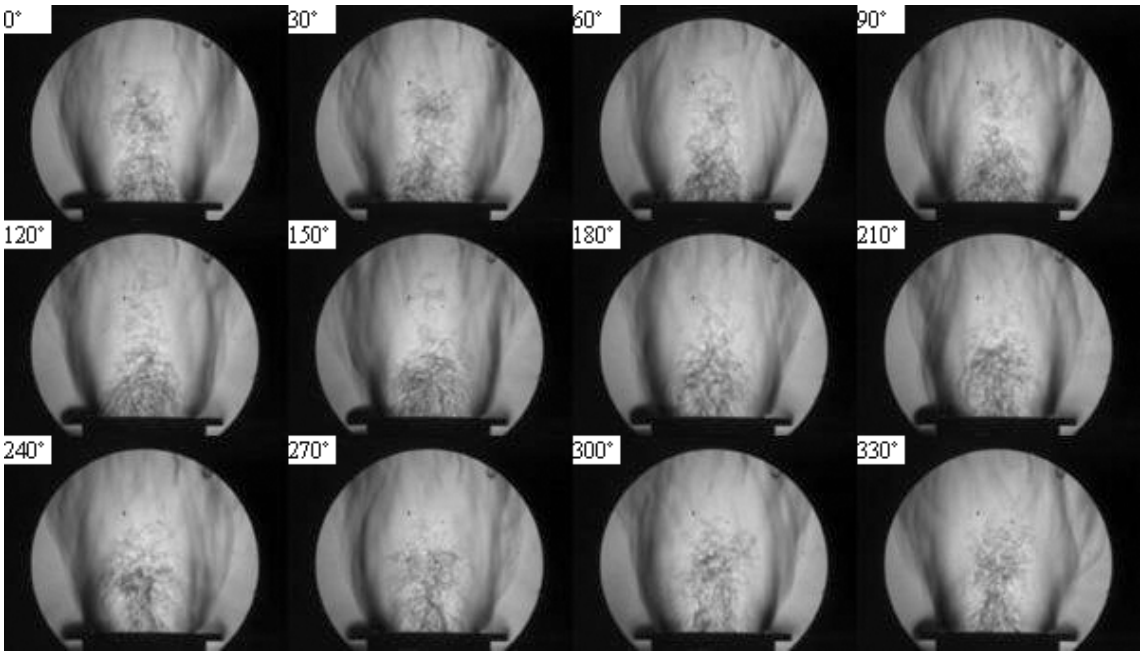

Fig. C.10: Phase-lock-averaged Schlieren images of a cycle at forcing amplitude 5V and forcing frequency 300 Hz.

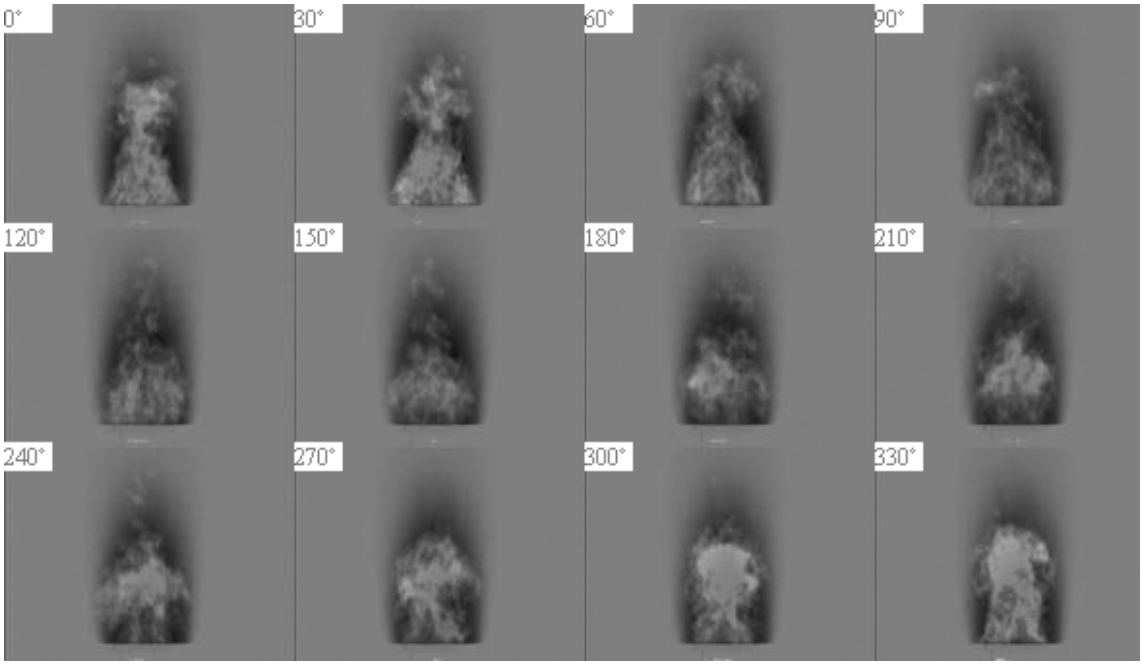

Fig. C.11: Phase-locked CH chemiluminescence oscillation images of a cycle at forcing amplitude 5V and forcing frequency 300 Hz.

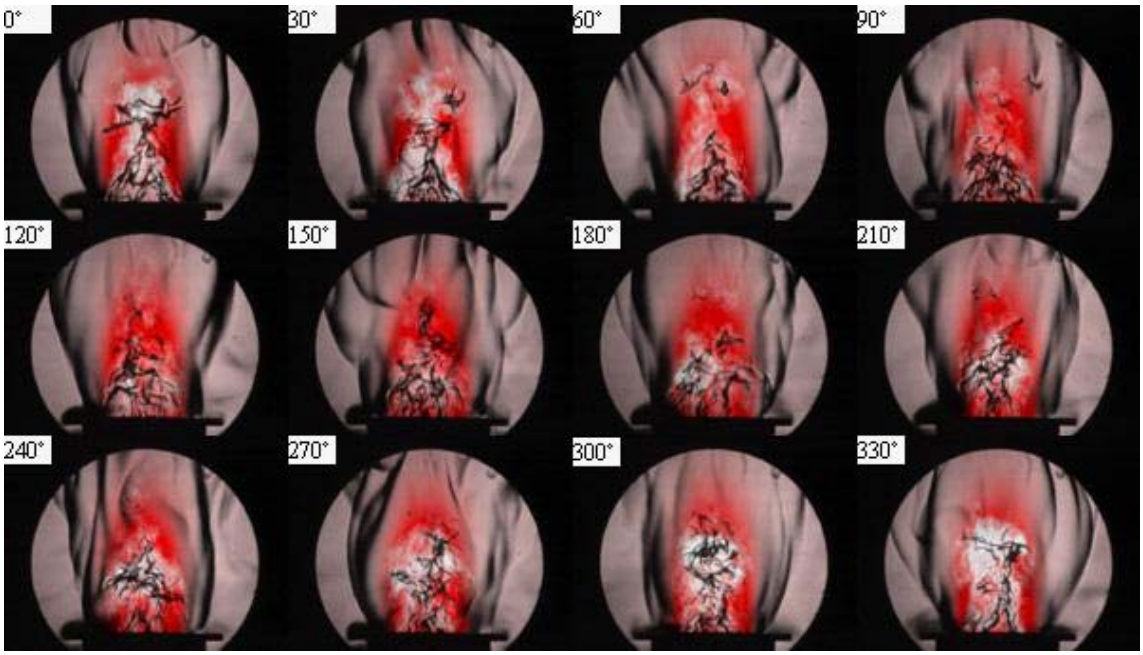

Fig. C.12: Phase-resolved visualization of instantaneous Schlieren and CH chemiluminescence images of a cycle at forcing amplitude 5V and forcing frequency 300 Hz.

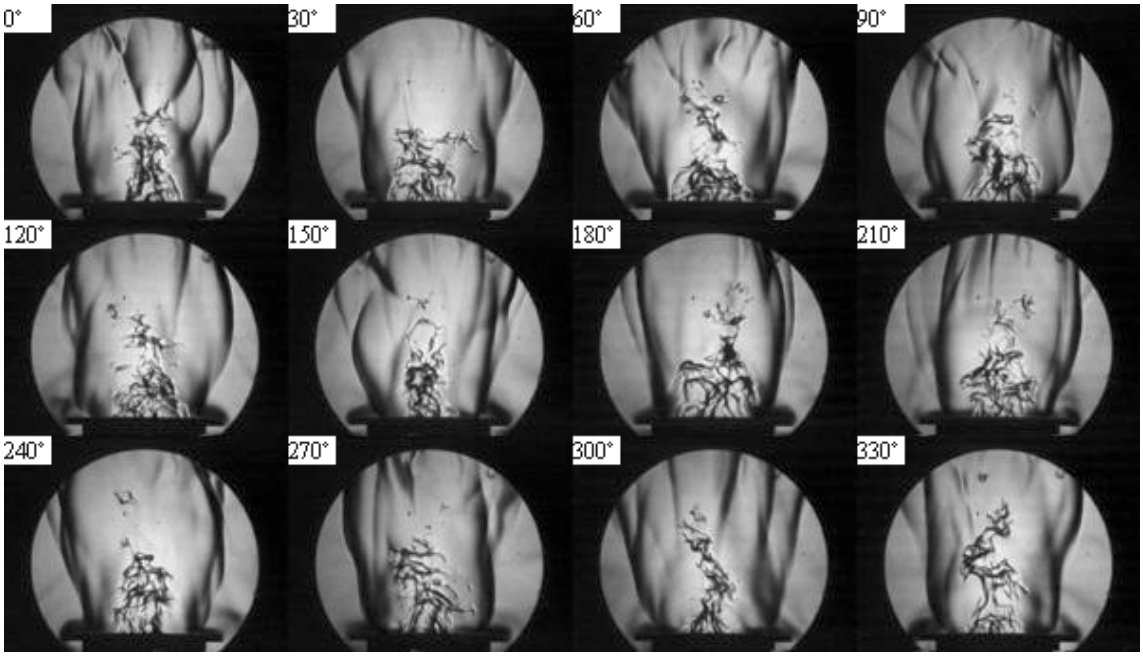

Fig. C.13: Phase-locked instantaneous Schlieren images of a cycle at forcing amplitude 5V and forcing frequency 360 Hz.

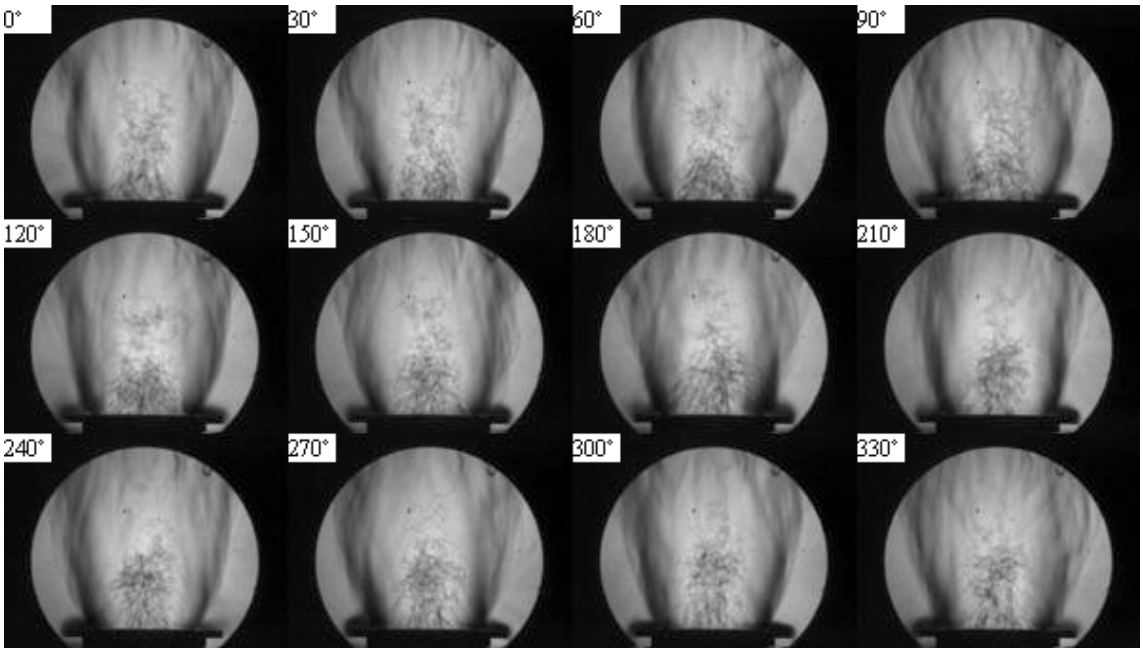

Fig. C.14: Phase-lock-averaged Schlieren images of a cycle at forcing amplitude 5V and forcing frequency 360 Hz.

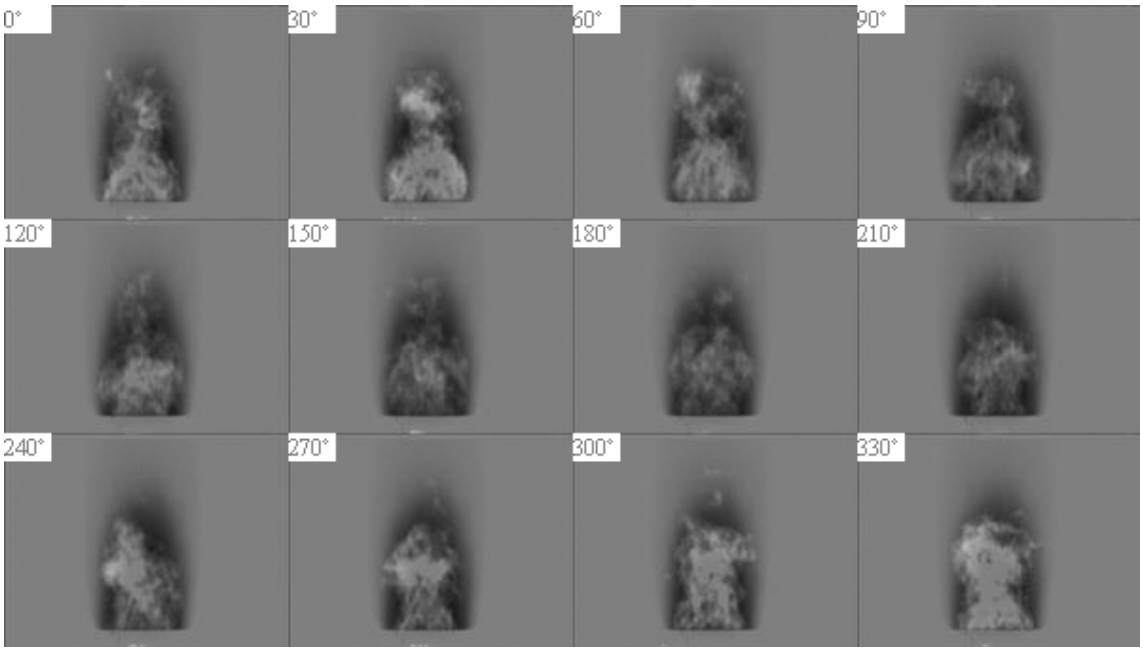

Fig. C.15: Phase-locked CH chemiluminescence oscillation images of a cycle at forcing amplitude 5V and forcing frequency 360 Hz.

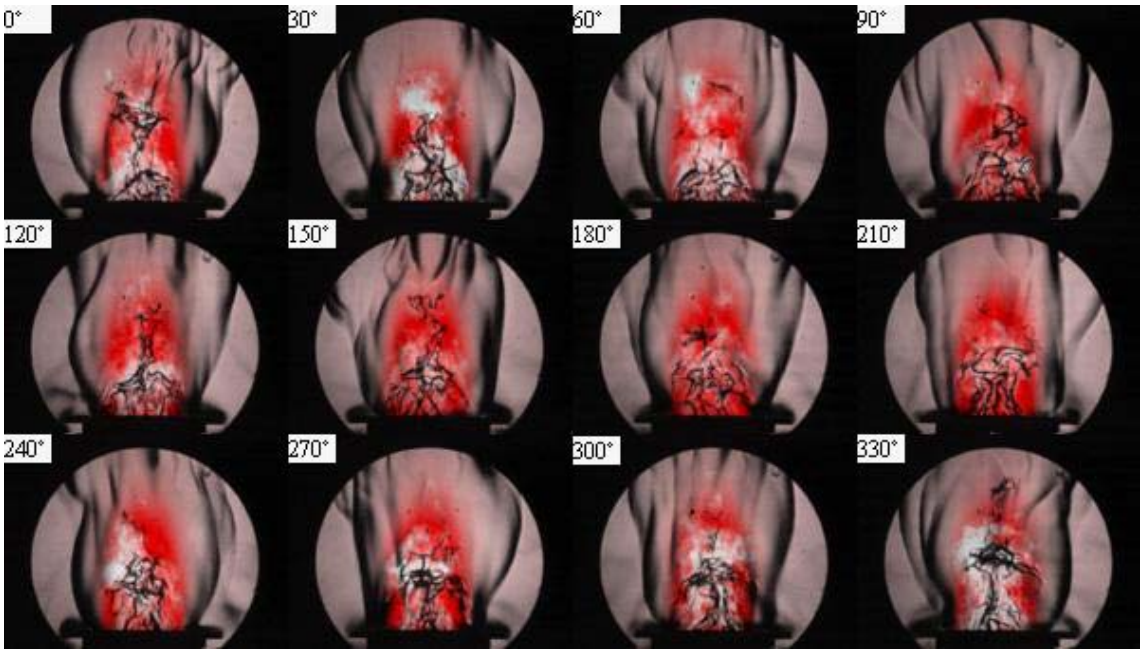

Fig. C.16: Phase-resolved visualization of instantaneous Schlieren and CH chemiluminescence images of a cycle at forcing amplitude 5V and forcing frequency 360 Hz.

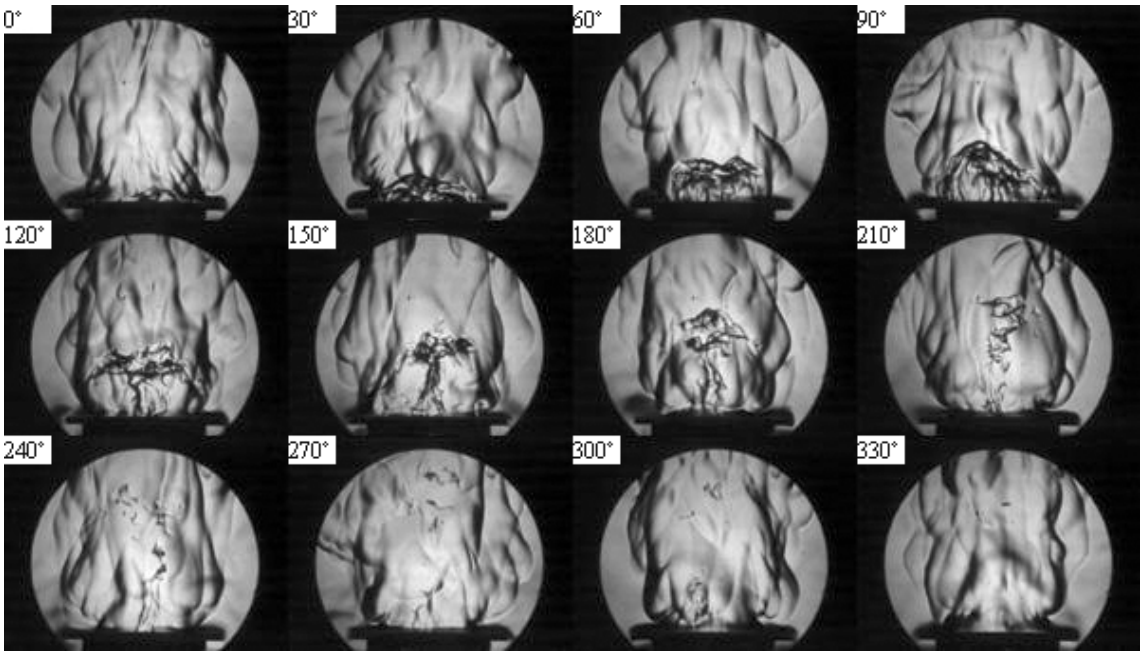

Fig. C.17: Phase-locked instantaneous Schlieren images of a cycle at forcing amplitude 10V and forcing frequency 180 Hz.

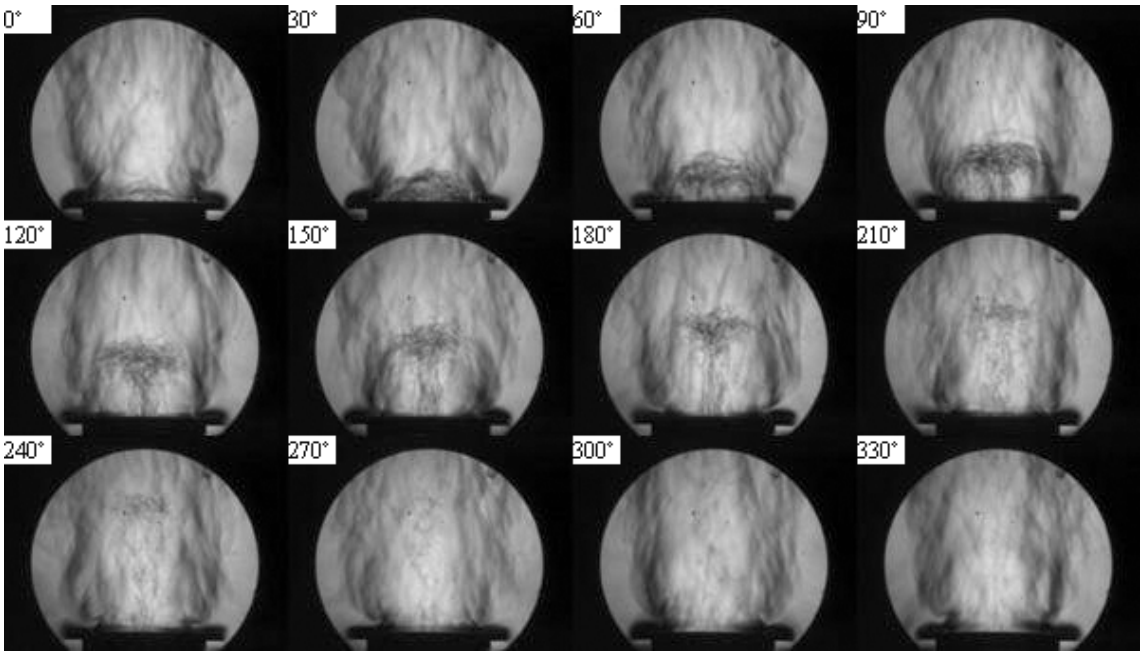

Fig. C.18: Phase-lock-averaged Schlieren images of a cycle at forcing amplitude 10V and forcing frequency 180 Hz.

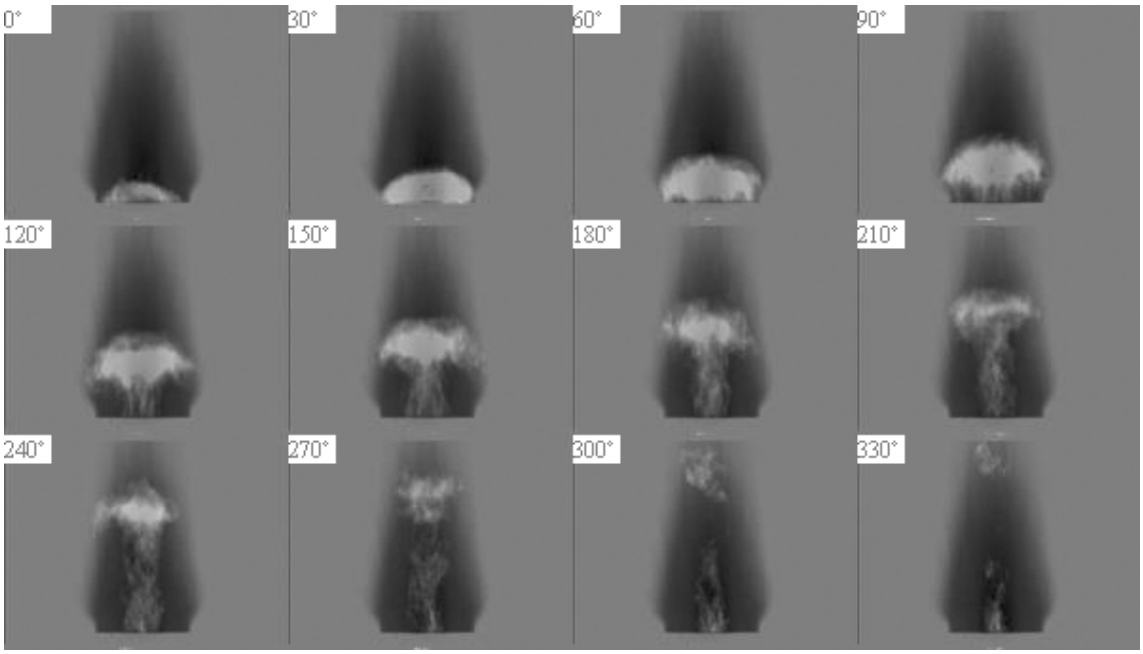

Fig. C.19: Phase-locked CH chemiluminescence oscillation images of a cycle at forcing amplitude 10V and forcing frequency 180 Hz.

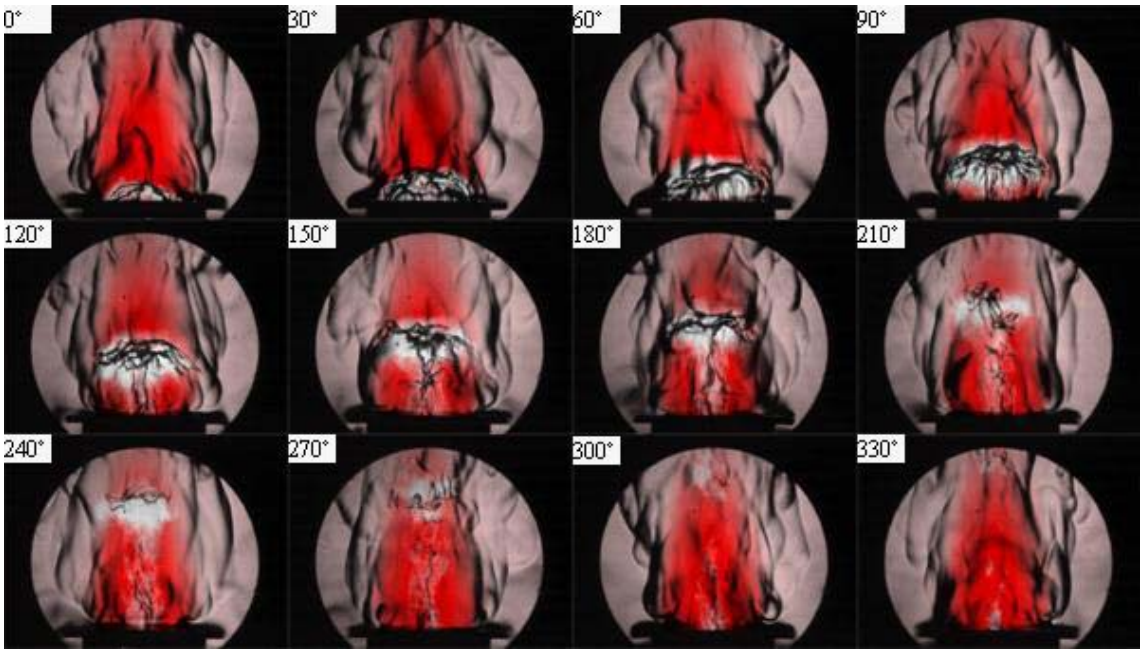

Fig. C.20: Phase-resolved visualization of instantaneous Schlieren and CH chemiluminescence images of a cycle at forcing amplitude 10V and forcing frequency 180 Hz.

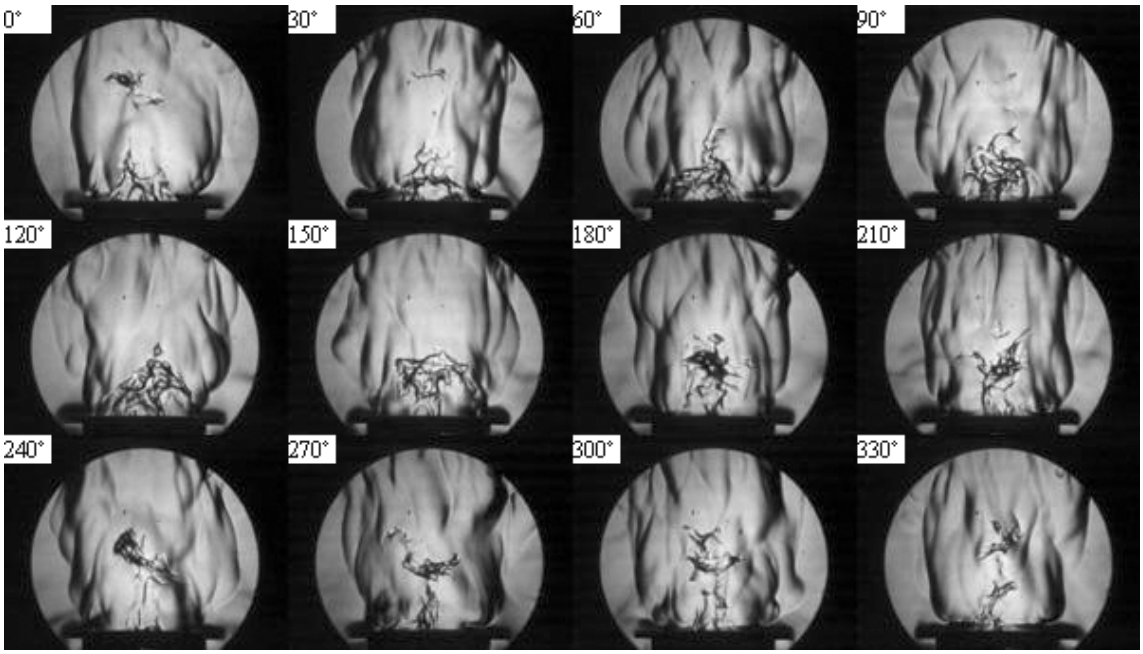

Fig. C.21: Phase-locked instantaneous Schlieren images of a cycle at forcing amplitude 10V and forcing frequency 240 Hz.

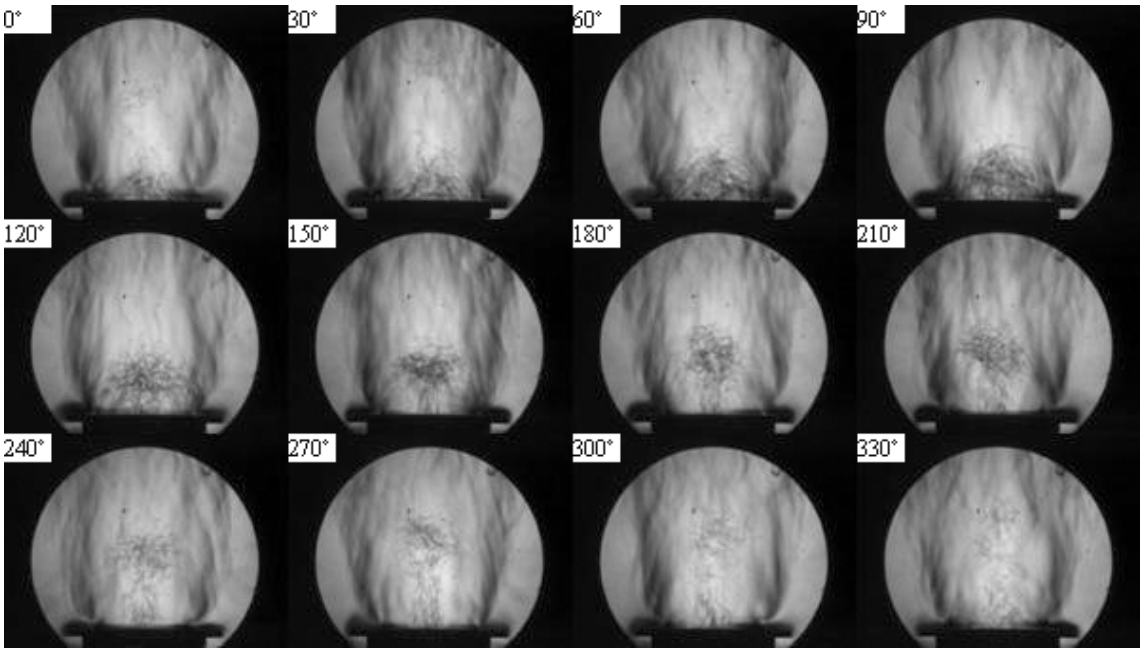

Fig. C.22: Phase-lock-averaged Schlieren images of a cycle at forcing amplitude 10V and forcing frequency 240 Hz.

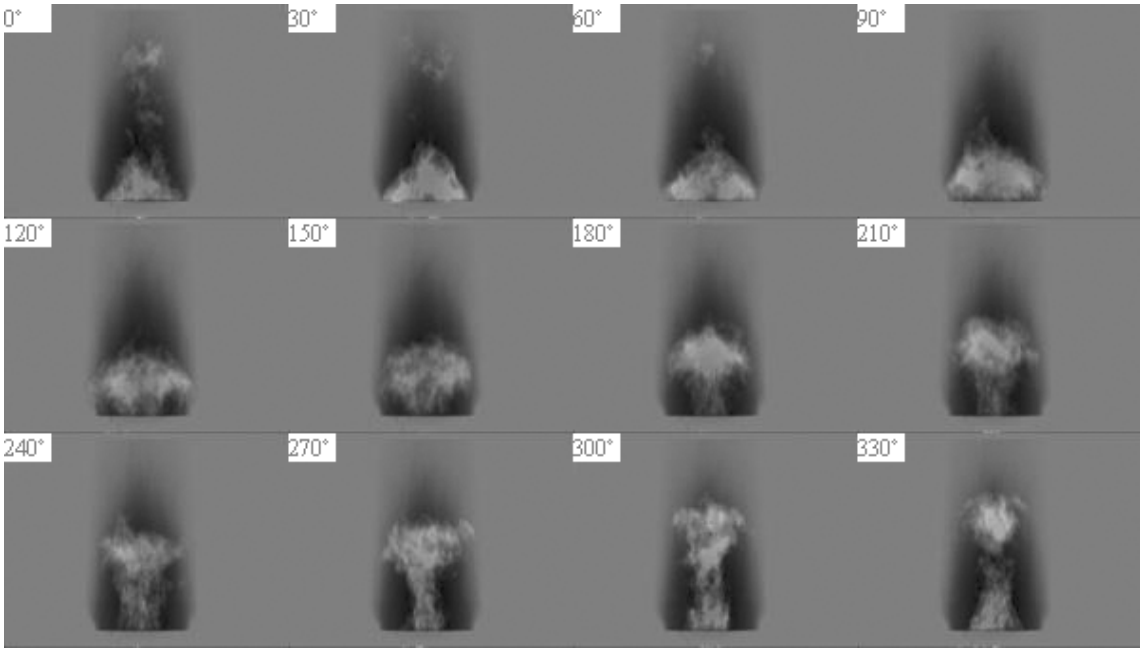

Fig. C.23: Phase-locked CH chemiluminescence oscillation images of a cycle at forcing amplitude 10V and forcing frequency 240 Hz.

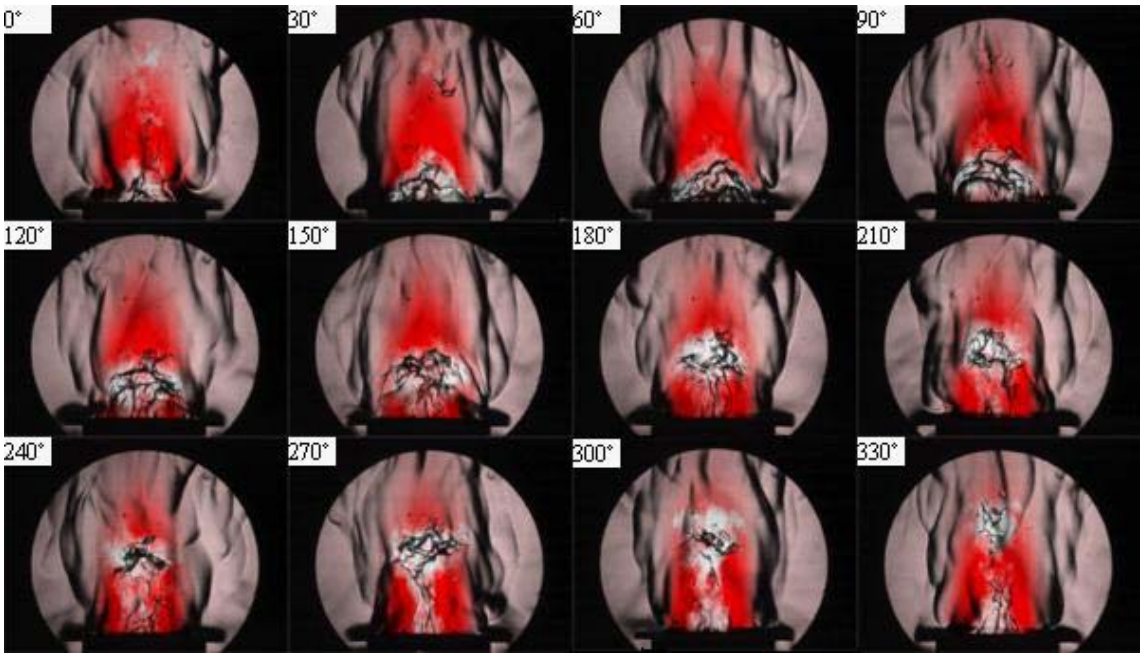

Fig. C.24: Phase-resolved visualization of instantaneous Schlieren and CH chemiluminescence images of a cycle at forcing amplitude 10V and forcing frequency 240 Hz.

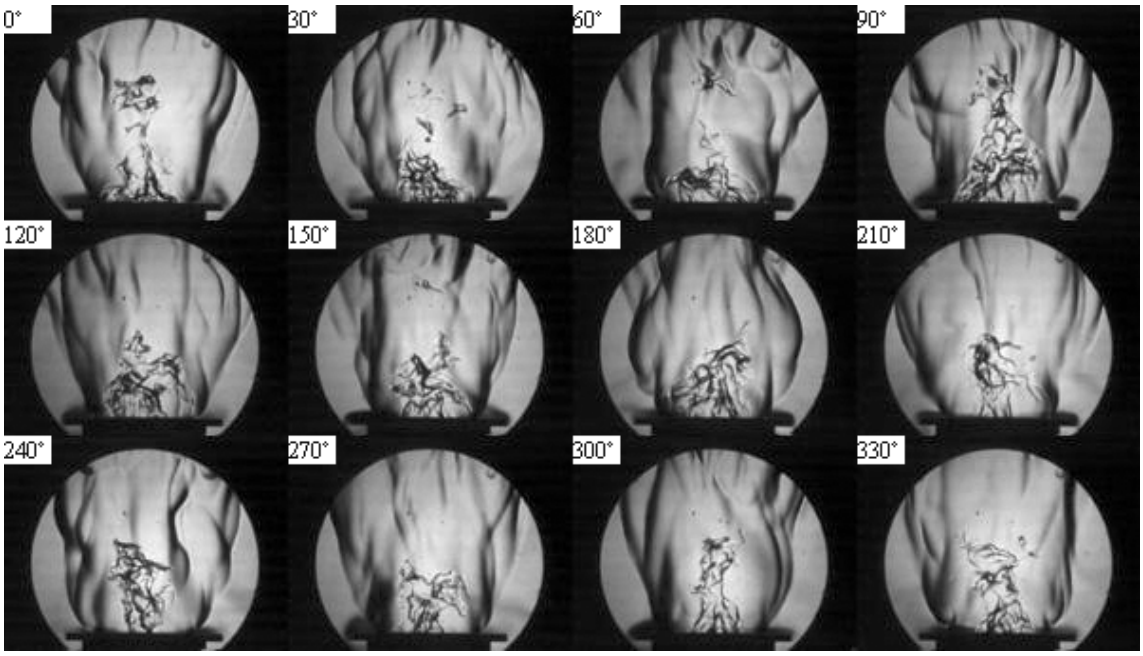

Fig. C.25: Phase-locked instantaneous Schlieren images of a cycle at forcing amplitude 10V and forcing frequency 300 Hz.

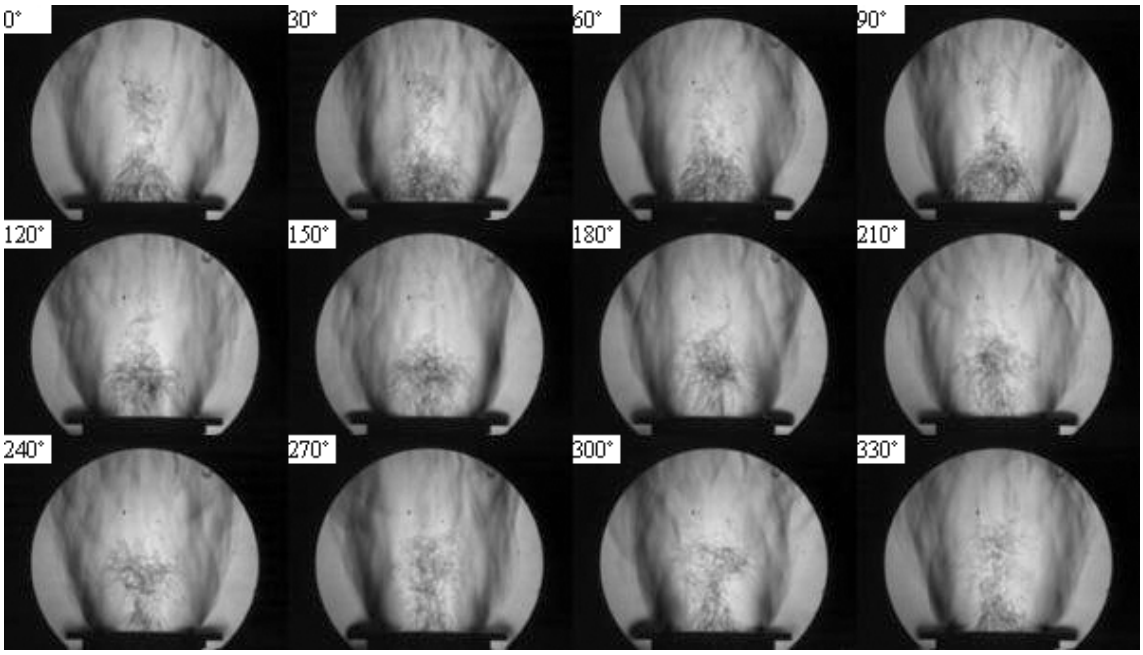

Fig. C.26: Phase-lock-averaged Schlieren images of a cycle at forcing amplitude 10V and forcing frequency 300 Hz.

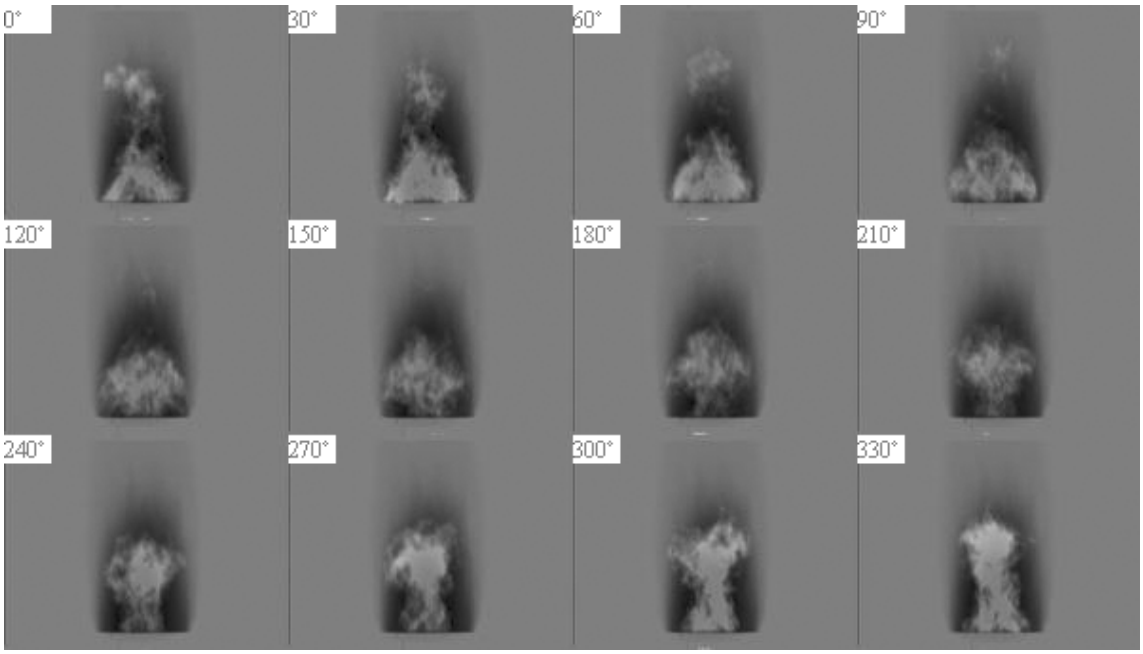

Fig. C.27: Phase-locked CH chemiluminescence oscillation images of a cycle at forcing amplitude 10V and forcing frequency 300 Hz.

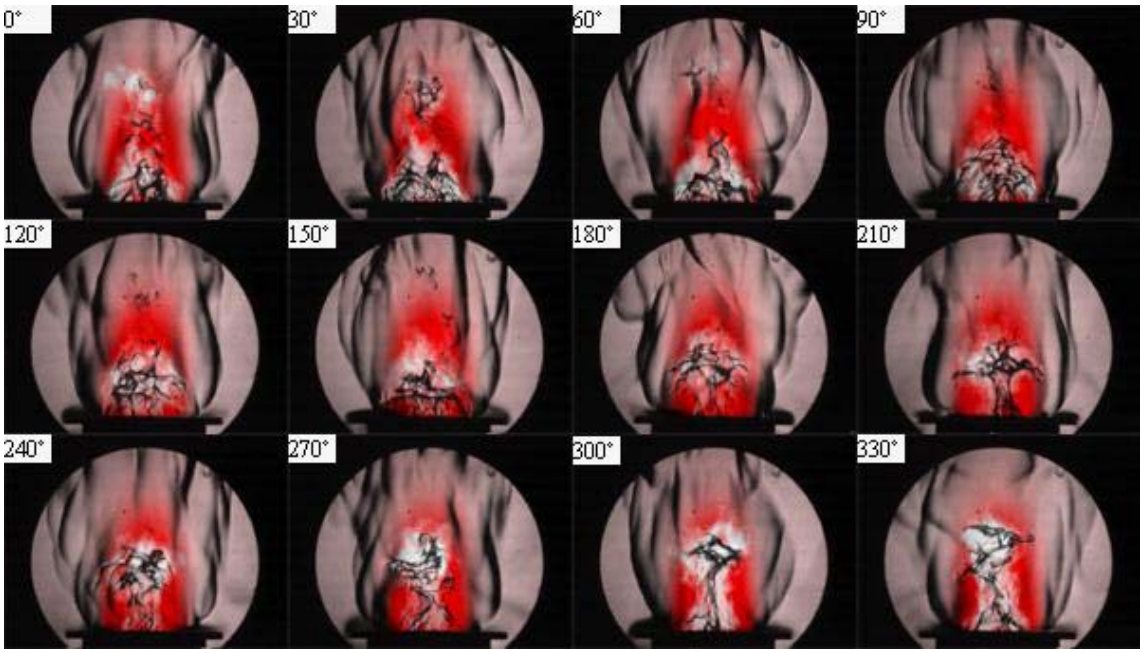

Fig. C.28: Phase-resolved visualization of instantaneous Schlieren and CH chemiluminescence images of a cycle at forcing amplitude 10V and forcing frequency 300 Hz.

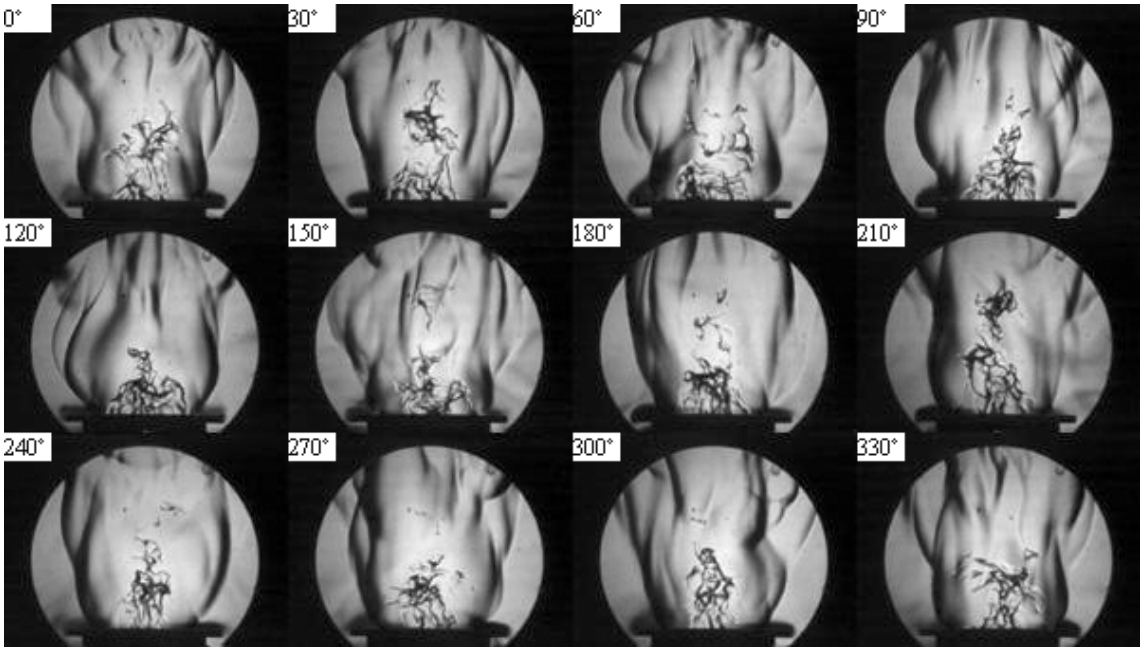

Fig. C.29: Phase-locked instantaneous Schlieren images of a cycle at forcing amplitude 10V and forcing frequency 360 Hz.

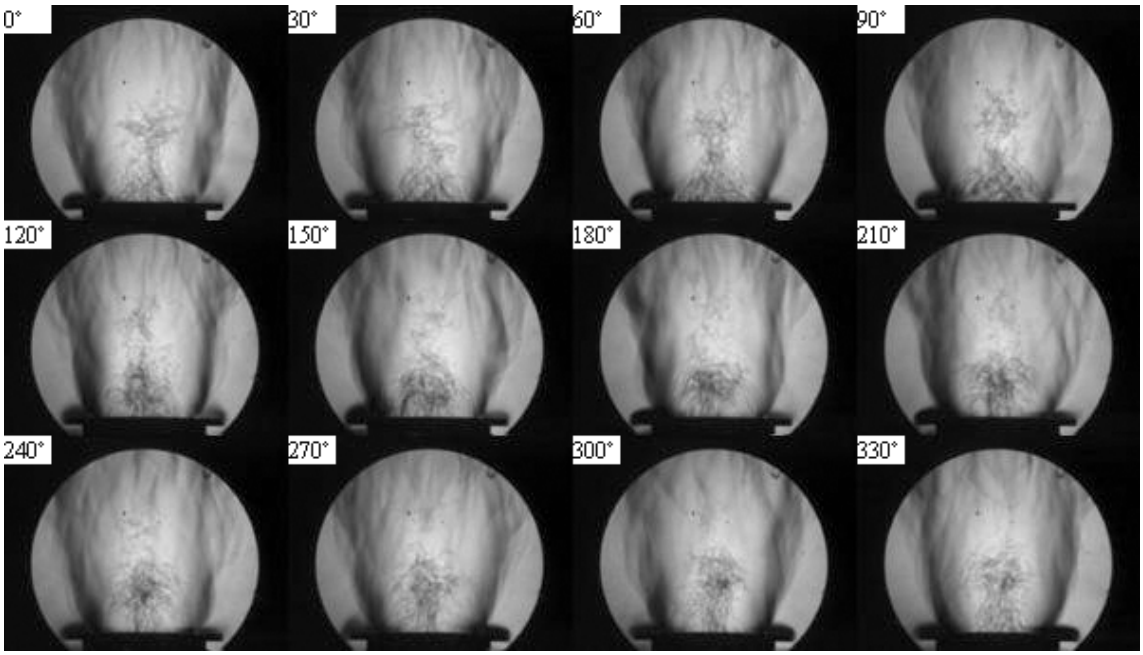

Fig. C.30: Phase-lock-averaged Schlieren images of a cycle at forcing amplitude 10V and forcing frequency 360 Hz.

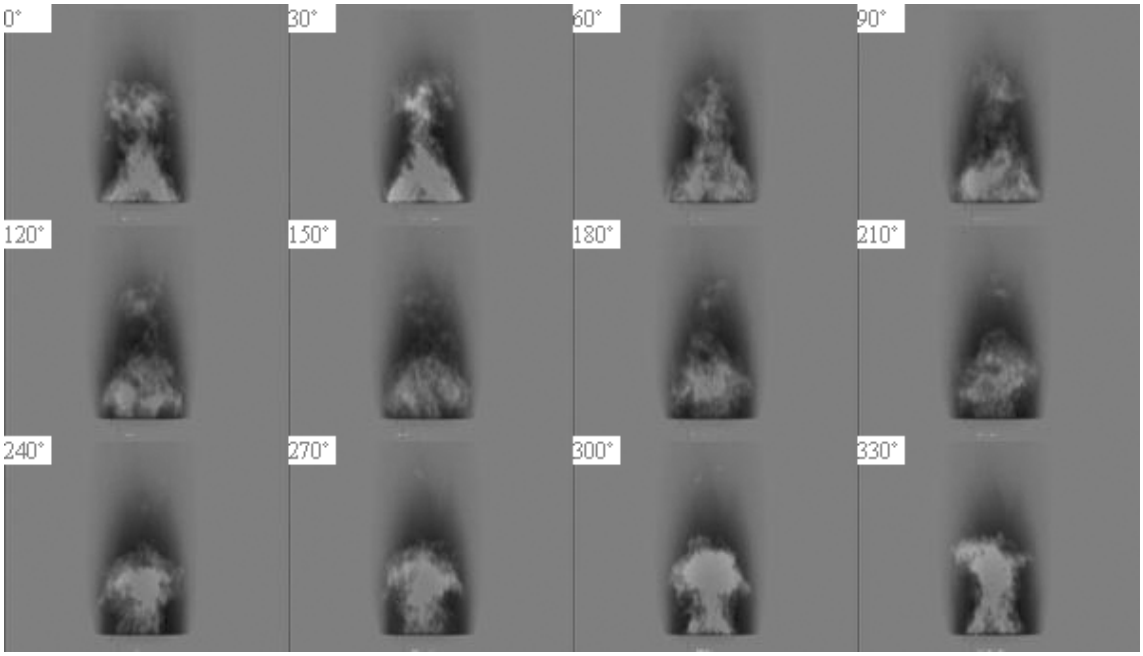

Fig. C.31: Phase-locked CH chemiluminescence oscillation images of a cycle at forcing amplitude 10V and forcing frequency 360 Hz.

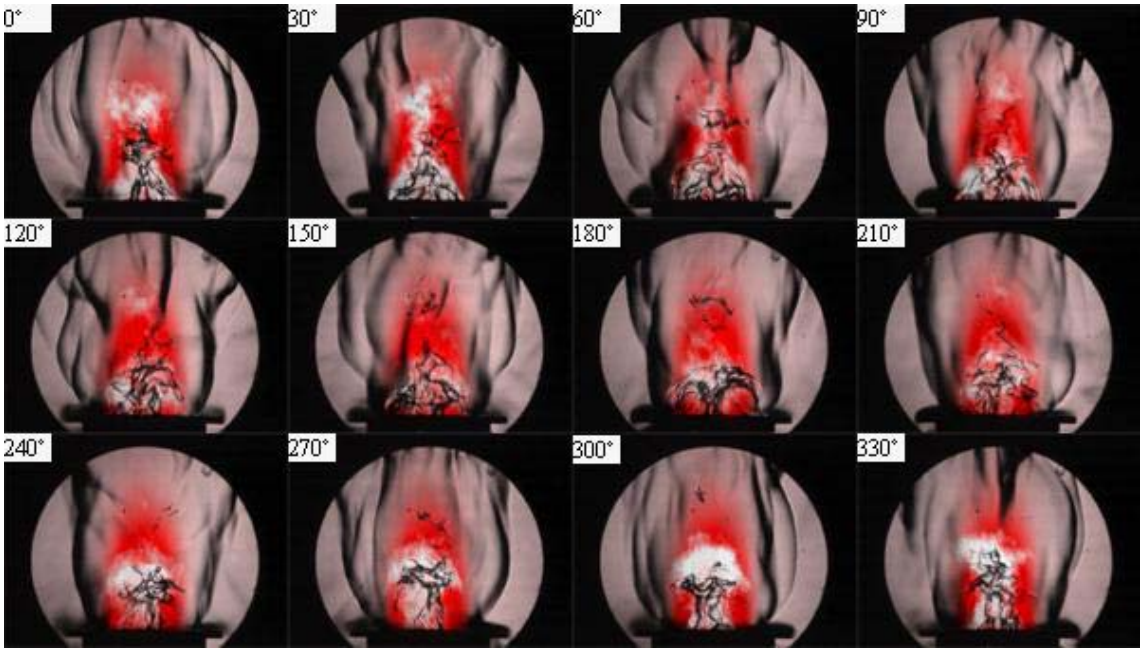

Fig. C.32: Phase-resolved visualization of instantaneous Schlieren and CH chemiluminescence images of a cycle at forcing amplitude 10V and forcing frequency 360 Hz.

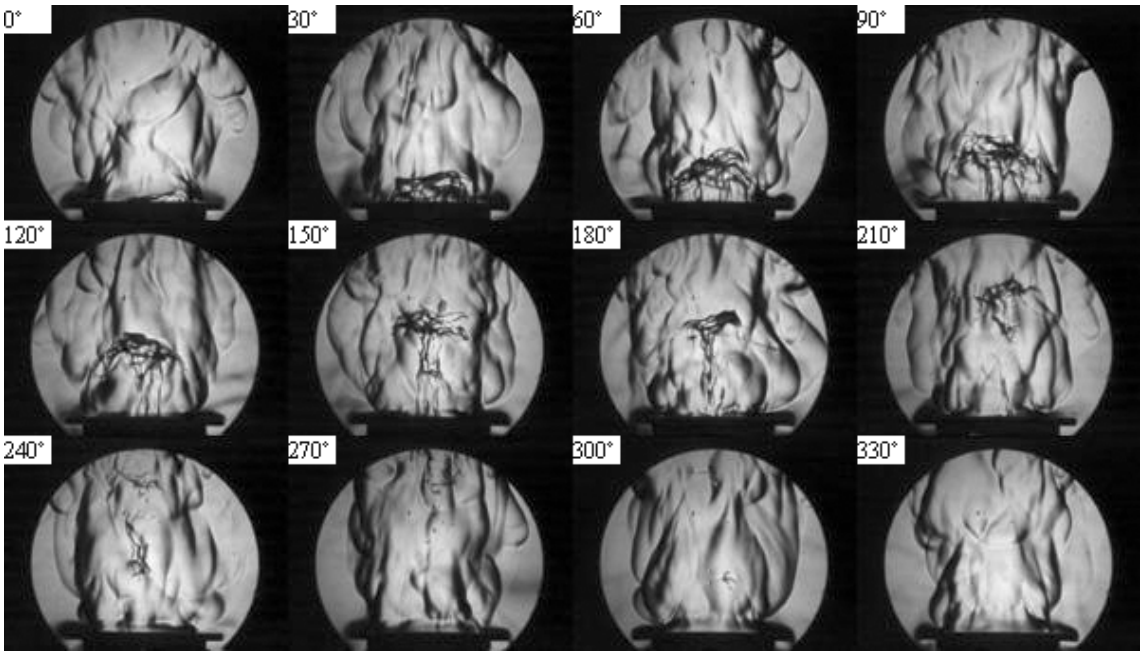

Fig. C.33: Phase-locked instantaneous Schlieren images of a cycle at forcing amplitude 15V and forcing frequency 180 Hz.

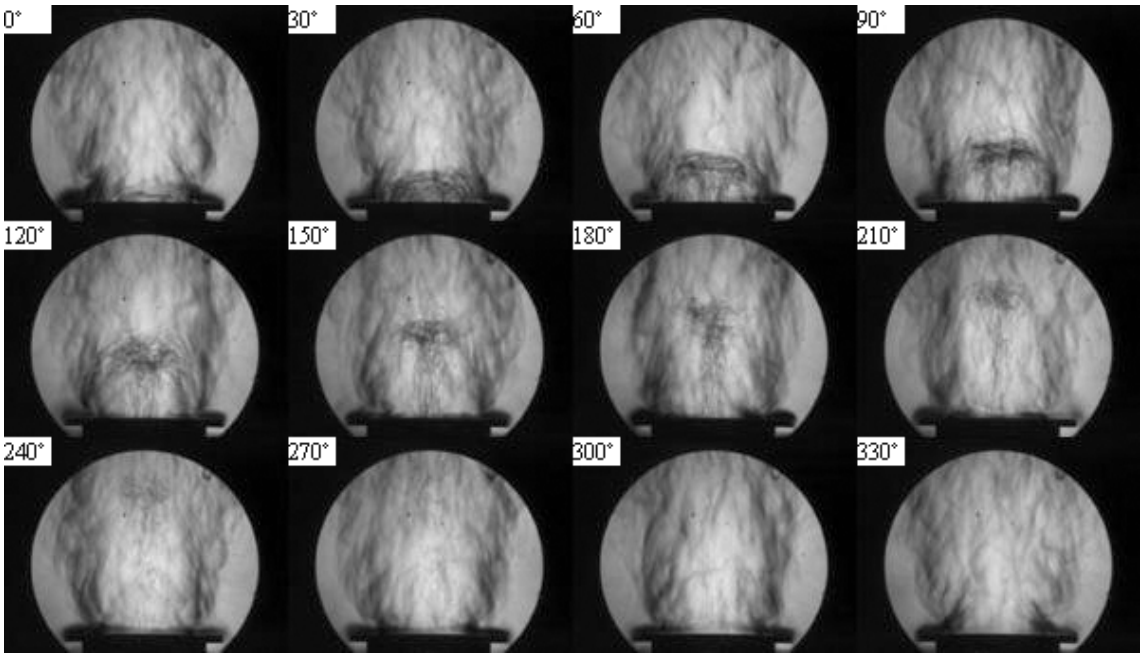

Fig. C.34: Phase-lock-averaged Schlieren images of a cycle at forcing amplitude 15V and forcing frequency 180 Hz.

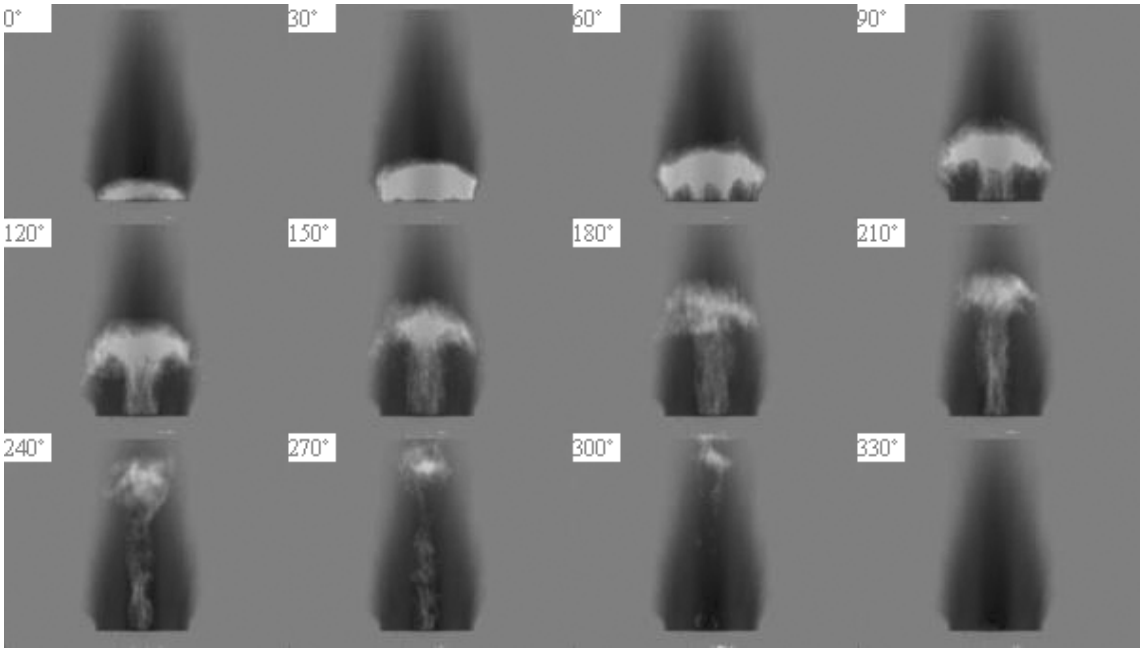

Fig. C.35: Phase-locked CH chemiluminescence oscillation images of a cycle at forcing amplitude 15V and forcing frequency 180 Hz.

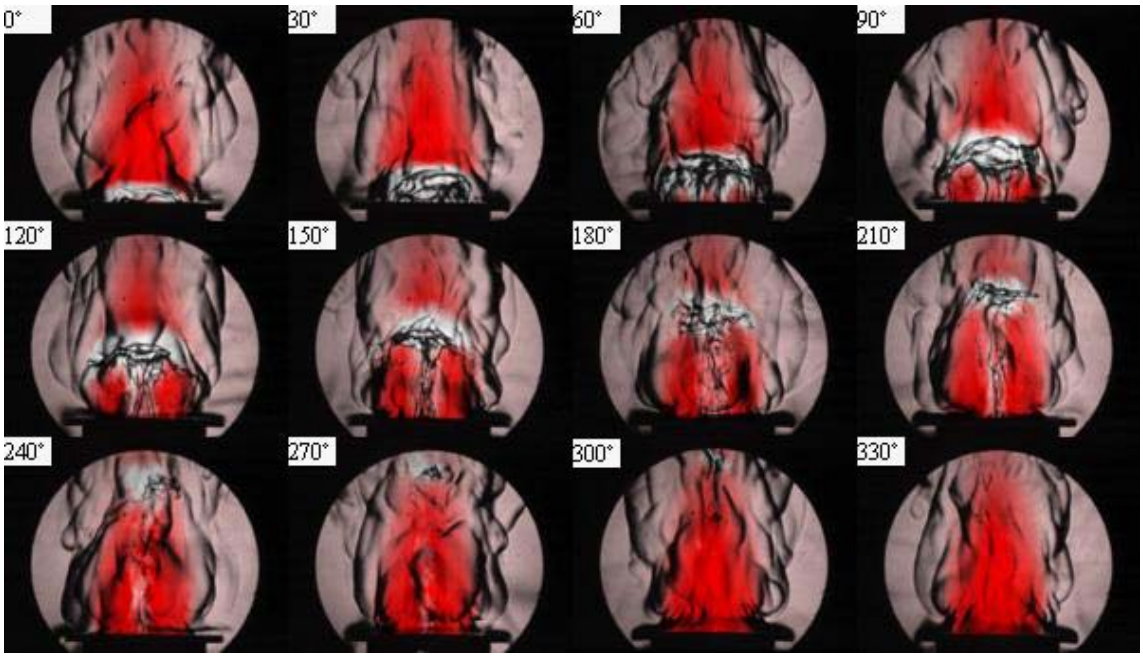

Fig. C.36: Phase-resolved visualization of instantaneous Schlieren and CH chemiluminescence images of a cycle at forcing amplitude 15V and forcing frequency 180 Hz.

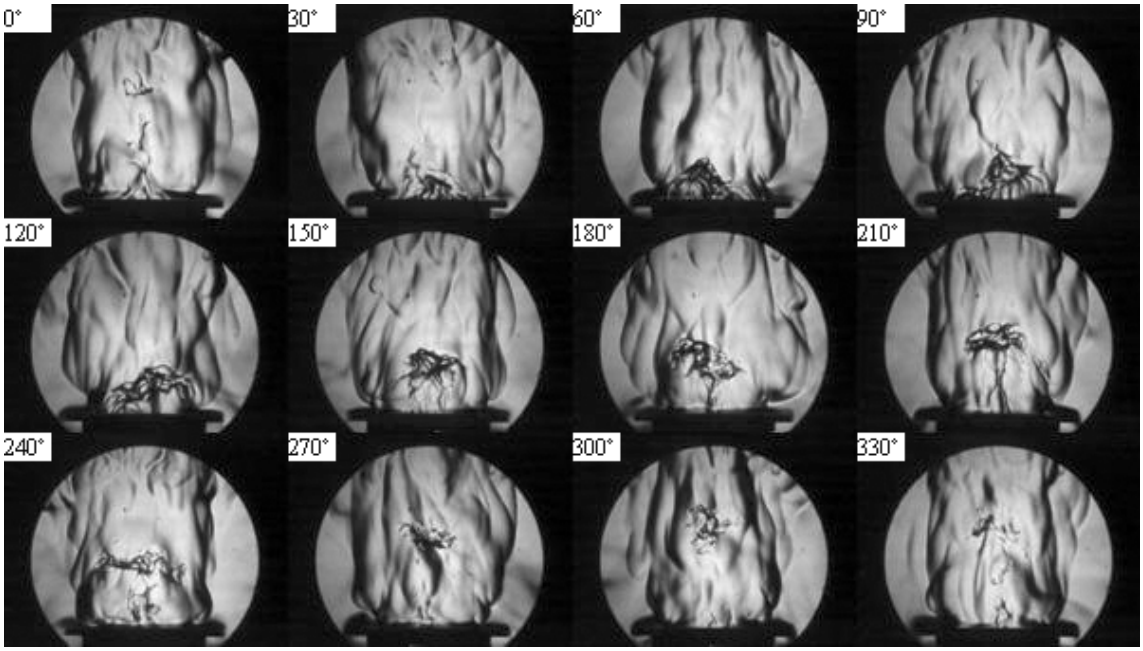

Fig. C.37: Phase-locked instantaneous Schlieren images of a cycle at forcing amplitude 15V and forcing frequency 240 Hz.

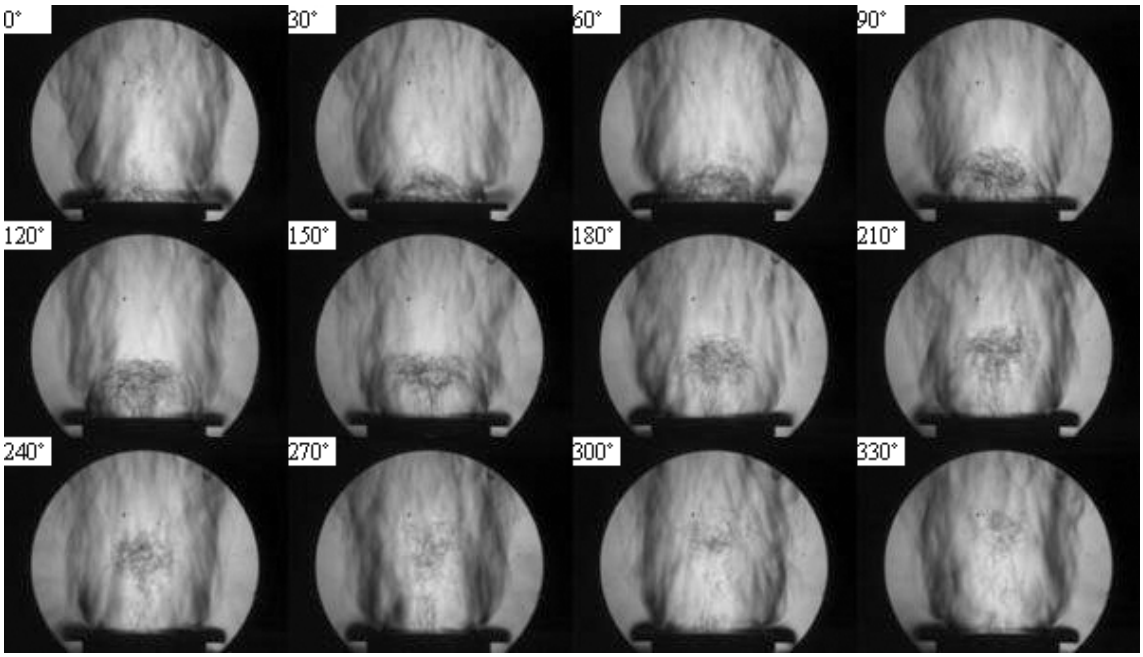

Fig. C.38: Phase-lock-averaged Schlieren images of a cycle at forcing amplitude 15V and forcing frequency 240 Hz.

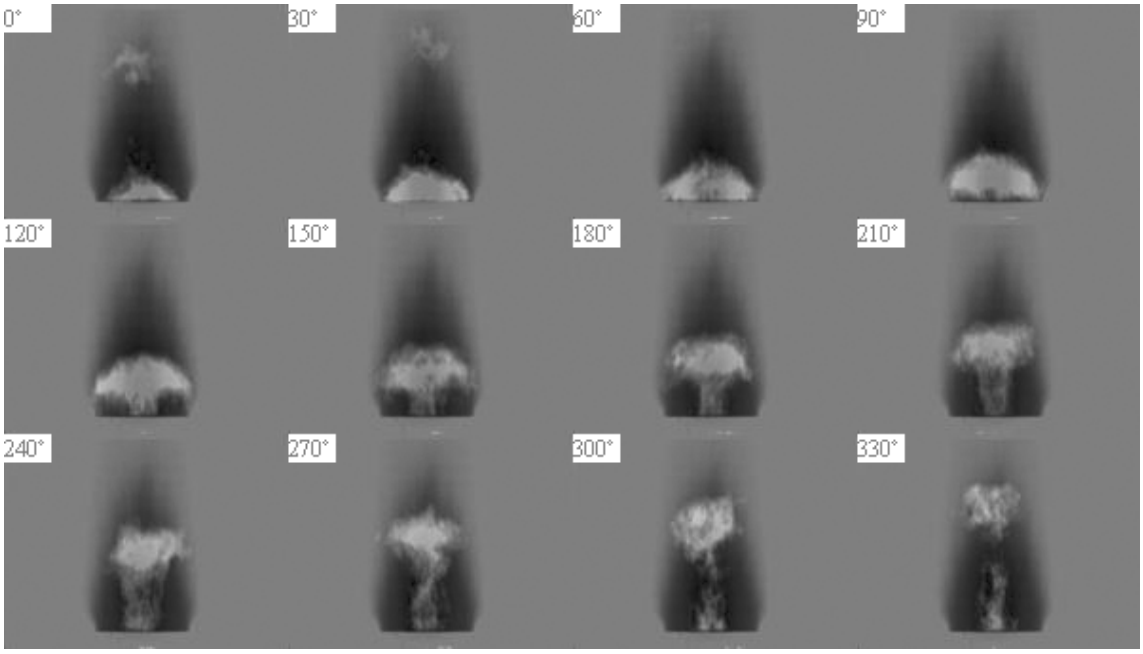

Fig. C.39: Phase-locked CH chemiluminescence oscillation images of a cycle at forcing amplitude 15V and forcing frequency 240 Hz.

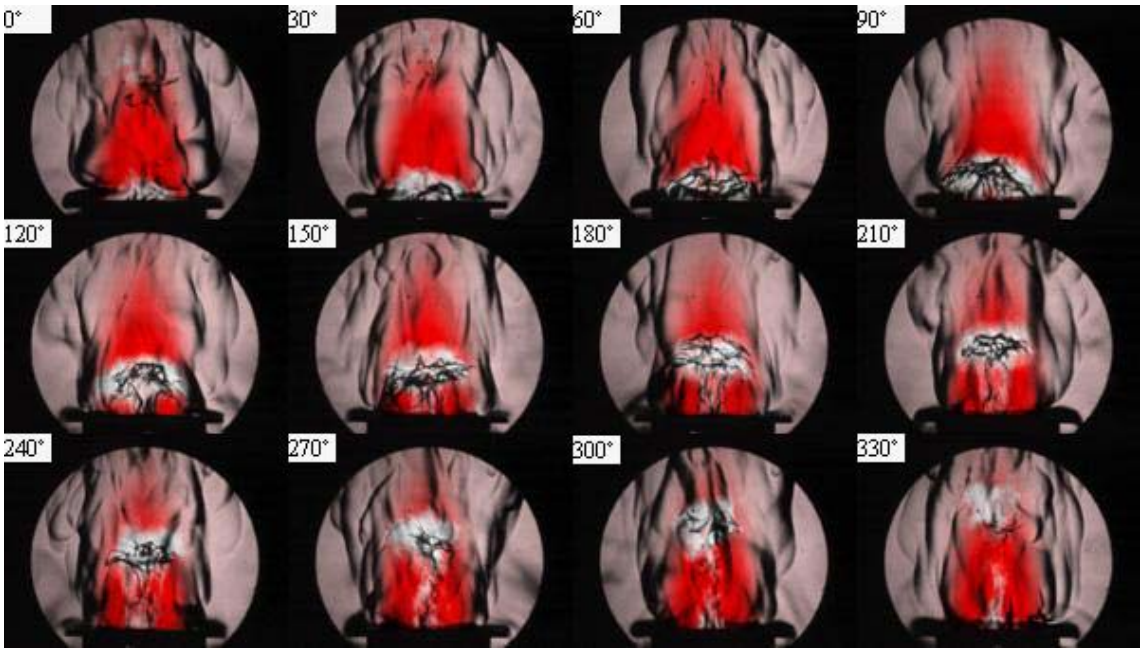

Fig. C.40: Phase-resolved visualization of instantaneous Schlieren and CH chemiluminescence images of a cycle at forcing amplitude 15V and forcing frequency 240 Hz.

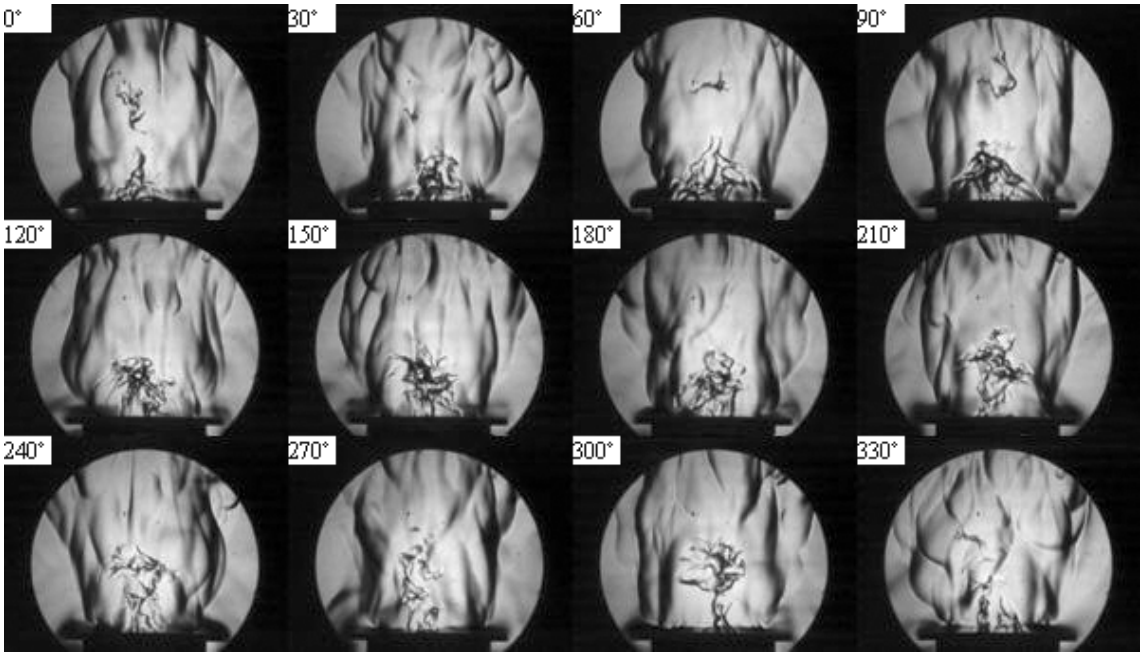

Fig. C.41: Phase-locked instantaneous Schlieren images of a cycle at forcing amplitude 15V and forcing frequency 300 Hz.

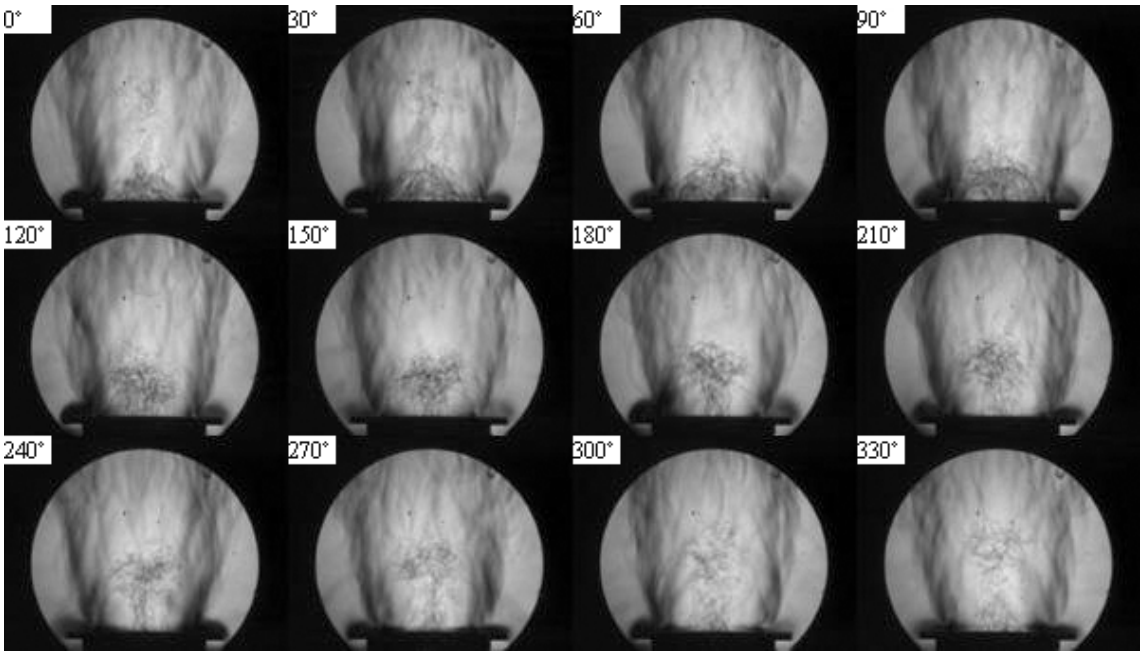

Fig. C.42: Phase-lock-averaged Schlieren images of a cycle at forcing amplitude 15V and forcing frequency 300 Hz.

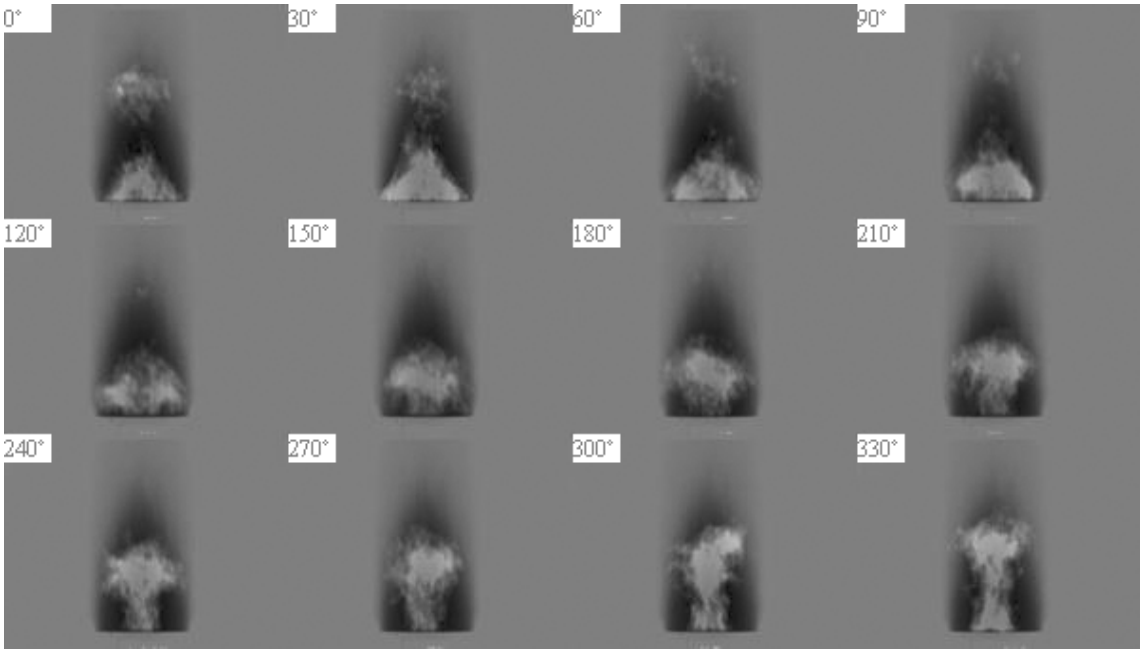

Fig. C.43: Phase-locked CH chemiluminescence oscillation images of a cycle at forcing amplitude 15V and forcing frequency 300 Hz.

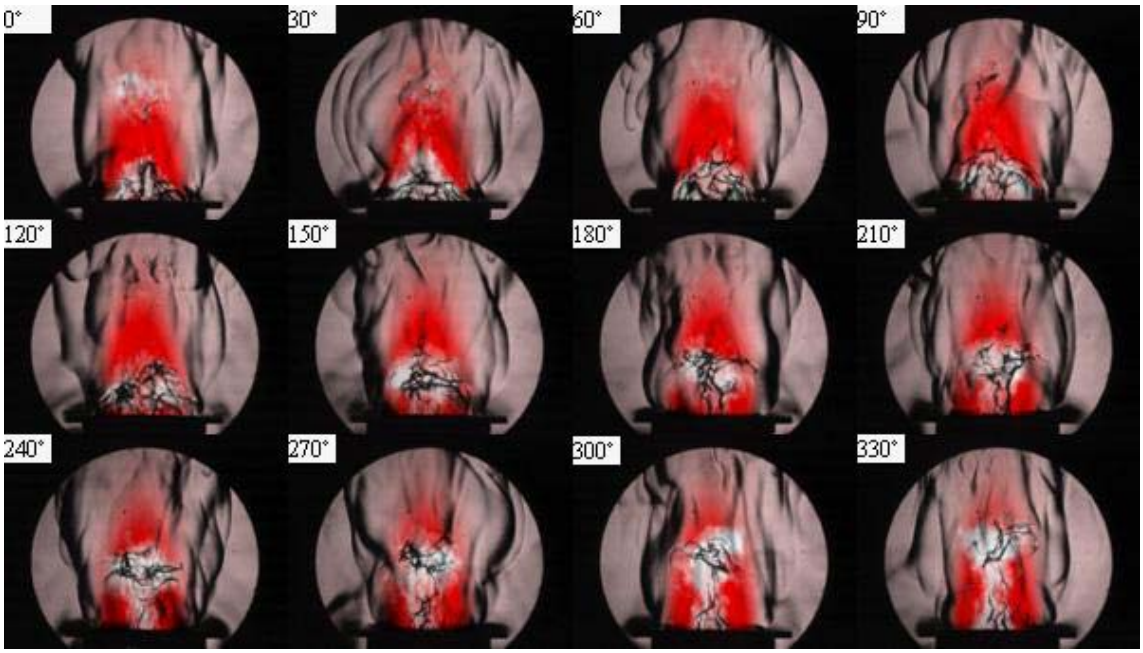

Fig. C.44: Phase-resolved visualization of instantaneous Schlieren and CH chemiluminescence images of a cycle at forcing amplitude 15V and forcing frequency 300 Hz.

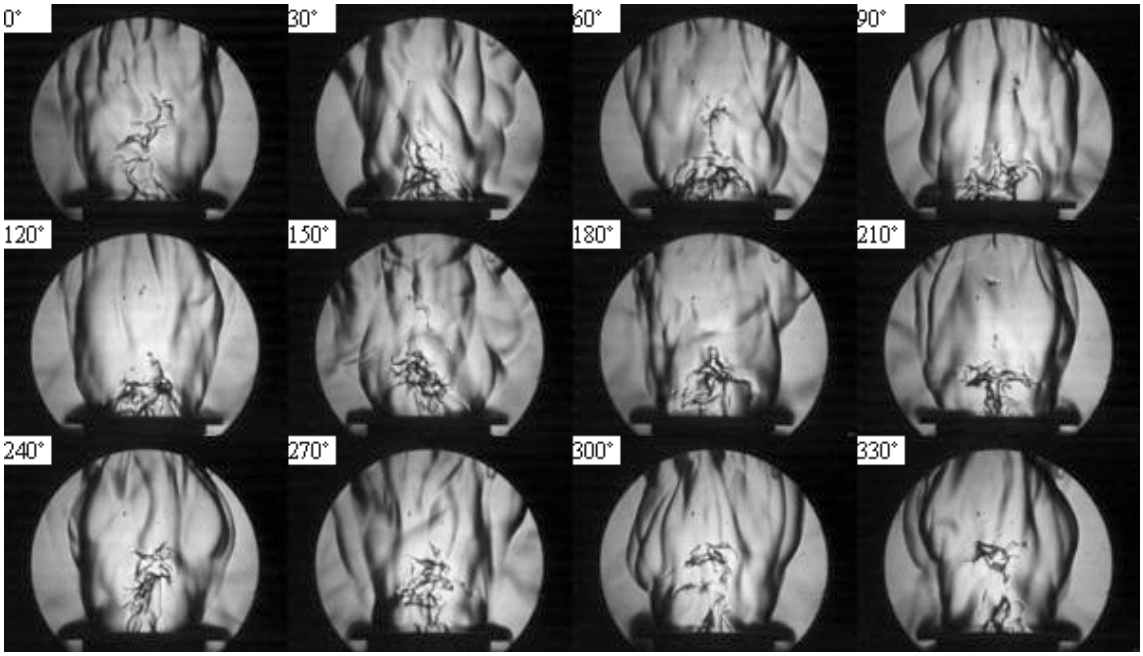

Fig. C.45: Phase-locked instantaneous Schlieren images of a cycle at forcing amplitude 15V and forcing frequency 360 Hz.

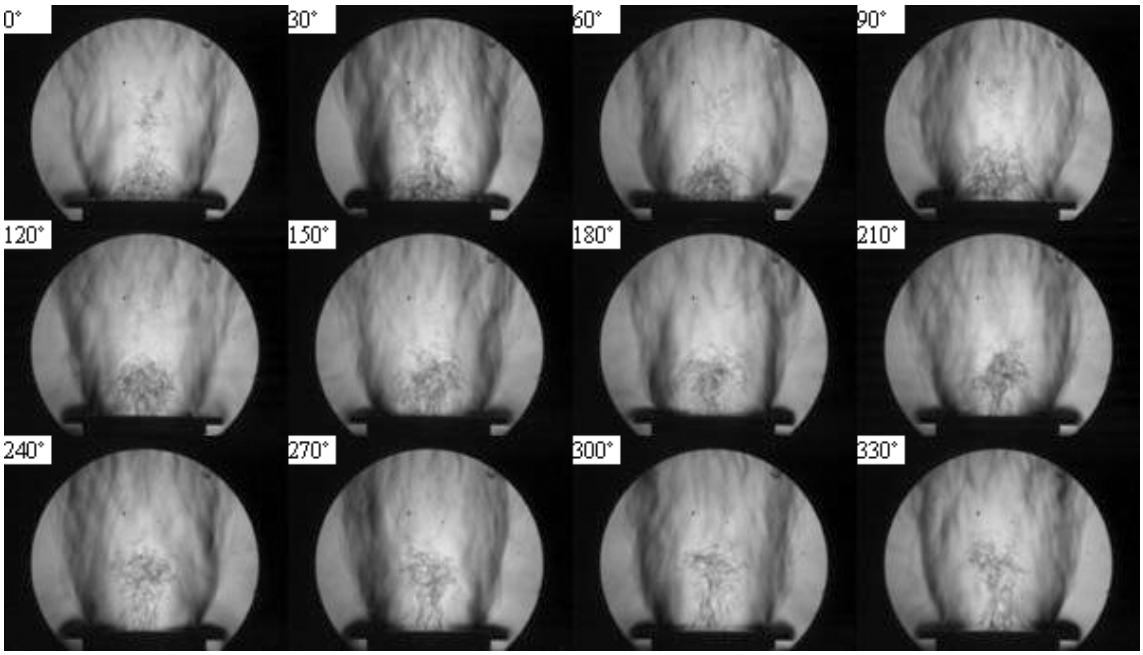

Fig. C.46: Phase-lock-averaged Schlieren images of a cycle at forcing amplitude 15V and forcing frequency 360 Hz.

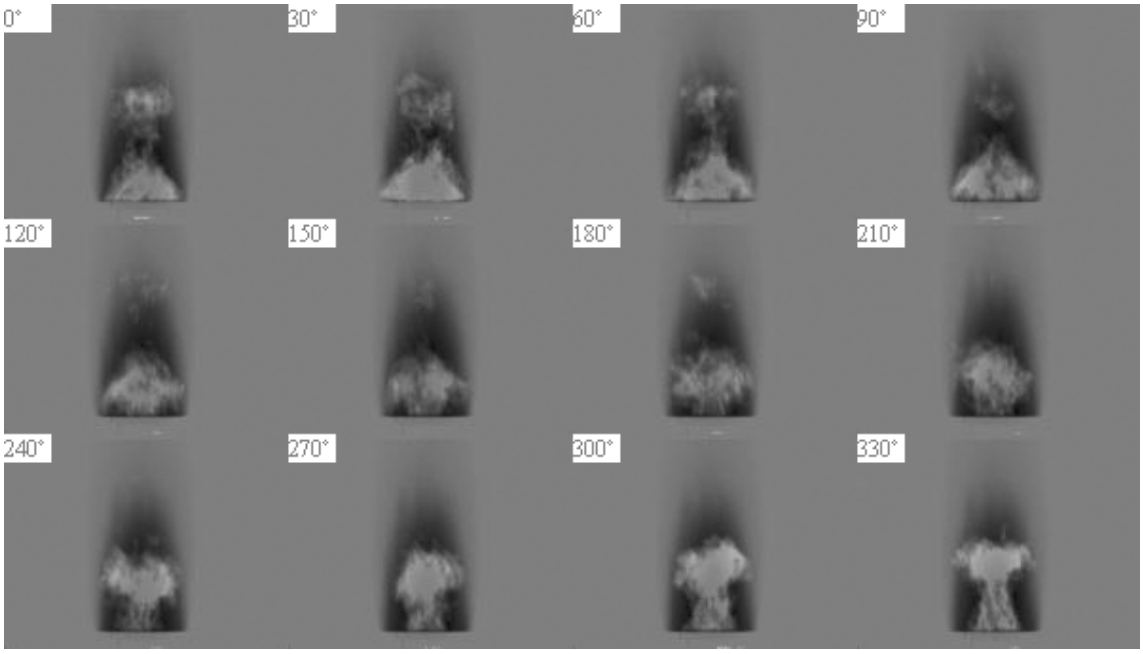

Fig. C.47: Phase-locked CH chemiluminescence oscillation images of a cycle at forcing amplitude 15V and forcing frequency 360 Hz.

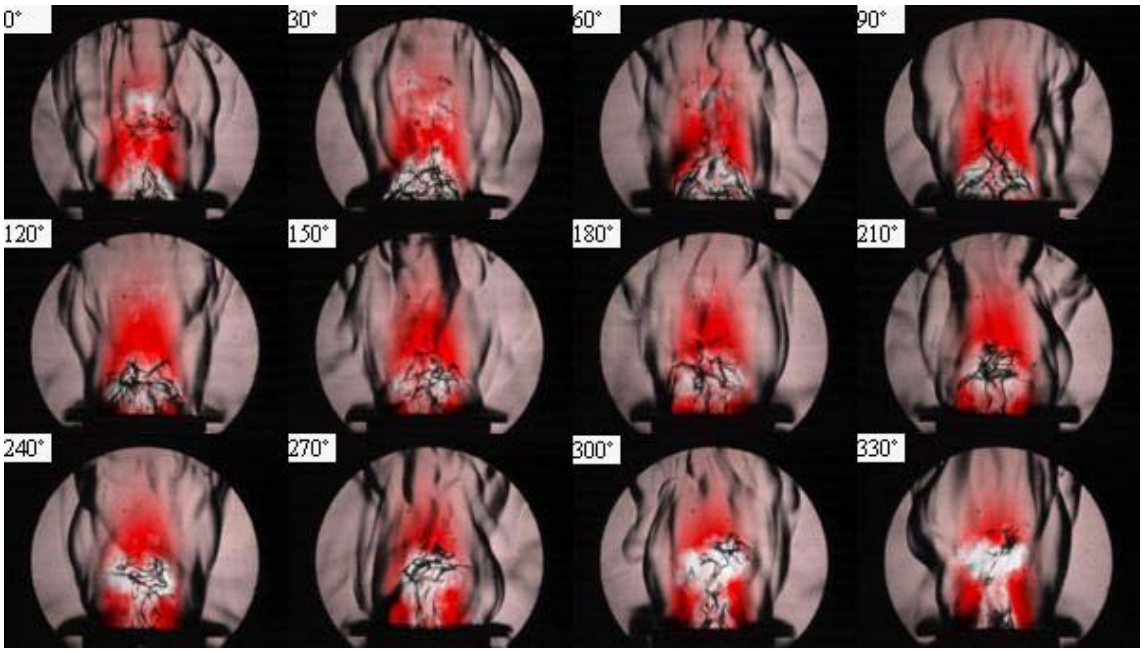

Fig. C.48: Phase-resolved visualization of instantaneous Schlieren and CH chemiluminescence images of a cycle at forcing amplitude 15V and forcing frequency 360 Hz.

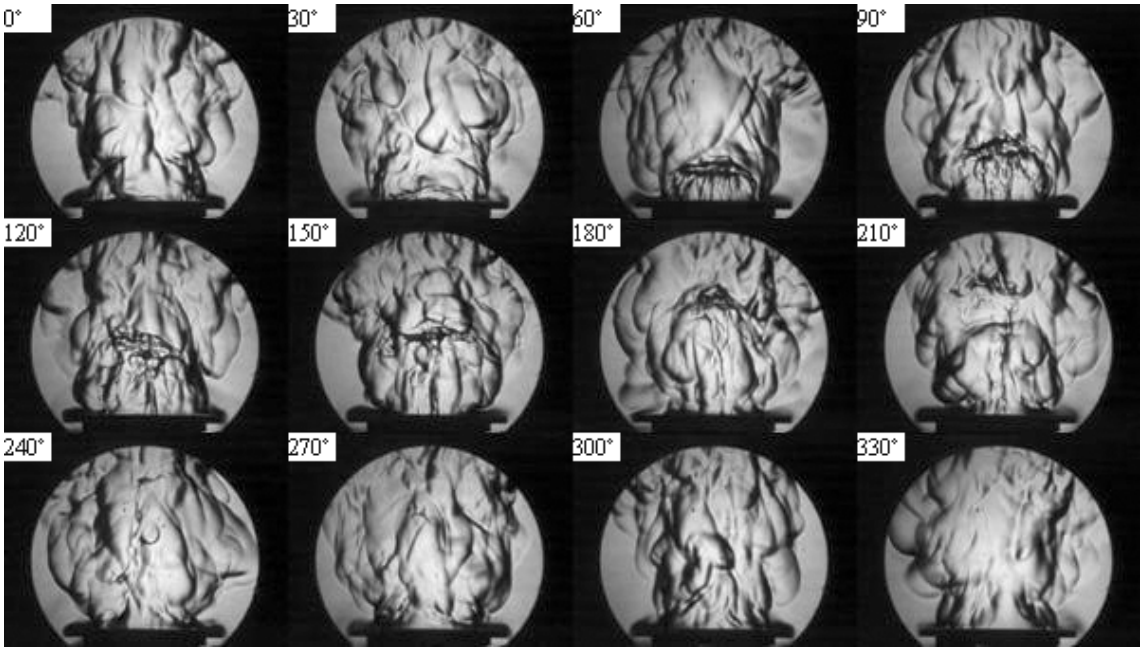

Fig. C.49: Phase-locked instantaneous Schlieren images of a cycle at forcing amplitude 20V and forcing frequency 180 Hz.

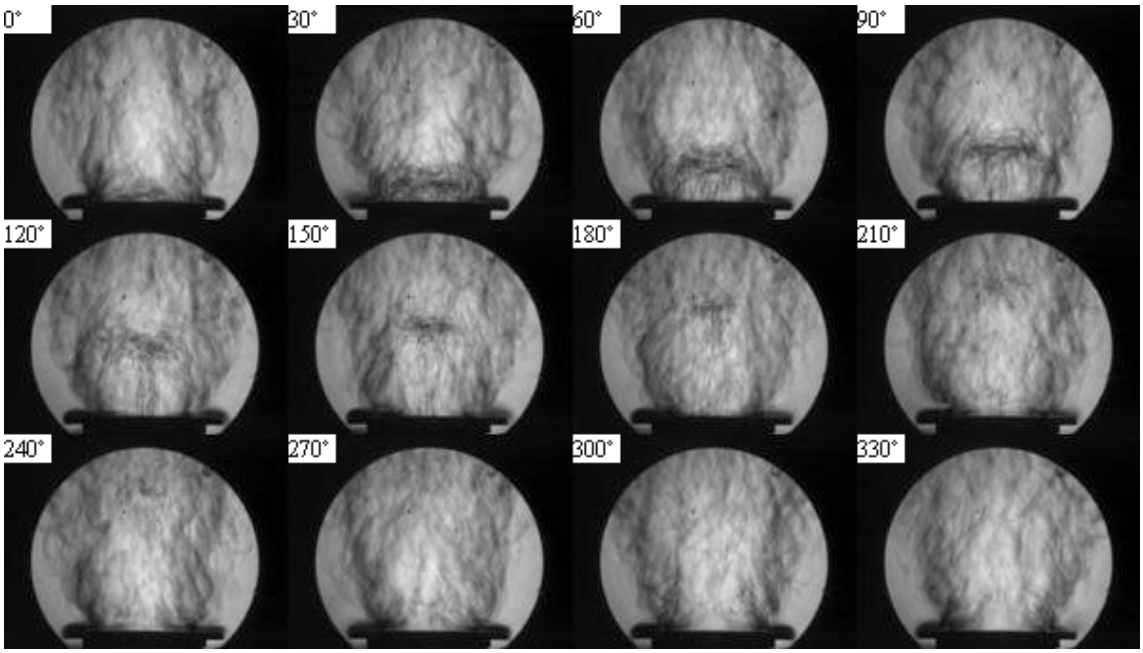

Fig. C.50: Phase-lock-averaged Schlieren images of a cycle at forcing amplitude 20V and forcing frequency 180 Hz.

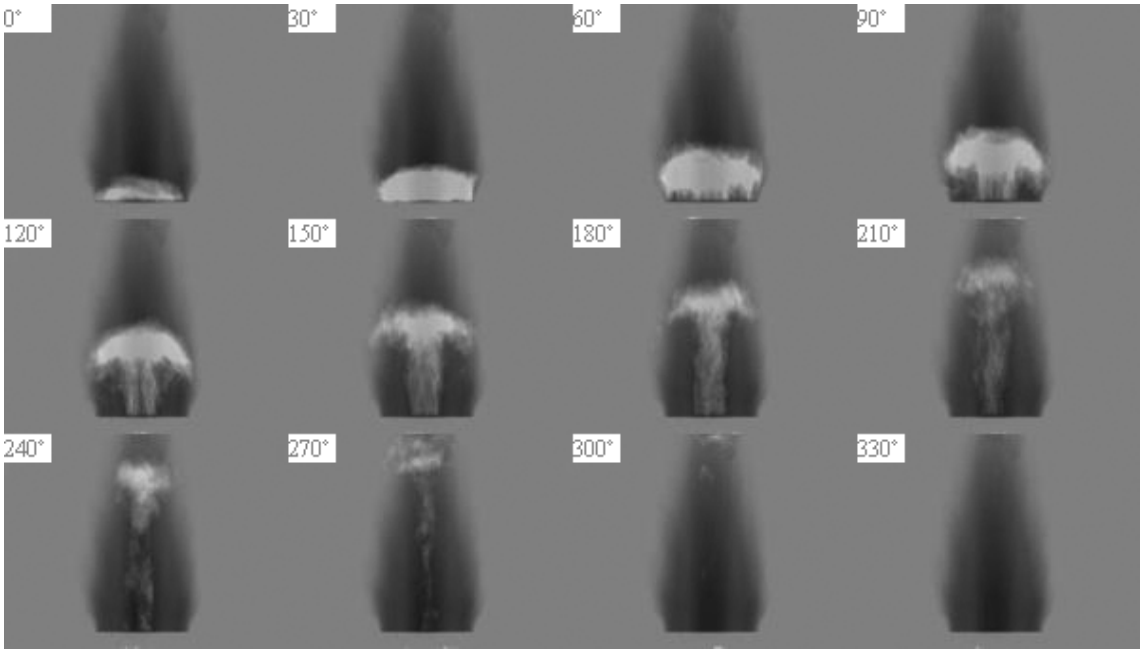

Fig. C.51: Phase-locked CH chemiluminescence oscillation images of a cycle at forcing amplitude 20V and forcing frequency 180 Hz.

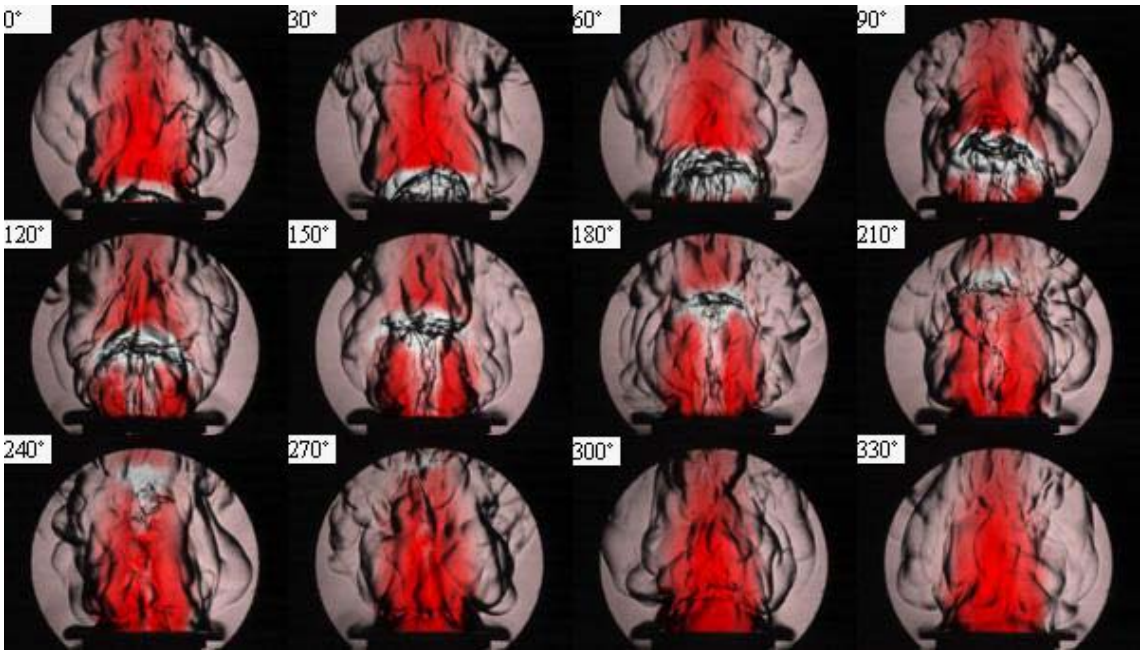

Fig. C.52: Phase-resolved visualization of instantaneous Schlieren and CH chemiluminescence images of a cycle at forcing amplitude 20V and forcing frequency 180 Hz.

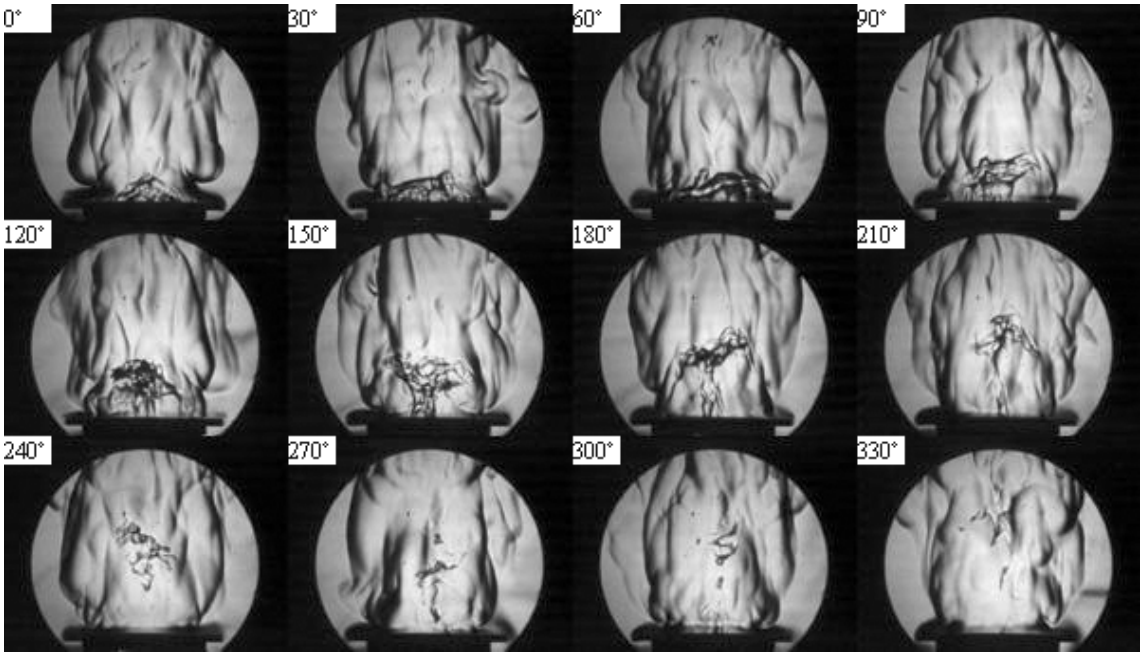

Fig. C.53: Phase-locked instantaneous Schlieren images of a cycle at forcing amplitude 20V and forcing frequency 240 Hz.

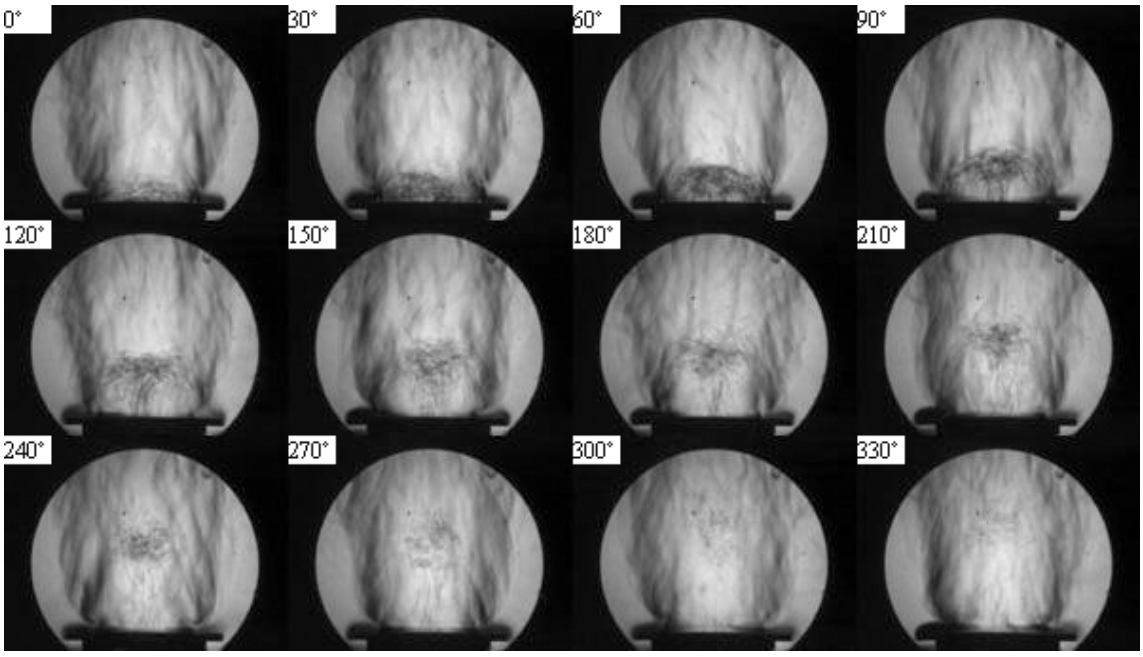

Fig. C.54: Phase-lock-averaged Schlieren images of a cycle at forcing amplitude 20V and forcing frequency 240 Hz.

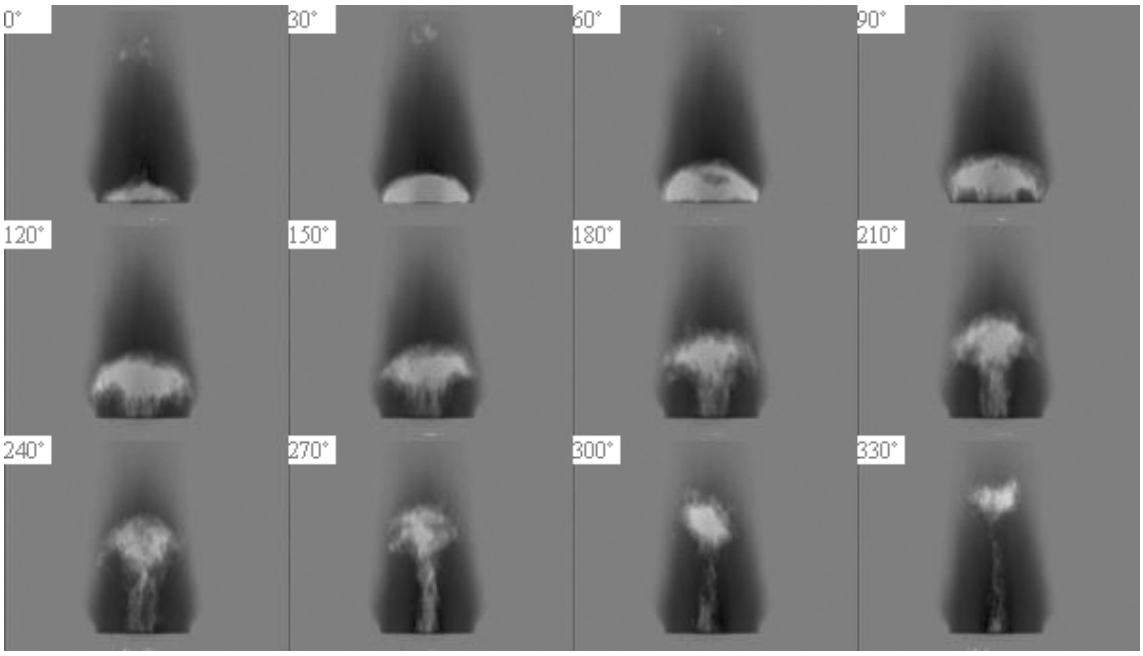

Fig. C.55: Phase-locked CH chemiluminescence oscillation images of a cycle at forcing amplitude 20V and forcing frequency 240 Hz.

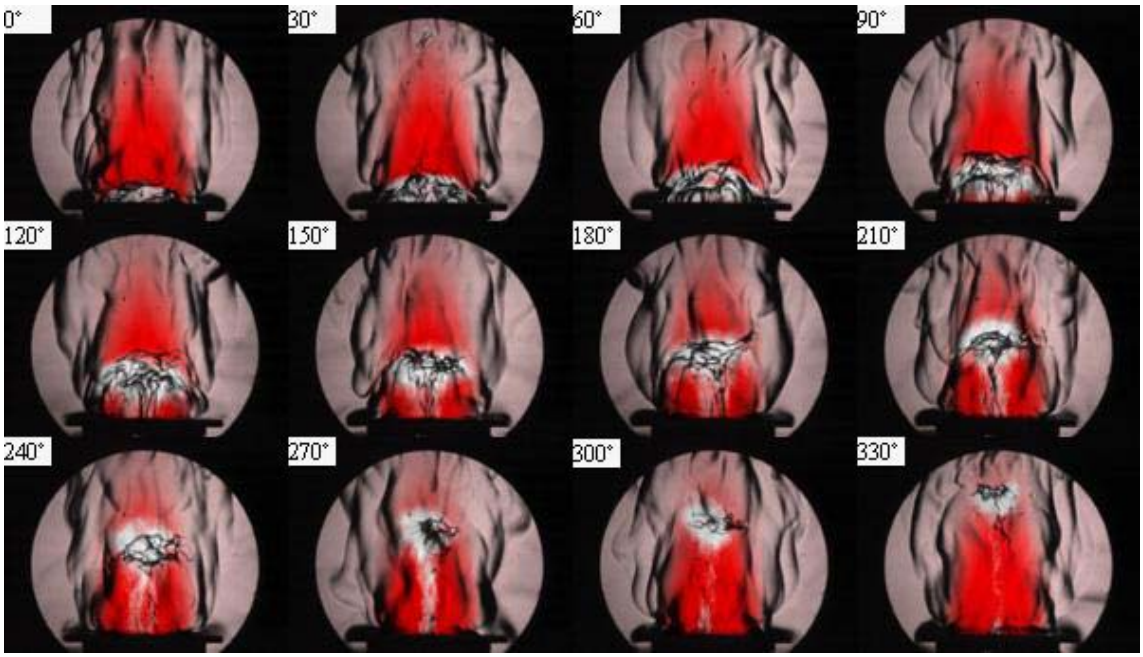

Fig. C.56: Phase-resolved visualization of instantaneous Schlieren and CH chemiluminescence images of a cycle at forcing amplitude 20V and forcing frequency 240 Hz.

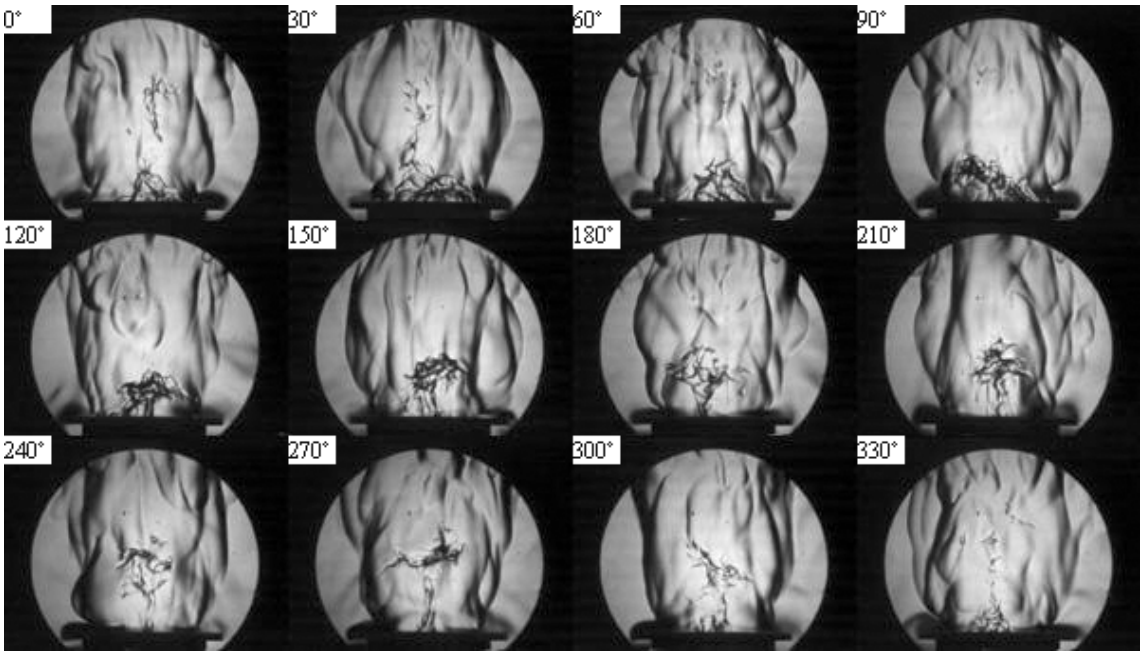

Fig. C.57: Phase-locked instantaneous Schlieren images of a cycle at forcing amplitude 20V and forcing frequency 300 Hz.

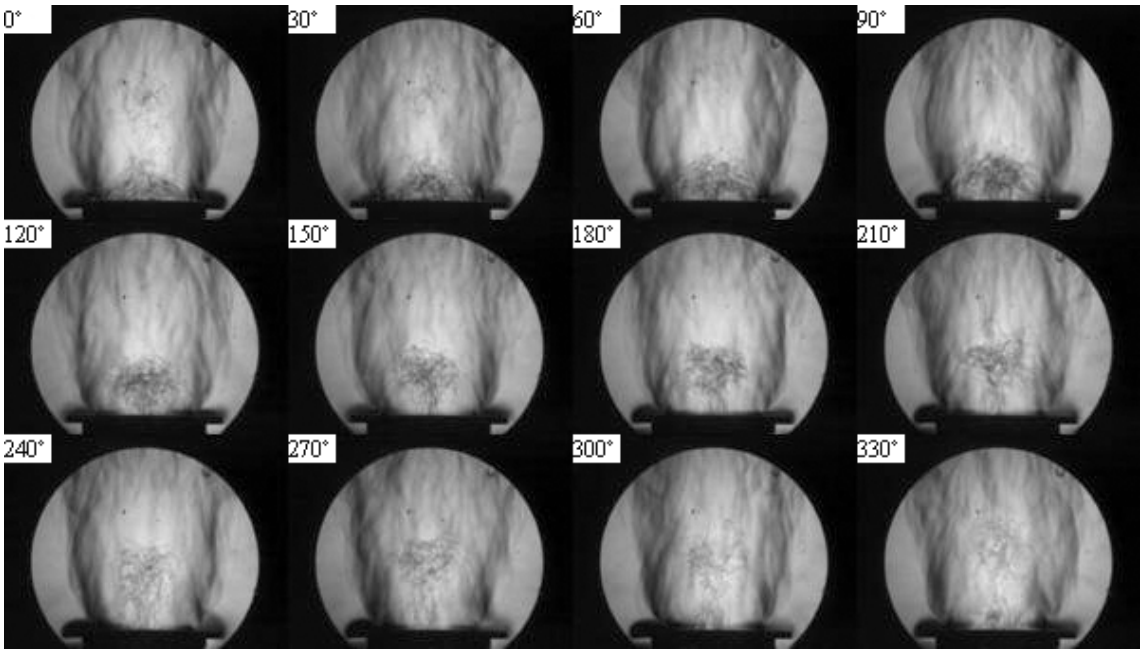

Fig. C.58: Phase-lock-averaged Schlieren images of a cycle at forcing amplitude 20V and forcing frequency 300 Hz.

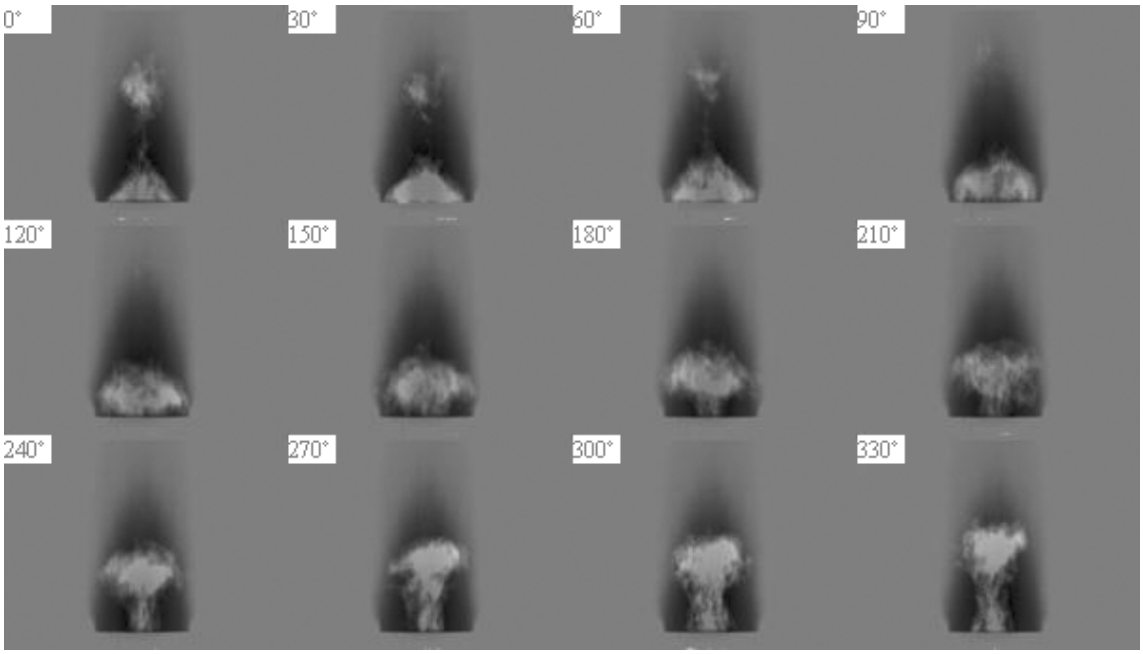

Fig. C.59: Phase-locked CH chemiluminescence oscillation images of a cycle at forcing amplitude 20V and forcing frequency 300 Hz.

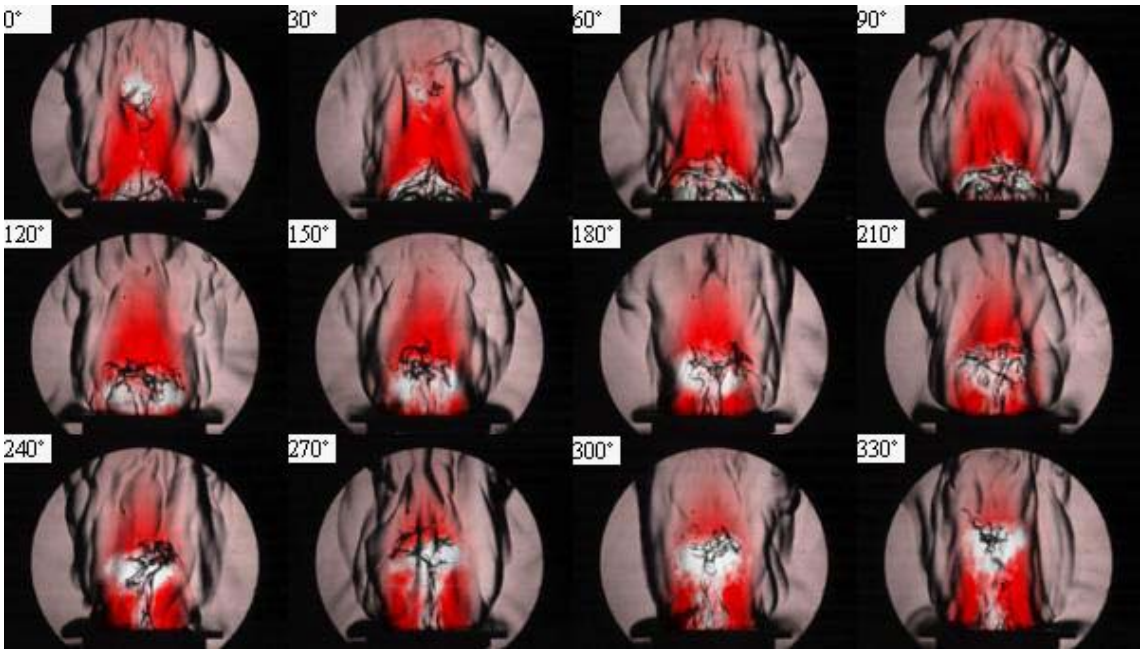

Fig. C.60: Phase-resolved visualization of instantaneous Schlieren and CH chemiluminescence images of a cycle at forcing amplitude 20V and forcing frequency 300 Hz.

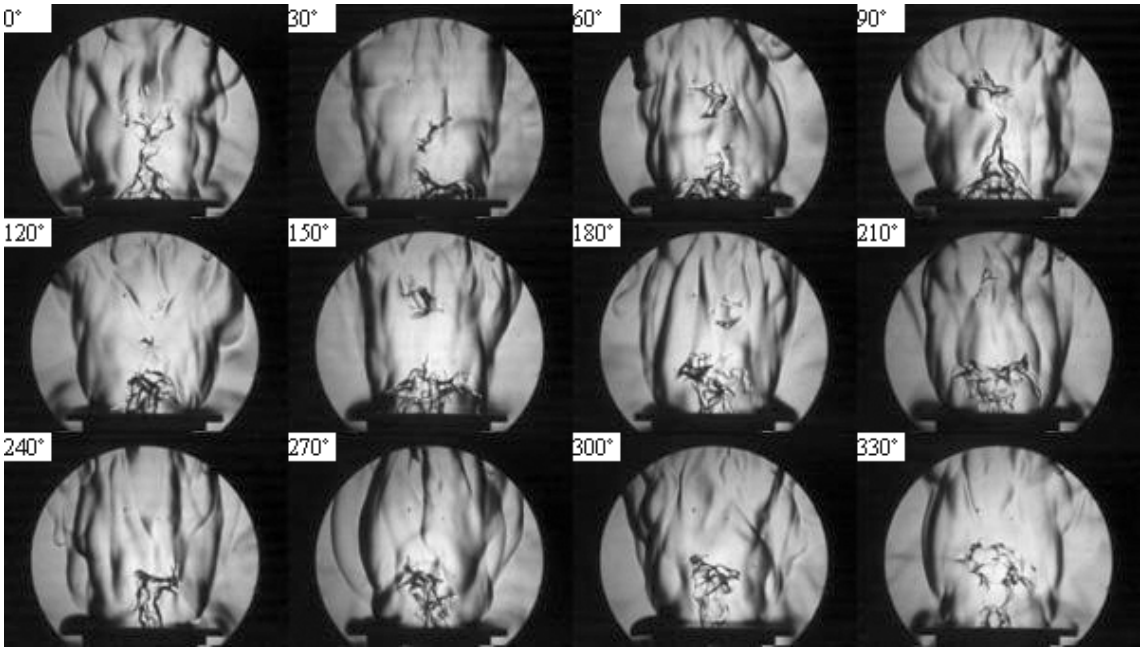

Fig. C.61: Phase-locked instantaneous Schlieren images of a cycle at forcing amplitude 20V and forcing frequency 360 Hz.

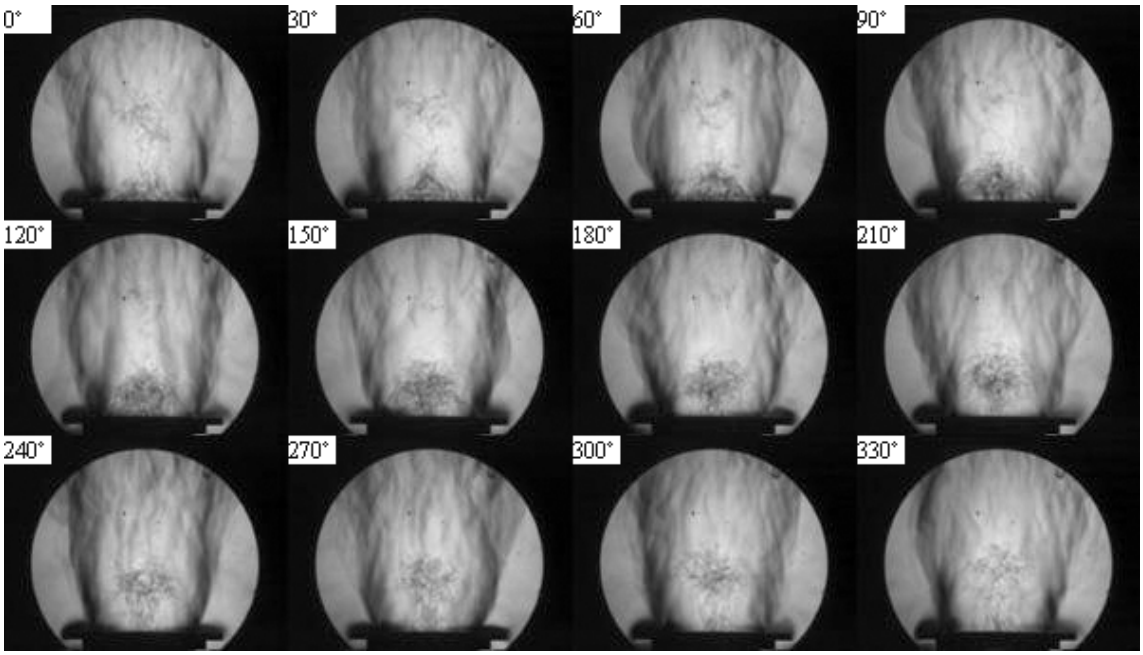

Fig. C.62: Phase-lock-averaged Schlieren images of a cycle at forcing amplitude 20V and forcing frequency 360 Hz.

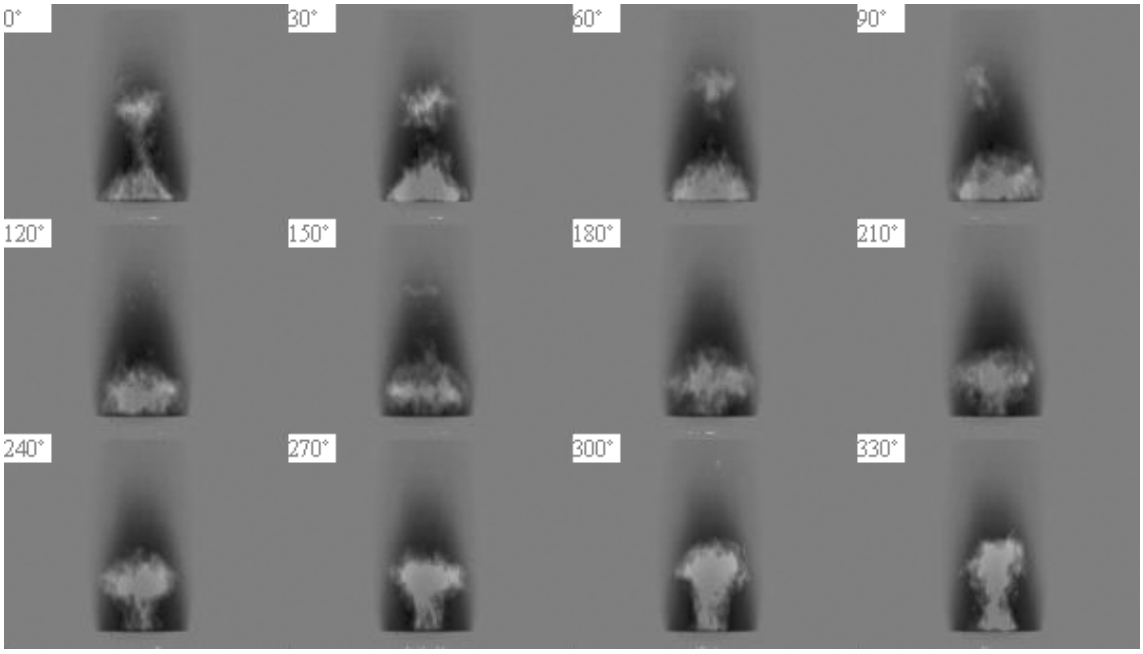

Fig. C.63: Phase-locked CH chemiluminescence oscillation images of a cycle at forcing amplitude 20V and forcing frequency 360 Hz.

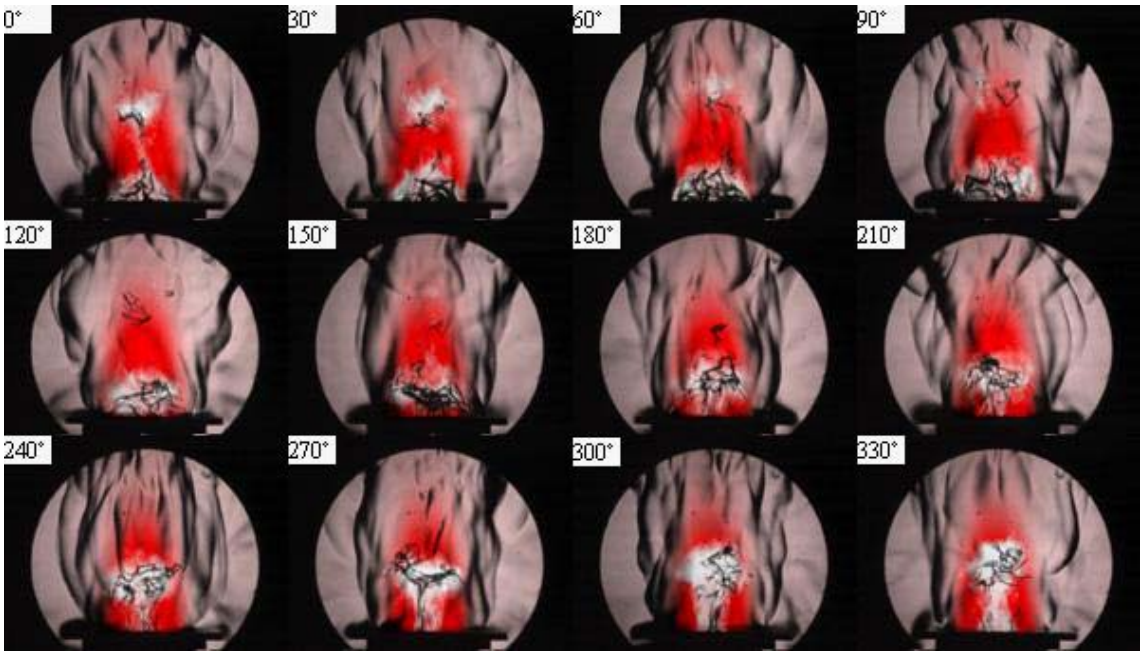

Fig. C.64: Phase-resolved visualization of instantaneous Schlieren and CH chemiluminescence images of a cycle at forcing amplitude 20V and forcing frequency 360 Hz.

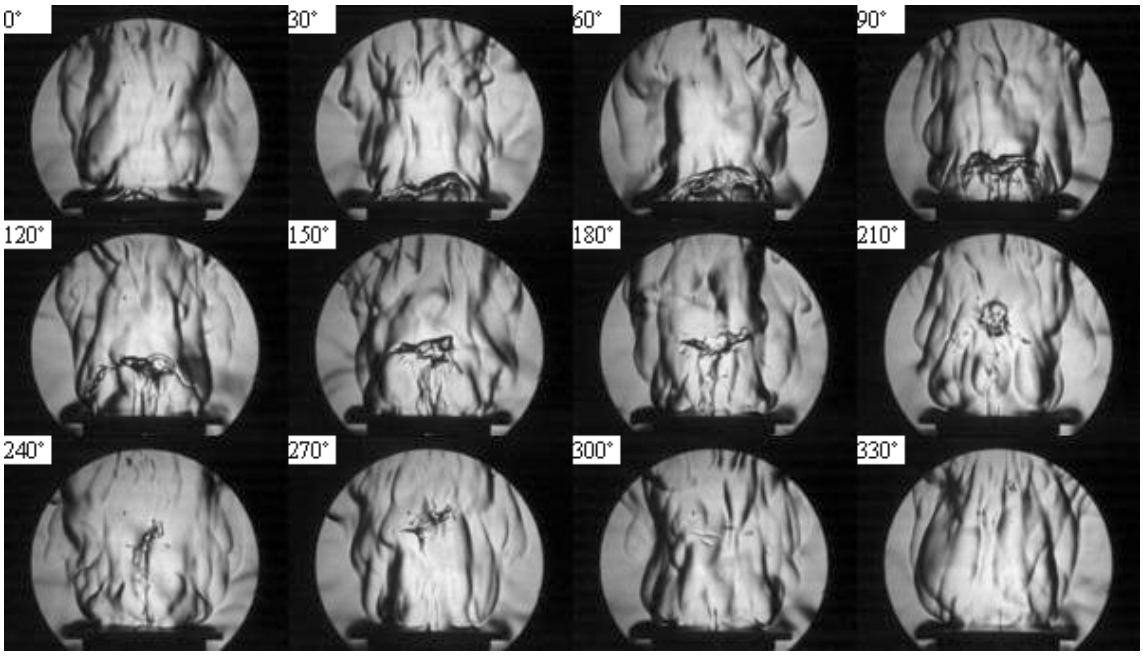

Fig. C.65: Phase-locked instantaneous Schlieren images of a cycle at forcing amplitude 25V and forcing frequency 240 Hz.

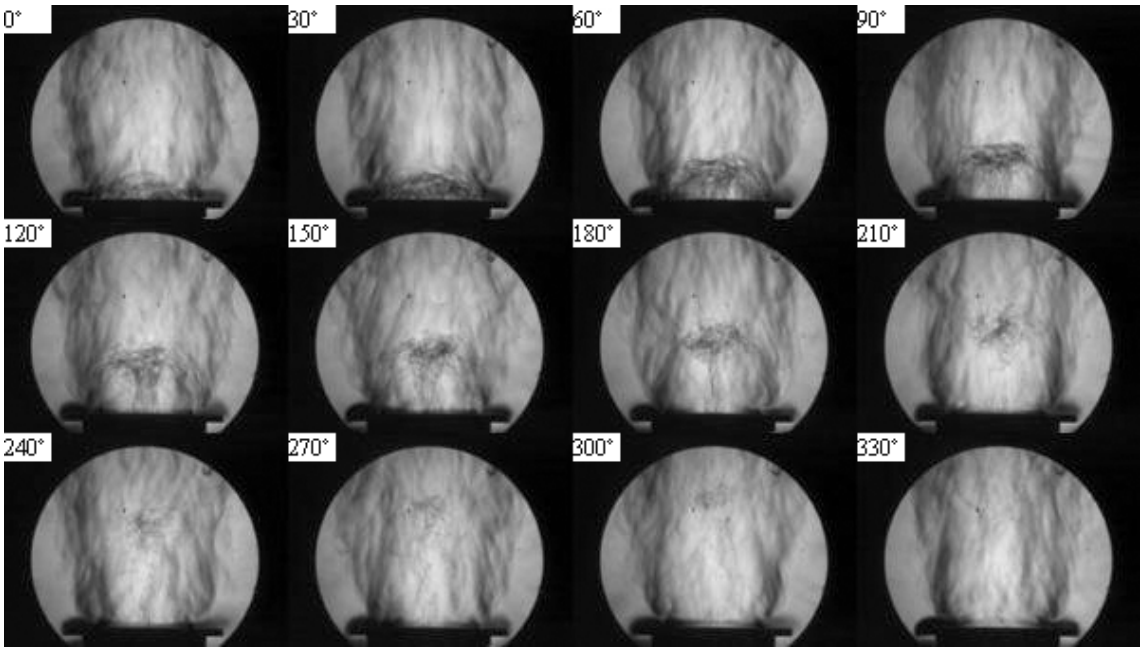

Fig. C.66: Phase-lock-averaged Schlieren images of a cycle at forcing amplitude 25V and forcing frequency 240 Hz.

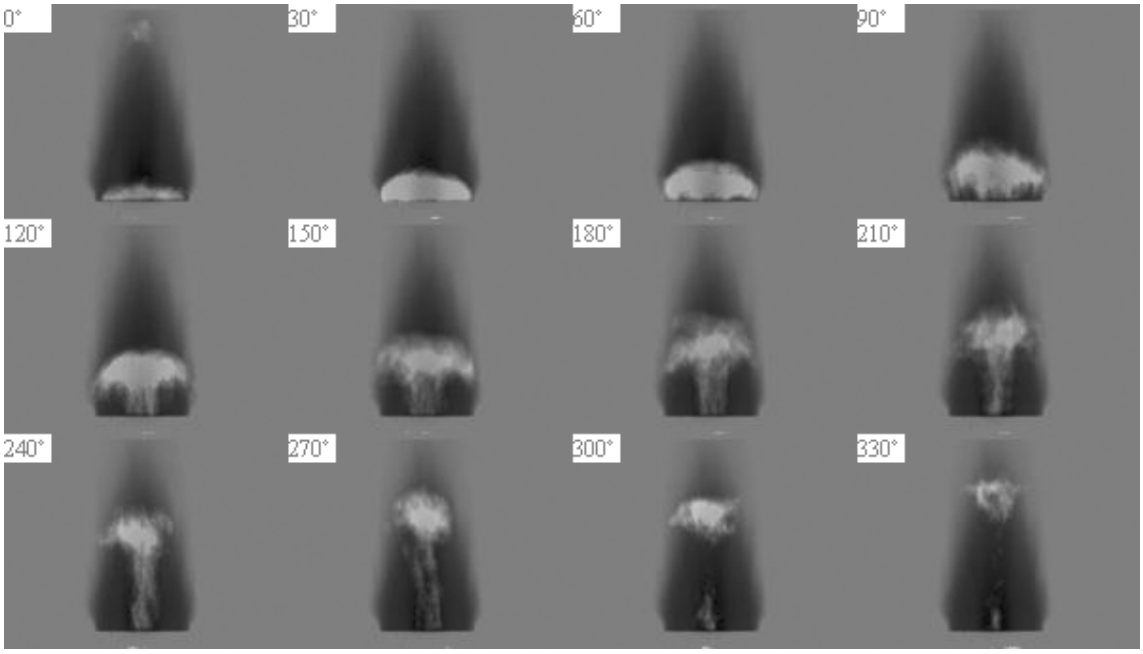

Fig. C.67: Phase-locked CH chemiluminescence oscillation images of a cycle at forcing amplitude 25V and forcing frequency 240 Hz.

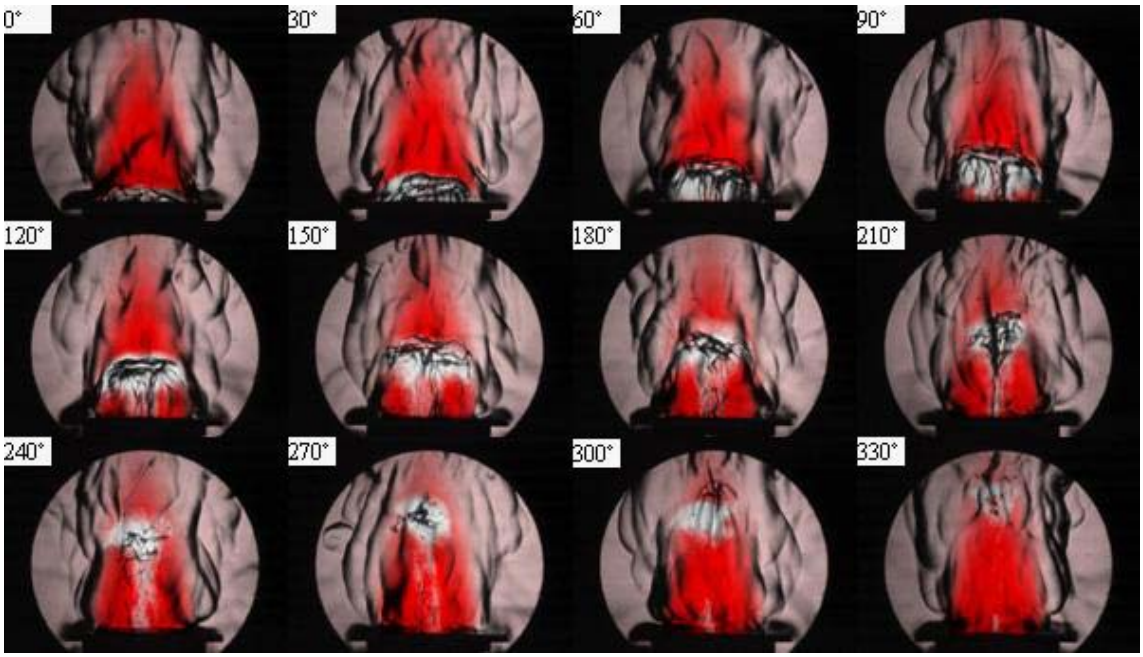

Fig. C.68: Phase-resolved visualization of instantaneous Schlieren and CH chemiluminescence images of a cycle at forcing amplitude 25V and forcing frequency 240 Hz.

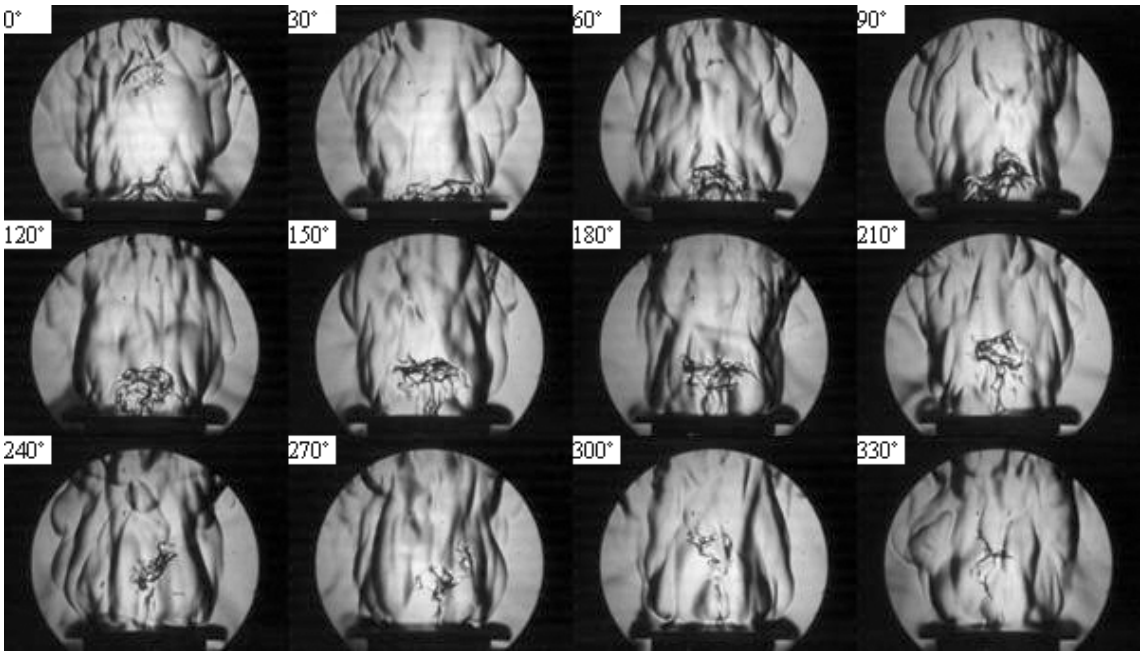

Fig. C.69: Phase-locked instantaneous Schlieren images of a cycle at forcing amplitude 25V and forcing frequency 300 Hz.

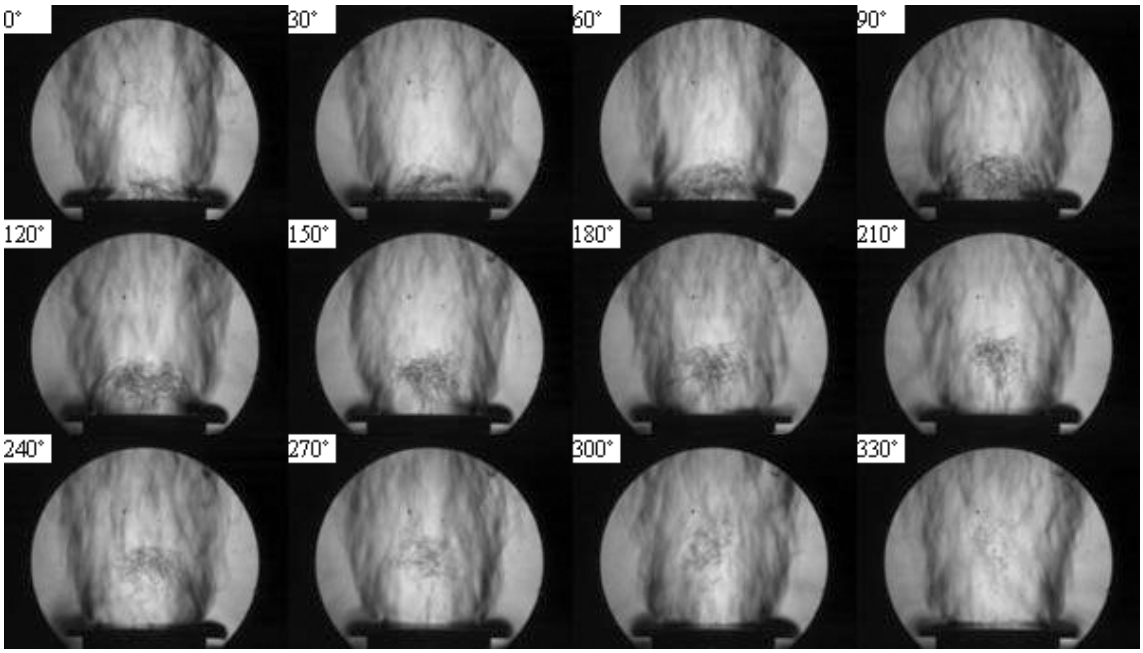

Fig. C.70: Phase-lock-averaged Schlieren images of a cycle at forcing amplitude 25V and forcing frequency 300 Hz.

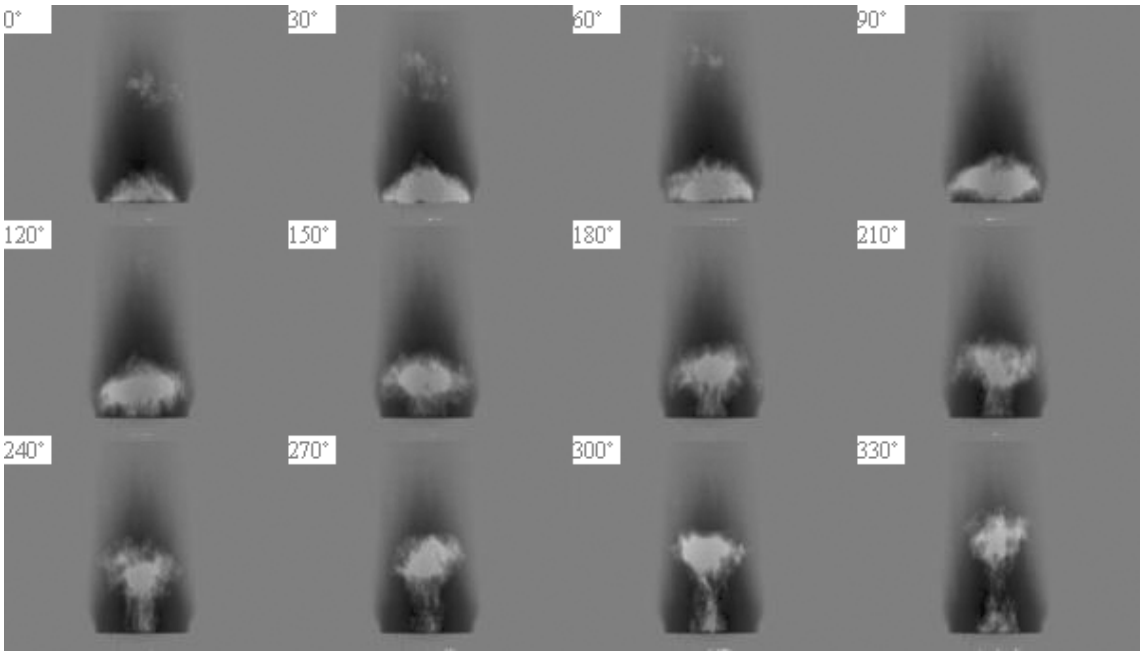

Fig. C.71: Phase-locked CH chemiluminescence oscillation images of a cycle at forcing amplitude 25V and forcing frequency 300 Hz.

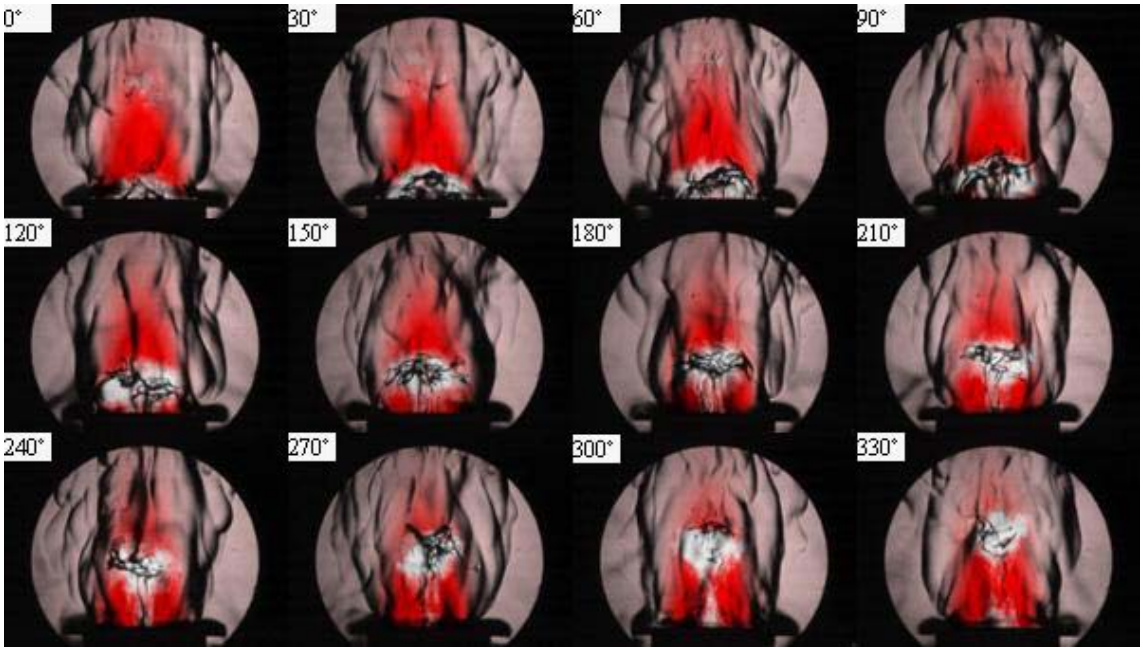

Fig. C.72: Phase-resolved visualization of instantaneous Schlieren and CH chemiluminescence images of a cycle at forcing amplitude 25V and forcing frequency 300 Hz.

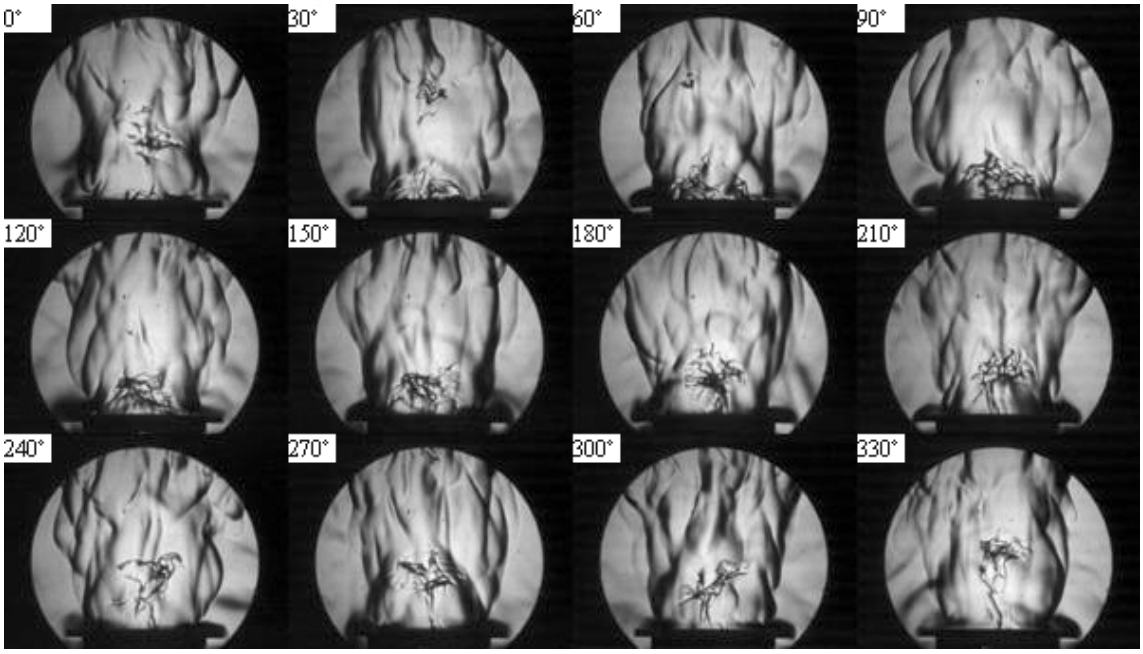

Fig. C.73: Phase-locked instantaneous Schlieren images of a cycle at forcing amplitude 25V and forcing frequency 360 Hz.

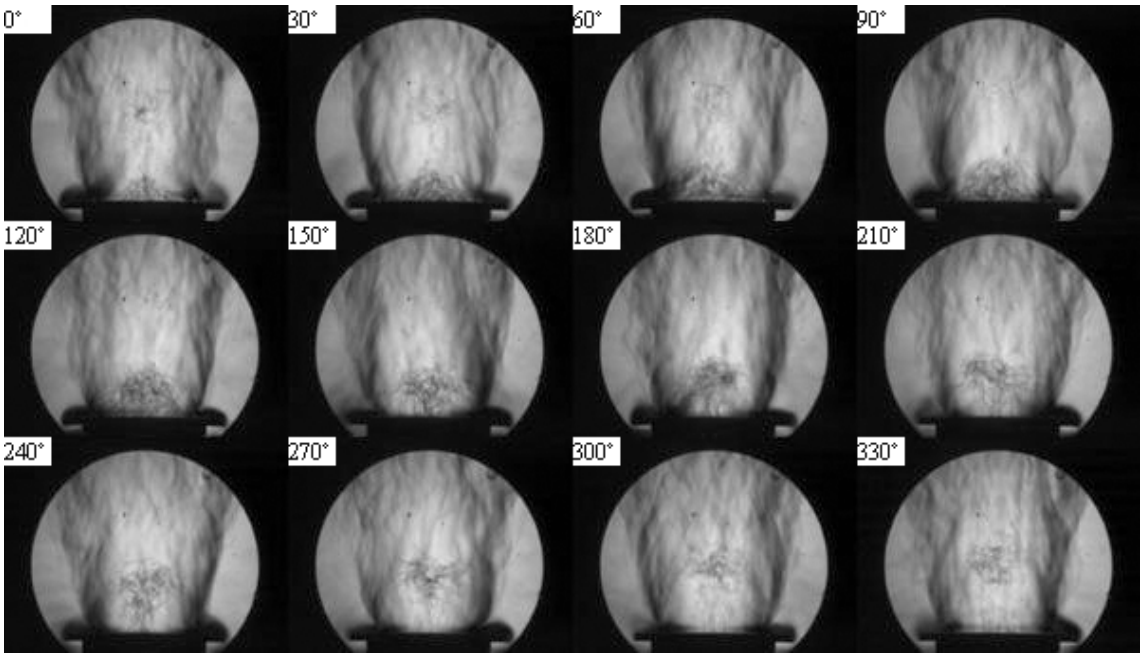

Fig. C.74: Phase-lock-averaged Schlieren images of a cycle at forcing amplitude 25V and forcing frequency 360 Hz.

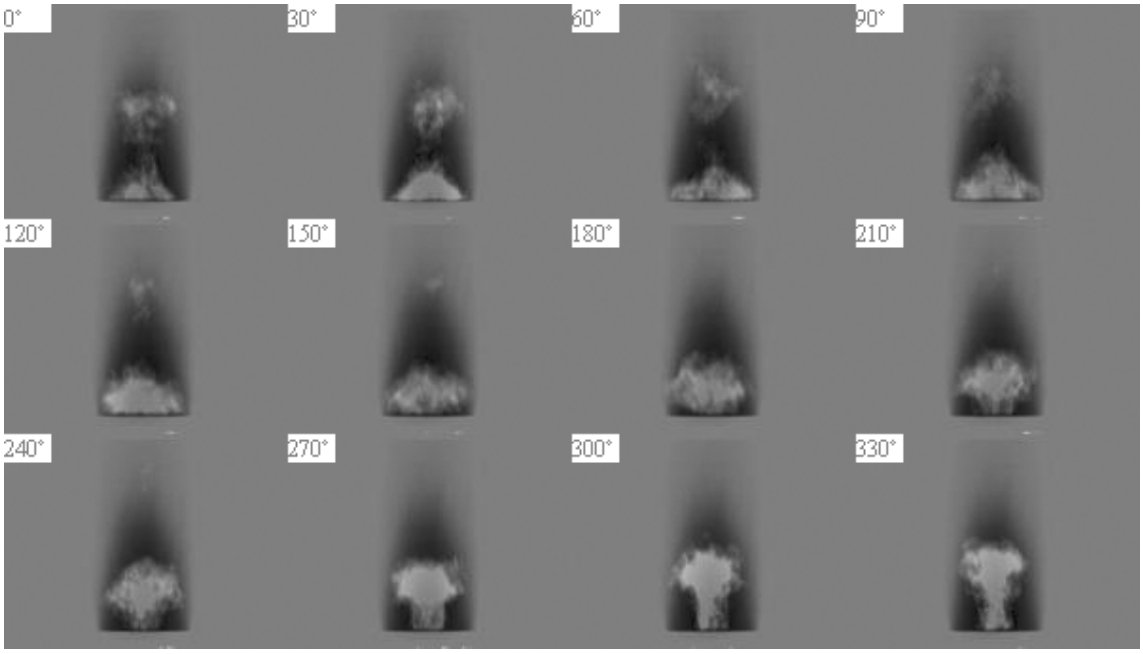

Fig. C.75: Phase-locked CH chemiluminescence oscillation images of a cycle at forcing amplitude 25V and forcing frequency 360 Hz.

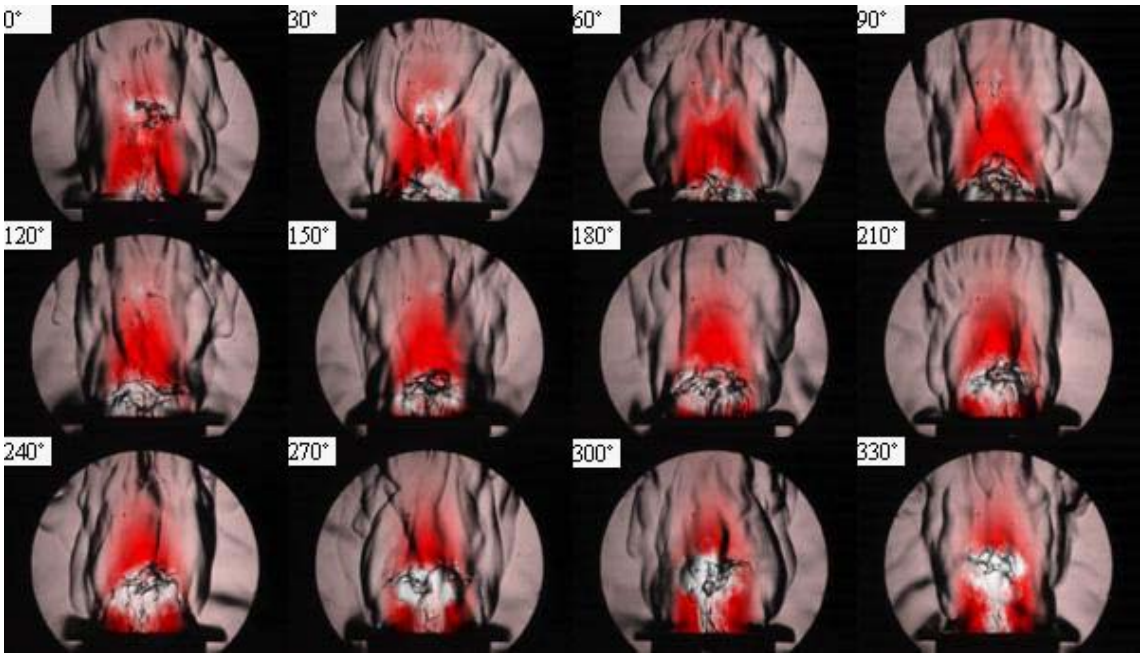

Fig. C.76: Phase-resolved visualization of instantaneous Schlieren and CH chemiluminescence images of a cycle at forcing amplitude 25V and forcing frequency 360 Hz.

Appendix D – Dynamic Pressure Trace and Spectra

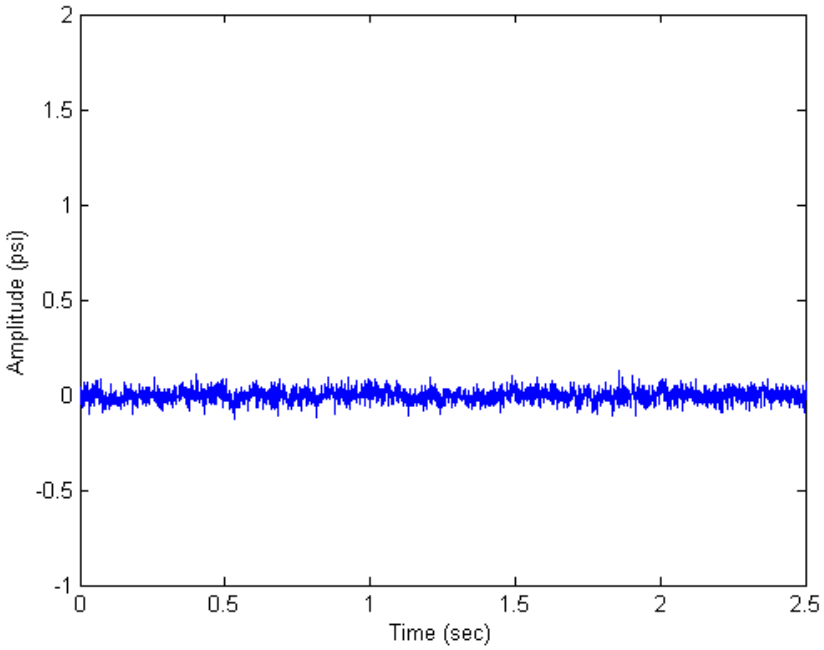

Fig. D.1: Dynamic pressure trace inside the dump combustor at equivalence ratio 0.5 and reference velocity 10 m/s.

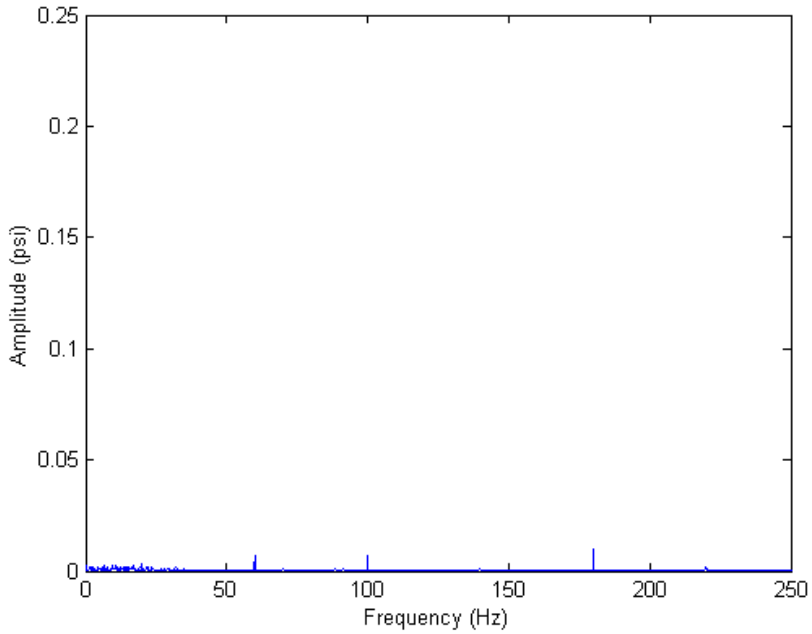

Fig. D.2: FFT of dynamic pressure trace inside the dump combustor at equivalence ratio 0.5 and reference velocity 10 m/s.

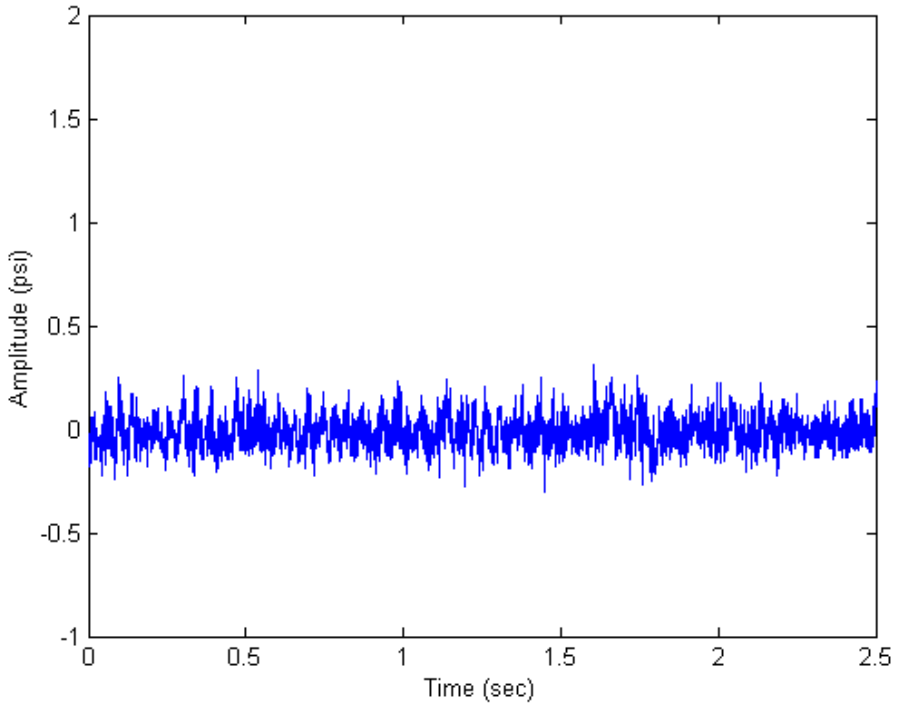

Fig. D.3: Dynamic pressure trace inside the dump combustor at equivalence ratio 0.5 and reference velocity 15 m/s.

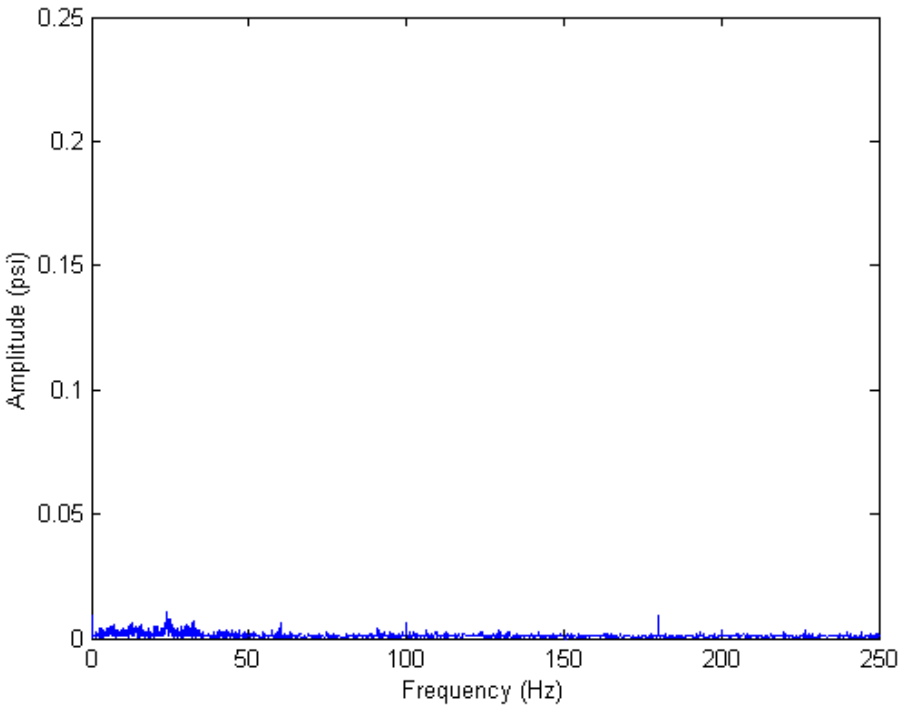

Fig. D.4: FFT of dynamic pressure trace inside the dump combustor at equivalence ratio 0.5 and reference velocity 15 m/s.

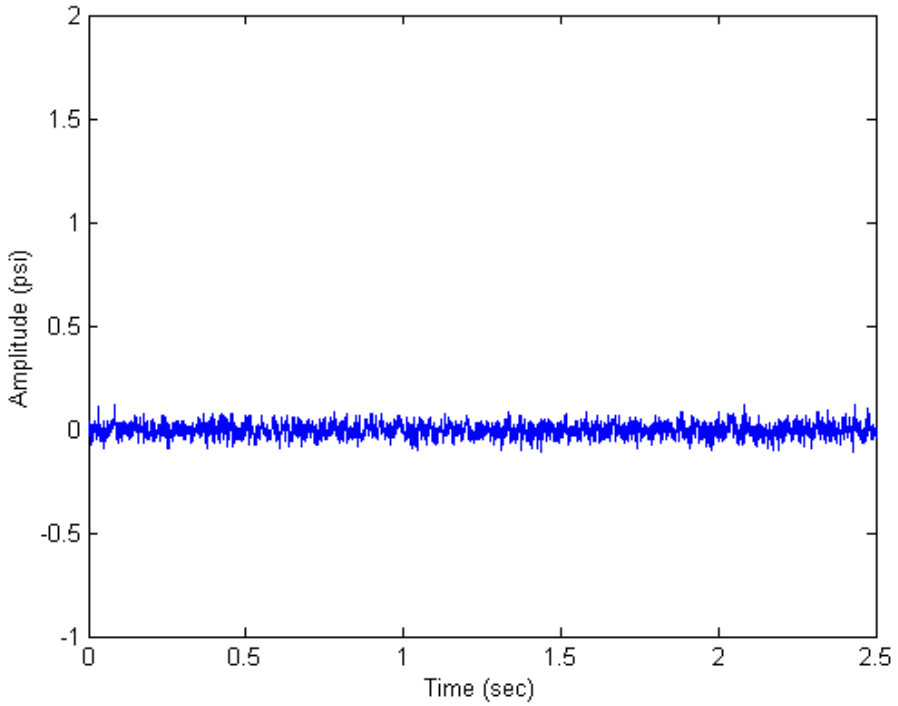

Fig. D.5: Dynamic pressure trace inside the dump combustor at equivalence ratio 0.525 and reference velocity 10 m/s.

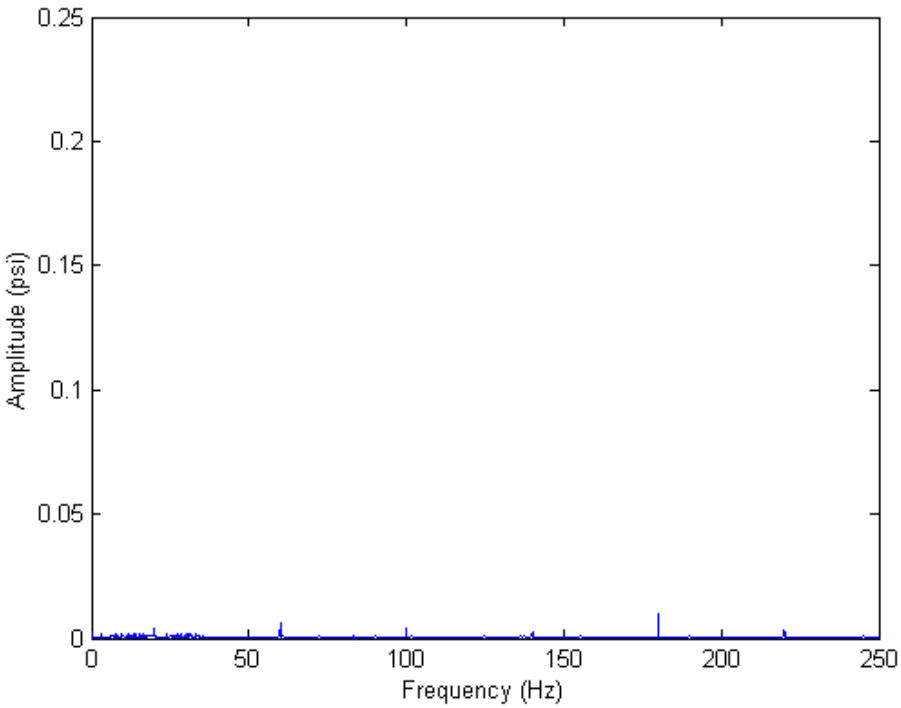

Fig. D.6: FFT of dynamic pressure trace inside the dump combustor at equivalence ratio 0.525 and reference velocity 10 m/s.

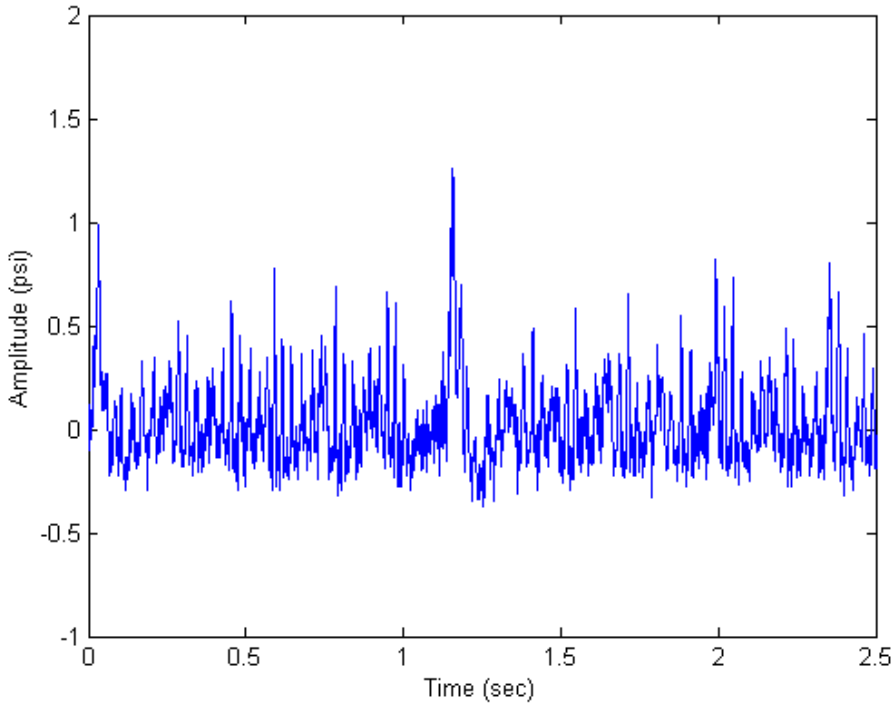

Fig. D.7: Dynamic pressure trace inside the dump combustor at equivalence ratio 0.525 and reference velocity 15 m/s.

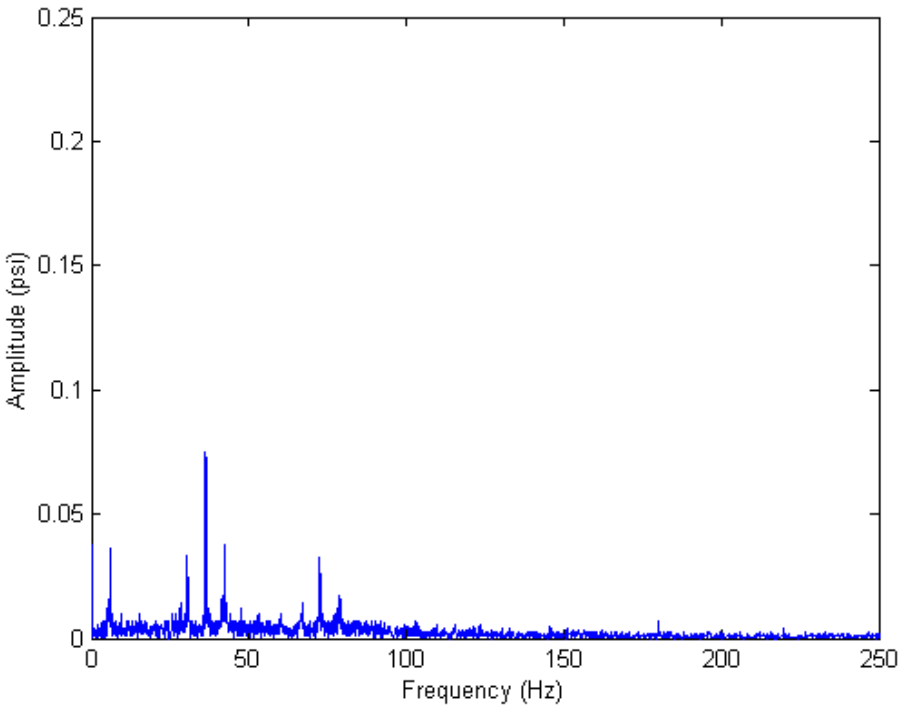

Fig. D.8: FFT of dynamic pressure trace inside the dump combustor at equivalence ratio 0.525 and reference velocity 15 m/s.

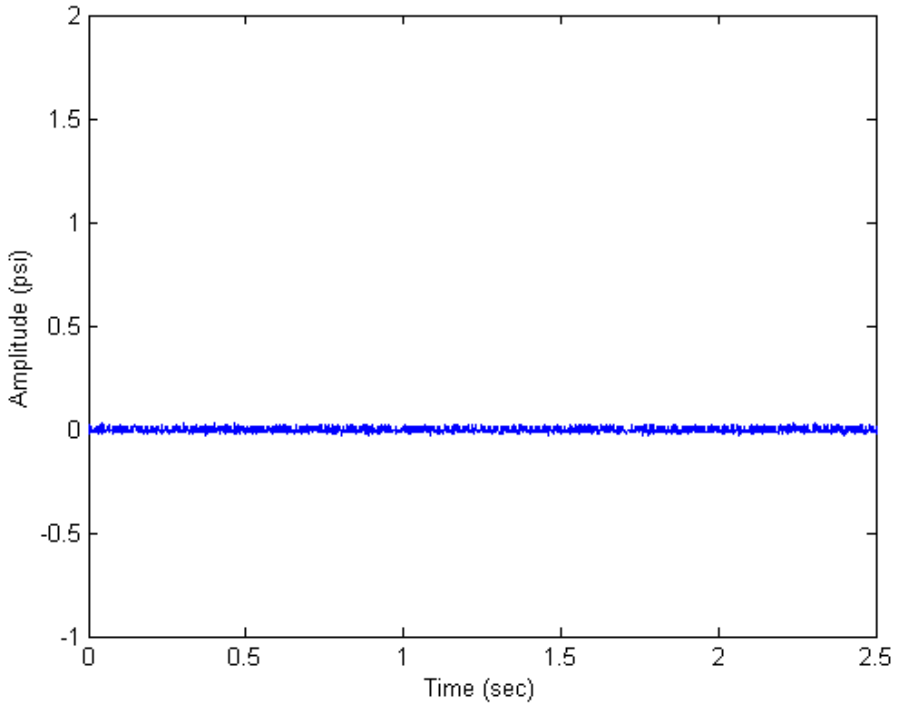

Fig. D.9: Dynamic pressure trace inside the dump combustor at equivalence ratio 0.55 and reference velocity 10 m/s.

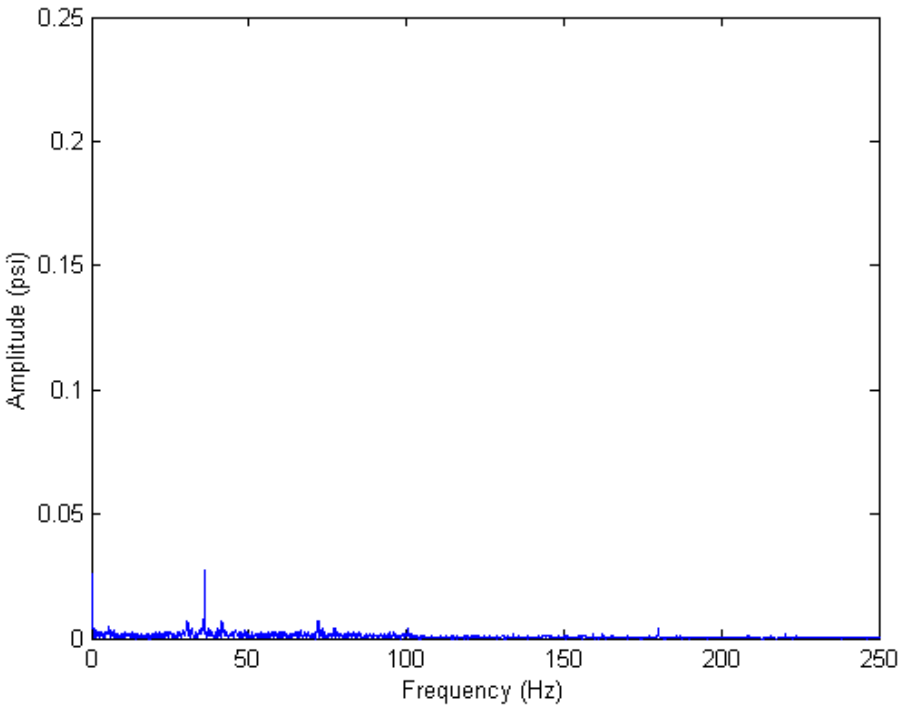

Fig. D.10: FFT of dynamic pressure trace inside the dump combustor at equivalence ratio 0.55 and reference velocity 10 m/s.

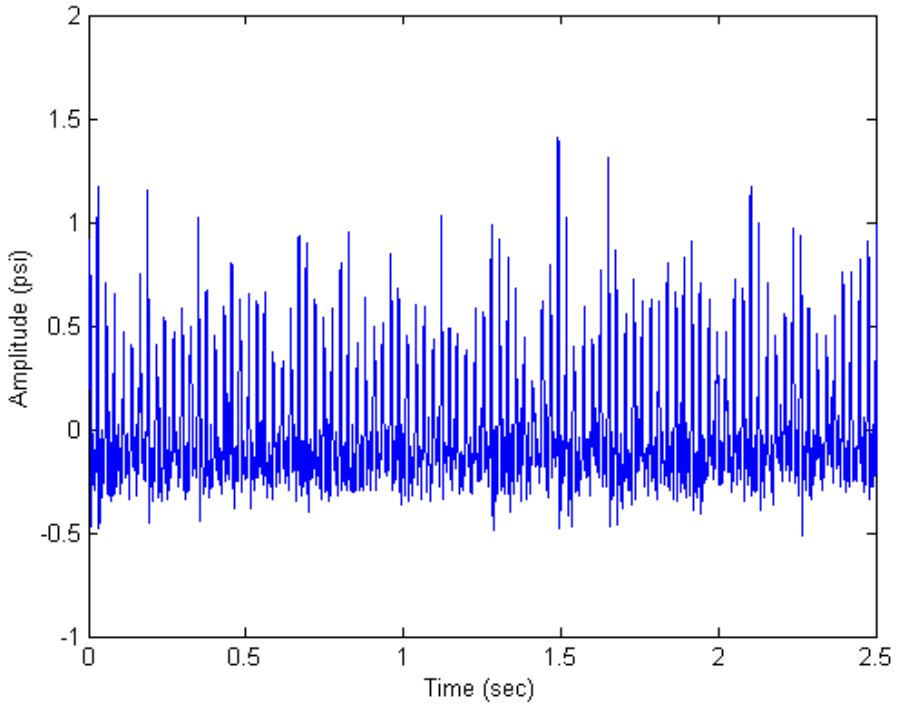

Fig. D.11: Dynamic pressure trace inside the dump combustor at equivalence ratio 0.55 and reference velocity 15 m/s.

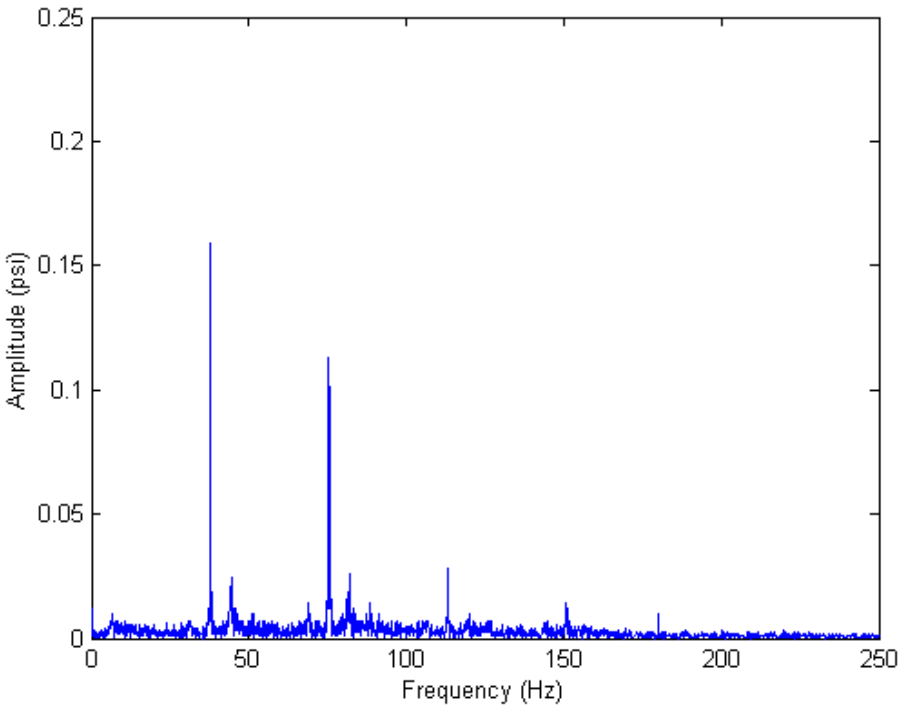

Fig. D.12: FFT of dynamic pressure trace inside the dump combustor at equivalence ratio 0.55 and reference velocity 15 m/s.

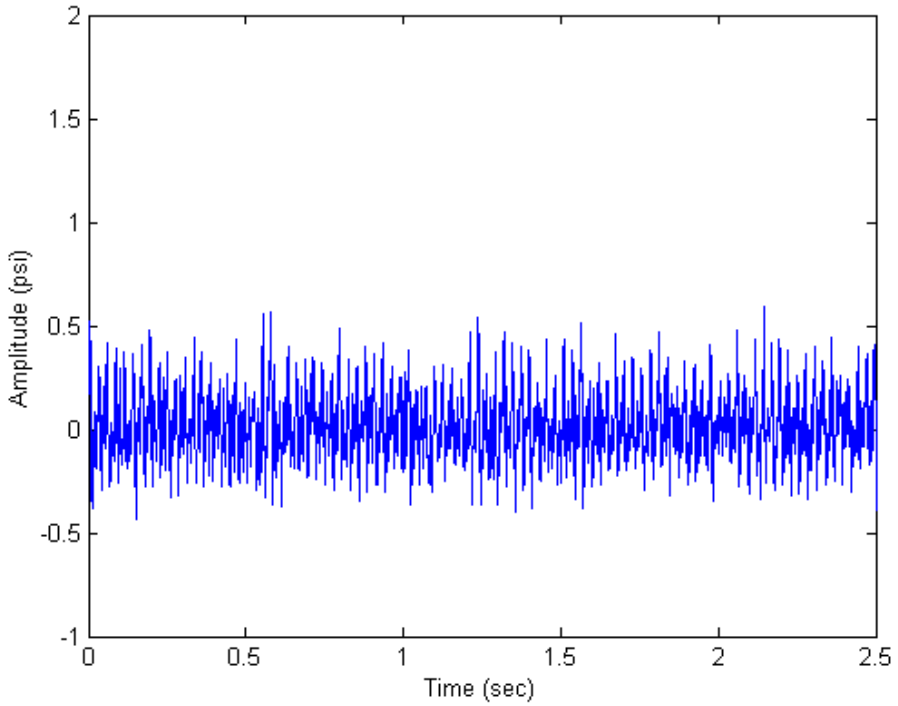

Fig. D.13: Dynamic pressure trace inside the dump combustor at equivalence ratio 0.55 and reference velocity 20 m/s.

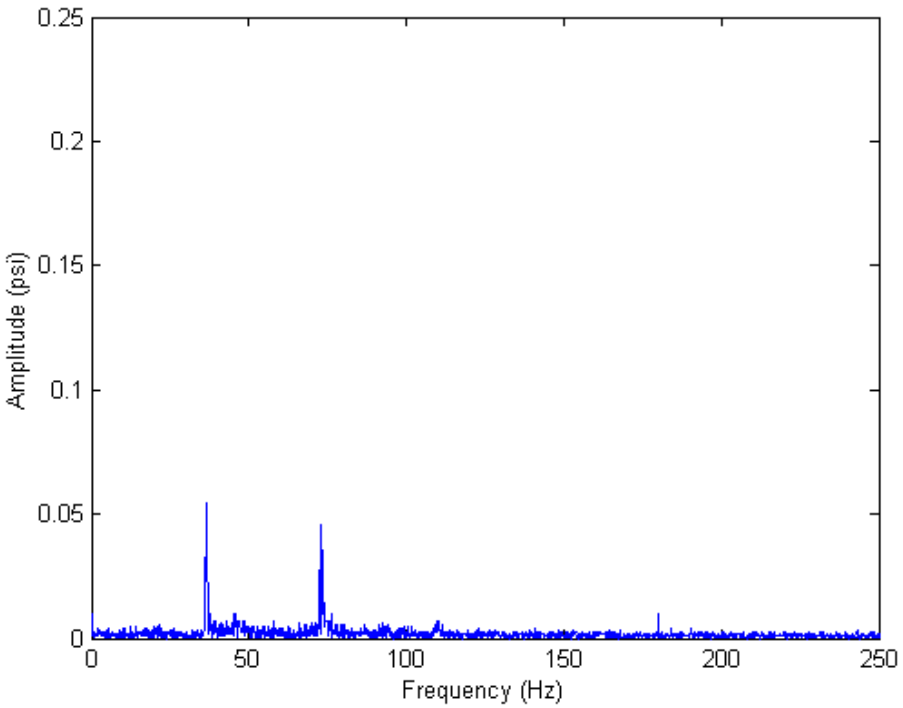

Fig. D.14: FFT of dynamic pressure trace inside the dump combustor at equivalence ratio 0.55 and reference velocity 20 m/s.

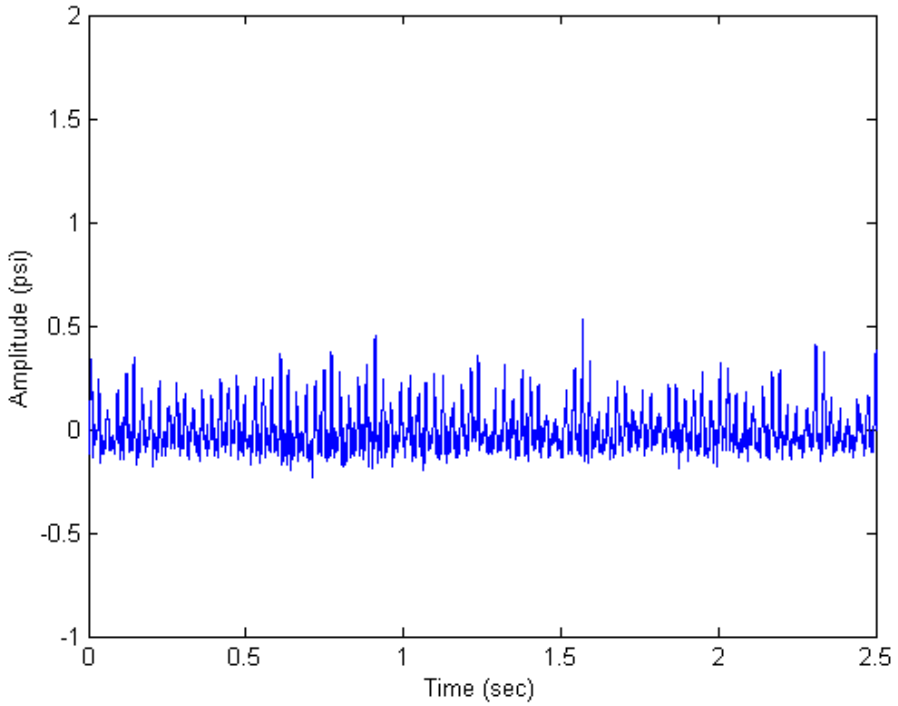

Fig. D.15: Dynamic pressure trace inside the dump combustor at equivalence ratio 0.575 and reference velocity 10 m/s.

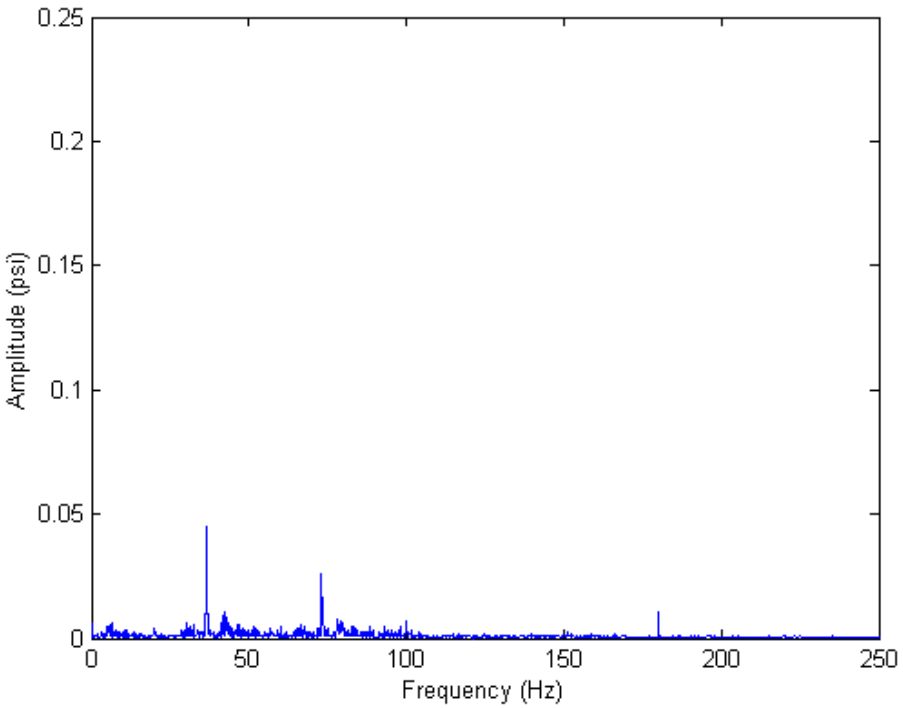

Fig. D.16: FFT of dynamic pressure trace inside the dump combustor at equivalence ratio 0.575 and reference velocity 10 m/s.

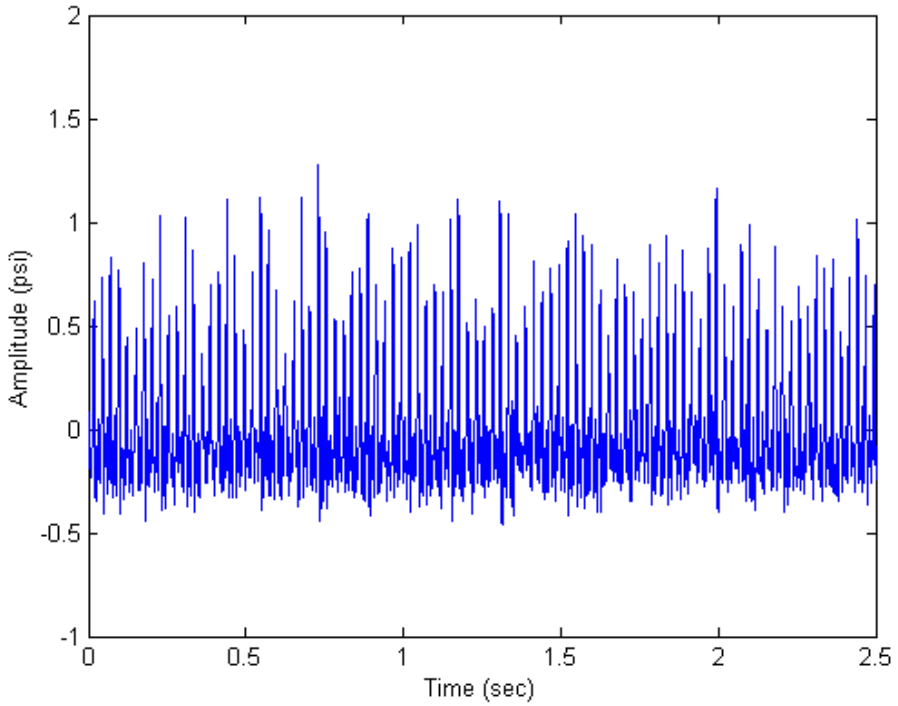

Fig. D.17: Dynamic pressure trace inside the dump combustor at equivalence ratio 0.575 and reference velocity 15 m/s.

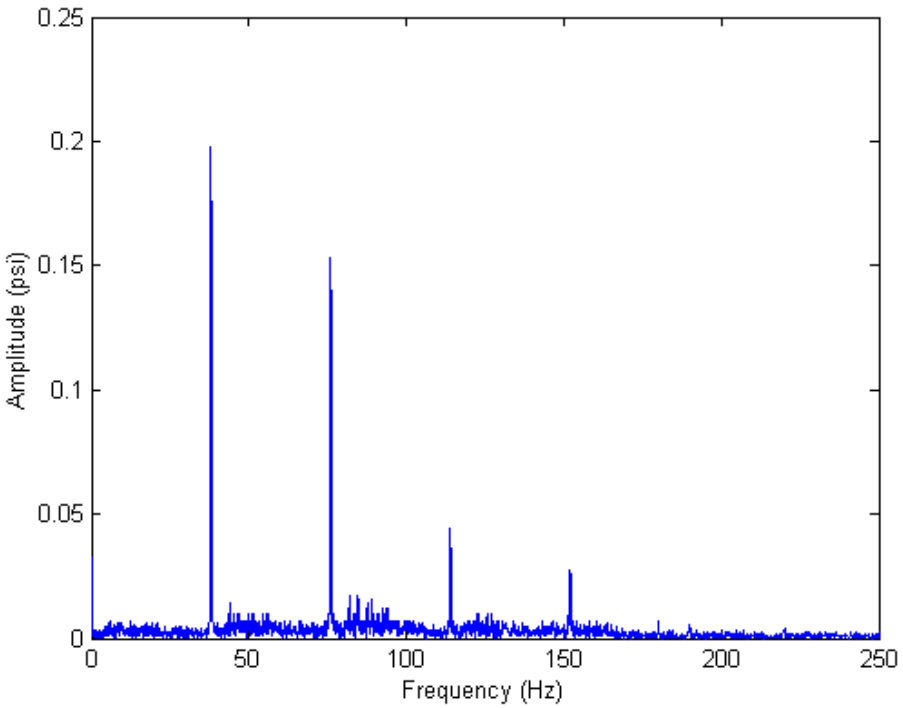

Fig. D.18: FFT of dynamic pressure trace inside the dump combustor at equivalence ratio 0.575 and reference velocity 15 m/s.

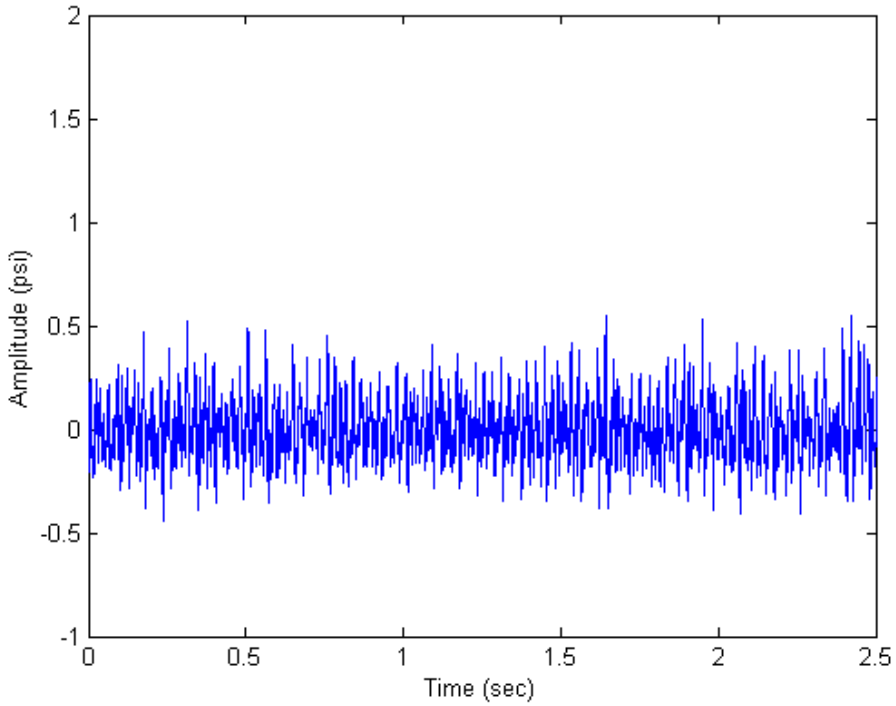

Fig. D.19: Dynamic pressure trace inside the dump combustor at equivalence ratio 0.575 and reference velocity 20 m/s.

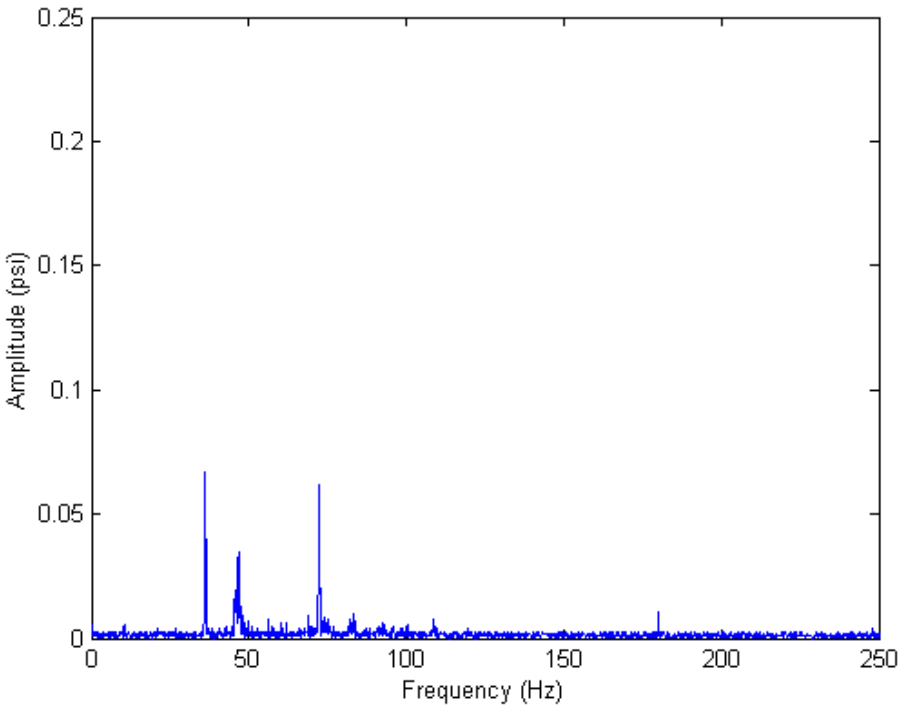

Fig. D.20: FFT of dynamic pressure trace inside the dump combustor at equivalence ratio 0.575 and reference velocity 20 m/s.

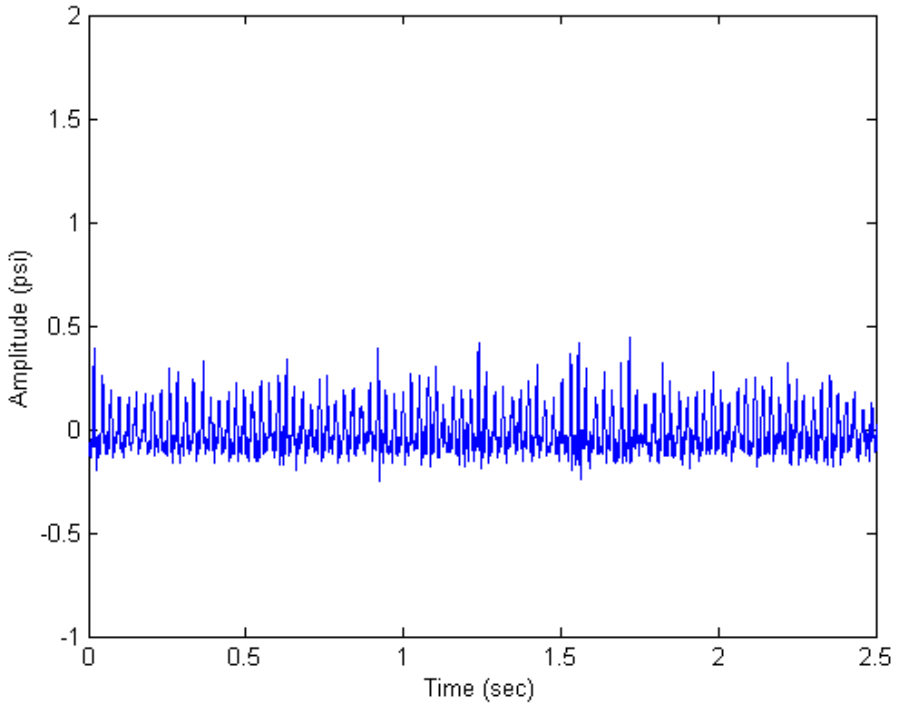

Fig. D.21: Dynamic pressure trace inside the dump combustor at equivalence ratio 0.6 and reference velocity 10 m/s.

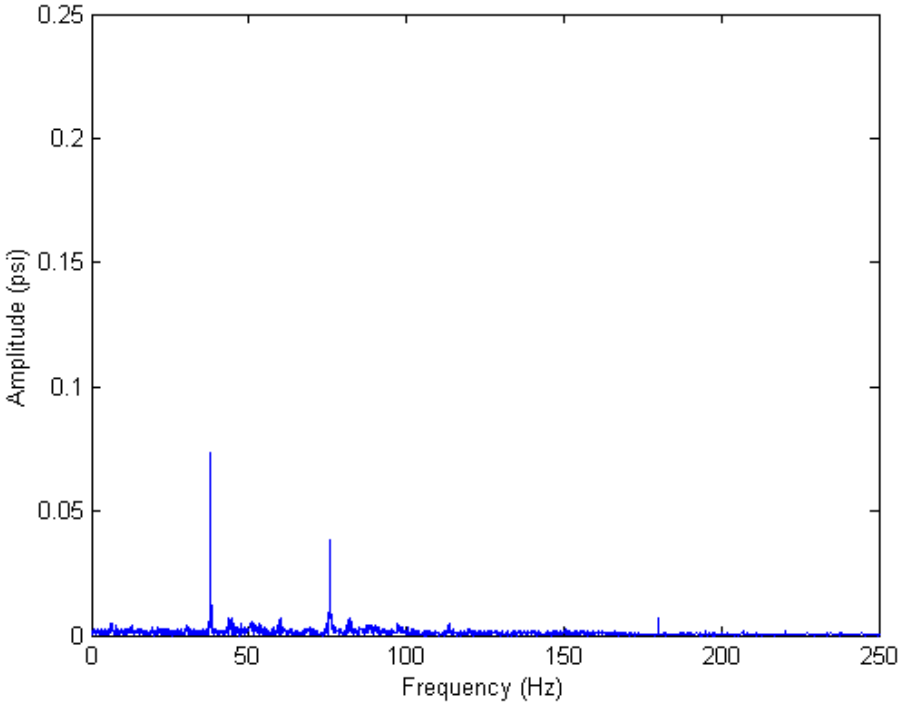

Fig. D.22: FFT of dynamic pressure trace inside the dump combustor at equivalence ratio 0.6 and reference velocity 10 m/s.

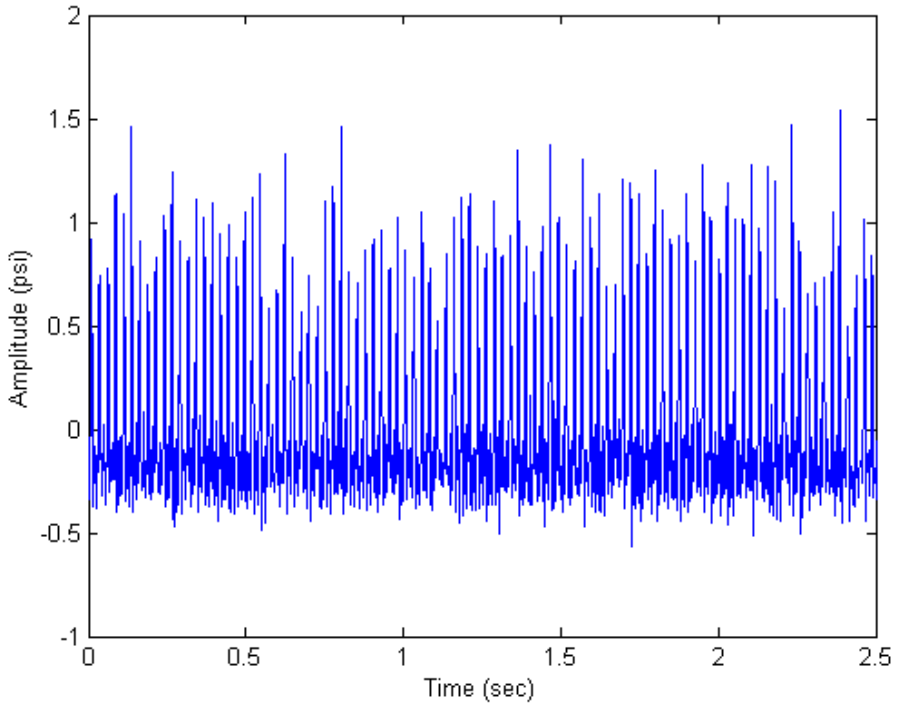

Fig. D.23: Dynamic pressure trace inside the dump combustor at equivalence ratio 0.6 and reference velocity 15 m/s.

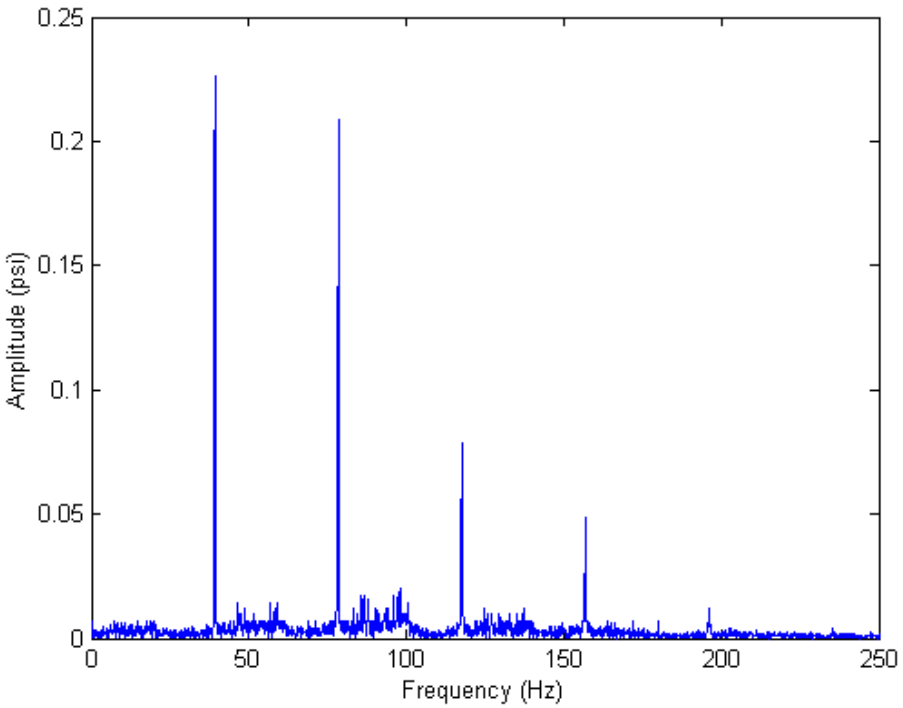

Fig. D.24: FFT of dynamic pressure trace inside the dump combustor at equivalence ratio 0.6 and reference velocity 15 m/s.

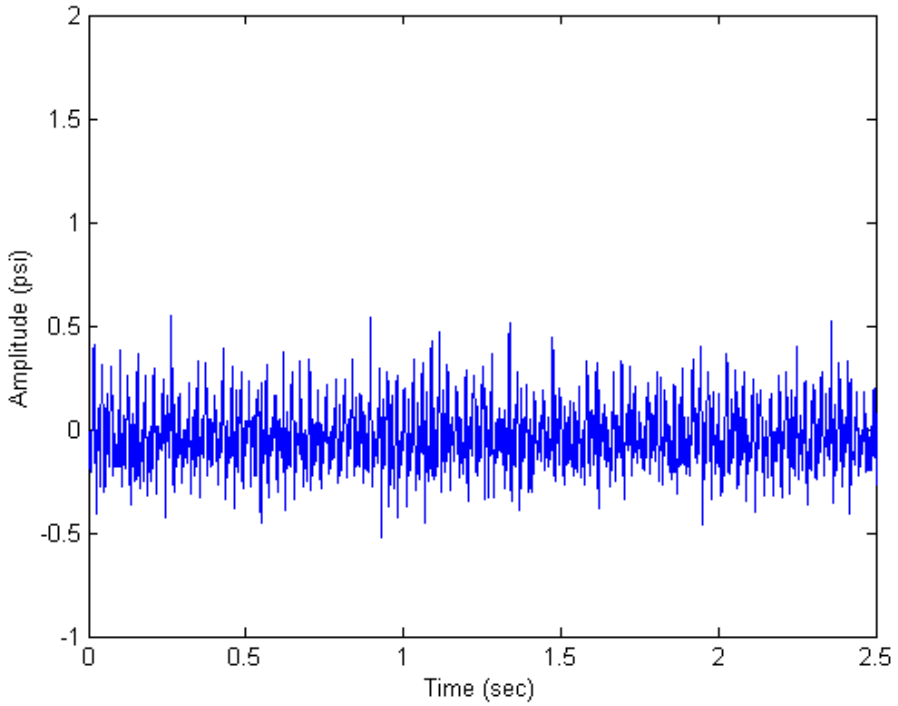

Fig. D.25: Dynamic pressure trace inside the dump combustor at equivalence ratio 0.6 and reference velocity 20 m/s.

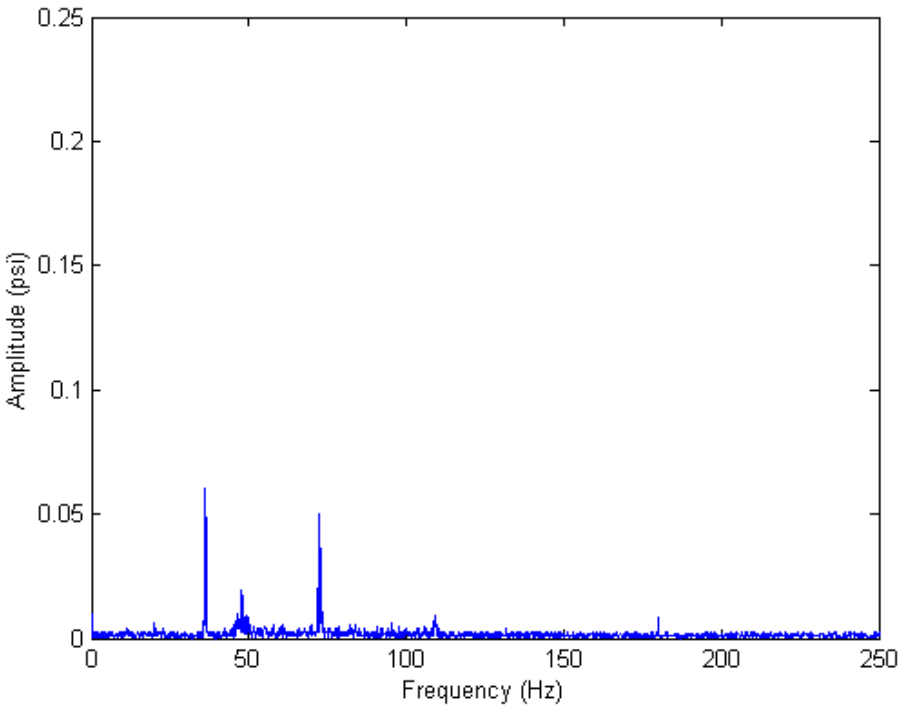

Fig. D.26: FFT of dynamic pressure trace inside the dump combustor at equivalence ratio 0.6 and reference velocity 20 m/s.

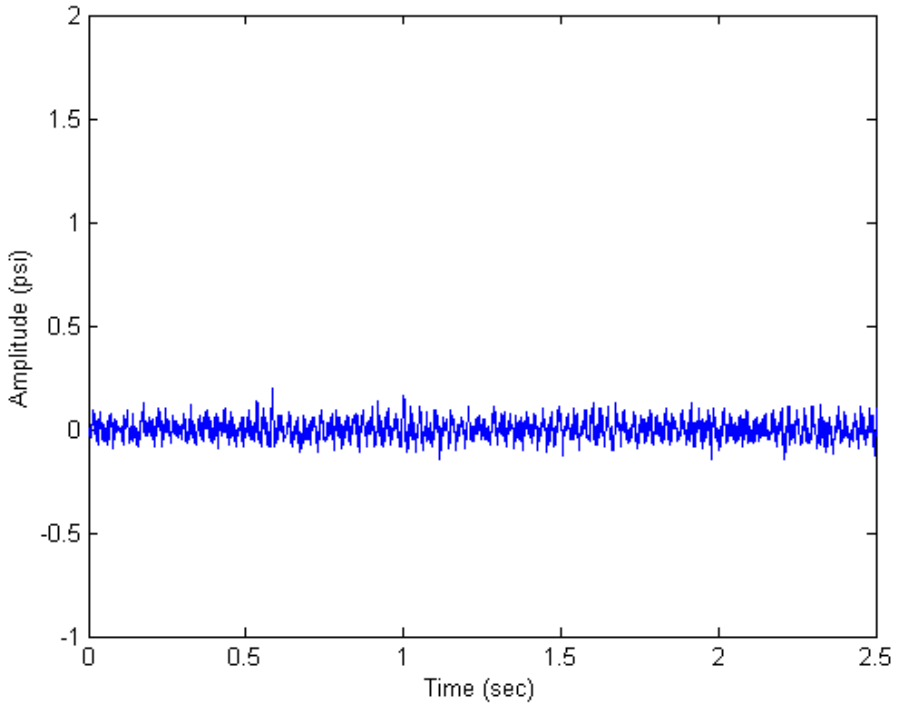

Fig. D.27: Dynamic pressure trace inside the dump combustor at equivalence ratio 0.65 and reference velocity 10 m/s.

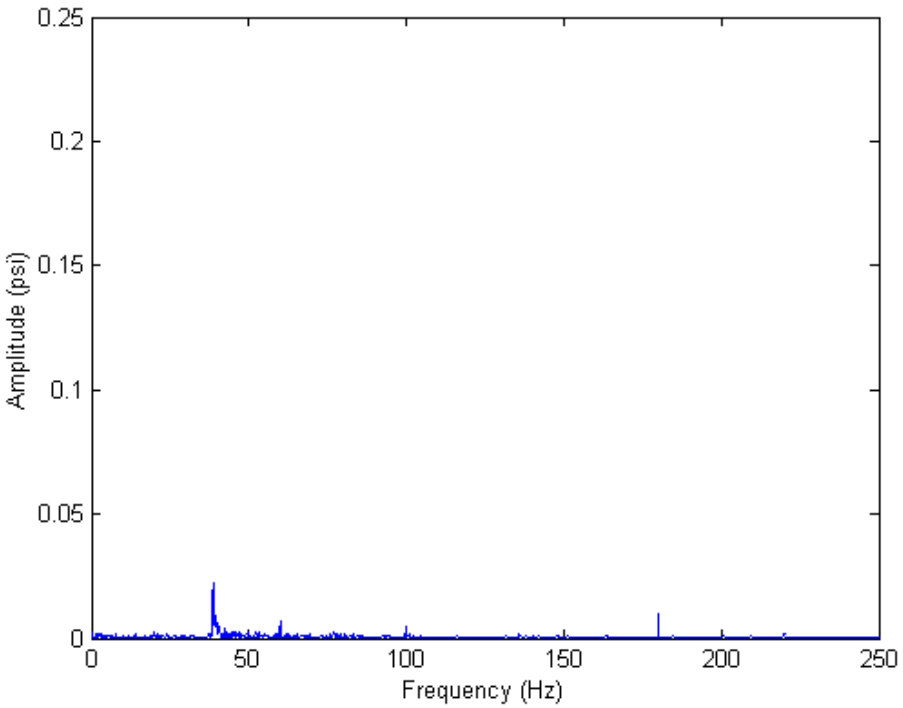

Fig. D.28: FFT of dynamic pressure trace inside the dump combustor at equivalence ratio 0.65 and reference velocity 10 m/s.

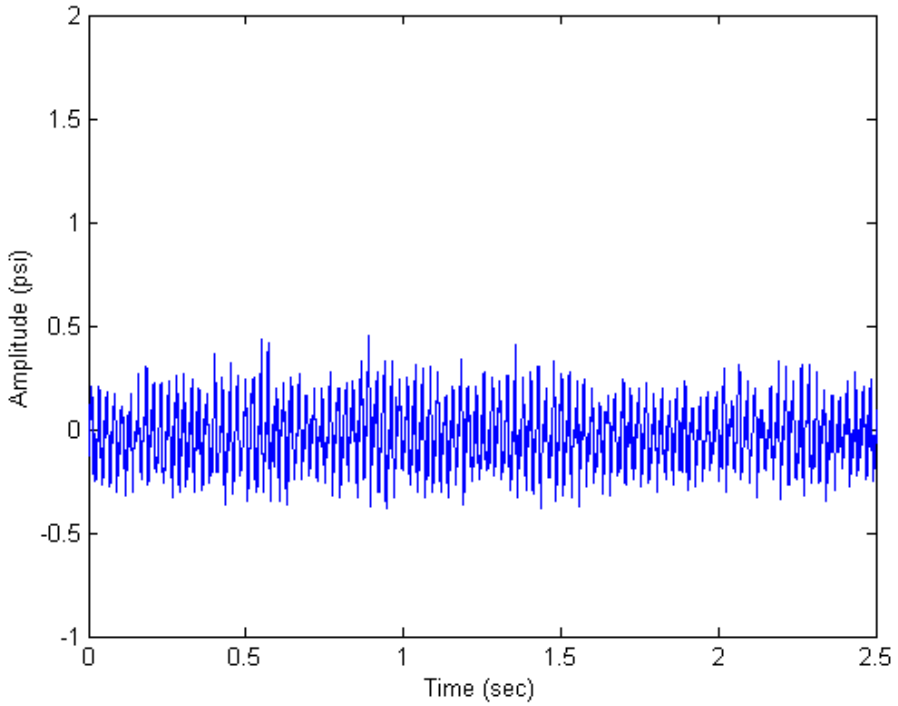

Fig. D.29: Dynamic pressure trace inside the dump combustor at equivalence ratio 0.65 and reference velocity 15 m/s.

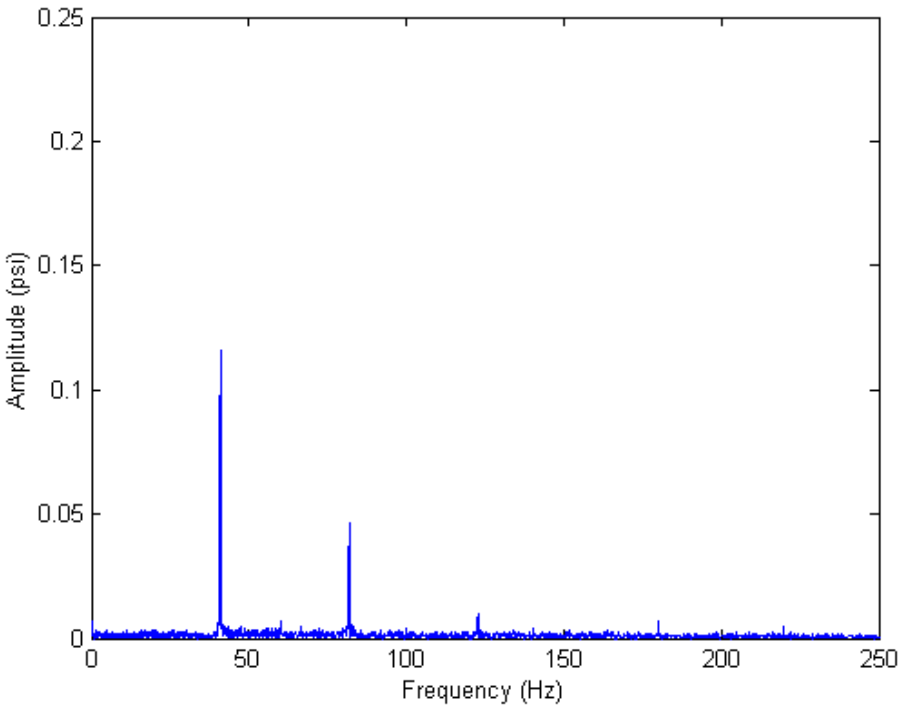

Fig. D.30: FFT of dynamic pressure trace inside the dump combustor at equivalence ratio 0.65 and reference velocity 15 m/s.

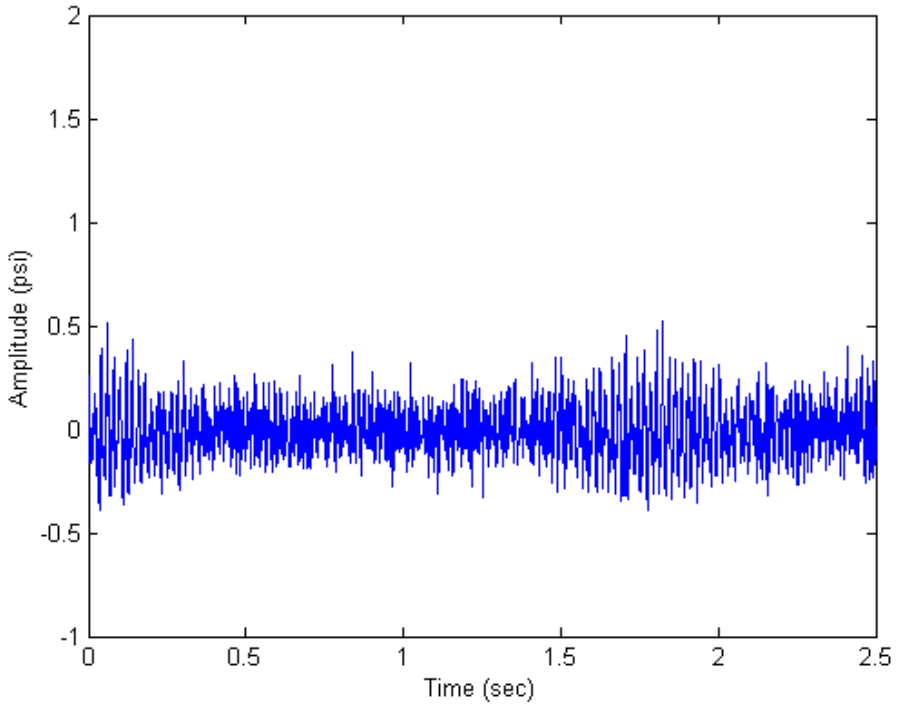

Fig. D.31: Dynamic pressure trace inside the dump combustor at equivalence ratio 0.65 and reference velocity 20 m/s.

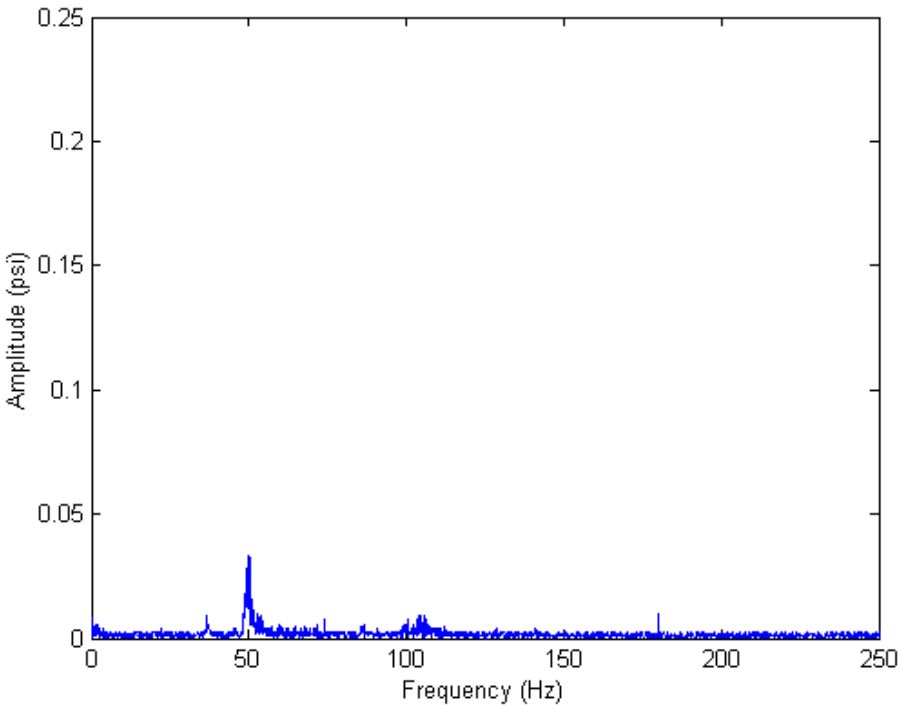

Fig. D.32: FFT of dynamic pressure trace inside the dump combustor at equivalence ratio 0.65 and reference velocity 20 m/s.

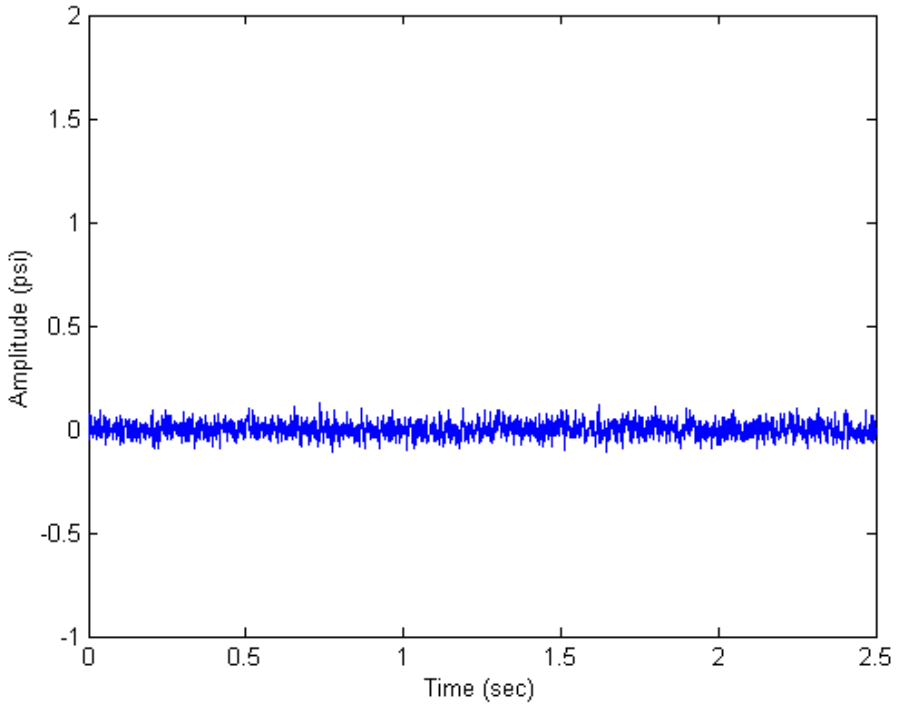

Fig. D.33: Dynamic pressure trace inside the dump combustor at equivalence ratio 0.7 and reference velocity 10 m/s.

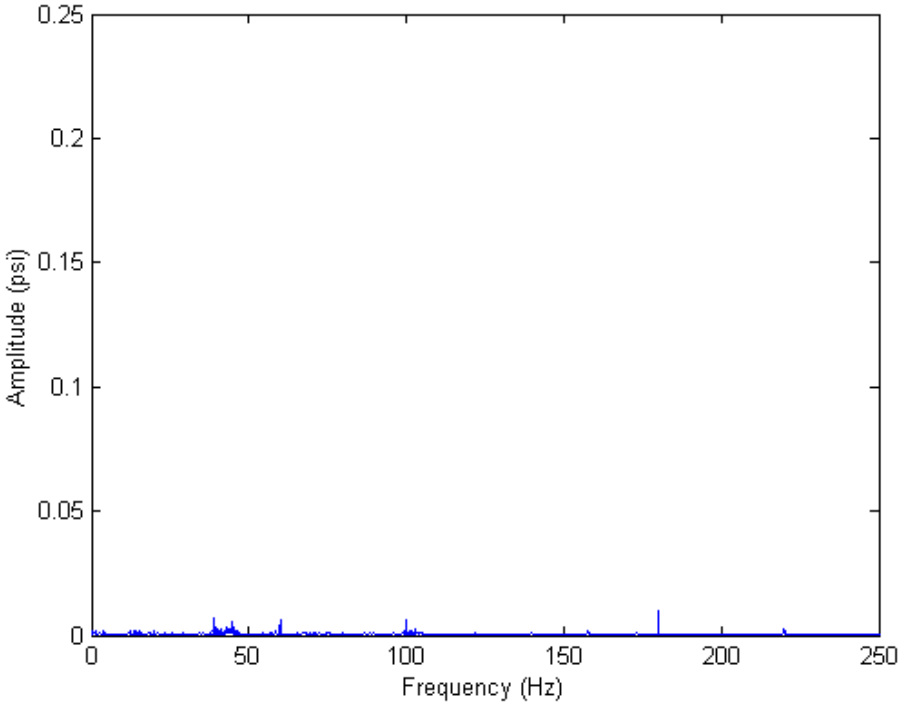

Fig. D.34: FFT of dynamic pressure trace inside the dump combustor at equivalence ratio 0.7 and reference velocity 10 m/s.

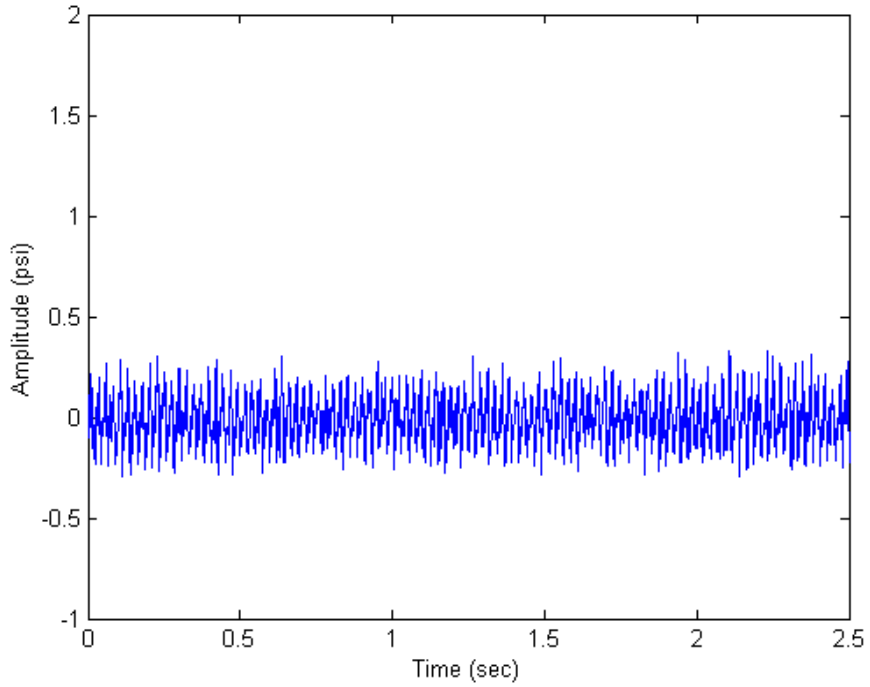

Fig. D.35: Dynamic pressure trace inside the dump combustor at equivalence ratio 0.7 and reference velocity 15 m/s.

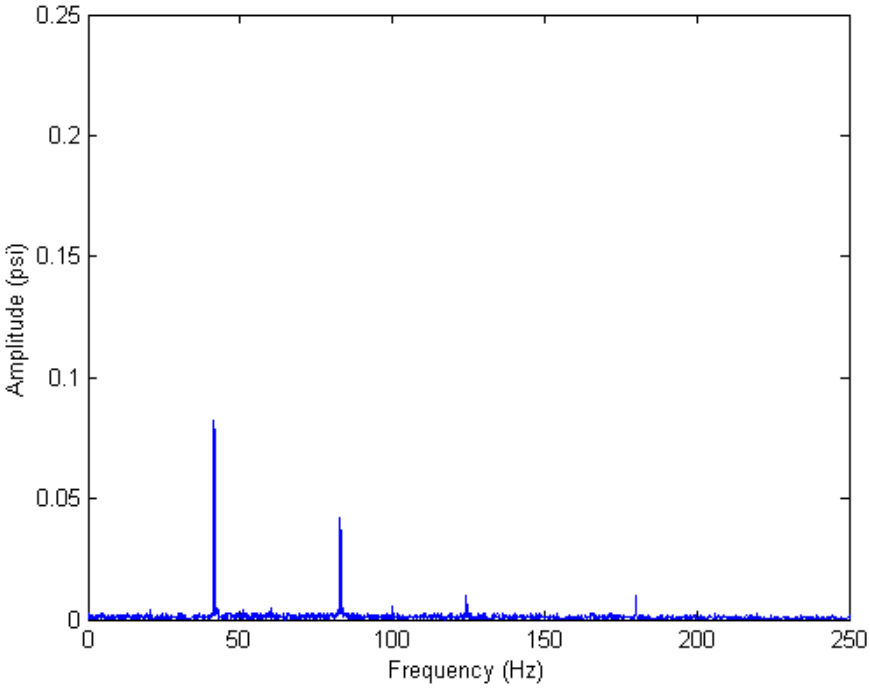

Fig. D.36: FFT of dynamic pressure trace inside the dump combustor at equivalence ratio 0.7 and reference velocity 15 m/s.

Appendix E – Transient Spark Schlieren Image Sequence

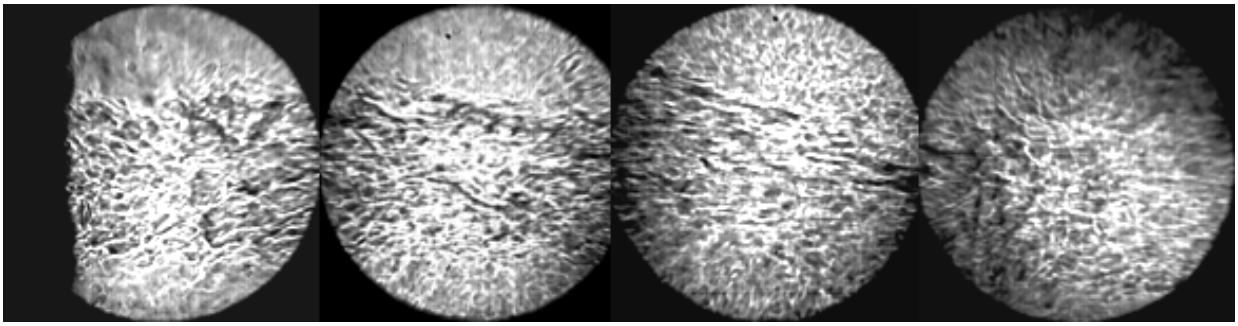

Fig. E1.1: Schlieren image of flow inside the combustor at phase 0^o without control.

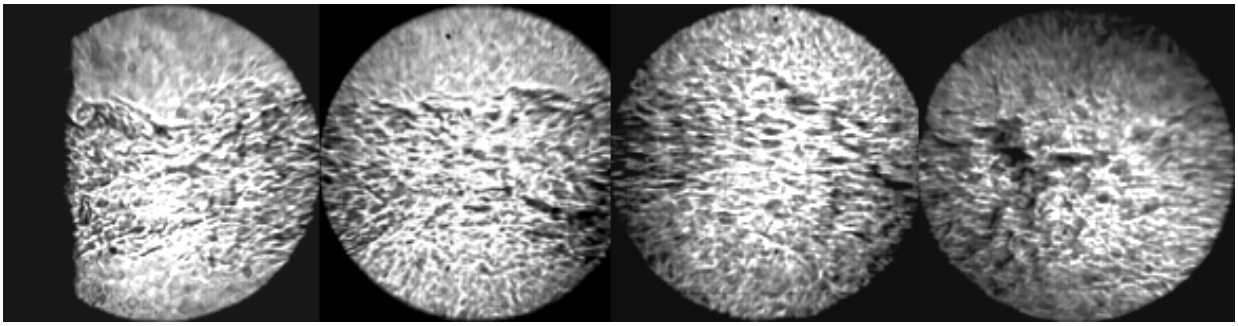

Fig. E1.2: Schlieren image of flow inside the combustor at phase 14^o without control.

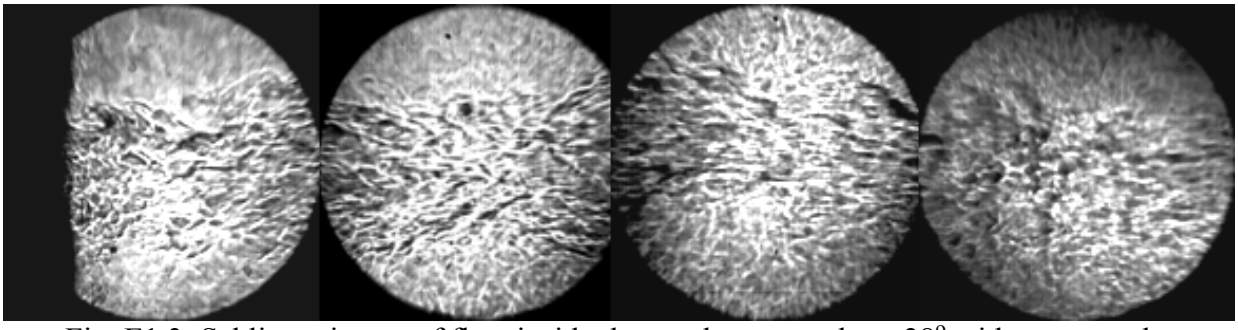

Fig. E1.3: Schlieren image of flow inside the combustor at phase 28^o without control.

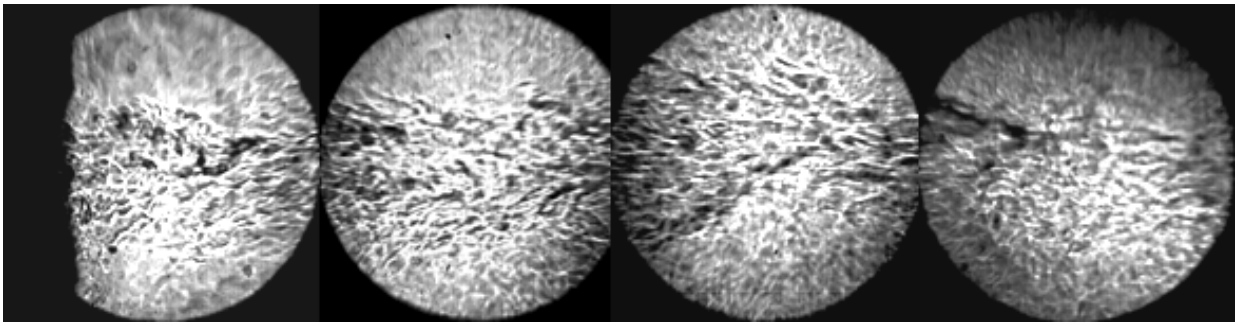

Fig. E1.4: Schlieren image of flow inside the combustor at phase 43^{o} without control.

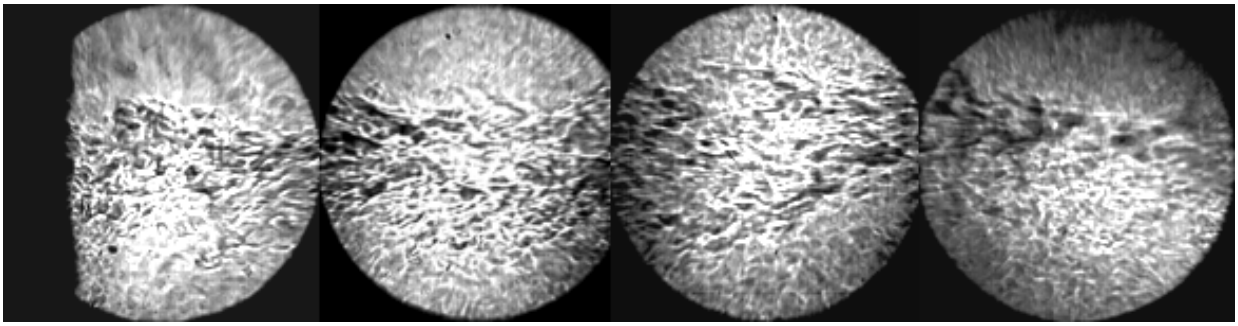

Fig. E1.5: Schlieren image of flow inside the combustor at phase 57^{o} without control.

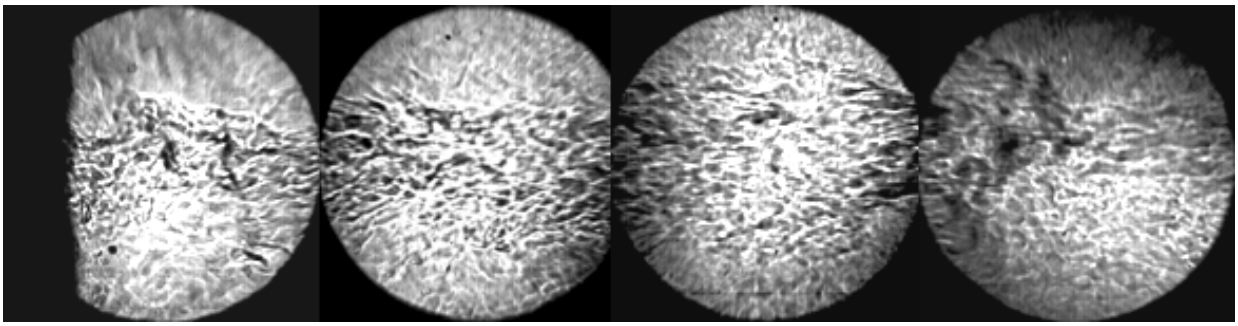

Fig. E1.6: Schlieren image of flow inside the combustor at phase 71^{o} without control.

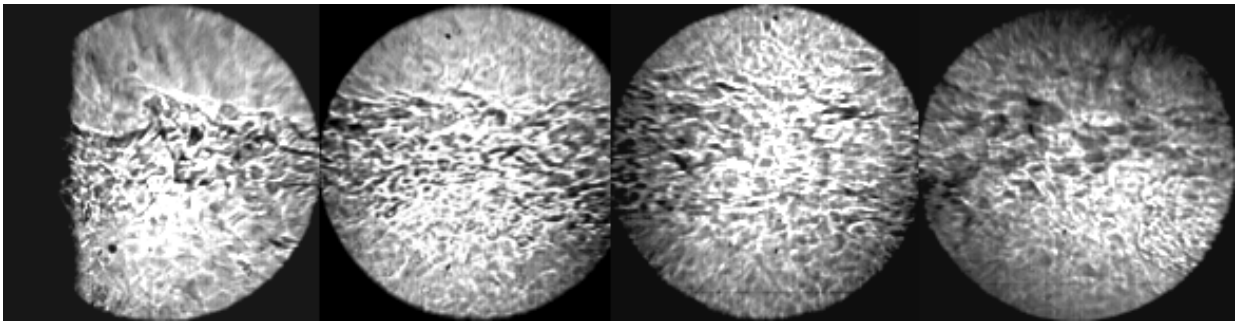

Fig. E1.7: Schlieren image of flow inside the combustor at phase 85^{o} without control.

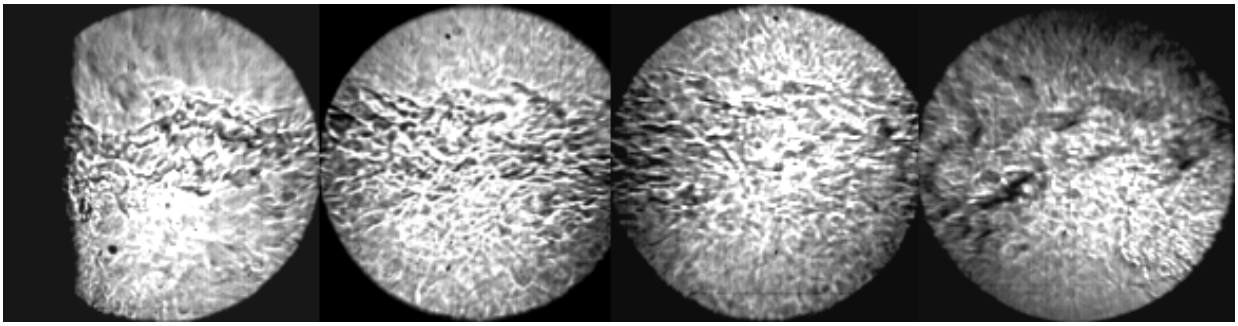

Fig. E1.8: Schlieren image of flow inside the combustor at phase 100^{o} without control.

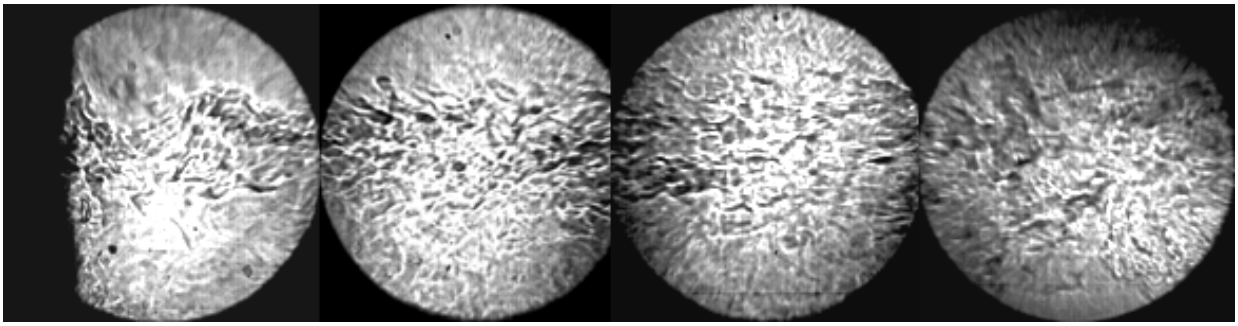

Fig. E1.9: Schlieren image of flow inside the combustor at phase 114^{o} without control.

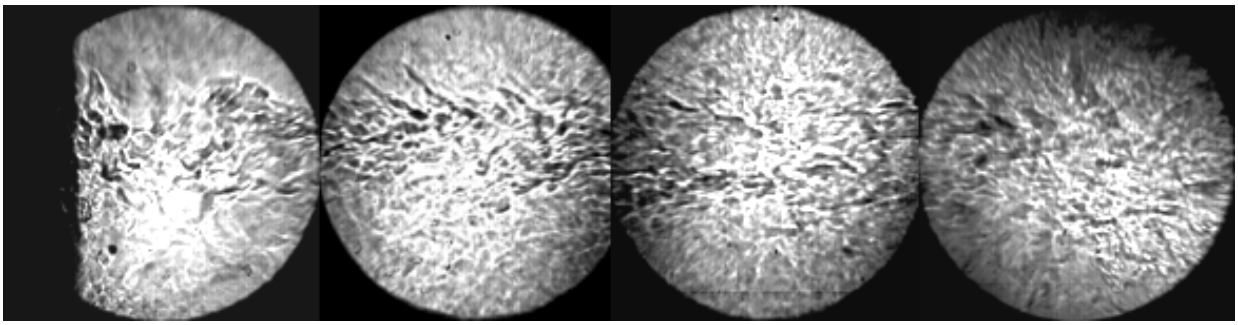

Fig. E1.10: Schlieren image of flow inside the combustor at phase 128^{o} without control.

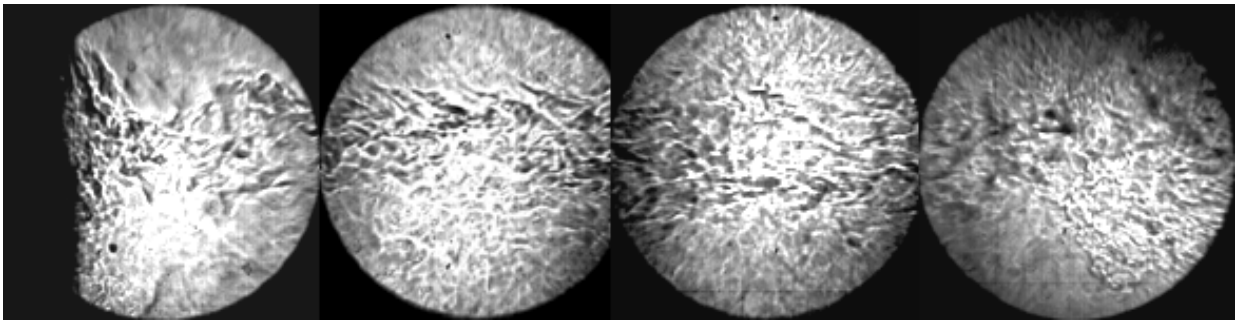

Fig. E1.11: Schlieren image of flow inside the combustor at phase 142^{o} without control.

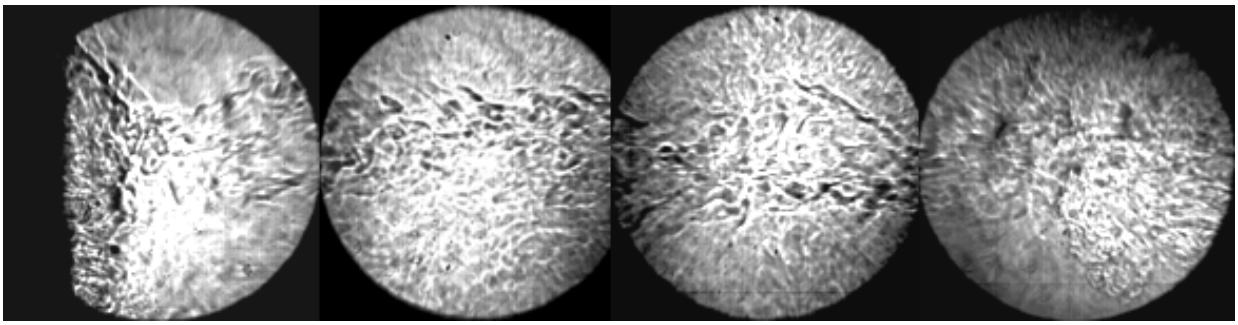

Fig. E1.12: Schlieren image of flow inside the combustor at phase 156^{o} without control.

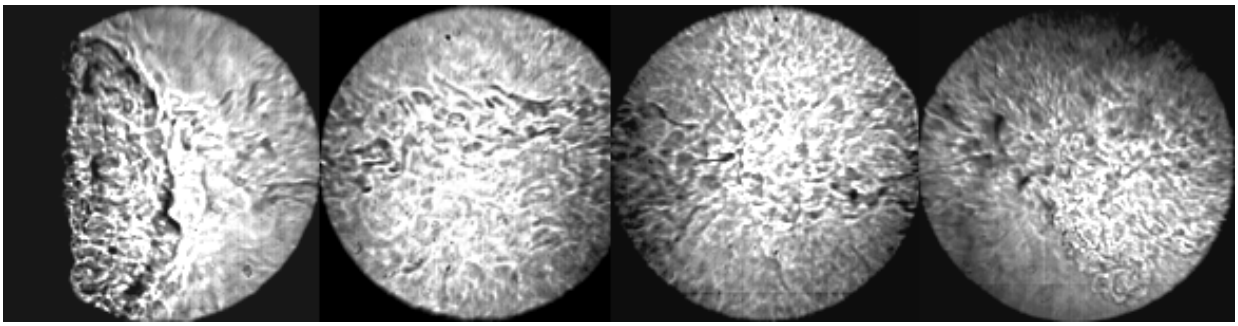

Fig. E1.13: Schlieren image of flow inside the combustor at phase 171^{o} without control.

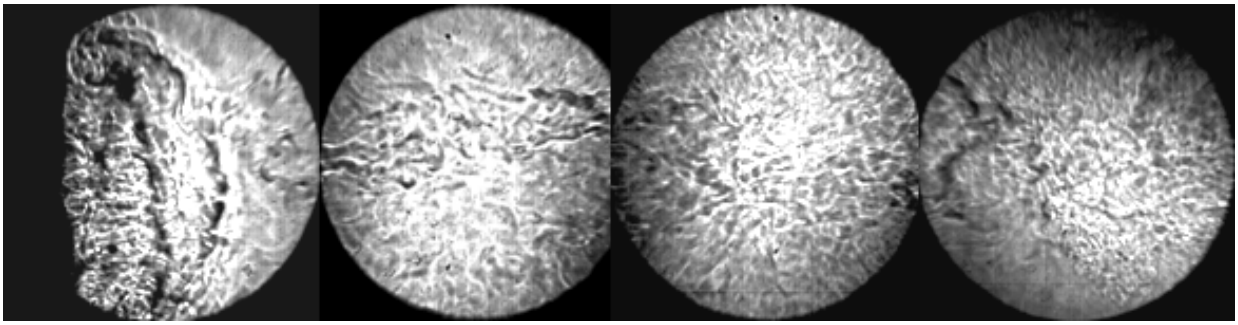

Fig. E1.14: Schlieren image of flow inside the combustor at phase 185^{o} without control.

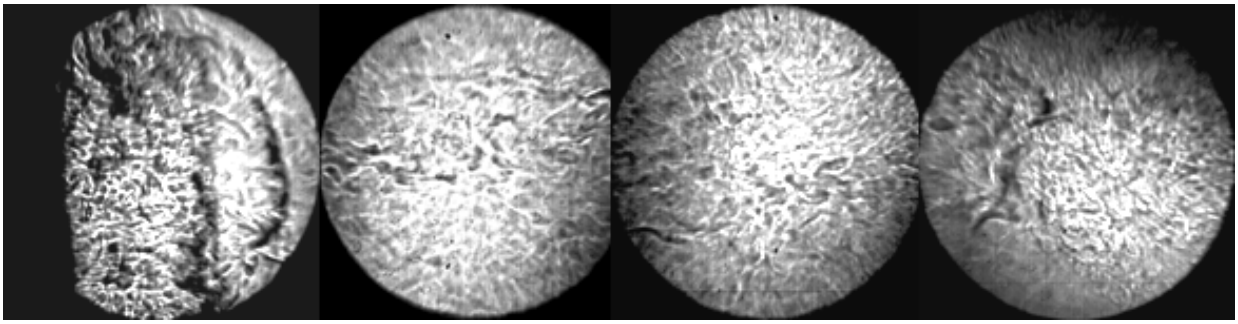

Fig. E1.15: Schlieren image of flow inside the combustor at phase 199^{o} without control.

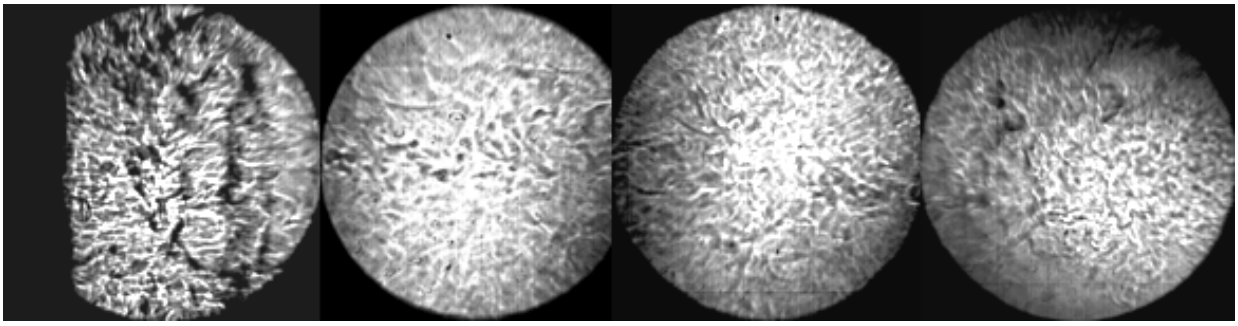

Fig. E1.16: Schlieren image of flow inside the combustor at phase 213^{o} without control.

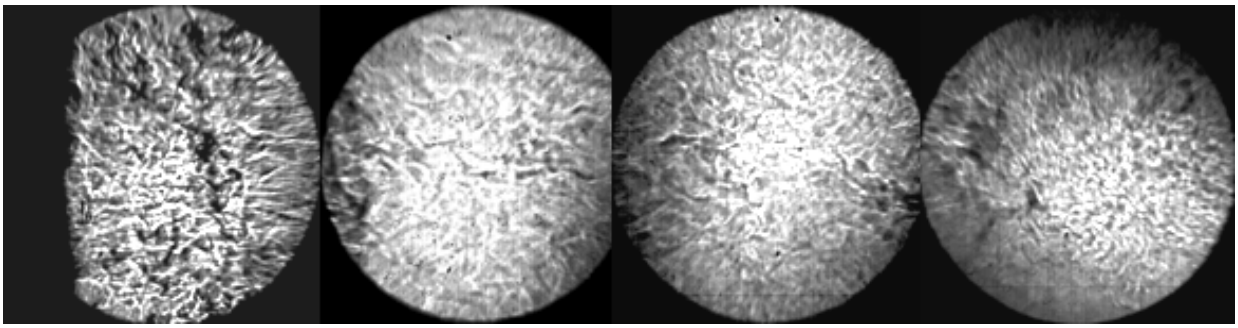

Fig. E1.17: Schlieren image of flow inside the combustor at phase 228^{o} without control.

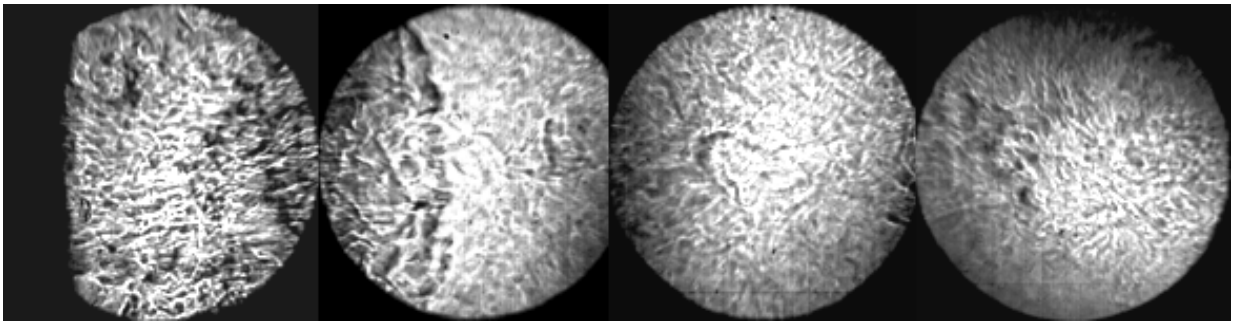

Fig. E1.18: Schlieren image of flow inside the combustor at phase 242^{o} without control.

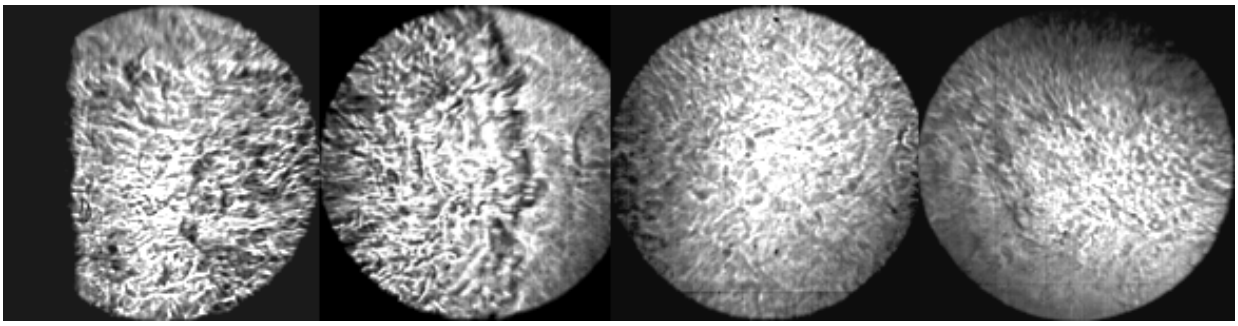

Fig. E1.19: Schlieren image of flow inside the combustor at phase 256^{o} without control.

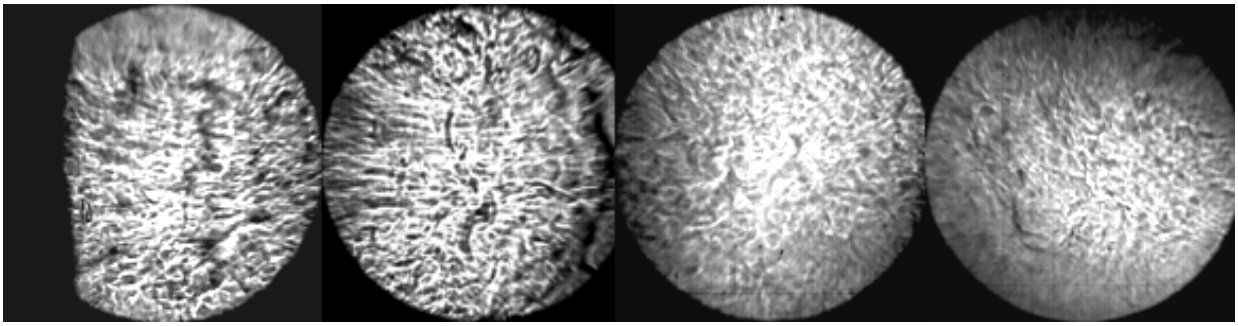

Fig. E1.20: Schlieren image of flow inside the combustor at phase 270^{o} without control.

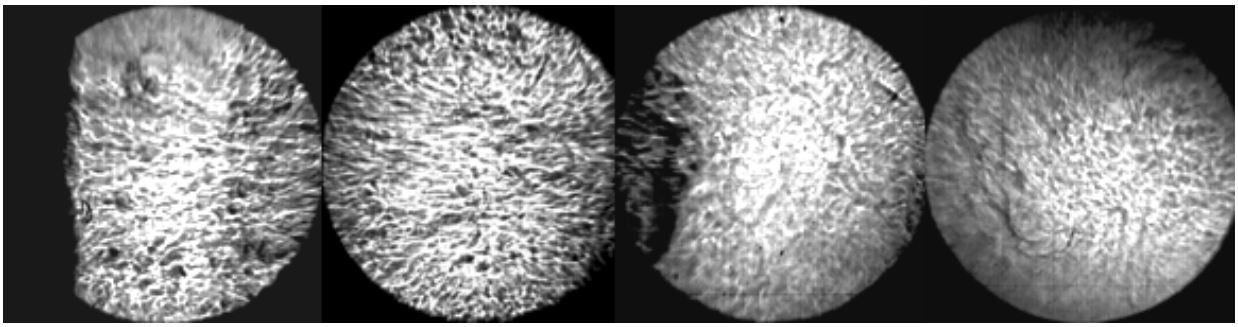

Fig. E1.21: Schlieren image of flow inside the combustor at phase 284^{o} without control.

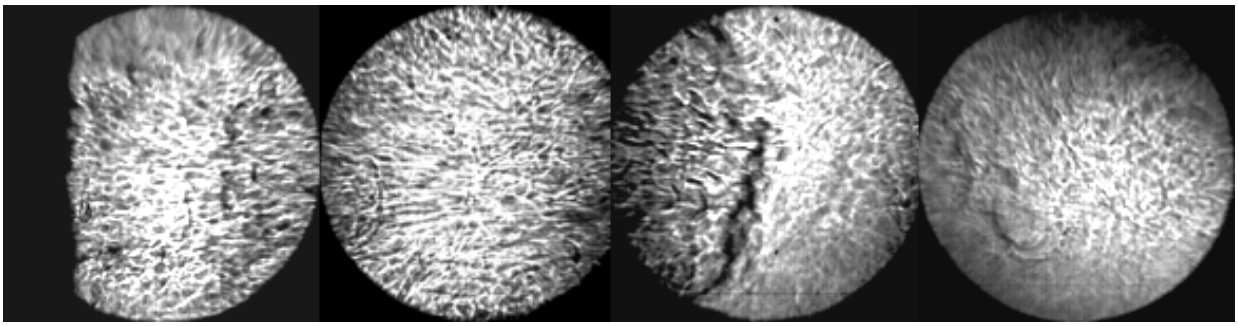

Fig. E1.22: Schlieren image of flow inside the combustor at phase 299^{o} without control.

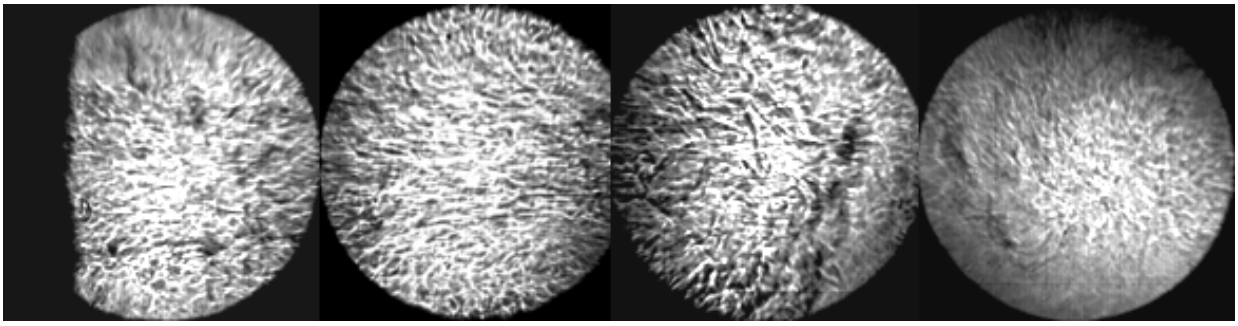

Fig. E1.23: Schlieren image of flow inside the combustor at phase 313^{o} without control.

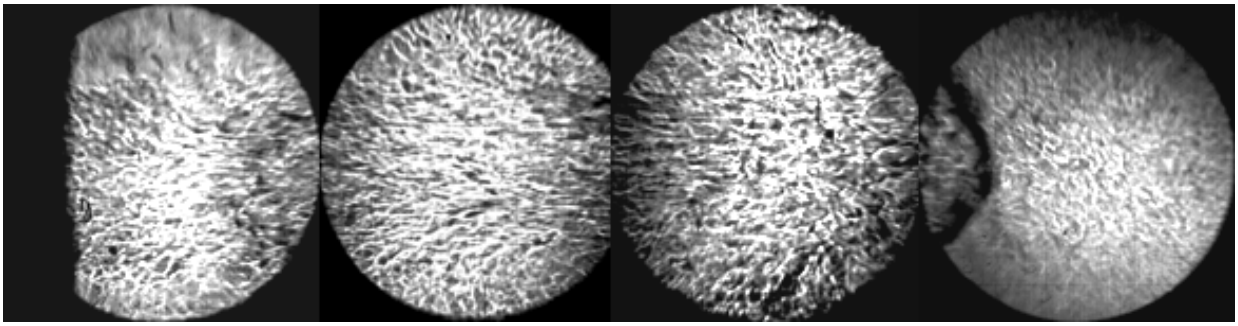

Fig. E1.24: Schlieren image of flow inside the combustor at phase 327^{o} without control.

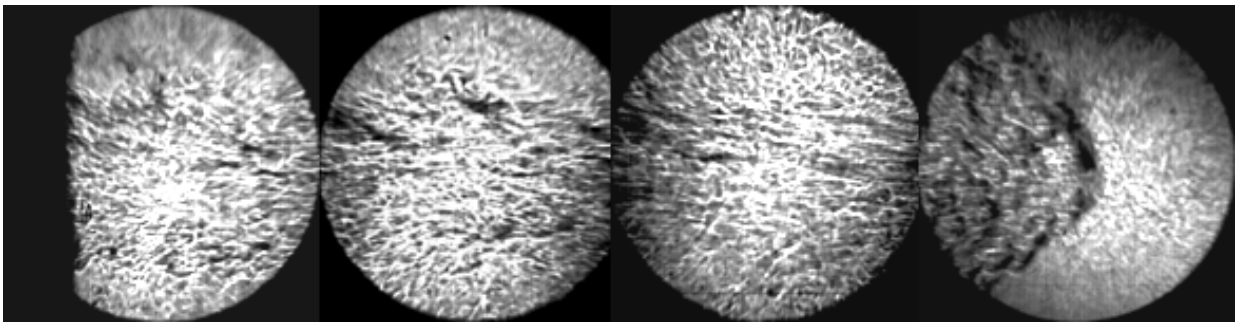

Fig. E1.25: Schlieren image of flow inside the combustor at phase 341^{o} without control.

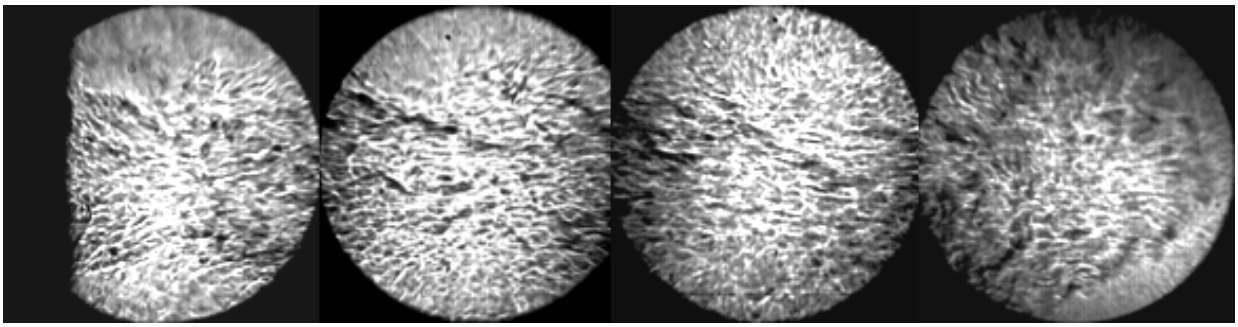

Fig. E1.26: Schlieren image of flow inside the combustor at phase 356^{o} without control.

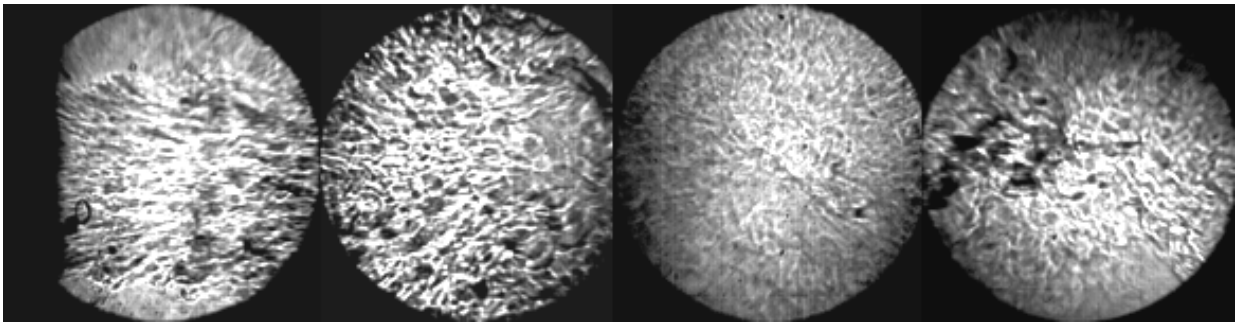

Fig. E2.1: Schlieren image of flow inside the combustor at phase 0^o with open-loop control.

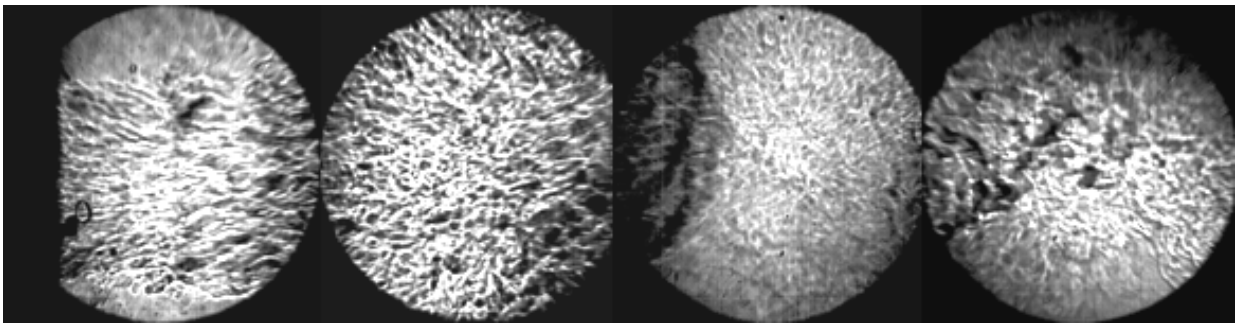

Fig. E2.2: Schlieren image of flow inside the combustor at phase 14^o with open-loop control.

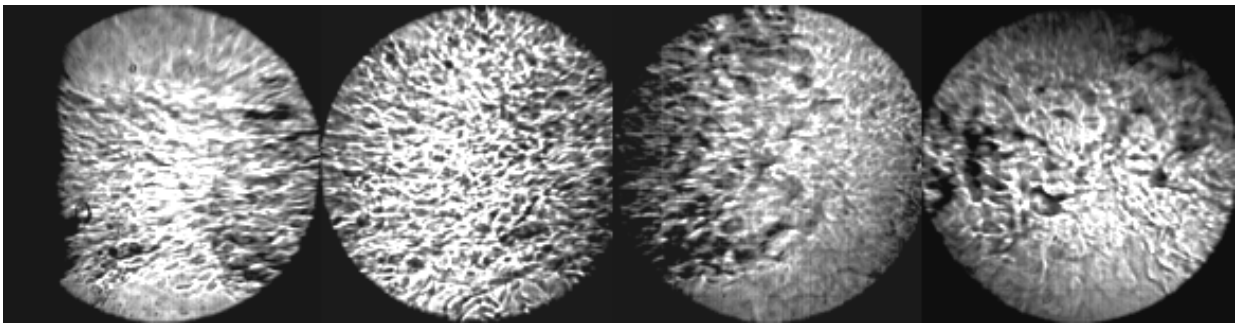

Fig. E2.3: Schlieren image of flow inside the combustor at phase 28^o with open-loop control.

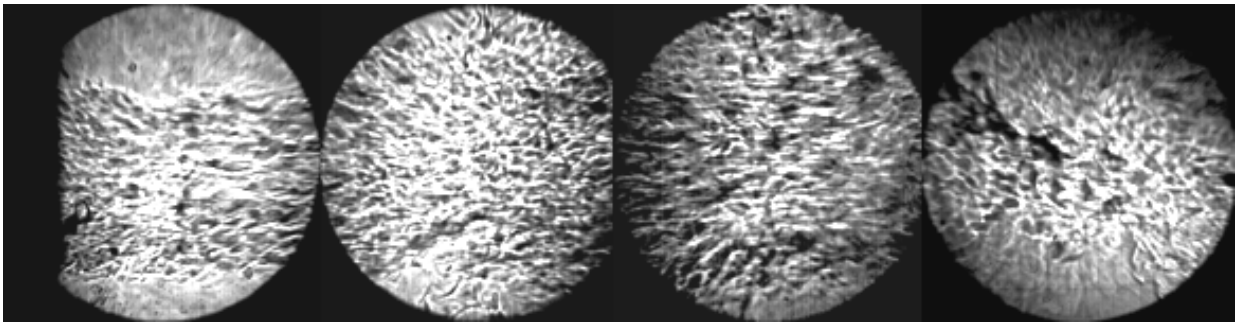

Fig. E2.4: Schlieren image of flow inside the combustor at phase 43^o with open-loop control.

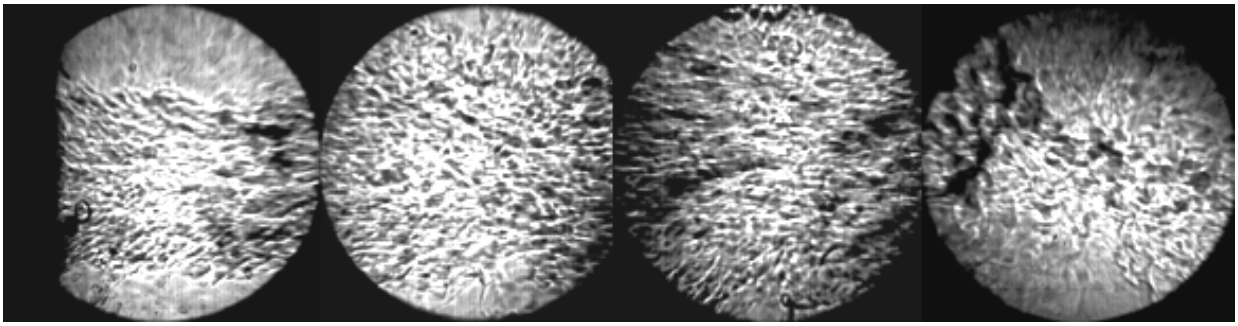

Fig. E2.5: Schlieren image of flow inside the combustor at phase 57^{o} with open-loop control.

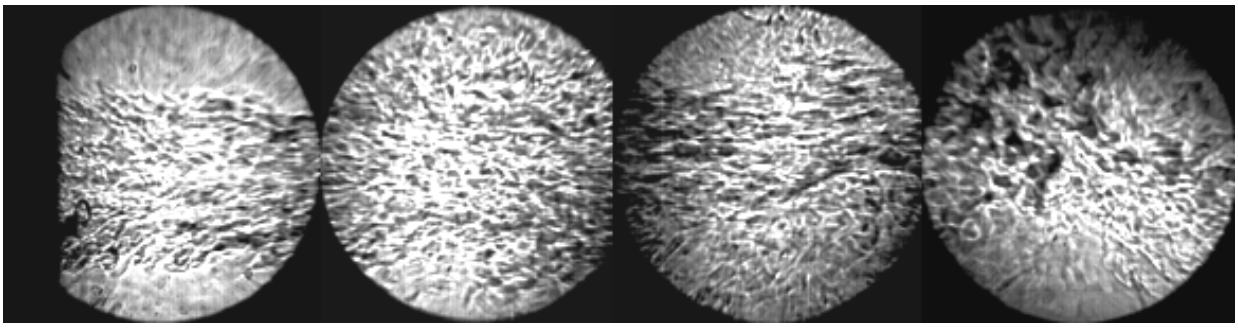

Fig. E2.6: Schlieren image of flow inside the combustor at phase 71^{o} with open-loop control.

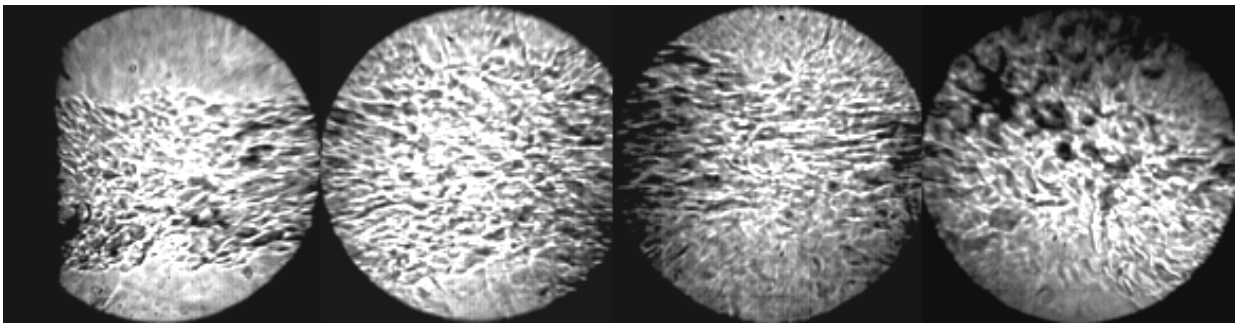

Fig. E2.7: Schlieren image of flow inside the combustor at phase 85^{o} with open-loop control.

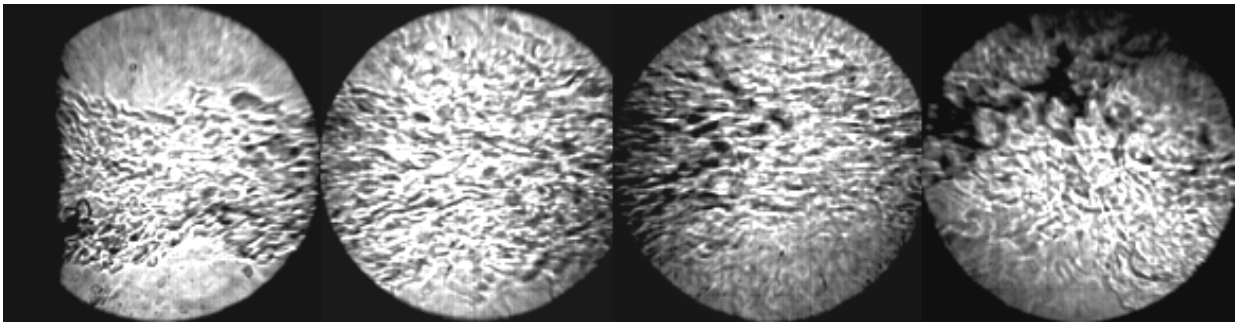

Fig. E2.8: Schlieren image of flow inside the combustor at phase 100^{o} with open-loop control.

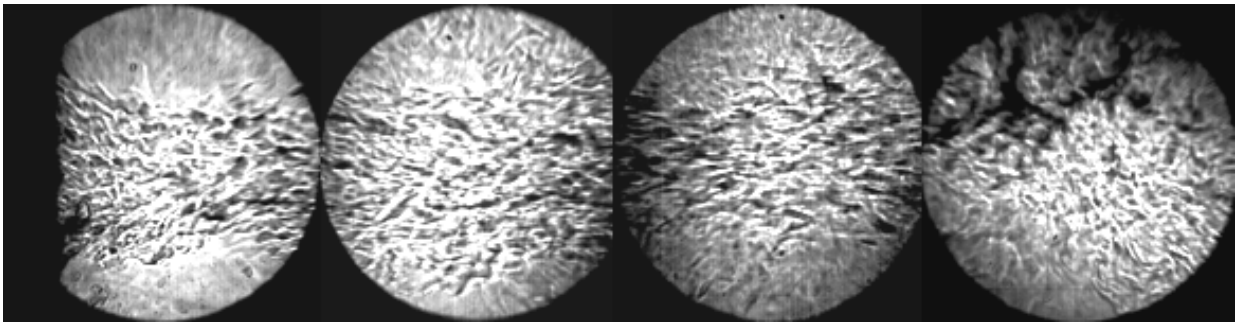

Fig. E2.9: Schlieren image of flow inside the combustor at phase 114^{o} with open-loop control.

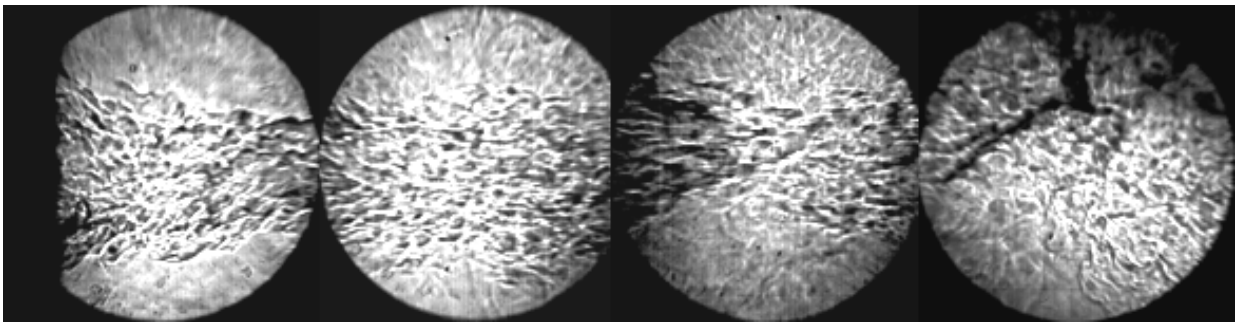

Fig. E2.10: Schlieren image of flow inside the combustor at phase 128^{o} with open-loop control.

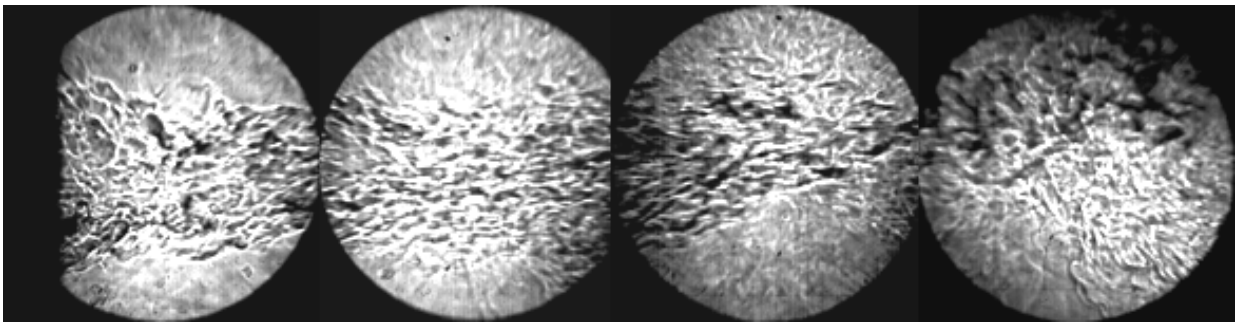

Fig. E2.11: Schlieren image of flow inside the combustor at phase 142^{o} with open-loop control.

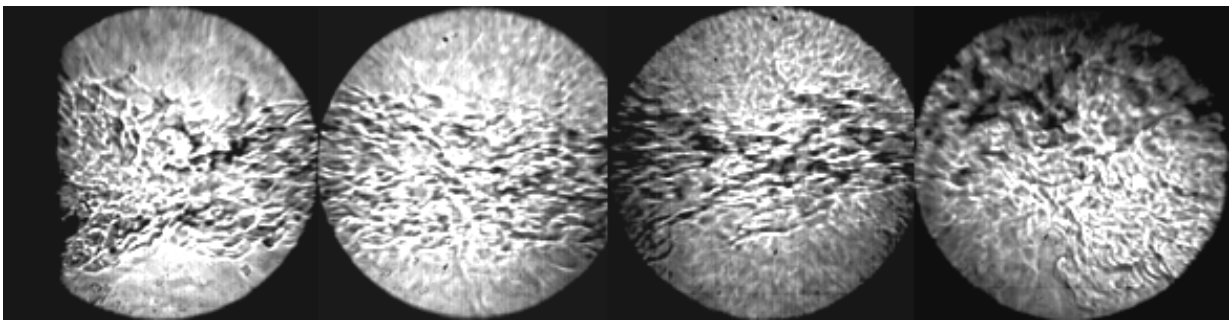

Fig. E2.12: Schlieren image of flow inside the combustor at phase 156^{o} with open-loop control.

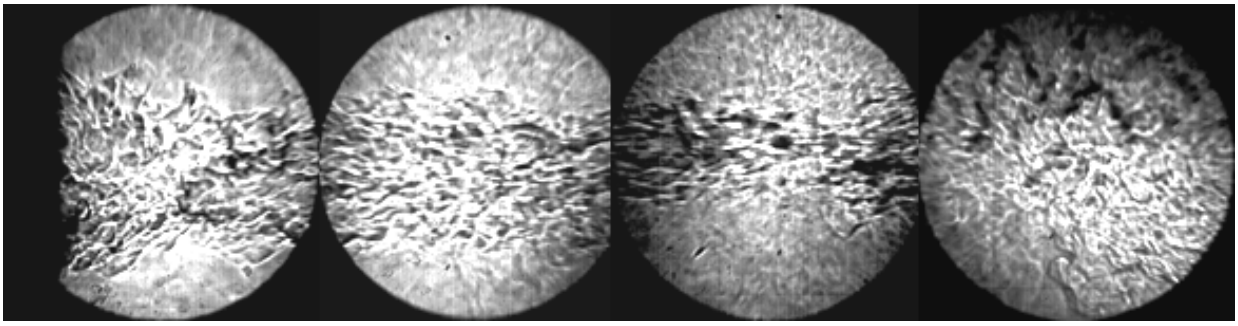

Fig. E2.13: Schlieren image of flow inside the combustor at phase 171^{o} with open-loop control.

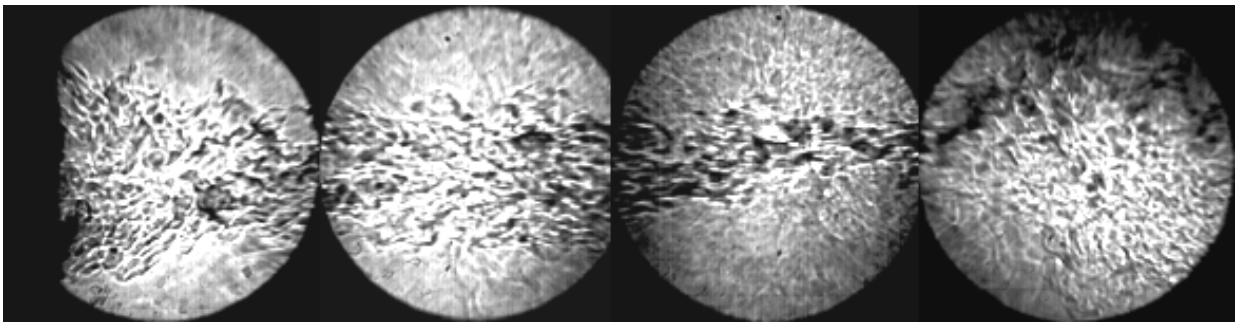

Fig. E2.14: Schlieren image of flow inside the combustor at phase 185^{o} with open-loop control.

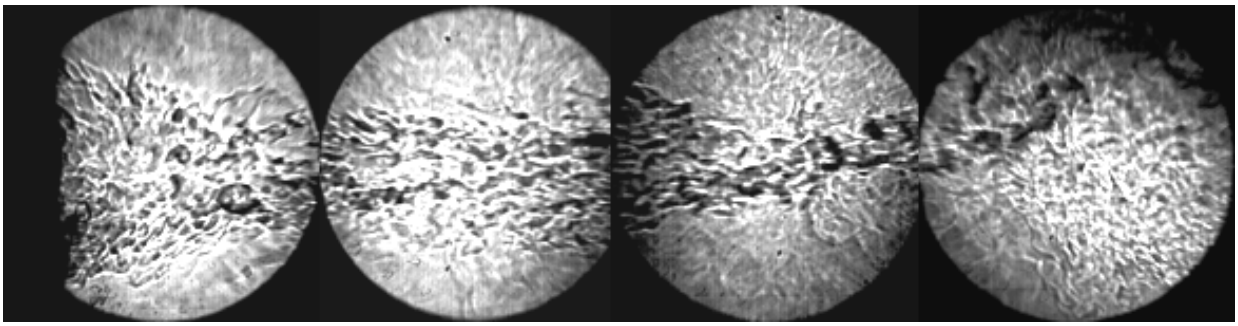

Fig. E2.15: Schlieren image of flow inside the combustor at phase 199^{o} with open-loop control.

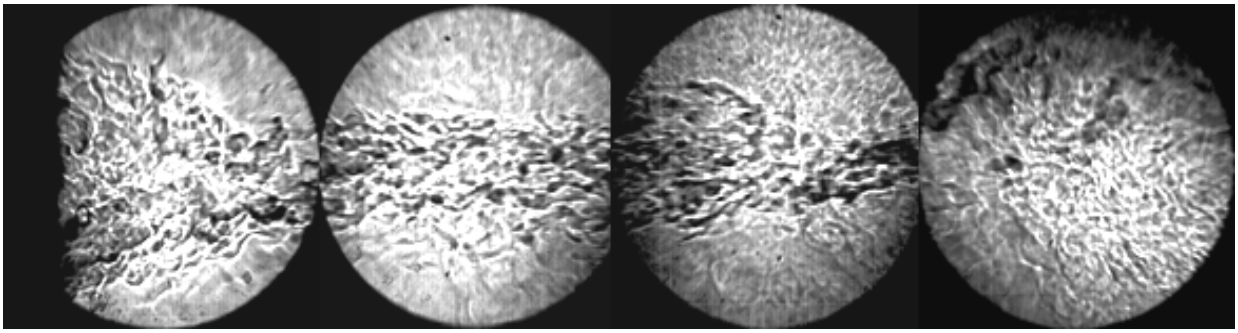

Fig. E2.16: Schlieren image of flow inside the combustor at phase 213^{o} with open-loop control.

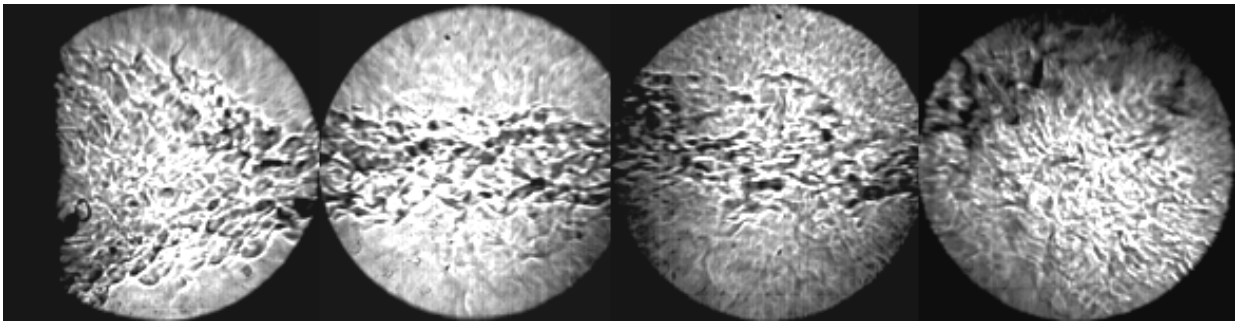

Fig. E2.17: Schlieren image of flow inside the combustor at phase 228^{o} with open-loop control.

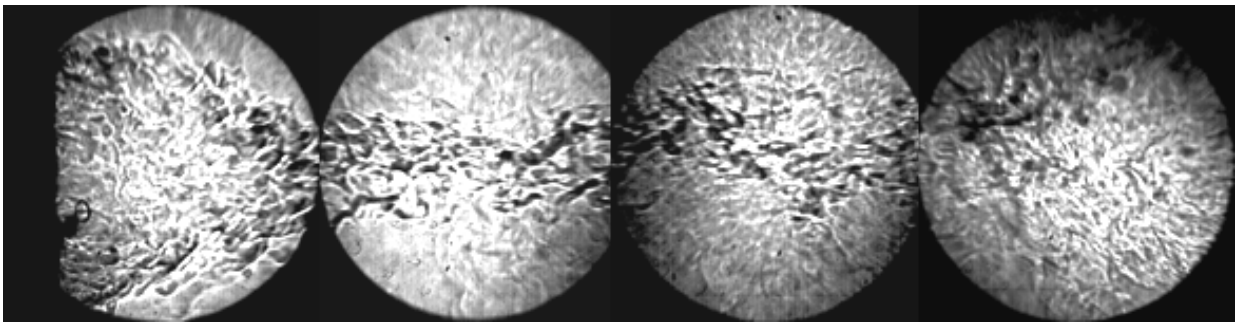

Fig. E2.18: Schlieren image of flow inside the combustor at phase 242^{o} with open-loop control.

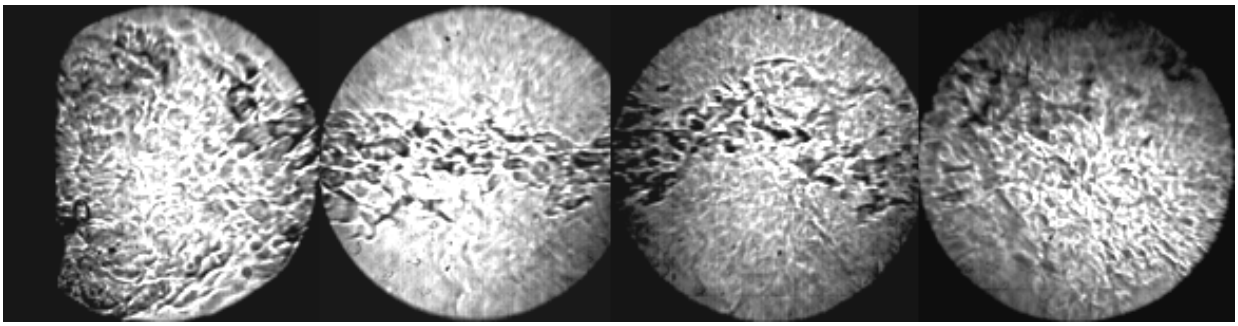

Fig. E2.19: Schlieren image of flow inside the combustor at phase 256^{o} with open-loop control.

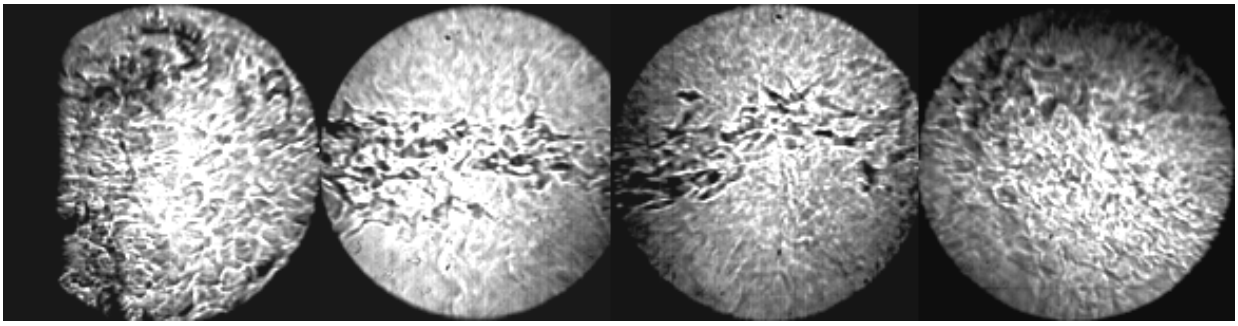

Fig. E2.20: Schlieren image of flow inside the combustor at phase 270^{o} with open-loop control.

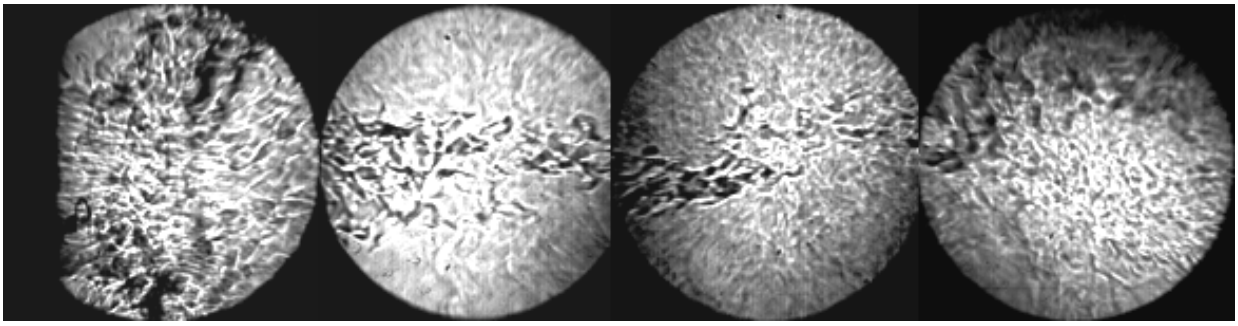

Fig. E2.21: Schlieren image of flow inside the combustor at phase 284^{o} with open-loop control.

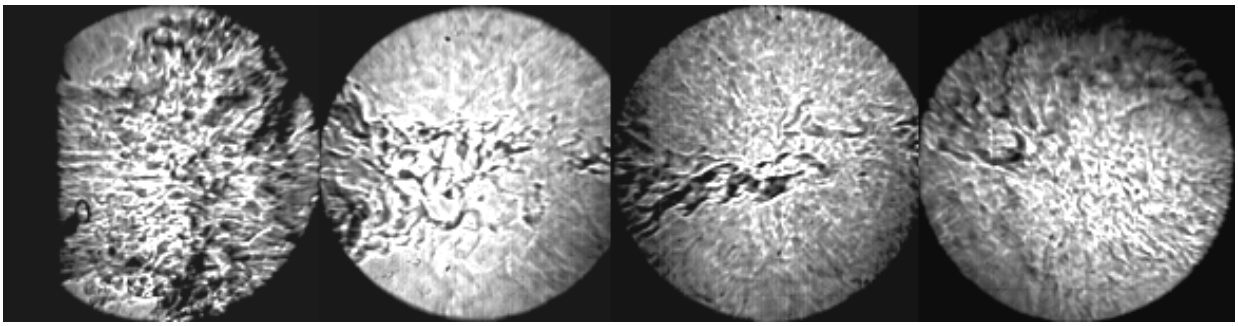

Fig. E2.22: Schlieren image of flow inside the combustor at phase 299^{o} with open-loop control.

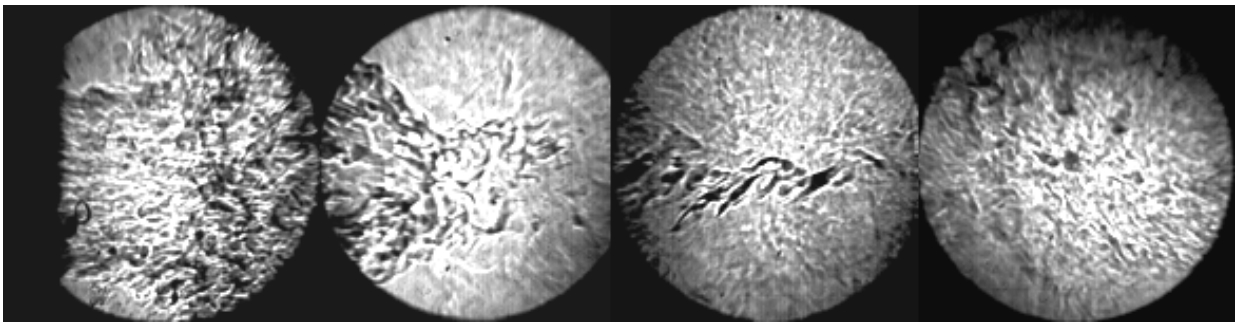

Fig. E2.23: Schlieren image of flow inside the combustor at phase 313^{o} with open-loop control.

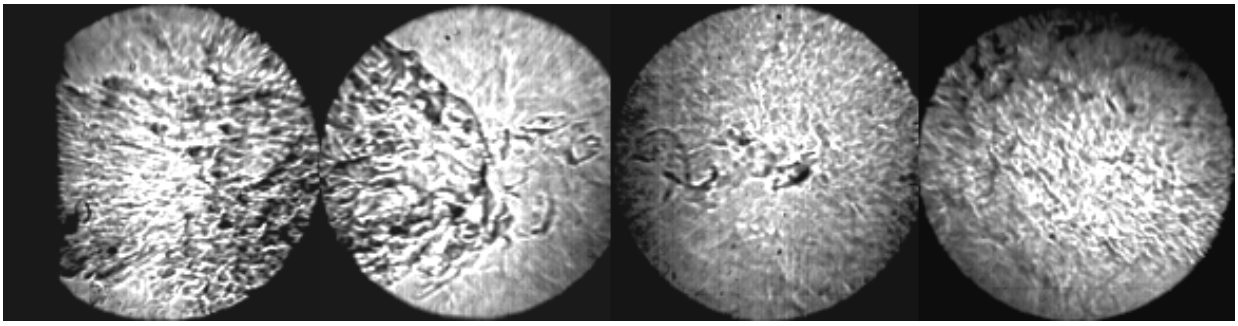

Fig. E2.24: Schlieren image of flow inside the combustor at phase 327^{o} with open-loop control.

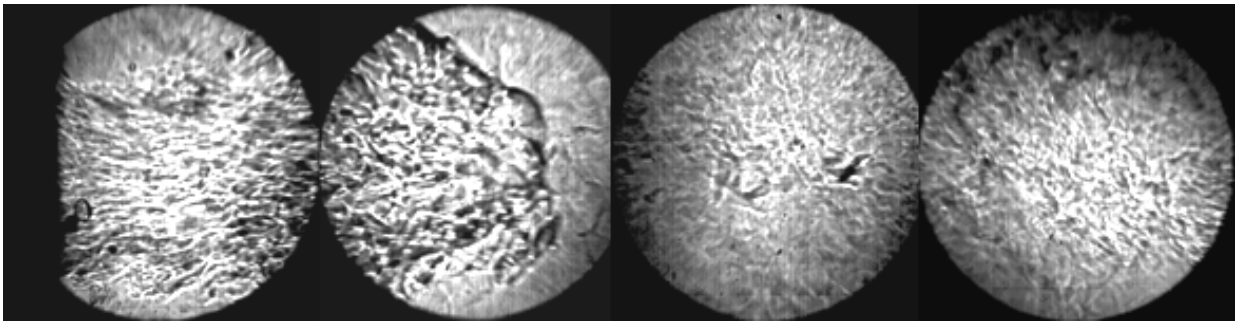

Fig. E2.25: Schlieren image of flow inside the combustor at phase 341^{o} with open-loop control.

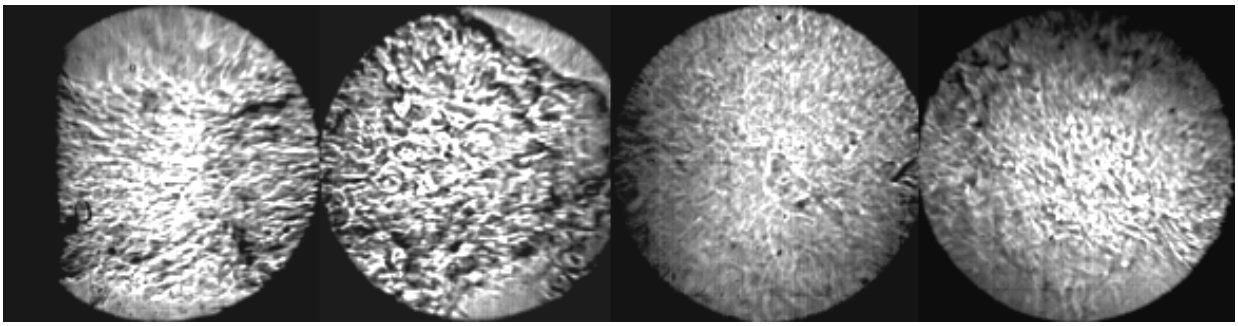

Fig. E2.26: Schlieren image of flow inside the combustor at phase 356^{o} with open-loop control.

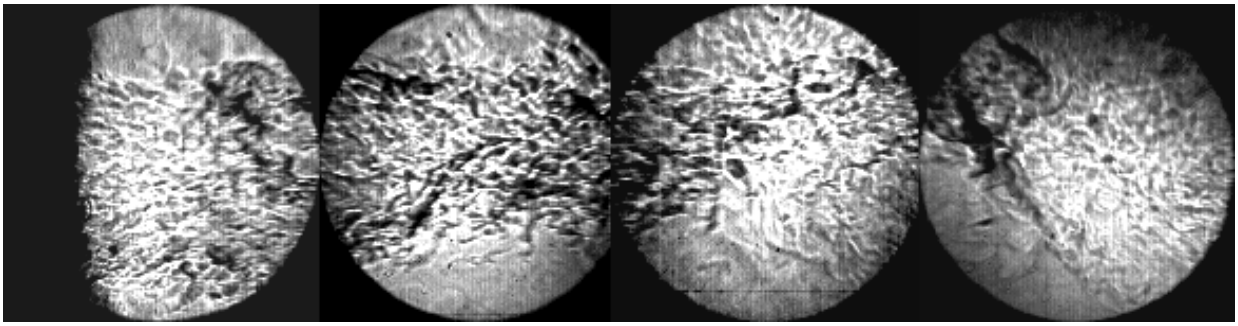

Fig. E3.1: Schlieren image of flow inside the combustor at phase 0^o with close-loop control.

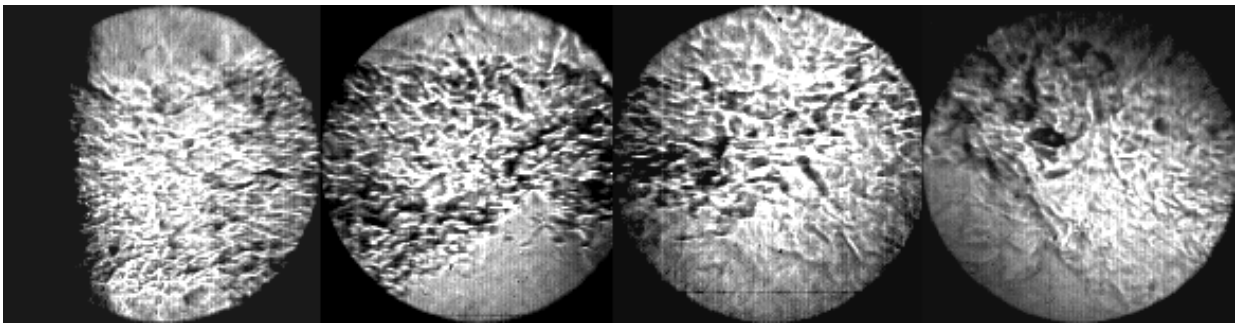

Fig. E3.2: Schlieren image of flow inside the combustor at phase 14^o with close-loop control.

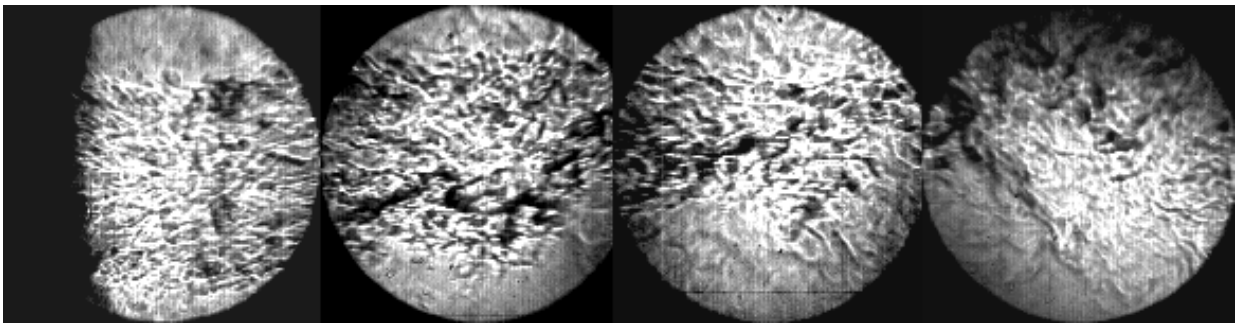

Fig. E3.3: Schlieren image of flow inside the combustor at phase 28^o with close-loop control.

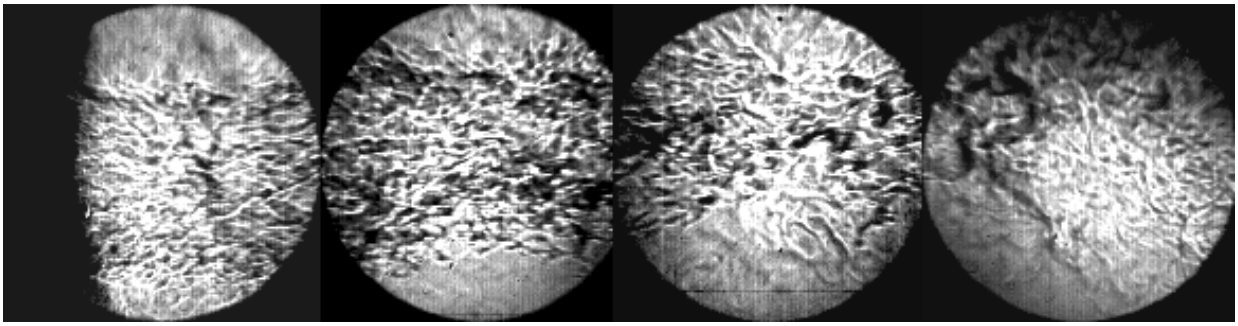

Fig. E3.4: Schlieren image of flow inside the combustor at phase 43^o with close-loop control.

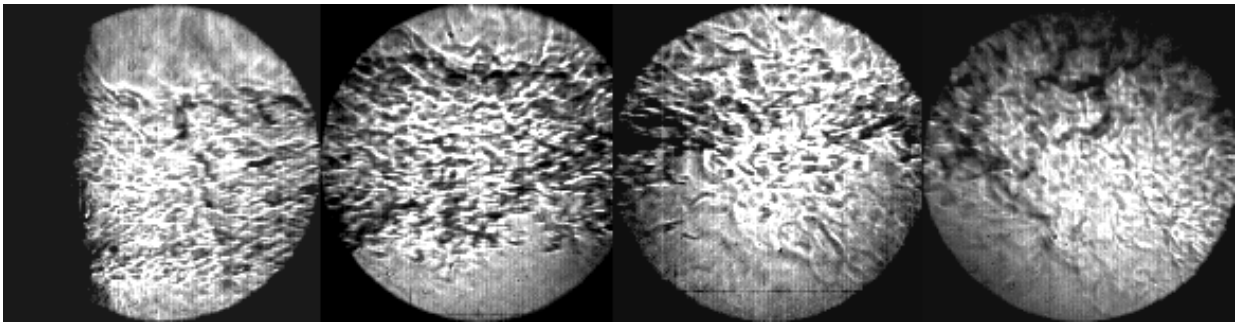

Fig. E3.5: Schlieren image of flow inside the combustor at phase 57^{o} with close-loop control.

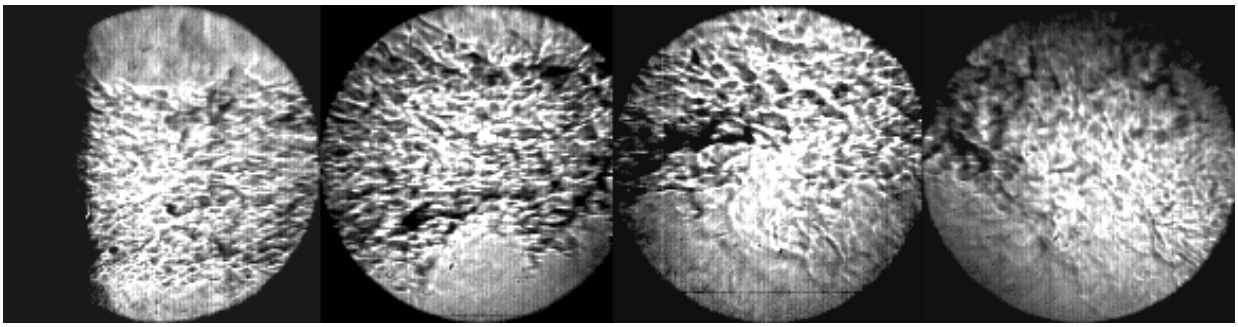

Fig. E3.6: Schlieren image of flow inside the combustor at phase 71^{o} with close-loop control.

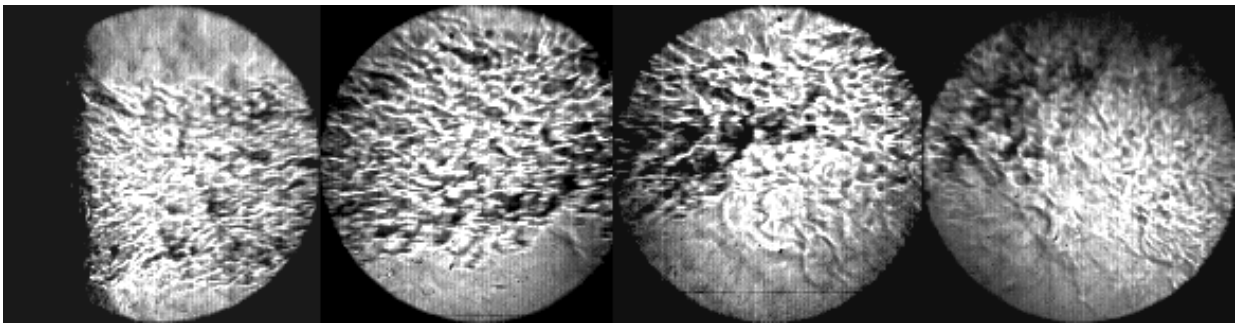

Fig. E3.7: Schlieren image of flow inside the combustor at phase 85^{o} with close-loop control.

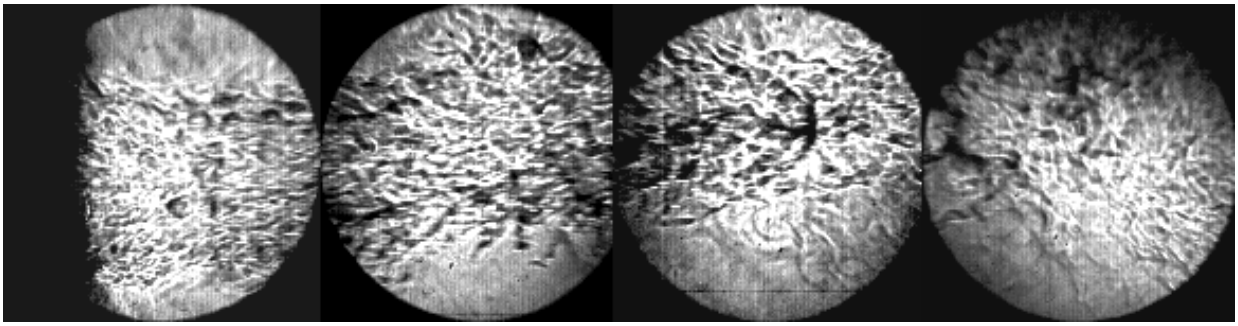

Fig. E3.8: Schlieren image of flow inside the combustor at phase 100^{o} with close-loop control.

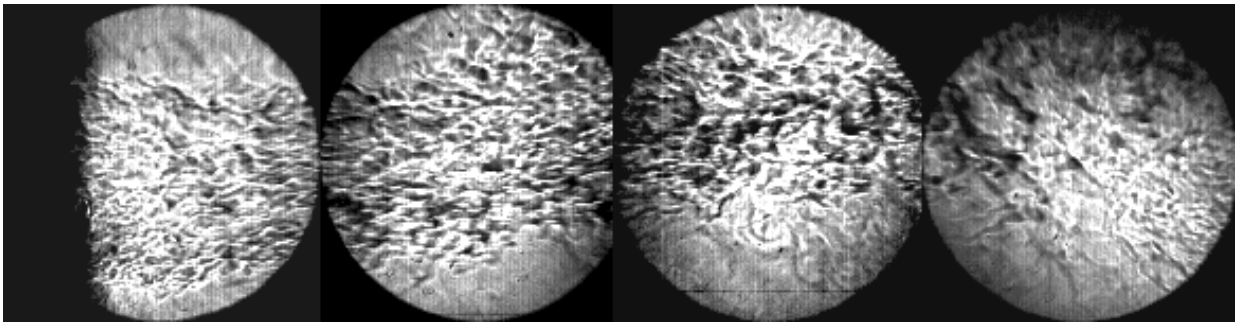

Fig. E3.9: Schlieren image of flow inside the combustor at phase 114^{o} with close-loop control.

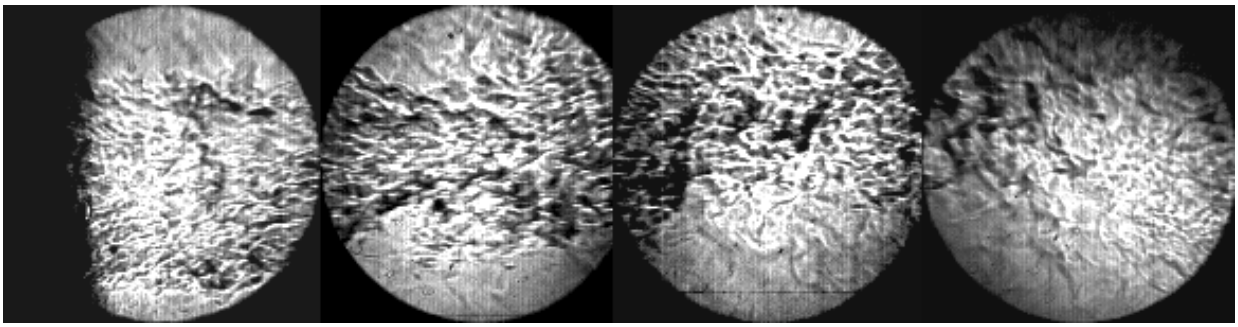

Fig. E3.10: Schlieren image of flow inside the combustor at phase 128^{o} with close-loop control.

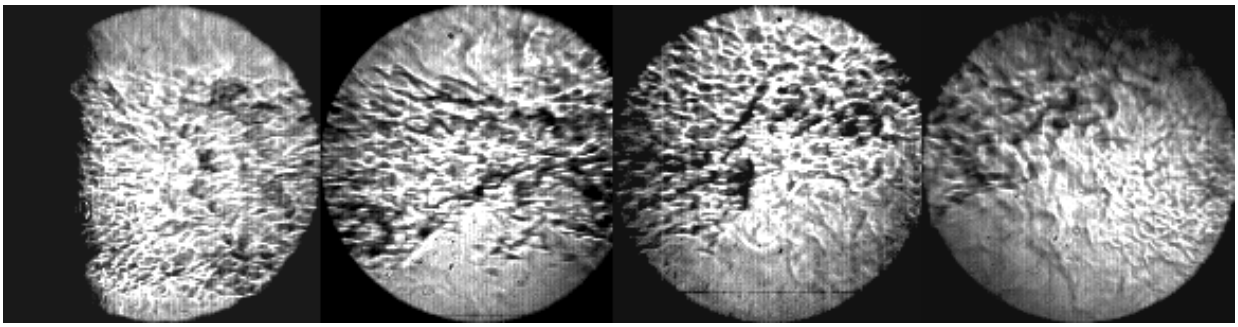

Fig. E3.11: Schlieren image of flow inside the combustor at phase 142^{o} with close-loop control.

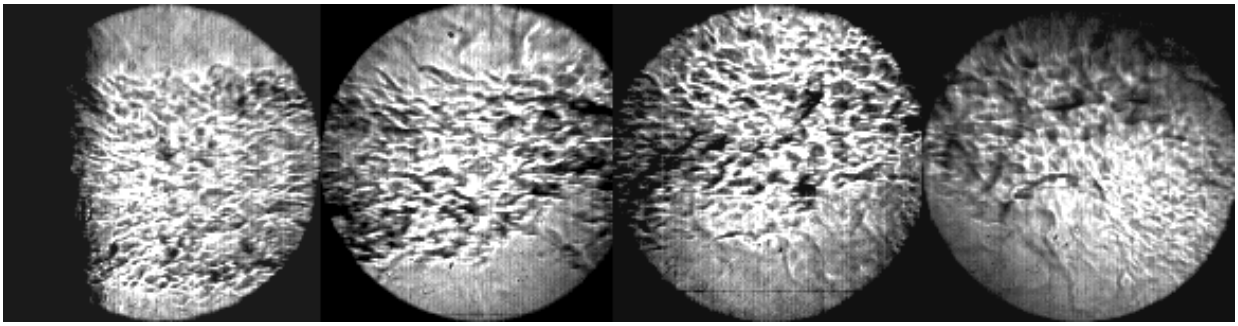

Fig. E3.12: Schlieren image of flow inside the combustor at phase 156^{o} with close-loop control.

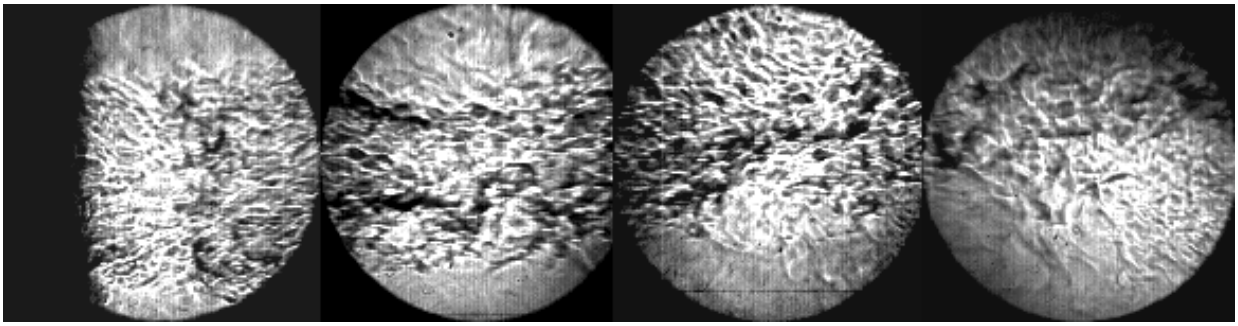

Fig. E3.13: Schlieren image of flow inside the combustor at phase 171^{o} with close-loop control.

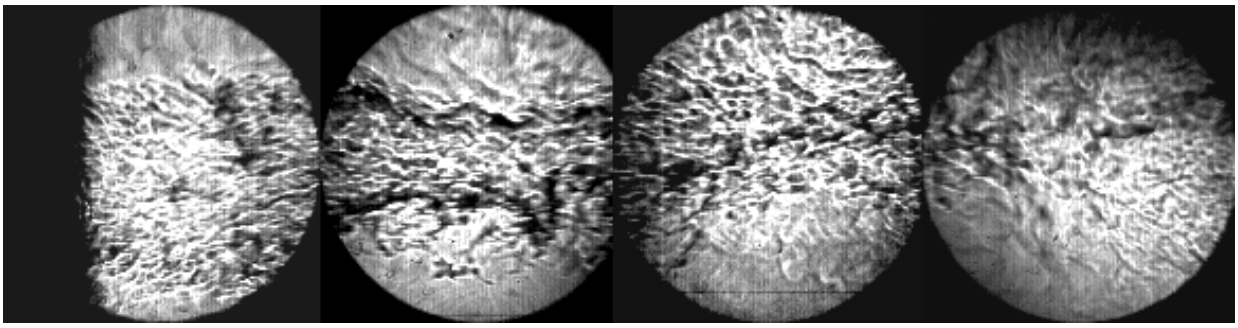

Fig. E3.14: Schlieren image of flow inside the combustor at phase 185^{o} with close-loop control.

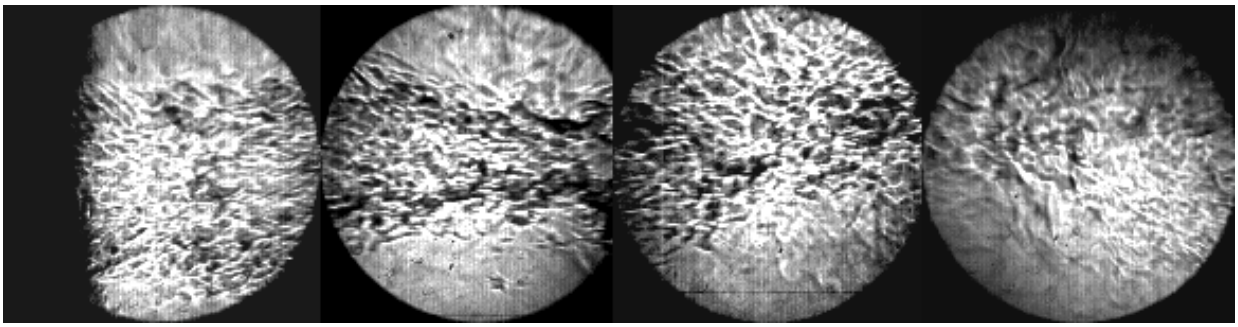

Fig. E3.15: Schlieren image of flow inside the combustor at phase 199^{o} with close-loop control.

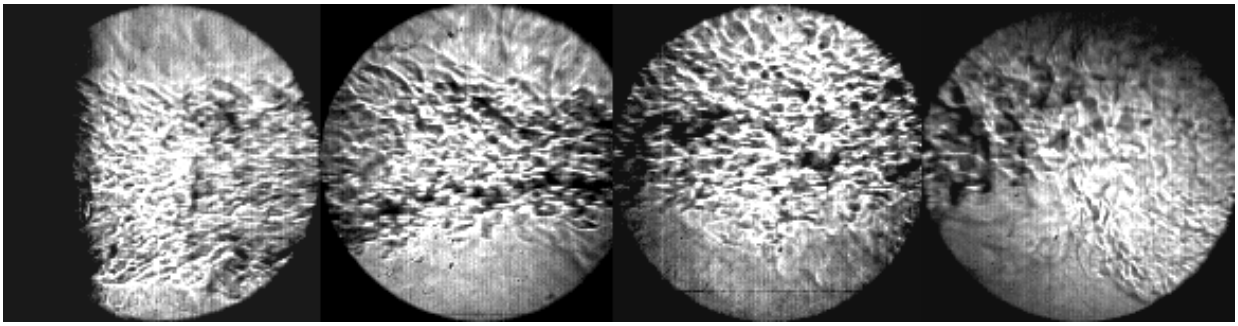

Fig. E3.16: Schlieren image of flow inside the combustor at phase 213^{o} with close-loop control.

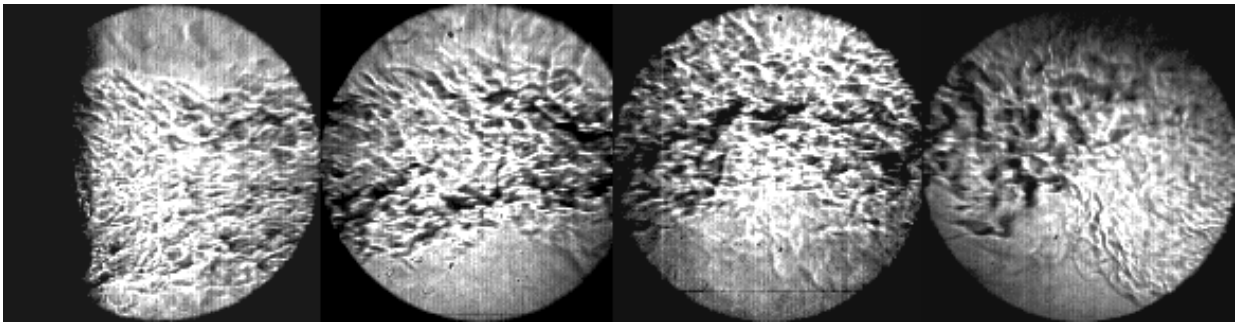

Fig. E3.17: Schlieren image of flow inside the combustor at phase 228^{o} with close-loop control.

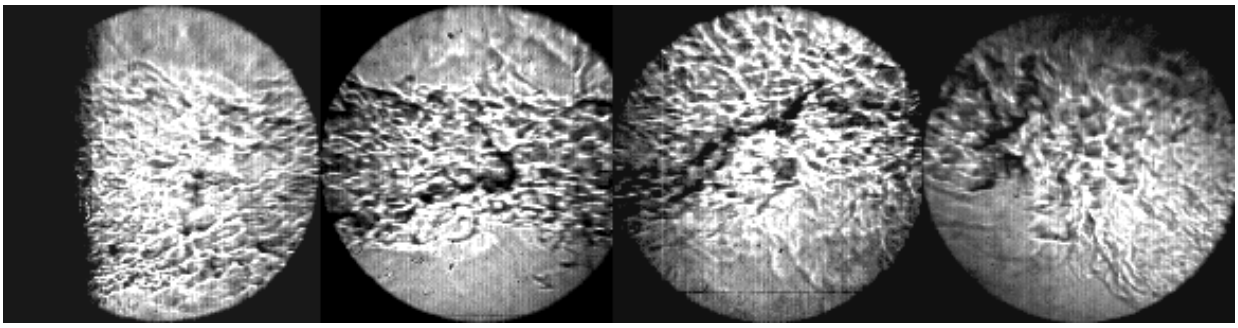

Fig. E3.18: Schlieren image of flow inside the combustor at phase 242^{o} with close-loop control.

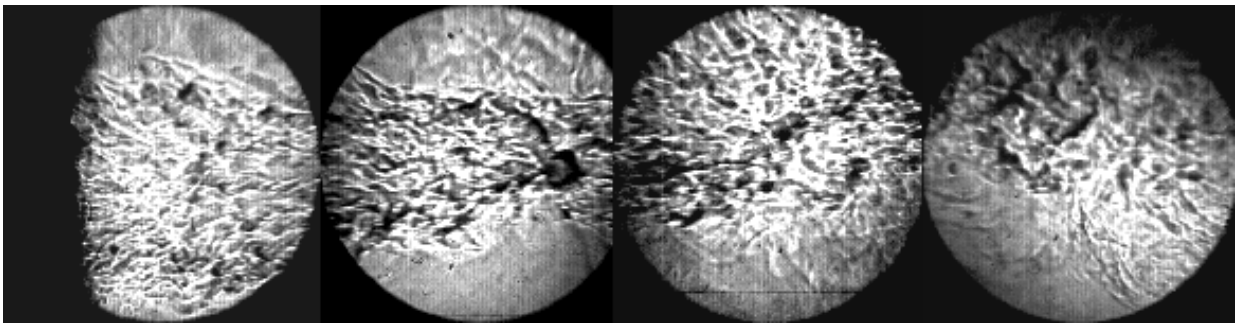

Fig. E3.19: Schlieren image of flow inside the combustor at phase 256^{o} with close-loop control.

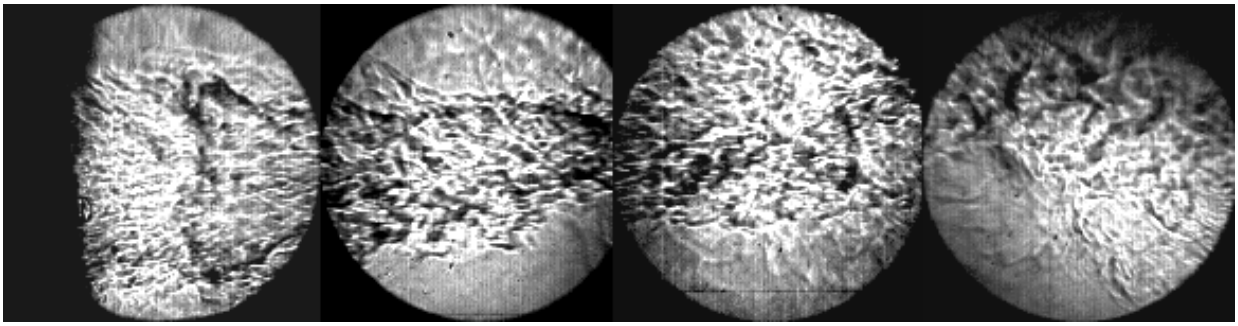

Fig. E3.20: Schlieren image of flow inside the combustor at phase 270^{o} with close-loop control.

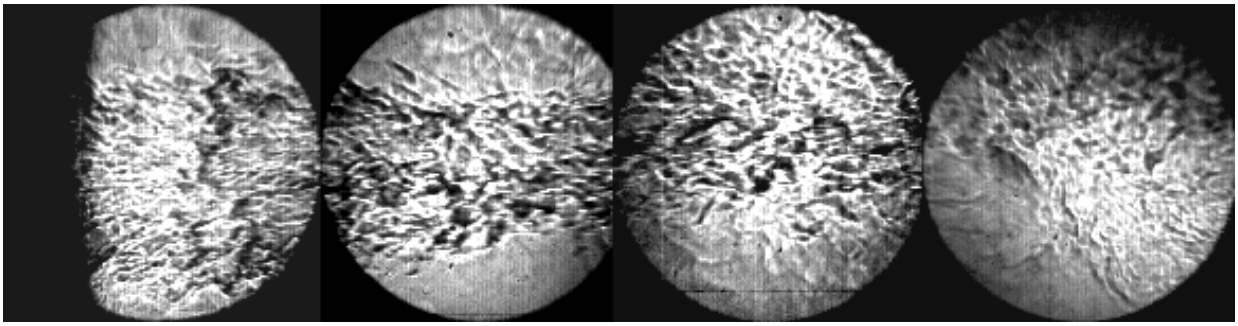

Fig. E3.21: Schlieren image of flow inside the combustor at phase 284^{o} with close-loop control.

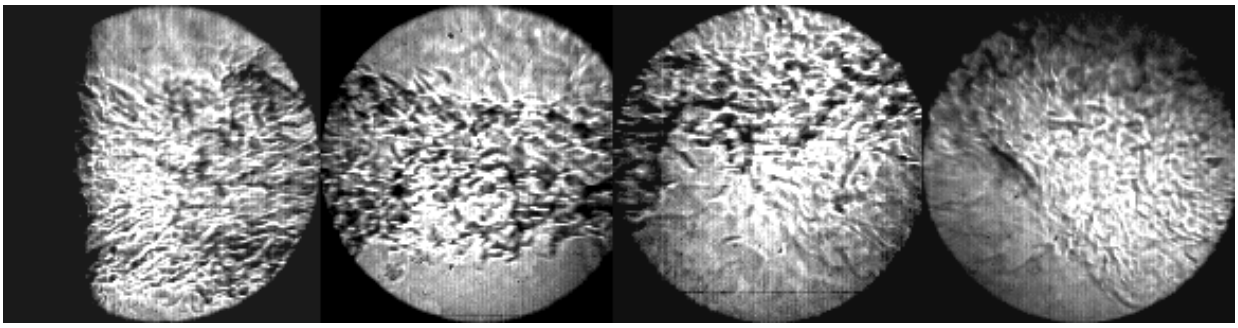

Fig. E3.22: Schlieren image of flow inside the combustor at phase 299^{o} with close-loop control.

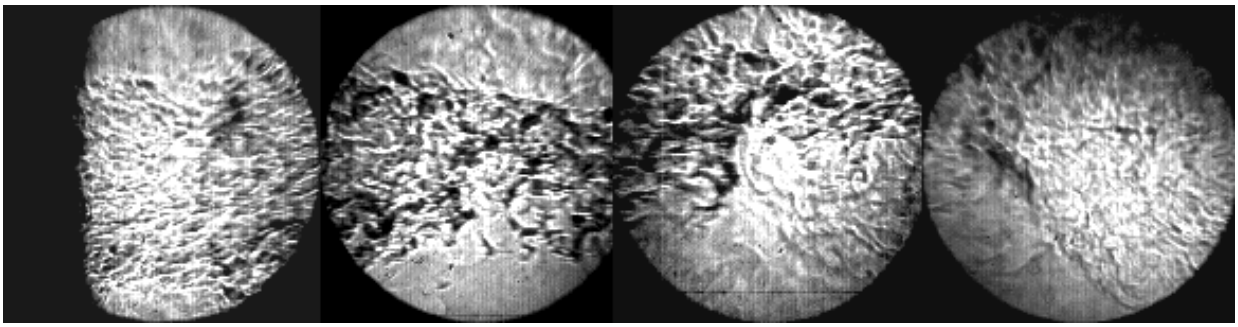

Fig. E3.23: Schlieren image of flow inside the combustor at phase 313^{o} with close-loop control.

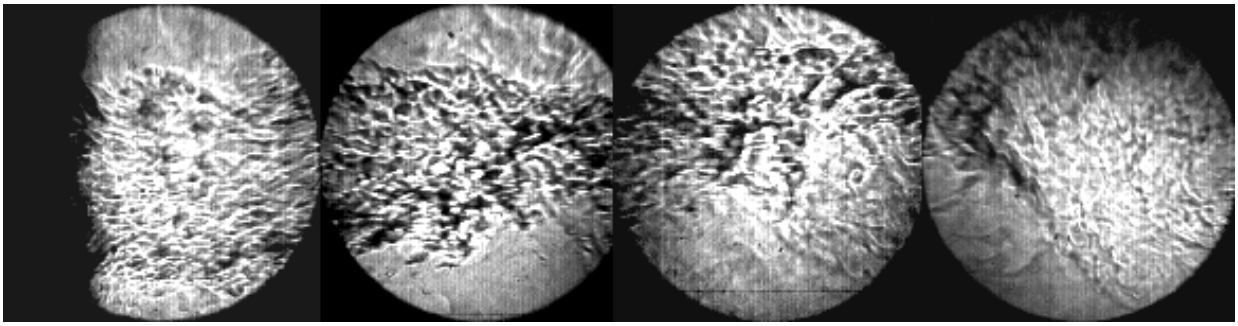

Fig. E3.24: Schlieren image of flow inside the combustor at phase 327^{o} with close-loop control.

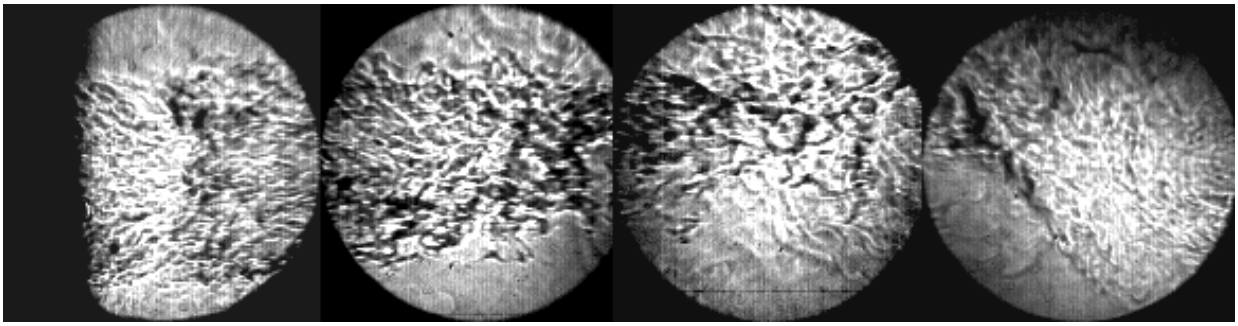

Fig. E3.25: Schlieren image of flow inside the combustor at phase 341^{o} with close-loop control.

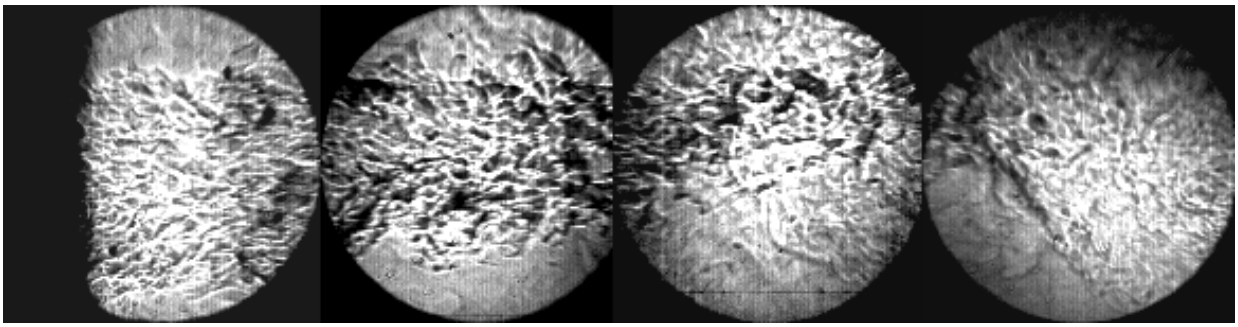

Fig. E3.26: Schlieren image of flow inside the combustor at phase 356^{o} with close-loop control.

References

[1] Lang, W., Poinsot, T., Candel, S., "Active Control of Combustion Instability," Combustion and Flame, Vol. 70, pp. 281-289, 1987.

[2] Bloxsidge, G.J., Dowling, A.P., Hooper, N., and Langhorne, P.J., "Active Control of an Acoustically Driven Combustion Instability," Journal of Theoretical and Applied Mechanics, Supplement to Vol. 6, pp. 161-175, 1987.

[3] Poinsot, T., Bourienne, F., Candel, S., Esposito, E., and Lang, W., "Suppression of Combustion Instabilities by Active Control," Journal of Propulsion and Power, Vol. 5, No. 1, pp. 14-20, 1989.

[4] Langhorne, P.J., Dowling, A.P., and Hooper, N., "Practical Active Control System for Combustion Oscillations," Journal of Propulsion and Power, Vol. 6, No. 3, pp. 324-333, 1990.

[5] Candel, S.M., "Combustion Instabilities Coupled by Pressure Waves and Their Active Control," Twenty-Fourth Symposium (International) on Combustion, The Combustion Institute, pp. 1277-1296, 1992.

[6] Culick, F.E.C., "Combustion Instabilities in Liquid-Fueled Propulsion Systems: An Overview," AGARD-CP-450, 1988.

[7] Schadow, K.C., Yang, V., Culick, F., Rosfjord, T., Sturgess, G., Zinn, B.T., "Active Combustion Control for Propulsion Systems," AGARD-R-820, 1997.

[8] Yang, V. and Schadow, K.C., "AGARD Workshops on Active Combustion Control for Propulsion Systems," Proceeding of NATO/RTO Symposium on Gas Turbine Engine Combustion, Emissions, and Alternative Fuels, RTO-MP-14, pp. 36/1-36/20, 1998.

[9] DeLaat, J.C., Breisacher, K.J., Saus, J.R., Paxson, D.E., "Active Combustion Control for Aircraft Gas Turbine Engines," Thirty-Sixth AIAA/ASME/SAE/ASEE Joint Propulsion Conference and Exhibit, AIAA 2000-3500, 2000.

[10] Richman, M.H., and Richman, S.R., "Active Control for Military Engines", NATO/RTO Spring 2000 Symposium on Active Control Technology for Enhanced Performance Operation Capabilities of Military Aircraft, Land Vehicles and Sea Vehicles, Braunschweig, Germany, 2000.

[11] Przybylko, S.J., "Active-Control Technologies for Aircraft Engines," Thirty-Third AIAA/ASME/SAE/ASEE Joint Propulsion Conference and Exhibit, AIAA 1997-2769, 1997.

[12] Kailasanath, K. and Gutmark, E.J., "Combustion Instability," Propulsion Combustion: Fuels to Emissions, Roy, G.D., ed., pp. 129-172, Taylor & Francis, 1998.

[13] Roy, G.D., "Combustion Enhancement and Control," Propulsion and Combustion: Fuels to Emissions, Roy, G.D., ed, pp. 173-212, Taylor & Francis, 1998.

[14] Tyndal, J., "Sound." D. Appleton & Company, New York, 1897.

[15] Le Conte, J., Philosop. Mag., pp. 235, 1958.

[16] Rijke P. Ann. Phys., pp.107-339, 1959.

[17] Rayleigh, L., "The Theory of Sound," Dover, 1945.

[18] Chu, B.-T., and Kovasznay, L.S.G., "Non-linear Interactions in a Viscous Heat-Conducting Compressible Gas," Journal of Fluid Mechanics, Vol. 3, pp. 494-514, 1957.

[19] Joos, F, and Vortmeyer, D., "Self-Exited Oscillations in Combustion Chambers with Premixed Flames and Several frequencies," Combustion and Flame, Vol. 65, pp. 253-262, 1986.

[20] Putnam, A., "Combustion Driven Oscillations in Industry," Elsevier, New York, 1971.

[21] Schadow, K.C., and Gutmark, E., "Combustion Instability Related to Vortex Shedding in Dump Combustors and Their Passive Control," Progress in Energy Combustion and Science, Vol. 18, No. 2, pp. 117-132, 1992.

[22] McManus, K.R., Poinsot, T., and Candel, S.M., "A Review of Active Control of Combustion Instabilities," Progress in Energy and Combustion Science, Vol. 19, No. 1, pp. 1-29, 1993.

[23] Culick, F.E.C., "Combustion Instabilities in Propulsion Systems," Combustion Instabilities Driven By Thermo-Chemical Acoustic Sources, ASME, NCA Vol. 4, HTD.Vol. 128, pp. 33-52, 1989.

[24] Tsien, H.S., "Servo-Stabilization of Combustion in Rocket Motors," ARS Journal Vol. 22, pp. 256, 1953.

[25] Marble, F.E., Cox, D.W., Jr., "Servo-Stabilization of Low-Frequency Oscillations in A Liquid Bipropellant Rocket Motor," ARS Journal Vol. 22, pp. 63-81, 1953.

[26] Sivasegaram, S., and Whitelaw, J.H., "Suppression of Oscillations in Confined Disk-Stabilized Flames," Journal of Propulsion and Power, Vol. 3., No. 4., pp. 291-295, 1987.

[27] Dines, P.J., "Active Control of Flame Noise," Ph.D. Dissertation, Cambridge University, Cambridge, England, 1983.

[28] Heckl, M.A., "Active Control of the Noise from a Rijke tube," IUTAM Symposium on Aero and Hydro-Acoustics, Lyon Springer. Verlag, pp. 211-216, 1985.

[29] Bloxsidge, G.J., Dowling, A.P., Hooper, N., and Langhorne, P.J., "Active Control of Reheat Buzz," AIAA Journal, Vol. 26, No. 7, pp. 783-790, 1988.

[30] Poinsot, T., Veynante, D., Bourienne, F., Candel, S., Esposito, E., and Surget, J., "Initiation and Suppression of Combustion Instabilities by Active Control," Twenty-Second Symposium (International) on Combustion, The Combustion Institute, pp. 1363-1370, 1988.

[31] Gutmark, E., Parr, T.P., Hanson-Parr, D.M., and Schadow, K.C., "Use of Chemiluminescence and Neural Networks in Active Combustion Control," Twenty-Third Symposium (International) on Combustion, The Combustion Institute, pp. 1101-1106, 1990.

[32] Jones, C.M., Stone, F., Shih, W.P., and Santavicc, D.A., "Active Control of Combustion Instabilities through Periodic Secondary Fuel Injection," Chemical and Physical Processes in Combustion, 0277-1128 pp. 233, 1995.

[33] Jones, C.M., Lee, J.G., Santavicca, D.A., "Closed-Loop Active Control of Combustion Instabilities Using Subharmonic Secondary Fuel Injection," Journal of Propulsion and Power, Vol. 15, No. 4, pp. 584-590, 1999.

[34] Menon, S., "Secondary Fuel Injection Control of Combustion Instability in A Ramjet," Combustion Science and Technology, Vol. 100, No. 1-6, pp. 385-393, 1994.

[35] Schadow, K.C., Yu, K.H., Parr, T.P., and Wilson, K.J., "Active Combustion Control with Pulsed Fuel Injection," 13th International Symposium on Air Breathing Engines, Vol. 7 No. 12, 1997.

[36] Yu, K.H., Wilson, K.J., Schadow, K.C., "Active Combustion Control in A Liquid-Fueled Dump Combustor," Thirty-Fifth Aerospace Sciences Meeting and Exhibit, AIAA 1997-0462, 1997.

[37] Yu, K.H., Wilson, K.J., Schadow, K.C., "Active Instability Suppression by Controlled Injection of Liquid Fuel," Thirty-Third AIAA/ASME/SAE/ASEE Joint Propulsion Conference and Exhibit, AIAA 1997-3324, 1997.

[38] Park, S., Wachsman, A., Annawamy, A.M., and Ghoniem, A.F., Pang, B., and Yu, K.H., "Experimental Study of POD-Based Control for Combustion Instability Using a Linear Photodiode Array," Fourty-Second Aerospace Sciences Meeting and Exhibit, AIAA 2004-0639, 2004.

[39] Heising, R., Lubarsky, E., Neumaier, M., Neumeier, Y., Zinn, B.T., "Periodic Liquid Fuel Sprays Combustion Processes and Their Damping of Combustion Instabilities," Thirty-Eighth Aerospace Sciences Meeting and Exhibit, AIAA 2000-1024, 2000.

[40] Kidin, N. I, Afanasiev, V. V., and Ilyin, S.V., "Active Control of Combustion Instabilities by Electrical Discharges" Proceedings of 10th ONR Propulsion Meeting, pp. 118-129, 1997.

[41] Hermann, J., Orthmann, A., Hoffmann, S., and Berenbrink, P., "Combination of Active Instability Control and Passive Measures to Prevent Combustion Instabilities in a 260 MW Heavy Duty Gas Turbine." NATO/RTO Spring 2000 Symposium on Active Control Technology for Enhanced Performance Operation Capabilities of Military Aircraft, Land Vehicles and Sea Vehicles, Braunschweig, Germany, 2000.

[42] Mizutani, Y., Nakabe, K., Matsumoto, Y., Saeki, T., and Matsui, T., "Processing of Luminescent Radical Images for Flame Diagnostics," JSME International Journal Series II Vol. 32, No. 3, pp. 455-463, 1989.

[43] Lawn, C.J., "Distributions of Instantaneous Heat Release by the Cross-Correlation of Chemiluminescent Emissions," Combustion and Flame, Vol. 123, pp. 227-240, 2000.

[44] Chigier, N.A., "Combustion Measurements," Hemisphere Publishing Corporation, 1991.

[45] Gutmark, E., Parr, T.P., Wilson, K.J., Hanson-Parr, D.M., and Shadow, K.C., "Closed-Loop Control in a Flame and a Dump Combustor," IEEE Control Systems, Vol. 13, No. 2, pp. 73-78, 1993.

[46] Yu, K.H., Wilson, K.J., "Scale-Up Experiments on Liquid-Fueled Active Combustion Control," Journal of Propulsion & Power, Vol. 18, No. 1, pp. 53-60, 2002.

[47] Fung, Y.-T. and Yang, V., "Active Control of Nonlinear Pressure Oscillations in Combustion Chambers," Journal of Propulsion and Power, Vol. 8, No. 6, pp. 1282-1289,1992.

[48] Billoud, G., Galland, M.A., and Huu, C., Candel, S.M., "Adaptive Active Control of Combustion Instabilities," Combustion Science and Technology, Vol. 81, No. 4-6, pp. 257-283, 1992.

[49] Kurtz, A.D., Chivers, J., Ned, A., and Epstein, A.H., "Sensor Requirements for Active Gas Turbine Engine Control," NATO/RTO Spring 2000 Symposium on Active Control Technology for Enhanced Performance Operation Capabilities of Military Aircraft, Land Vehicles and Sea Vehicles, Braunschweig, Germany, 2000.

[50] Yu, K.H., Trouve, A., and Daily, J.W., "Low-Frequency Pressure Oscillations in A Model Ramjet Combustor," Journal of Fluid Mechanics, Vol. 232, pp. 47-72, 1991.

[51] Parr, T.P., Gutmark, E., Wilson, K.J., Hanson-Parr, D.M., Yu, K., Smith, R.A., and Schadow, K.C. "Compact Incinerator Afterburner Concept Based On Vortex Combustion," Twenty-Sixth Symposium (International) on Combustion, The Combustion Institute, Vol. 2, pp. 2471-2477, 1996.

[52] Parr, T.P., Wilson, K. J., Smith, R. A., Schadow, K. C., Hansell, D.W., and Cole, J.A., "Actively Controlled Afterburner for Compact Waste Incinerator," International Conference on Incineration and Thermal Treatment Technologies, 1997.

[53] Furlong, E.R., Baer, D.S., and Hanson, R.K., "Real-time Adaptive Combustion Control Using Diode-laser Absorption Sensors," 27th Symposium (International) on Combustion, The Combustion Institute, Vol. 1, pp. 103-111, 1998.

[54] Furlong, E.R., Mihalcea, R.M., Webber, M.E., Baer, D.S., and Hanson, R.K., "Diode-Laser Sensors for Real-Time control of Pulsed Combustion Systems," AIAA Journal, Vol. 37, No. 6, pp. 732-737, 1999.

[55] Hanson, R.K., and Baer, D.S., "Diode-Laser Absorption Sensors for Combustion Measurements and Control," Naval Research Reviews, Vol. 51, No. 3-4, pp. 14-23, 1999.

[56] Eckbreth, A.C. Laser Diagnostics For Combustion Temperature And Species, Gordon & Breach Pub., 1986.

[57] Mihalcea, R.M., Baer, D.S., and Hanson, R.K., "Advanced Diode Laser Absorption Sensor for In-Situ Combustion Measurements of CO_2, H_2O and

Gas Temperature," Twenty-Seventh Symposium (International) on Combustion, The Combustion Institute, Vol. 1, pp. 95-101, 1998.

[58] Ho, C-M, and Tai, Y-C, "Review: MEMS and Its Applications for Flow Control," Journal of Fluids Engineering, Vol. 118, pp. 437-447, 1996.

[59] Tsao, T., Liu, C., Tai, Y.C., and Ho, C.M., "Micromachined Magnetic Actuator for Active Fluid Control," Application of Microfabrication to Fluid Mechanics, ASME FED Vol. 197, pp. 31-38, 1994.

[60] Liu, C., Tsao, T., Tai, Y., Leu, J., Ho, C.M., Tang, W.L., and Miu, D., "Out-of-Plane Permanent Magnetic Actuators for Delta Wing Control," Proceedings of IEEE Micro Electro Mechanical Systems, pp. 7-12, 1995.

[61] Liu, C., Tai, Y.C., Huang, J., Ho, C.M., "Surface-Micromachined Thermal Shear Stress Sensor," Application of Microfabrication to Fluid Mechanics, ASME FED Vol. 197, pp. 9-16, 1994.

[62] Gulati, A., and Mani, R., "Active Control of Unsteady Combustion-Induced Oscillations," Journal of propulsion and power, Vol. 8, No. 5, pp. 1109-1115, 1992.

[63] Gleis, S., Vortmeyer, D., and Rau, W., "Experimental Investigations on the Transition from Stable to Unstable Combustion by means of Active Instability Control," Propulsion and Energetics Panel, 75th Symposium, AGARD, 1990.

[64] Yu, K.H., Wilson, K.J., Parr, T.P., and Schadow, K.C., "Active Combustion Control Using Multiple Vortex Shedding," Thirty-Second ASME/SAE/ASEE Joint Propulsion Conference and Exhibit, AIAA 1996-2760, 1996.

[65] Choudhury, P.R., Gerstein, M., and Mojaradi, R., "A Novel Feedback Concept for Combustion Instability in Ramjets," 22nd JANNAF Combustion Meeting, 1985.

[66] Gutmark, E.J., Parr, T.P., Wilson, K.J., Yu, K.H., Smith, R.A., Hanson-Parr, D.M., and Schadow, K.C. "Compact Waste Incinerator Based On Vortex Combustion," Combustion Science and Technology Vol. 121, pp. 333-349, 1996.

[67] Schadow, K.C., Gutmark, E., and Wilson, K.J., "Active Combustion Control in A Coaxial Dump Combustor," Combustion Science and Technology, Vol. 81, No. 4-6, pp. 285-300, 1992.

[68] Brouwer, J., Ault, B.A., Bobrow, J.E., and Samuelsen, G.S., "Active Control for Gas Turbine Combustors," Twenty-Third Symposium (International) on Combustion, The Combustion Institute, pp. 1087-1092, 1990.

[69] Jackson, M.D., and Agrawal, A.K., "Active Control of Combustion for Optimal Performance," Journal of Engineering for Gas Turbines and Power, Vol. 121, No 3, pp. 437-443, 1999.

[70] Richards, G.A., Janus, M., Robey, E.H., "Control of Flame Oscillations With Equivalence Ratio Modulation," Journal of Propulsion and Power, Vol. 15, No. 2, pp. 232-240, 1999.

[71] Bloxsidge, G.J., Dowling, A.P., and Langhorne, P.J., "Reheat Buzz: An Acoustically Coupled Combustion Instability. Part 2. Theory," Journal of Fluid Mechanics, Vol. 193, pp. 445-473, 1988.

[72] McManus, K.R., Vandsburger, U., and Bowman, C.T., "Combustor Performance Enhancement Through Direct Shear Layer Excitation," Combustion and Flame, Vol. 82, pp. 75-92, 1990.

[73] Afanasiev, V.V., Frost, V.A., Kidin, N.I., and Kuxmin, A.K., "Diagnostics and Active Control of Acoustic Instabilities in Combustors by Electrical Discharges and Plasma Jets," Challenges in Propellants and Combustion: 100 years after Nobel, Ed. Kui, L.L., Begell House Inc, pp. 943-961, 1997.

[74] Schadow, K.C., Wilson, K.J., Gutmark, E., and Yu, K.H., "Periodic Chemical Energy Release for Active Combustion Control," 11th International Symposium on Air Breathing Engines, Vol. 11, 1993.

[75] Hermann, J., Orthmann, A., Hoffmann, S., "Active Instability Control of Combustion Oscillations in Heavy Duty Gas Turbines," International Congress on Sound and Vibration, Vol. 7, 1999.

[76] Yu, K.H., Parr, T.P., Wilson, K.J., Schadow, K.C., and Gutmark, E., "Active Control of Liquid-Fueled Combustion Using Periodic Vortex-Droplet Interaction," Twenty-Sixth Symposium (International) on Combustion, The Combustion Institute, Vol. 2, pp. 2843-2850, 1996.

[77] Yu, K.H., Wilson, K.J., and Schadow, K.C., "Liquid-Fueled Active Instability Suppression," Twenty-Seventh Symposium (International) on Combustion, The Combustion Institute, Vol. 2, pp. 2039-2046, 1998.

[78] Chang, E.J., and Kaliasanath, K., "Suppression of Combustion Instabilities Using Timed Injection of High Energy Fuels," Thirty-Fourth AIAA/ASME/SAE/ASEE Joint Propulsion Conference and Exhibit, AIAA 1998-3765, 1998.

[79] Yu, K.H., Wilson, K.J., Parr, T.P., and Schadow, K.C., "An Experimental Study on Actively Controlled Dump Combustors," NATO/RTO Spring 2000

Symposium on Active Control Technology for Enhanced Performance Operation Capabilities of Military Aircraft, Land Vehicles and Sea Vehicles, Braunschweig, Germany, 2000.

[80] Yu, K.H., and Schadow, K.C., "Liquid-fueled Combustion Control: Scale-Up Experiments and Effect of Fuel Droplet Size," Thirty-Seventh Aerospace Science Meeting and Exhibit, AIAA 1999-0328, 1999.

[81] Cohen, J. M., Rey, N.M., Jacobson, C.A., and Anderson, T.J., "Active Control of Combustion Instability in a Liquid-Fueled Low-Nox Combustor," Journal of Engineering for Gas Turbines and Power, Vol. 121, No. 2, pp. 281-284, 1999.

[82] Mcmanus, K.R., Magill, J., and Miller, M.F., "Combustion Instability Suppression in Liquid-Fueled Combustors," Thirty-Sixth Aerospace Science Meeting and Exhibit, AIAA 1998-0642, 1998.

[83] Wilson, K.J., Parr, T.P., Smith, R.A., Yu. K.H., and Schadow, K.C. "Mass-Flux Actuator with High Frequency Response," U.S. Patent No.: 6065688, 2000.

[84] Neumeier, Y., and Zinn, B.T., "Theoretical and Experimental Investigation of the Performance of an Actively Controlled Fuel Actuator," AIAA 1998-0355, 1998.

[85] Lazaro, B.J., and Lasheras, J.C., "Particle Dispersion in A Turbulent, Plane, Free Shear layer," Physics of Fluids, Vol. A No.1, pp. 1035-1044, 1989.

[86] Chung, J.N., and Troutt, T.R., "Simulation of Particle Dispersion in An Axisymmetric Jet," Journal of Fluid Mechanics Vol. 186, pp. 199-222, 1988.

[87] Longmire, E.K., and Eaton, J.K., "Structure of A Particle-Laden Round Jet," Journal of Fluid Mechanics Vol. 236, pp. 217-257, 1992.

[88] Chang, E.J., Kaliasanath, K., and Aggarwal, S.K., "Compressible Flows of Gas-Particle Systems in an Axisymmetric Ramjet Combustor," Thirty-First ASME/SAE/ASEE Joint Propulsion Conference and Exhibit, AIAA 1995-2561, 1995.

[89] Glawe, D.D., and Samimy, M., "Dispersion of Solid Particles in Compressible Mixing Layers," Journal of Propulsion & Power, Vol. 9 No.1, pp. 83-89, 1993.

[90] Chang, E.J., and Kaliasanath, K., "Simulations of Particle Dynamics in an Axisymmetric Ramjet Combustor," Thirty-Third Aerospace Sciences Meeting and Exhibit, AIAA 1995-0812, 1995.

[91] Chang, E.J., and Kaliasanath, K., "Simulations of Particle Dynamics in a Confined Shear Flow," AIAA Journal, Vol. 34, No. 6, pp. 1160-1166, 1996.

[92] Yu, K.H., Wilson, K.J., and Schadow, K.C., "Liquid-Fueled Combustion Control: Scale-Up Experiments and Effect of Fuel Droplet Size," Thirty-Seventh Aerospace Sciences Meeting and Exhibit, AIAA 1999-0328, 1999.

[93] Pang, B., Stamp, G., Marshall, A.W., and Yu, K.H., "Investigation of Two-Phase Flowfield in Actively Controlled Dump Combustor," Thirty-Ninth AIAA/ASME/SAE/ASEE Joint Propulsion Conference and Exhibit, AIAA 2003-4935, 2003.

[94] Pang, B., and Yu, K.H., "Temporal and Spatial Control of Two-phase Reacting Flow," Proceedings of the 16th ONR Propulsion Meeting, pp. 220-225, June, 2003.

[95] Yu, K.H., Schadow, K.C., "A Study On Active Combustion Control For Advanced Combustors," Naval Research Reviews, Vol. 51, No. 3-4, pp. 2-13, 1999.

[96] Hsu, O., Yu, K.H., and Wilson, K.J., "Liquid-fueled Active Combustion Control: Effect of Inlet Flow Temperature," Thirty-Ninth Aerospace Sciences Meeting and Exhibit, AIAA 2001-1131, 2001.

[97] Hoffmann, S., Weber, G., Judith, H., and Hermann, J., "Application of Active Combustion Control to Siemens Heavy Duty Gas Turbines," RTO-MP-14, 1999.

[98] Poinsot, T., Trouve, A., Veynante, D., Andel, S., and Esposito, E., "Vortex Driven Acoustically Coupled Combustion Instabilities," Journal of Fluid Mechanics, Vol. 177, pp. 265-292, 1987.

[99] McManus, K.R., and Bowman, C.T., "Effects of Controlling Vortex Dynamics on the Performance of a Dump Combustor," Twenty-Third Symposium (International) on Combustion, The Combustion Institute, pp. 1093-1099, 1990.

[100] Yu, K.H., Schadow, K.C., "Role of Large Coherent Structures in Turbulent Compressible Mixing," Experimental Thermal and Fluid Science, Vol. 14, pp. 75-84, 1997.

[101] Paschereit, C.O., Gutmark, E., Weisenstein, W., "Coherent Structures in Swirling Flows and Their Role in Acoustic Combustion Control," Physics of Fluids, Vol. 11 No. 9, pp. 2667-2678.

[102] Zukoski, E.E., and Smith, D.A., "Combustion Instability Sustained by Unsteady Vortex Combustion," Twenty-First SAE/ASME/ASEE Joint Propulsion Conference, AIAA 1985-1248, 1985.

[103] Smith, D.A., "An Experimental Study of Acoustically Excited, Vortex Driven, Combustion Instability within a Rearward Facing Step Combustor," Ph.D. Dissertation, California Institute of Technology, 1985.

[104] Sterling, J.D., and Zukoski, E.E., "Longitudinal Mode Combustion Instabilities in A Dump Combustor," Twenty-Fifth Aerospace Sciences Meeting, AIAA 1987-0220, 1987.

[105] Langhorne, P.J., "Reheat Buzz: An Acoustically Coupled Combustion Instability. Part I. Experiment." Journal of Fluid Mechanics, Vol. 193, pp. 417-443, 1988.

[106] Schadow, K.C., Gutmark, E., Parr, T.P., Parr, D.M., Wilson, K.J., and Crump, J.E., "Large-scale Coherent Structures as Drivers of Combustion Instability," Combustion Science and Technology, Vol. 64, No. 4-6, pp. 167-186, 1989.

[107] Kailasanath, K., Gardner, J.H., Boris, J.P., and Oran, E.S., "Numerical Simulations of Acoustic-Vortex Interactions in a Central-Dump Ramjet Combustor," Journal of Propulsion and Power, Vol. 3, No. 6, pp. 525-533, 1987.

[108] Kailasanath, K., Gardner, J.H., Boris, J.P., and Oran, E.S., "Acoustic-Vortex Interactions and Low-Frequency Oscillations in Axisymmetric Combustors," Journal of Propulsion and Power, Vol. 5, No. 2, pp. 165-171, 1989.

[109] Pang, B., Cipolla, S., and Yu, K.H., "Oscillatory Heat Release Associated with Periodic Vortices in Dump Combustor," Forty-First Aerospace Sciences Meeting and Exhibit, AIAA 2003-0115, 2003.

[110] Yu, K.H., Shadow, K.C., "Phase-controlled Mie-scattering Visualization for Studying Periodic Fuel Injection into Oscillating Flowfield," Journal of Flow Visualization and Image Processing, Vol. 4, pp. 201-210, 1997.

[111] Sterling, J.D., "Longitudinal Mode Combustion Instabilities in Air Breathing Engines," Ph.D. Dissertation, California Institute of Technology, 1987.

[112] Pang, B., Yu, K.H., Park, S., Wachsman, A., Annaswamy, A.M., and Ghoniem, A.F., "Characterization and Control of Vortex Dynamics in an Unstable Dump Combustor," Forty-Second Aerospace Sciences Meeting and Exhibit, AIAA 2004-1162, 2004.

[113] Keller, J.O., Vaneveld, L., Korschelt, D., Hubbard, G.L., Ghoniem, A.F., Daily, J.W., and Oppenheim, A.K., "Mechanisms of Instabilities in Turbulent Combustion Leading to Flashback," AIAA Journal, Vol. 20 No. 2, pp. 254-262, 1982.

[114] Yu, K.H., Gutmark, E., Wilson, K.J., and Schadow, K.C., "Active Control of Organized Oscillations in a Dump Combustor Shear Layer," 1st International Symposium on Pulsating Combustion, 1991.

[115] Yu, K.H., Trouve, A., Candel, S., "Combustion Enhancement of A Premixed Flame by Acoustic Forcing with Emphasis on Role of Large-Scale Vortical Structures," Twenty-Ninth Aerospace Sciences Meeting, AIAA 1991-0367, 1991.

[116] Bai, T., Cheng, X.C., Daniel, B.R., Jagoda, J.I., and Zinn, B.T., "Vortex Shedding and Periodic Combustion Process in a Rijke Type Pulse Combustor," Combustion Science and Technology, Vol. 94, No. 1-6, pp. 245-258, 1993.

[117] Yu, K.H., "Active Control of Engine Dynamics: Fundamentals and Fluid Dynamics: Experiments," Active control of engine dynamics, Von Karman Institute for Fluid Dynamics, RTO AVT/VKI special courses, 2001.

[118] Annaswamy, A.M., Fleifil, M., Rumsey, J.W., Prasanth, R., Hathout, J.-P., and Ghoniem, A.F., "Thermoacoustic Instability: Model-Based Optimal Control Designs and Experimental Validation," IEEE Transactions on Control Systems Technology, Vol. 8, No.6, pp. 905-918, 2000.

[119] Evesque, S., Dowling, A.P., and Annaswamy, A.M., "Self-Tuning Regulators for Combustion Oscillations", Royal Society Journal Proceedings of the Mathematical, Physical and Engineering Science, Vol. 459, Issue 2035, pp. 1709-1749, 2003.

[120] Park, S., Wee, D., Annaswamy, A.M., and Ghoniem, A.F., "Adaptive Low-Order Posi-Cast Control of A Combustor Test-Rig Model," IEEE Conference on Decision and Control, 2002.